



**HAL**  
open science

# Effet de la gravité sur la condensation convective à faible vitesse massique

Lan Phuong Le Nguyen

► **To cite this version:**

Lan Phuong Le Nguyen. Effet de la gravité sur la condensation convective à faible vitesse massique. Energie électrique. Université Paul Sabatier - Toulouse III, 2017. Français. NNT : 2017TOU30280 . tel-01955907

**HAL Id: tel-01955907**

**<https://theses.hal.science/tel-01955907>**

Submitted on 14 Dec 2018

**HAL** is a multi-disciplinary open access archive for the deposit and dissemination of scientific research documents, whether they are published or not. The documents may come from teaching and research institutions in France or abroad, or from public or private research centers.

L'archive ouverte pluridisciplinaire **HAL**, est destinée au dépôt et à la diffusion de documents scientifiques de niveau recherche, publiés ou non, émanant des établissements d'enseignement et de recherche français ou étrangers, des laboratoires publics ou privés.



Université  
de Toulouse

# THÈSE

En vue de l'obtention du

## DOCTORAT DE L'UNIVERSITÉ DE TOULOUSE

Délivré par :

Université Toulouse 3 Paul Sabatier (UT3 Paul Sabatier)

---

**Présentée et soutenue par :**

**LE NGUYEN Lan Phuong**

Le jeudi 6 juillet 2017

**Titre :**

Effect of gravity on convective condensation at low mass velocity

---

ED MEGEP : Énergétique et transferts

**Unité de recherche :**

Laboratoire Plasma et Conversion d'Énergie - LAPLACE

**Directeur(s) de Thèse :**

Marc MISCEVIC, MCF at university of Toulouse, LAPLACE, France

Davide DEL COL, professor at university of Padova, DII, Italy

Encadrant: Pascal LAVIEILLE, MCF at university of Toulouse, LAPLACE, France

**Rapporteurs :**

DI MARCO Paolo, professor at l'university of Pisa, DESTEC, Italy

STUTZ Benoit, professor at polytech Annecy-Chambéry, LOCIE, France

**Autre(s) membre(s) du jury :**

PITCHFORD Leanne, CNRS Research director, LAPLACE, France

FILIPPESCHI Sauro, assistant professor at university of Pisa, DESTEC, Italy





UNIVERSITÀ  
DEGLI STUDI  
DI PADOVA

Sede Amministrativa: Università degli Studi di Padova

Dipartimento di Ingegneria Industriale  
SCUOLA DI DOTTORATO DI RICERCA IN INGEGNERIA  
INDUSTRIALE, INDIRIZZO IN INGEGNERIA DELL' ENERGIA  
CICLO XXII

# EFFECT OF GRAVITY ON CONVECTIVE CONDENSATION AT LOW MASS VELOCITY

**Direttore della Scuola:** Ch.mo Prof. MARC MISCEVIC

**Supervisore:** Ch.mo Prof. DAVIDE DEL COL

**Co-supervisore/i:** Ch.mo Prof./Dott. PASCAL LAVIEILLE

**Dottorando/a:** LAN PHUONG LE NGUYEN

Data consegna tesi



# ACKNOWLEDGMENT

Firstly, I would like to thank my supervisors: Mr. Marc Miscevic, Mr. Davide Del Col and Mr. Pascal Lavieille who gave me a great opportunity to work in a cotutelle PhD thesis in collaboration between Padova university and Paul Sabatier university. Their ideas, availability enabled me to realize my thesis in a formidable condition. I couldn't know how to express my gratitude to these people. During thesis period, in any situation or wherever I am, they are always listening to me. For me, they are ones of the best people I have met.

Secondly, I would like to thank Mr Di Marco Paolo, Mr Stutz Benoit, for agreeing to be reviewers of my thesis. They shared their time for reading my manuscript with such attention and bringing enriching insights into this work. Then, I would like to express my appreciation to Ms. Pitchford Leanne for being the jury chair. Finally, I would like to thank to Mr. Filippeschi Sauro for agreeing to be a jury member. His remarks and questions brought new insights to this project.

I would also like to thank to Mr. Jacques Lluc for his technical and friendly help in implementation and operation of the experimental system for many hours, as well as to all the technical and electronic services of the Laplace laboratory. I would also like to thank Stefano Bortolin and Marco Azzolin for their help and scientific advice during my stay in Italy. I would like to thank all members of the ENCOM2 project, especially Patrick Quekkers and Andrey Sayssok of the University of Brussels for their contribution and help during my stay in Belgium.

I would never forget all the people at Paul Sabatier University and Padova University with whom I had great moments: Felipe, Marie, Baptiste, Alex, Marco, Stefano, Paolo, Simone, Matteo ...

Finally, I would like to express my thanks to my family who supported me until the end of my studies. Especially my husband and my little daughter who are always beside me and gave me a lot of motivation and energy to finish this thesis.

Many thanks



# ABSTRACT

Liquid-vapor two-phase flows have common applications in many fields including space thermal management systems. The performances of such systems are entirely associated to the coupling between thermal and hydrodynamic phenomena. Therefore, two-phase flows in microgravity condition have emerged as an active research area in the last decades.

In order to complete the state of the art and to contribute to the increase in the knowledge of hydrothermal behavior of two-phase thermal management systems, the present study was conducted on convective condensation inside a mini tube, both in normal and micro gravity conditions.

To analyze the effect of gravity on such flows, a preliminary transient modeling of the two-phase flow has been established. Simultaneously, an experimental investigation was carried out on the hydrodynamic and thermal behaviors of condensation flows in two test sections of 3.4 mm inner diameter at low and intermediate mass velocities. The first experiment was conducted during the 62nd ESA parabolic flights campaign. The test section was made with copper and allowed measurements of the quasi-local heat transfer coefficient. A glass tube was also inserted in the middle of the test section for the visualization of the two-phase flow regime. From this study, the changes in heat transfer coefficient and flow regime according to gravity variations were determined. The second experiment was carried out on ground in a sapphire tube installed vertically considering downward flow. The set-up was designed in order to measure simultaneously the local heat transfer coefficient and the thickness of the liquid film falling down along the tube wall.

Keywords : micro-gravity, convective condensation, HFE-7000, mini-tube, heat transfer, visualisation, low mass velocity



## RIASSUNTO

Lo scambio termico bifase trova applicazione in molti settori, tra cui il controllo termico dei sistemi aerospaziali. Le prestazioni di questi sistemi bifase sono influenzate dall'interazione tra fenomeni termici e idrodinamici. Negli ultimi anni, il deflusso bi-fase in condizioni di gravità ridotta è diventato oggetto di diversi studi.

Il presente lavoro indaga il fenomeno della condensazione all'interno di canali in condizioni di gravità terrestre e di gravità ridotta, al fine di colmare il vuoto presente nello stato dell'arte e di aumentare le conoscenze sul comportamento idrodinamico e termico dei sistemi termici con deflusso bifase.

Per analizzare l'effetto della gravità su tali tipi di deflusso, lo studio preliminare si è concentrato su un modello transitorio del deflusso bifase. Contemporaneamente è stata condotta un'indagine sperimentale sui comportamenti idrodinamici e termici durante la condensazione in una sezione di prova con diametro interno pari a 3.4 mm con portate specifiche ridotte. Il primo esperimento è stato effettuato durante la 62a campagna di voli parabolici dell'Agenzia Spaziale Europea. La sezione di prova è stata realizzata partendo da un tubo in rame e ha permesso di misurare il coefficiente di scambio termico quasi locale. Un tubo di vetro è stato inserito tra i due scambiatori della sezione sperimentale per la visualizzazione del regime di flusso. Con questo studio si sono potute determinare le variazioni del coefficiente di scambio termico e del regime di deflusso in funzione della gravità. Il secondo esperimento è stato condotto a terra utilizzando un tubo in zaffiro durante il deflusso verticale con moto verso il basso. La nuova sezione sperimentale in zaffiro è stata progettata per misurare contemporaneamente il coefficiente di scambio termico locale e lo spessore del film liquido che si forma all'interno del tubo.

Parole chiave: gravità ridotta, condensazione convettiva, HFE-7000, mini-canali, scambio termico, visualizzazioni, portata di massa ridotta



# Contents

<b>Introduction</b>	<b>1</b>
<b>I State of the art</b>	<b>5</b>
I.1 Convective condensation inside conventional and mini channels . . . . .	6
I.1.1 Two phase flow pattern regimes in conventional and mini-tubes	6
I.1.2 Flow pattern maps . . . . .	9
I.1.3 Pressure drop of condensation two-phase flow inside conventional and mini tubes . . . . .	16
I.1.4 Heat transfer of condensation inside conventional and mini channels	19
I.2 Convective condensation inside micro channel . . . . .	30
I.2.1 Two phase flow pattern map in micro tube . . . . .	30
I.2.2 Pressure drop of two phase flow in micro tube . . . . .	37
I.2.3 Heat transfer coefficient inside micro tube . . . . .	38
I.3 Conclusion . . . . .	43
<b>II Opening model for condensation’s instabilities in a micro-channel</b>	<b>45</b>
II.1 Investigation of convective condensation inside condenser multi-channels	46
II.2 One dimensional two-fluid model . . . . .	49
II.2.1 Geometric configuration . . . . .	50
II.2.2 1D model . . . . .	51
II.2.3 Additional assumptions and closure laws . . . . .	53
II.2.4 Boundary and initial conditions . . . . .	55
II.2.5 Numerical solution . . . . .	56
II.2.6 Analyses of linear stability . . . . .	59
II.3 Conclusion . . . . .	62
<b>III Measurements of condensation inside a mini-channel during parabolic flights</b>	<b>63</b>
III.1 Preparation for parabolic flight experiment . . . . .	65
III.1.1 Micro-gravity simulation . . . . .	65
III.1.2 Condenser length design . . . . .	66
III.1.3 Characteristic time evaluation . . . . .	68

III.1.4	Consideration for an accurate determination of the HTC in the condenser . . . . .	72
III.2	Concept of condenser for condensation experiments . . . . .	78
III.2.1	Test section for parabolic flight experiments . . . . .	78
III.2.2	Boundary effects . . . . .	80
III.2.3	Calibration of test section . . . . .	88
III.3	Experimental investigation of condensation in parabolic flights . . . . .	93
III.3.1	Experimental apparatus . . . . .	93
III.3.2	Experimental procedure . . . . .	97
III.3.3	Experimental results of heat transfer coefficient . . . . .	98
III.3.3.1	Analysis of the transient effect . . . . .	98
III.3.3.2	Heat transfer coefficients . . . . .	101
III.3.4	Investigation of flow pattern . . . . .	103
III.3.5	Film thickness measurement analysis . . . . .	107
III.3.5.1	Ray tracing method and calibration curve . . . . .	107
III.3.5.2	Gravity effect on flow regime and film thickness . . . . .	112
III.4	Conclusion . . . . .	123
<b>IV</b>	<b>Set-up and measurement protocol on the vertical down stream sapphire test section on-ground</b>	<b>125</b>
IV.1	Experimental apparatus . . . . .	126
IV.1.1	Description . . . . .	126
IV.1.2	Test section and instrumentation . . . . .	131
IV.1.2.1	Test section . . . . .	131
IV.1.2.2	Inlet and outlet reservoir . . . . .	132
IV.1.2.3	Heating chamber . . . . .	132
IV.1.2.4	Air as secondary fluid . . . . .	132
IV.1.2.5	Mass flow rate . . . . .	132
IV.1.2.6	Acquisition system . . . . .	133
IV.1.2.7	Thermal camera . . . . .	133
IV.1.2.8	Interferometry . . . . .	134
IV.1.3	Measurement protocol and calibration procedure . . . . .	137
IV.1.3.1	Verification of vertical position of the tube . . . . .	138
IV.1.3.2	Filling and degassing . . . . .	138
IV.1.3.3	Calibration of thermocouple and absolute pressure transducer . . . . .	139
IV.1.3.4	Verification of degassing procedure and determination of the saturation curve for refrigerant HFE-7000 . . . . .	141
IV.1.3.5	First developments and analysis in order to determine wall temperature by infrared camera . . . . .	143
IV.2	Experimental results and discussion . . . . .	148
IV.2.1	Calibration procedure . . . . .	148
IV.2.1.1	Calibration curves for infrared camera . . . . .	148

---

IV.2.2	External heat transfer coefficient . . . . .	160
IV.2.3	Experimental tests . . . . .	167
IV.2.3.1	A test procedure . . . . .	167
IV.2.3.2	Test series . . . . .	168
IV.2.4	Condensation heat transfer coefficient and film thickness measurement of HFE-7000 . . . . .	168
IV.2.4.1	Condensation heat transfer coefficient measurement . . . . .	168
IV.2.4.2	Film thickness measurement . . . . .	175
IV.3	Conclusion and perspective . . . . .	178
	<b>Conclusion and perspectives</b>	<b>181</b>



# List of Figures

I.1	The succession of different flow regimes in the convective condensation at low mass flux and high mass flux inside centimeters hydraulic diameter pipe (figures taken from [1]). . . . .	7
I.2	Flow regimes and flow patterns for condensation in mini-channels ( $1\text{ mm} < Dh < 4.9\text{ mm}$ ) during condensation of refrigerant R134a with mass velocities from 150 to 750 $kg.m^{-2}.s^{-1}$ (figure taken from [2]). . . . .	8
I.3	Flow pattern maps of air-water at 25 <sup>0</sup> C for 50 mm internal diameter tubes developed by Taitel et al. (a): For horizontal tube at 1 atm [3],(b): For vertical tube at 1 atm [4] . . . . .	9
I.4	Flow regime map for convective condensation of R-134 in a 9.53 mm horizontal channel with new line transition regime (in comparison to that of El Hajal et al. [5]) (figure taken from [6]). . . . .	11
I.5	A comparison of experimental result of two-phase flow of air-water obtained by Coleman and Garimella [7] inside 5.5mm round tube with flow pattern maps developed by Damianides and Westwater [8] inside a 5 mm internal tube and by Taitel and Dukler[3]. . . . .	12
I.6	Comparison between flow pattern maps for adiabatic water-air flow and condensation flow of R134a inside 4.91mm hydraulic diameter tube [2]. . . . .	14
I.7	Effect of tube inclination on flow pattern map for water-air flow in a 12.7 mm hydraulic diameter tube [9]. . . . .	15
I.8	Effect of inclination angles on pressure drop at different mass fluxes and vapor qualities of a)0.25 b)0.5 and c)0.75 at saturation temperature of 30 <sup>0</sup> C	19
I.9	A comparison of actual model of Hajal et al. with experimental results of eleven different refrigerants [10]. . . . .	23
I.10	Application of the Cavallini et al. model to HFC pure fluids and an azeotropic mixture [11] . . . . .	25
I.11	Inclination effect on heat transfer coefficient for a) different vapor qualities at a constant mass velocity of 300 $kg.m^{-2}.s^{-1}$ b) different mass velocities at a constant vapor quality of 0.5 . . . . .	27
I.12	The two test sections used by Lee et al. [12] to analyze convective condensation in microgravity condition. . . . .	28

---

I.13	Variation of condensation heat transfer at four axial locations during gravity changes corresponding to two microgravity parabolas for $G = 264.1 \text{ kg.m}^{-2}.\text{s}^{-1}$ and inlet vapor quality of 0.73 at different positions. . . . .	29
I.14	The effect of superficial gas velocity on flow patterns of two phase flow inside $510 \times 470 \text{ }\mu\text{m}^2$ [13]. . . . .	31
I.15	The effect of superficial gas velocity on flow patterns of two phase flow inside $510 \times 470 \text{ }\mu\text{m}^2$ . . . . .	32
I.16	Structure of the different flow patterns encountered during the condensation process in a square cross-section micro-channel with n-pentane working fluid at $5 \text{ kg.m}^{-2}.\text{s}^{-1}$ with $22.62^0 \text{ C}$ conditioning air temperature in three different moments: (a) $t=0 \text{ ms}$ ; (b) $t=50 \text{ ms}$ ; (c) $t=51 \text{ ms}$ [14] . . . .	34
I.17	Evolution of average vapor quality at the location of formation of liquid bridge according the mass velocity for a) HFE-7000 flow at $23.13^0\text{C}$ conditioning temperature b) n-pentane flow at $22.67^0\text{C}$ air conditioning temperature [14]. . . . .	35
I.18	The experimental results of instability of the motion of silicon oils and glycerol inside micro tube [15]. . . . .	36
I.19	Test section schematic and micro-channel shapes used by Akhil Agarwal et al.[16], [17]. . . . .	42
II.1	The schema of condenser installation during test with n-pantane working fluid and an obtained flow regime inside 4 condensers for total mass velocity of $5.45 \text{ kg.m}^{-2}.\text{s}^{-1}$ and for flux density of $3970 \text{ W.m}^{-2}$ [14]. . . . .	46
II.2	Flow distribution inside 4 condensers for total mass velocity of $5.45 \text{ kg.m}^{-2}.\text{s}^{-1}$ and for flux density of $3970 \text{ W.m}^{-2}$ recorded by high speed camera recorded by El Achkar et al. [14]. . . . .	47
II.3	Flow distribution inside 4 condensers with mass velocity of $5.45 \text{ kg.m}^{-2}.\text{s}^{-1}$ and for flux density of $3970 \text{ W.m}^{-2}$ recorded by high speed camera and wave's position evolution versus time obtained from image processing program. . . . .	48
II.4	Evolution of average vapor velocity while liquid bridge arrives for n-pentane working fluid and flux density of $3970 \text{ W.m}^{-2}$ [experimental data measured by El Achkar et al.[14] at Laplace laboratory, University of Paul Sabatier]. . . . .	49
II.5	Geometrical configuration studied. The cooling is ensure by a flow of cold fluid at a constant temperature and with a constant external heat transfer coefficient over the whole length of the channel. Flow is assumed to be axisymmetric. . . . .	50
II.6	Vapor and liquid velocities' profiles assumed for this model. . . . .	55
II.7	Finite volume of uni-dimension around node i. . . . .	57
II.8	The axial profiles obtained with the assumption of annular uniform profile of interface. . . . .	58
II.9	Algorithm employed to determine the evolution of all parameters during time. . . . .	59

---

III.1	Configuration of a the studied domain between $z$ and $z+\Delta z$ with working fluid and secondary fluid in counter-current.. . . . .	67
III.2	Response time at different test conditions a) Internal heat transfer coefficient variations from 2000 to 1500 $Wm^{-2}K^{-1}$ with external heat exchange of 1000 $Wm^{-2}K^{-1}$ . b) Internal heat transfer coefficient variations from 2000 to 1500 $Wm^{-2}K^{-1}$ with external heat exchange of 4000 $Wm^{-2}K^{-1}$ . c) Internal heat transfer coefficient variations from 3000 to 2000 $Wm^{-2}K^{-1}$ with external heat exchange of 5000 $Wm^{-2}K^{-1}$ . . . . .	69
III.3	Configuration of liquid-vapor interface of stirring magnetic machine . . . .	70
III.4	Shape of the liquid-vapor interface in the evaporator for a constant filling ratio of 0.4 and for various speed of rotation : a) N=400 rpm b) N=600 rpm c) N=1000 rpm d) N=1200 rpm . . . . .	71
III.5	The configuration of simulated 100mm heat exchange with water in grey and copper in red. . . . .	72
III.6	Water circulation (in grey) and copper tube design (in red) of 100mm segment of the condenser.. . . . .	73
III.7	The temperature distribution when inner heat transfer coefficient is 5000 $W.m^{-2}.K^{-1}$ and a temperature of 40°C inside tube equivalent $T_{sat}$ ; water temperature and mass flow rate at the inlet of 25°C and 0.8 $m.s^{-1}$ . . . . .	74
III.8	Temperature field in the cross section at the inlet, middle and at the outlet	75
III.9	Position of fins where the temperature are measured for the calculation of heat transfer coefficient.. . . . .	76
III.10	The sketch of a subsection of 128 mm length for the heat exchange and picture of the machined copper tube.. . . . .	79
III.11	Whole test section designed for both on ground and parabolic flight experiments. . . . .	80
III.12	The geometry of a sub-section of 100 mm heat exchange used for Fluent simulation . . . . .	81
III.13	Temperature profiles of the wall and the water for a heat transfer coefficient of 6000 $W.m^{-2}.K^{-1}$ and a saturation temperature of 40°C, 5 million meshes and inlet water temperature of 20° C. The temperature gradients in the wall at the entrance and exit of the heat exchanger (upstream and downstream of the black lines) show that axial heat conduction is present and is not symmetrical. This effect must be taken into account to evaluate the heat transfer coefficient. . . . .	83
III.14	Trend of $Q_{axial}/(\Delta T_{log}.A_{tube})$ as a function of calculated heat transfer coefficient in the exchange zone for a) 100 mm length sub-sector and b) 128 mm length sub-sector.. . . . .	86
III.15	Experimental loop used to validate the test section in Padova university: FD (filter drier); PV (pressure vessel); CFM (Coriolis-effect mass flow meter); TV (throttling valve); MF (mechanical filter); HF (Dehumidifier); P (relative pressure transducer); DP (differential pressure transducer); T(thermocouple).. . . . .	89

---

III.16	The condensation test section installed in the experimental test rig of Padova university. . . . .	90
III.17	Wall temperatures before and after calibration . . . . .	91
III.18	Heat dissipation to the environment measured at a) second and b)third sub-sections.. . . .	92
III.19	All temperature profiles in test section. . . . .	92
III.20	Schema of the final loop for condensation tests used in parabolic flights.. .	94
III.21	The schema of final loop used in parabolic flights . . . . .	96
III.22	Picture of the test section installed into the loop and ready for flight. . . .	97
III.23	Experimental facility installed and ready to operate in the plane. . . . .	97
III.24	Configuration of experimental test section. . . . .	99
III.25	Quasi local heat transfer coefficient as a function of vapor quality for a mass velocity of $70 \text{ kg.m}^{-2}.s^{-1}$ : - left: the same experiment repeated 6 times in microgravity condition. - Right: gravity effect.. . . .	102
III.26	Heat transfer coefficient trends in microgravity and normal gravity conditions and for mass velocity of 100 and $170 \text{ kg.m}^{-2}.s^{-1}$ . . . . .	102
III.27	Ratio of the experimental heat transfer coefficient in microgravity and in normal gravity conditions for HFE-7000 working fluid at the different mass velocities ranging from 70 to $175 \text{ kg.m}^{-2}.s^{-1}$ and vapor qualities of 0.8, 0.6 and 0.4. . . . .	103
III.28	Flow pattern observed during condensation of HFE-7000 in normal (1,2,3) and microgravity (4,5,6) conditions at $G=170 \text{ kg.m}^{-2}.s^{-1}$ and $x=0.64$ . . .	104
III.29	Flow pattern observed during condensation of HFE-7000 in normal (1,2,3) and microgravity conditions (4,5,6) at $G=70 \text{ kg.m}^{-2}.s^{-1}$ and $x=0.32$ . . .	105
III.30	Evolution of the wall temperatures in the third sub-sector (immediately upstream the glass tube) during parabolic flight at three different positions for $G=70 \text{ kg.m}^{-2}.s^{-1}$ . . . . .	107
III.31	The optical configuration employed for ray tracing simulation . . . . .	108
III.32	Ray propagation from parallel light source to the camera receiver and reconstructed image on the camera.. . . .	109
III.33	Photo recorded with the tube full of liquid compared to the simulation one by ray tracing method.. . . .	111
III.34	Calibration curve obtained by the ray tracing method correlating the apparent (or seen) film thickness acquired by the camera to the real film thickness. . . . .	112
III.35	Original image a) and b) post-processed image using Matlab tool where liquid region is in blue and liquid contours are in green.. . . .	113
III.36	Flow regimes obtained in a) Normal gravity and b) Microgravity at mass velocity of $70 \text{ kg.m}^{-2}.s^{-1}$ and vapor quality of 0.24. . . . .	114
III.37	Flow regimes obtained at a) Normal gravity and b) Microgravity at mass velocity of $170 \text{ kg.m}^{-2}.s^{-1}$ and vapor quality of 0.64. . . . .	115
III.38	Example of image processing to obtain the apparent film thickness variation (in pixel) in normal gravity.. . . .	116

---

III.39	Profiles of liquid film thickness considering the two extreme values for the non-detectable liquid film thickness in micro gravity condition at $G=70 \text{ kg.m}^{-2}.\text{s}^{-1}$ and $x=0.30$ . . . . .	117
III.40	Top and bottom film thicknesses evolution for different vapor qualities and at mass velocity of $70 \text{ kg.m}^{-2}.\text{s}^{-1}$ a) In gravity condition and b) In microgravity condition. . . . .	118
III.41	Evolution of film thickness at the bottom and on the top in normal gravity and microgravity for different mass velocities and vapor qualities. . . . .	119
III.42	Film thickness as a function of heat transfer coefficient for different mass velocity in microgravity condition with two assumptions about invisible film thickness: For the "low" hypothesis when the film thickness is not visible, its value is set to 0. For the "high" hypothesis the thickness of invisible film is set to $106.5 \mu\text{m}$ corresponding to the minimum value that can be detected. . . . .	120
III.43	Heat transfer coefficient as a function of the measured average film thickness or the calculated film thickness . . . . .	121
III.44	Illustration of the difference between $\frac{1}{\delta}$ and $\frac{1}{\delta}$ according to the value of $\delta$ .	123
IV.1	Scheme of complete loop test used for this investigation. . . . .	126
IV.2	The real complete apparatus built at the laboratory. . . . .	128
IV.3	The air-conditionner conduct for the secondary fluid. . . . .	129
IV.4	The photo presents a) The general view of robot system with the arm to fix the interferometer position b) The winch attaching the robot c) The relative position of interferometer to the infrared camera. . . . .	130
IV.5	The complete STIL DUO employed to measure liquid film thickness with two pencils: one for confocal mode and one for interferometer mode. . . . .	134
IV.6	Schema illustrating the principle of white light interferometric measurement. . . . .	135
IV.7	The specific system used for filling the refrigerant to inlet reservoir. . . . .	138
IV.8	Set up used for on-site calibration of two absolute pressure transducers. . . . .	140
IV.9	Calibration curves of P1 and P2 to convert analogue signal to absolute pressure. . . . .	140
IV.10	The inlet or outlet reservoir employed during tests. . . . .	141
IV.11	The saturation curve obtained by calibration procedure. . . . .	143
IV.12	The transmittance of HFE-7000 measured for wavenumbers from 500 to $4000 \text{ cm}^{-1}$ with a depth of $60 \mu\text{m}$ at the university Paul Sabatier, Toulouse, France by Corinne Routaboul. . . . .	144
IV.13	An example of the measured intensity distribution by infrared camera for a water flow at axial position from 523 mm to 584 mm and for inlet and outlet temperatures of $34.55^\circ\text{C}$ and $34.43^\circ\text{C}$ respectively. The ambient temperature was $26^\circ\text{C}$ . . . . .	145
IV.14	The calibration curves of water and black paint at the middle point of recorded window obtained by circulating water. . . . .	146

IV.15	All contributions in a measured radiative flux received by the infrared camera from a gray body. . . . .	147
IV.16	Presentation of detected zones : black paint region and water emission region. The inlet water temperature is 45°C and a temperature drop of 0.25°C from the inlet to the outlet of whole test section has been measured. Part : a) Original image recorded by infrared camera and same image with a modification of scale intensity in order to visualize the black region in the middle delimited by green lines, and water region delimited by black boundaries and sapphire internal and external walls delimited by yellow and red lines b) The two boundaries radiative flux profile of black paint region (following the two green lines) c) Radial radiative flux profile at cut A-A or in the middle of recorded window. . . . .	150
IV.17	Calibration intensity trend versus position in pixel at vertical position of 523 mm (at the pixel 320 of the window) from the inlet test section for different inlet temperatures (the whole temperature drop from inlet test section to outlet test section of 0 to 0.35°C). a) Water b) Black paint zone.	151
IV.18	The superimposed calibration intensity trends of water and black paint versus position in pixel at vertical position of 523 mm from the inlet test section for different inlet temperatures (the whole temperature drop from inlet test section to outlet test section is less than 0.35°C). . . . .	152
IV.19	Radiative flux received versus temperature at the column number 320 in the camera window far from the inlet of test section for both water and black paint. . . . .	153
IV.20	The three studied positions with the temperature drop in each case. . . .	154
IV.21	Superposition of water calibration curves for the column number 320 of the sensor matrix at three different positions described in figure above at the same inlet and outlet conditions and the same day (17th November). . . . .	155
IV.22	Superposition of black paint calibration curves for the column number 320 of the sensor matrix at three different positions at the same inlet and outlet conditions at three different positions described in figure above and the same day (17th November). . . . .	156
IV.23	The two calibration curves at the column number 250 of the camera sensor (far from the beginning of infrared camera window) at ambient temperature of 23°C and 26°C a) For water b) For black paint c) Ambient temperature's evolution during the two experiments. . . . .	157
IV.24	Shift of referent image by a constant at a position in infrared window. . . .	158
IV.25	Water calibration curve at ambient temperature of 23°C and corrected water calibration from the referent one at ambient temperature of 26°C at the column number 320 of the camera sensor. . . . .	159
IV.26	Variation of error between the real temperature and the calculating one using the referent calibration curve or by using the corrected one at the mean temperature of 40°C. a) For water b) For black paint. . . . .	160
IV.27	External heat transfer coefficient measurement procedure. . . . .	161

---

IV.28	Internal wall temperature profile converted from the radiative flux received by thermal camera by using the calibration matrix. a) Original photo obtained by infrared camera with water zone inside white bands b) Converted profile temperature. . . . .	162
IV.29	Water temperature profiles for a) Water mass flow rate of 33.4 ml/min and forced air conditioner at cooling mode (T air conditioner=15°C) b) Water mass flow rate of 32.3 ml/min at forced air conditioner and ambient temperature (T air conditioner=27.8°C). . . . .	163
IV.30	Representation of heat exchanges in the domain between $z$ and $z + \delta z$ . . .	164
IV.31	Profile of a) The local heat flux b) Heat transfer coefficient obtained with a water mass flow rate of 33.4 ml/min and forced air conditioner at cooling mode (T air conditioner=15°C) b) The forced air conditioner's velocity measured by hot wire anemometer. . . . .	166
IV.32	Profiles of the external heat transfer coefficient obtained for a water mass flow rate of 33.4 ml/min and with forced air at cooling mode of 15°C air temperature and 20 ml/min and with forced air conditioner at ambient temperature mode. . . . .	167
IV.33	Results obtained at 240 mm from the inlet of the sapphire tube in the case of HFE-7000 as the working fluid without forced air flow a) the original image obtained by infrared camera b) the temperature profile versus position converted from radiative flux received from paint. The two black lines represented the borders of the zone taken into consideration (the left and right border zones of the sensor matrix are rejected due to the sensitivity to the focus setting). . . . .	169
IV.34	Temperature difference between the saturation and the wall temperature versus position with HFE-7000 as the working fluid without forced air flow. . . . .	171
IV.35	The profile of a) external wall temperature and saturation temperature during condensation test at mass velocity of $30 \text{ kg.m}^{-2}.\text{s}^{-1}$ b) temperature difference between saturation temperature and external wall temperature without forced air flow. . . . .	172
IV.36	Inner heat transfer coefficient of HFE-7000 versus position considering measured wall temperature and measured wall temperature plus $0.6^\circ\text{C}$ . . .	173
IV.37	Inner heat transfer coefficient of HFE-7000 versus axial position for 3 different mass velocities. . . . .	174
IV.38	The figure presents three temporal evolution in hundred of seconds at 40 mm far from the inlet at mass velocity of $30 \text{ kg.m}^{-2}.\text{s}^{-1}$ . The first is related to the path difference measured. The second graph presents signal quality factor and the last one the reflected intensity of light. . . . .	176
IV.39	Variation of the conduction thermal resistance in the liquid film and of the convective internal resistance as a function of the position for mass velocity of $30 \text{ kg.m}^{-2}.\text{s}^{-2}$ . . . . .	178
IV.40	Liquid-vapor interface in a centrifugal evaporator. . . . .	185
IV.41	Gravitational force in the studied domain. . . . .	188

IV.42 Sum of pressure in the studied domain. . . . . 190

# List of Tables

II.1	Definition of the model's interface variables and source terms. . . . .	52
II.2	Boundary condition found with all assumptions above. . . . .	56
III.1	Exchange parameters at mass flux of $200 \text{ kg.m}^{-2}.\text{s}^{-1}$ for a tube of 3mm hydraulic diameter. . . . .	67
III.2	The necessary length if vapor quality at the outlet is 0. . . . .	68
III.3	Comparison of inner heat transfer coefficient imposed and the calculated one for different values. . . . .	77
III.4	CFD analysis with different simulation cases was performed. . . . .	82
III.5	Simulation results of CFD for imposed heat transfer coefficient of $850 \text{ W.m}^{-2}.\text{K}^{-1}$ with different numbers of meshes. . . . .	83
III.6	Simulation results of CFD for imposed heat transfer coefficient of $5000 \text{ W.m}^{-2}.\text{K}^{-1}$ with different numbers of meshes. . . . .	84
III.7	Simulation results of CFD for imposed heat transfer coefficient of $850 \text{ W.m}^{-2}.\text{K}^{-1}$ with different water temperature at the inlet. . . . .	84
III.8	Simulation results of CFD for imposed heat transfer coefficient of $5000 \text{ W.m}^{-2}.\text{K}^{-1}$ with different water temperature at the inlet. . . . .	85
III.9	Axial heat flux obtained from simulation results for subsection of 100 mm length . . . . .	86
III.10	Various cases tested for simulation of a sector of 128mm length. . . . .	87
III.11	Heat transfer coefficient evaluated with axial correction for 100mm length. . . . .	88
III.12	Heat transfer coefficient evaluated with axial correction for 128mm length. . . . .	88
III.13	Heat balance verification of water and refrigerant. . . . .	93
III.14	Two phase condition inside adiabatic glass tube. . . . .	114



Nomenclature

$A$	cross area [ $m^2$ ]
$a(chap.1)$	capillary length [m]
$c$	constant [-]
$c_p$	thermal capacity [ $J.kg^{-1}.K^{-1}$ ]
$D$	diameter $m$
$e(chap.2)$	liquid film thickness [ $\mu m$ ]
$Fr$	Froude number [-]
$f_i$	inter-facial roughness correction factor [-]
$g$	gravity acceleration [ $m.s^{-2}$ ]
$G$	Mass flux [ $kg.m^{-2}.s^{-1}$ ]
$h$	heat transfer coefficient, [ $W.m^{-2}.K^{-1}$ ]
$H$	enthalpy per unit volume [ $J.m^{-3}$ ]
$I$	fluorescence intensity [ $U.A$ ]
$L$	length [m]
$L_c$	Characteristic length [m]
$l_v$	latent heat [ $J.kg^{-1}$ ]
$\dot{m}$	mass flow rate [ $kg.s^{-1}$ ]
$Nu$	Nusselt number [-]
$p$	pressure [Pa]
$P(chap.2)$	perimeter [m]
$P$	average pressure in a cross section [Pa]
$Q$	Heat exchange [W]
$Q$	heat flux [W]
$Re$	Reynold number[-]
$R(chap.2)$	radius [m]
$R$	thermal resistance [ $K.W^{-1}$ ]
$Su$	Suratman number [-]
$S$	exchange area [ $m^2$ ]
$t$	time [s]
$T$	temperature [K]
$u$	velocity [ $m.s^{-1}$ ]
$u^*$	friction velocity [ $m.s^{-1}$ ]
$U$	average velocity in a cross section [ $m.s^{-1}$ ]
$U^2$	average square of velocity [ $m^2.s^{-2}$ ]
$We$	Weber number [-]
$x$	vapor quality [-]
$X$	Lockhart-Martinelli number [-]
$y$	distance perpendicular to wall [m]
$z$	axial position of tube [m]

*Greek symbols*

$\alpha$ (chap.1)	void fraction [-]
$\alpha$ (chap.2)	heat transfer coefficient [ $W.m^{-2}.K^{-1}$ ]
$\alpha_{RA}$	void fraction of non homogeneous two phase proposed by Rouhani-Axelsson [-]
$\beta$	channel aspect ratio [-]
$\Delta T$	$T_{sat} - T_w$ [K]
$\delta$	liquid film thickness [ $m$ ]
$\epsilon$ (chap.2)	void fraction [-]
$\lambda$ (chap.1)	thermal conductivity [ $W.m^{-1}.K^{-1}$ ]
$\lambda$ (chap.3)	wave length [ $m$ ]
$\mu$	dynamic viscosity [ $Pa.s$ ]
$\nu$	kinematic viscosity [ $m^2.s^{-1}$ ]
$\omega$	rotary speed [ $rad.s^{-1}$ ]
$\Phi$ (chap.3)	heat flux [ $W.m^{-2}$ ]
$\Phi^2$	liquid phase multiplier [-]
$\phi$ (chap.1)	heat flux [ $W.m^{-2}$ ]
$\rho$	density [ $kg.m^{-3}$ ]
$\sigma$	surface tension [ $N.m^{-1}$ ]
$\theta$	angle [°]
$\tau$	shear stress [ $N.m^{-2}$ ]
$\epsilon_m$	eddy momentum diffusivity [ $Pa.s$ ]

*Subscripts*

<i>amb</i>	ambiance
<i>c</i>	coolant
<i>c1s</i>	coolant in first sector
<i>c2s</i>	coolant in second sector
<i>c3s</i>	coolant in third sector
<i>c4s</i>	coolant in fourth sector
<i>c5s</i>	coolant in fifth sector
<i>cap</i>	capillary
<i>cond</i>	condensation
<i>ctot</i>	coolant in all sectors
<i>de - sh</i>	desuperheat
<i>ext</i>	external
<i>h</i>	hydraulic
<i>Hm</i>	homogeneous
<i>in</i>	internal
<i>i</i>	interface

<i>L</i>	liquid
<i>Lo</i>	liquid phase with total flow rate
<i>log</i>	logarithmic
<i>mix</i>	mixture
<i>out</i>	outlet
<i>ref</i>	refrigerant
<i>strat</i>	fully stratified flow regime
<i>sat</i>	saturation
<i>sub</i>	sub-cooling
<i>S</i>	superficial
<i>TP</i>	two phase
<i>V</i>	vapor
<i>Vo</i>	vapor phase with total flow rate
<i>w</i>	wall



# Introduction

Two-phase flows (vapor-liquid) have commonly important applications in many fields such as: cooling in space, cooling of embedded systems... These systems allow transporting heat flux from hot source to cold source by using the phase change mechanisms (evaporation and condensation) to absorb and reject heat. Their performances are thus entirely associated with the system architecture and the coupling between thermal and hydrodynamic mechanisms. Therefore many researches have been undertaken to understand and improve their performances. Due to their popular existence in industrial processes and in ordinary life (as for example: engineering processes, air conditioning and refrigeration systems, and heat exchangers...), two-phase flows have been widely studied. Heat pipes are the first two-phase cooling systems that have been used. Today, they are largely used in space field. However, their heat transport capacities are still limited and become insufficient for some applications. Possible solutions are the mechanically pumped two-phase loop and the two-phase loops with capillary pumping.

Two types of two-phase loops with capillary pumping exist: CPL (Capillary-Pumped Loops) and LHP (Loop Heat Pipes). Even though they have different technology, these systems have a large number of similarities. The main parts of these systems are: the condenser, the evaporator, a vapor line, a liquid line, a compensation chamber. Among parts of these systems, condenser plays a major roles in both the overall performance of the loop and its stability.

In recent decades, convective condensation has been extensively studied primarily in conventional channels (diameter greater than 8 mm) and a number of correlations to predict the heat transfer coefficients and two-phase flow laws were developed. More recently, due to the growing interest in miniature devices, the researchers focused their attention on micro-channels with a hydraulic diameter of about or less than 1 mm. For intermediate diameters, which industrial interest is also considerable, most of the studies focus on high mass velocities. For low mass velocities for ground and spatial applications, available designs are rarer and very sensitive to the relative roles of gravitational, interfacial and inertia forces.

On the other hand, most of the previous researches on gas-liquid flows were conducted on-ground where gravity plays an important role. However, due to the demand for active heat transport systems in future communications and earth observation satel-

lites as well as space stations, two-phase gas-liquid flows in micro-gravity condition have emerged as an active research area in the last decade and the mastery of condensation flows in microgravity conditions at low and intermediate mass velocities is an important issue. Indeed, gravitational field strongly impact the two-phase liquid-vapor distribution in condensers. When the effect of gravity is high enough, the stratification regime is observed. In some previous studies about condensation in mini tubes, no stratification regime is observed, if mass velocity is greater than  $200 \text{ kg.m}^{-2}.\text{s}^{-1}$ . This is due to the dominance of viscous force in comparison of the gravitational one. When the mass velocity is lower than  $100 \text{ kg.m}^{-2}.\text{s}^{-1}$ , the effect of gravity is high enough and the stratification regime appears. To reduce this effect at low mass velocities, the hydraulic diameter of the tube can be reduced in order to increase the surface tension forces which become dominant in comparison to gravity forces. Nowadays, one way to simulate the space environment is to perform parabolic flights. The limitation is the duration of micro-gravity which is only 20 (s) for each parabola.

Convective condensation experiments are available for different orientations and different flow passage geometries, but mainly for mass velocities greater than one hundred of  $\text{kg.m}^{-2}.\text{s}^{-1}$ . In the absence of a general theory for predicting condensation mechanisms based on thermo-physical properties of the fluid, cross section shape and boundary conditions, the literature provides many correlations on flow laws to predict data such as the heat flux and the pressure drops. To establish the parameters involved in these relationships it is necessary to develop models based on the observation of flow regimes. In a two-phase loop with capillary pumping, low mass velocities of about several tens of  $\text{kg.m}^{-2}.\text{s}^{-1}$  are commonly encountered. To address the lack of information given by literature in this range of the mass velocity, specific studies should be conducted. Two-phase heat transfers are highly correlated to the distribution of phases, it is thus important to know simultaneously the flow regime, the pressure drop and heat transfer coefficient to validate the models.

So, the convective condensation at low mass velocities and in reduced gravity condition is one of major concern for the Laplace laboratory. From 2004, Laplace is part of ESA ENCOM project. One aim of this project is to study the effect of gravity for low mass velocity condensation flows. This thesis is took place during the end of ENCOM2 and the beginning of ENCOM3. Considering with the objectives of the laboratory, the aim of this thesis is to study the convective condensation flow pattern and heat transfer at low mass velocities and in reduced gravity condition. The study concerns tube of intermediate dimension. On the other hand, a part of this thesis has been done in collaboration with two other laboratories: university of Padova, Italy and university of Brussels, Belgium. This work has also been carried out at university of Padova for designing test section used both on-ground and during parabolic flights. The manuscript is organized as below:

- Chapter 1: The first chapter is the state of art of the effect of gravity on con-

vective condensation. This chapter is also to highlight the context of the study. This bibliography chapter presents the main experimental, theoretical and numerical studies about convective condensation inside conventional, mini and micro channels on-ground and in microgravity. It focuses on structure of two-phase flow, heat transfer coefficient and pressure drop in convective condensation. The effect of gravity, tube dimension and shape, as well as mass velocities will be exploited.

- Chapter 2: In the second chapter, based on some experimental results obtained on ground inside micro tube where the gravitational effect is negligible in comparison to the other forces, a development of a physical and numerical model of liquid film instabilities is initiated. This modelisation could help in the future to understand the mechanisms leading to the observed flow patterns in microgravity. The choice of the model, the equation system and the boundary conditions will be described. A linear analysis of stability and the first results of the model will then be presented.

- Chapter 3: In chapter 3, the test section and the set-up dedicated for convective condensation of HFE-7000 in parabolic flights will be presented. This test-section was built to be used in parabolic flight where the microgravity takes place only for 20s. The validation test for the test section before parabolic flight campaign will be presented in this chapter. Results of heat transfer coefficients, pressure drop and two-phase flow structure will be described. A comparison between the results on-ground and the ones in reduced gravity condition at low and intermediate mass velocities will be realized. On the other hand, thanks to high speed camera, the flow patterns were observed. An attempt to obtain the film thickness of condensate film was also performed.

- Chapter 4: The measurements of heat transfer simultaneously with the visualization of flow pattern were not possible with the previous test section. On the other hand, the mass velocity was not really low (the minimum of mass velocity during the parabolic flight campaign was only  $70 \text{ kg.m}^{-2}.\text{s}^{-1}$ ). So, another set-up has been built and tested on-ground. This test section is in sapphire and totally transparent. It is placed vertically in order to have the same two-phase configuration as the micro-gravity where the two phase distribution is also axysymmetric. This experiment apparatus allows the convective condensation at low mass velocity from 10 to  $40 \text{ kg.m}^{-2}.\text{s}^{-1}$ . This test section can be considered as the first step to prepare parabolic flights campaign in ENCOM3. This test section will firstly be tested and studied on-ground, the heat transfer coefficient and the flow pattern will be reported in this chapter. In this chapter, a calibration procedure with thermal camera for wall temperature measurement to determine the condensation heat transfer coefficient will be presented. Thanks to a white light interferometer, the thin film thickness will be measured simultaneously of thermal measurement. The first result will be presented.

Finally, a general conclusion and some highlighted points of perspectives of this thesis will close this manuscript.



# Chapter I

## State of the art

For convective condensation inside tubes, laws of heat transfer and pressure drop are directly correlated to the liquid-vapor interface distribution and more precisely to the liquid film thickness when the flow regime is annular. The two-phase structure, heat transfer and pressure drop are important aspects in the design of the condensers of two-phase cooling loops. Therefore many investigations have focused on flow maps, flow laws and heat transfer laws considering convective condensation inside tubes and many papers are available today. These studies consider tubes of various dimensions, cross-section's shapes, working fluids, ... A synthesis of the most important available investigations on in-tube convective condensation is proposed in this chapter.

First, a general bibliographic study about convective condensation inside conventional and mini tube is presented. The influence of tube's dimension and of gravity, as well as of mass velocity is presented. Secondly, a synthesis of the studies on convective condensation inside micro tube is proposed. In these two parts, the flow maps, pressure drop and heat transfer laws as a function of other parameters such as mass velocity, gravity intensity and tube's dimension determined from both empirical and experimental investigations are presented. This bibliographic study is not only to investigate the available and useful studies but also to highlight the context of the study of this thesis.

## I.1 Convective condensation inside conventional and mini channels

In a conventional tube ( $Dh \geq 8mm$ ), the capillary force is negligible in comparison to the gravitational force and shear stress. In this range of tube's dimension, we can summarize the two-phase flow patterns for convective condensation in four main different groups : stratified flows, intermittent flows, annular flows and dispersed flows. For convective condensation in mini-tube, the surface tension plays a more important role in comparison to convective condensation in conventional one. Despite this difference, the two-phase flow patterns that can be observed in mini-tubes are the same than in conventional tubes. Because of these similar observed two-phase flow patterns, the available investigations on flow pattern maps, heat transfer and pressure drop laws for both conventional and mini-tube are regrouped hereafter.

### I.1.1 Two phase flow pattern regimes in conventional and mini-tubes

Flow regime represents how the liquid and vapor phases are distributed inside a tube. It is an essential input to predict the heat exchange occurring between the fluid and its environment. Hence, the prediction of two-phase flow structures is one of the most important aspects in the design of condensers of two-phase cooling loops.

Considering few centimeters hydraulic diameter pipes, Palen et al. [1] presented some flow structures encountered in horizontal tube during convective condensation, for both low and high mass flow rates (figure I.1). With such a tube's dimension, gravity force and shear stress are the dominant forces influencing the liquid-vapor phase configuration. The authors classified the two-phase flow patterns into annular, slug, plug and bubbly for high mass flow rates and annular, wavy and stratified for low mass flow rates.

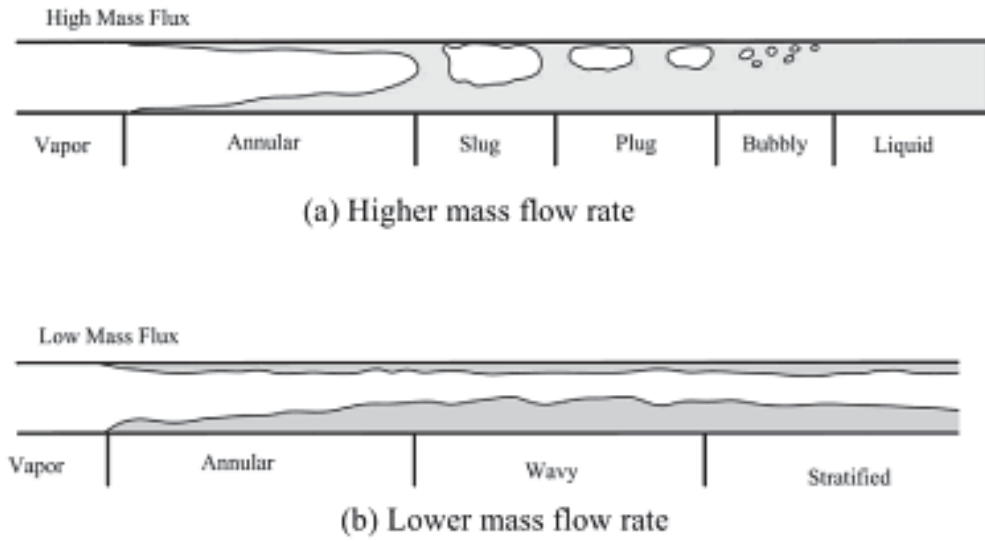


Figure I.1: The succession of different flow regimes in the convective condensation at low mass flux and high mass flux inside centimeters hydraulic diameter pipe (figures taken from [1]).

Barnea et al. [18] observed the two-phase flow structure inside circular tubes of hydraulic diameter from 4 to 12 mm in the case of adiabatic flows. They named and classified the flow patterns in four groups: stratified regime, annular regime, intermittent and dispersed regime.

For smaller tubes, i.e. in the range of millimeter hydraulic diameter, two-phase flow patterns encountered have been presented by Coleman and Garimella [2] (figure I.2). The experimental investigation was conducted in channels with round, square and rectangular cross-sections of hydraulic diameter from 1 to 4.9 mm during convective condensation of refrigerant R134a with mass velocities from 150 to 750  $kg.m^{-2}.s^{-1}$ . They classified the two-phase flow patterns into annular, wavy, intermittent and dispersed flow. The authors regroup the slug flow and plug flow of Palen et al. [1] to the so-called "intermittent flow", while the bubbly flow described in Palen et al. is renamed "dispersed flow" by these authors.

		FLOW REGIMES			
		Annular	Wavy	Intermittent	Dispersed
Flow Patterns					
	Mist Flow	Discrete Wave (0)	Slug Flow	Bubbly Flow	
					
	Annular Ring	Discrete Wave (1)	Slug Flow	Bubbly Flow	
					
Wave Ring	Discrete Wave (2)	Plug Flow	Bubbly Flow		
					
Wave Packet	Disperse Wave (3)	Plug Flow			
	Note: Numbers above denote intensity of secondary waves				
Annular Film	Note: Numbers above denote intensity of secondary waves				

Figure I.2: Flow regimes and flow patterns for condensation in mini-channels ( $1\text{ mm} < Dh < 4.9\text{ mm}$ ) during condensation of refrigerant R134a with mass velocities from  $150$  to  $750\text{ kg.m}^{-2}.s^{-1}$  (figure taken from [2]).

From these studies, and more generally from the literature about two-phase flows, a wide variety of flow pattern’s definitions and their detailed descriptions have been given, each of them depending on the authors. These flow patterns depend on many parameters such as flow orientation, working fluid(s), size and shape of the channel, the thermodynamic process and the flow properties. For this reason, flow pattern maps are used to predict the local flow patterns in a tube. A flow regime map is a diagram that displays the transition boundaries between the two-phase flow regimes. Its two axes are generally the superficial velocities of liquid and vapor phases or a function formulated from these velocities and other parameters, or the mass velocity and the vapor quality. It should be pointed out that the flow pattern is also influenced by a number of others variables such as hydraulic diameter, working fluid properties, ... but it is not possible to represent their influence using only a two-dimensional plot. Therefore, one should be aware that one flow pattern map is valid for the respective working fluid and the respective shape of the tube in test conditions.

On ground, the influence of gravity compared to other forces (as for example shear stress and surface tension force) depends on tube’s dimension. Hereafter, some common flow pattern maps are presented. A general investigation of influence of gravity, mass velocity, tube shape,... in this range of dimension is developed.

### I.1.2 Flow pattern maps

First, some flow patterns maps in the case of adiabatic flow are studied to point out the phase change in condensation flow. Many researchers have studied flow regime transitions in adiabatic two-phase flows by doing experiments on ground in conventional tubes. We may cite, for instance, Baker [19], Fair [20], Mandhane et al.[21], Hewitt et al.[22], Taitel et al.[3]... Most of these flow regime maps were developed with air-water as working fluids.

One of the most popular flow regime maps in for adiabatic flow is that of Taitel et al. for both horizontal [3] and vertical [4] configurations with air-water as working fluids. These maps are reported in figure I.3. In horizontal configuration, they classified the two-phase flow in five groups: dispersed bubble, intermittent, stratified smooth, stratified wavy and annular dispersed liquid. In vertical configuration, they also classified the two-phase flow in five groups: bubble, slug, churn, annular and finely dispersed bubble.

In the paper about two-phase flow in horizontal tube [3], Taitel et al. gave some physical criteria using dimensionless parameters for the transition between :

- stratified and intermittent or annular-dispersed liquid regimes,
- intermittent and annular dispersed liquid regimes,
- stratified smooth and stratified wavy regimes,
- intermittent and dispersed bubble regimes

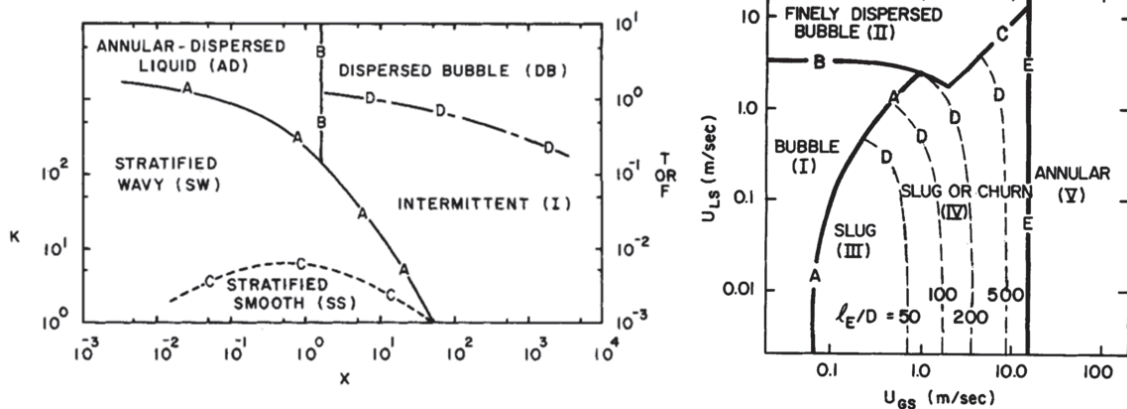


Figure I.3: Flow pattern maps of air-water at 25°C for 50 mm internal diameter tubes developed by Taitel et al. (a): For horizontal tube at 1 atm [3],(b): For vertical tube at 1 atm [4]

So, a diagram showing the transitions between the various two-phase flow regimes was developed using Martinelli number, modified Froude number and two other parameters: T and K, as reported hereafter:

$$X = \left[ \frac{(dp/dx)_L^S}{(dp/dx)_V^S} \right]^{1/2} \quad Fr = \sqrt{\frac{\rho_V}{(\rho_L - \rho_V)}} \cdot \frac{u_V^S}{\sqrt{D \cdot g \cdot \cos\theta}} \quad (\text{I.1.2.1})$$

$$T = \left[ \frac{(dp/dx)_L^S}{(\rho_L - \rho_V) \cdot g \cdot \cos\theta} \right]^{1/2} \quad (\text{I.1.2.2})$$

$$K = \left[ \frac{\rho_V \cdot u_V^{S^2} \cdot u_L^S}{(\rho_L - \rho_V) \cdot g \cdot \mu_L \cdot \cos\theta} \right]^{1/2} \quad (\text{I.1.2.3})$$

This diagram was developed considering centimeter tubes where the gravitational force is dominant on the structure of the two-phase flow, i.e. surface tension effect was negligible in their study. In the other hands, this study has been performed in adiabatic condition where no condensation phenomena occurs.

Concerning the flow pattern maps involving condensation inside conventional tube, Suliman et al. [6] have conducted a study with R-134a as the working fluid inside a 9.53 mm internal diameter smooth horizontal tube. Many experimental tests were performed for a mass velocity range of 75 to 300  $kg \cdot m^{-2} \cdot s^{-1}$ , at 40°C saturation temperature and with vapor quality ranging from 0.76 down to 0.03. In this study, authors found five different flow regimes: intermittent, annular, mist, stratified wavy and stratified regimes. Results highlighted a different transition between the intermittent or annular regime and stratified wavy regime in comparison to that previously reported by El Hajal et al. [5].

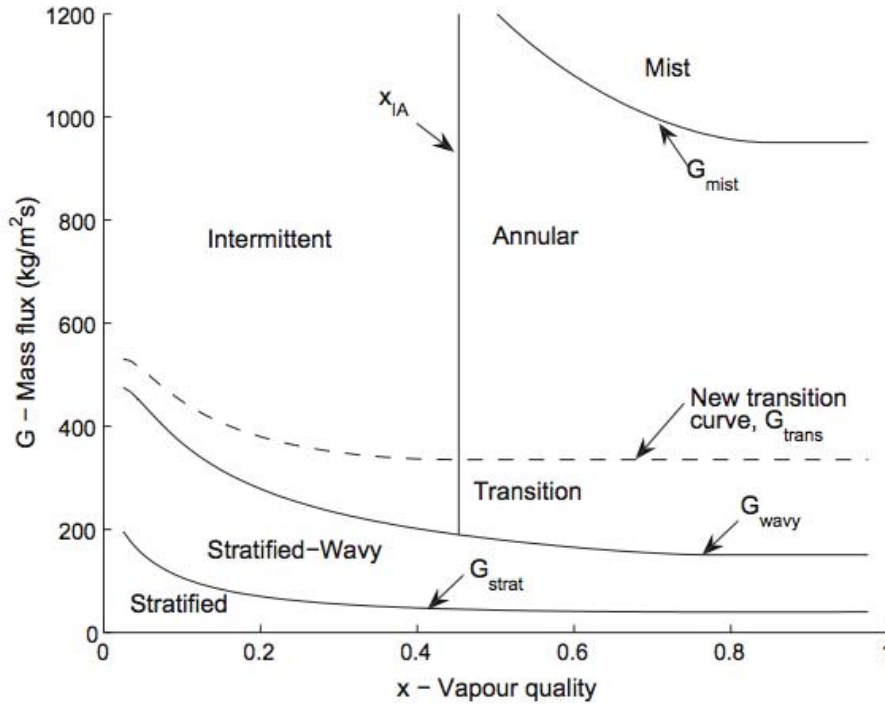


Figure I.4: Flow regime map for convective condensation of R-134 in a 9.53 mm horizontal channel with new line transition regime (in comparison to that of El Hajal et al. [5]) (figure taken from [6]).

Breber et al.[23] conducted many experimental tests inside tubes from 4.8 mm up to 25.4 mm internal diameter with R-12, R-113 and n-pentane as working fluids. They used the approach of Taitel and Dukler [3] to build their flow pattern map with dimensionless parameters  $X$ ,  $Fr$ ,  $T$  and  $K$ . The conclusion of this study is that the dimensionless flow regime map developed by Taitel and Dukler may also be applied for condensation two-phase flow to determine local flow regimes.

Inside smaller tube dimension, many flow pattern maps exist that can predict the transition of flow regime according to the cross-section geometry, the dimension of the tube and the working fluid. In the case of adiabatic two-phase flows, Barnea et al.[18], Coleman et al.[7], Fukano et al.[24], Damianides et al.[8] investigated flow regime transitions for both horizontal and vertical configurations, for many different tube cross-section shapes (round, rectangular, square) and many different tube hydraulic diameters. They concluded that the flow regime transition cannot be predicted by the flow pattern map developed for conventional tube's size developed by Taitel and Dukler [3] or Weisman et al. [25] when the internal diameter is smaller than 5 mm.

Damianides and Westwater [8] developed flow pattern maps for water-air flow inside tube with diameter between 1 and 5 mm. They can thus analyse the effect of

tube dimension on regime transition. When tube diameter decreases, the transition regime between the intermittent and annular flows was found to occur successively for a decreasing, then increasing, and then decreasing gas superficial velocity.

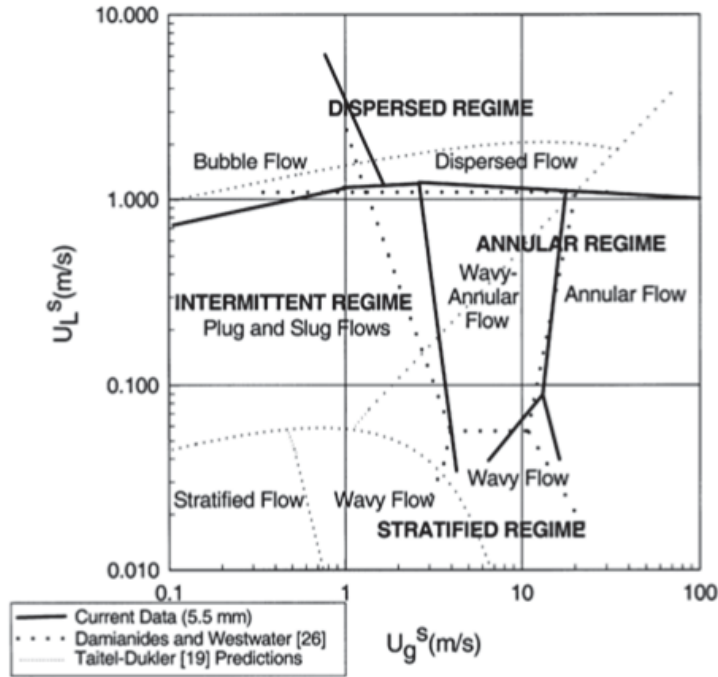


Figure I.5: A comparison of experimental result of two-phase flow of air-water obtained by Coleman and Garimella [7] inside 5.5mm round tube with flow pattern maps developed by Damianides and Westwater [8] inside a 5 mm internal tube and by Taitel and Dukler[3].

Coleman and Garimella [7] performed an investigation of adiabatic air-water two-phase flow inside round tubes with diameter from 1.3 to 5.5 mm. When the tube dimension decreases, the transition to dispersed flow shifts to higher liquid superficial velocity and the suppression of stratified flow was observed. They compared then the obtained result with flow pattern maps of Taitel and Dukler [3] and Damianides and Westwater [8]. The figure I.5 presents a comparison of their results with the flow pattern maps of Damianides and Westwater [8] inside a 5 mm hydraulic diameter tube and of Taitel and Dukler [3]. A good agreement between experimental study and the flow pattern map developed by Damianides and Westwater [8] is obtained. Contrariwise, big deviations can be observed between the experimental data and the flow pattern map developed by Taitel and Dukler. From experimental data, the transition line between the intermittent and annular zones occurs at a quite constant gas superficial velocity what was not observed by previous study. In the other hands, the stratified flow was not observed during experimental study and the wavy flow was obtained at high gas

superficial velocity, which is not predicted by the transition modeling. Therefore, in this case the flow pattern map of Taitel and Dukler cannot predict the regime transition because it doesn't take into account the surface tension effect.

Concerning condensation two-phase flow inside mini tube, Coleman and Garimella [7] made many experiments in round ( $D_h=4.91$  mm), square ( $D_h=4$ mm) and rectangular tubes (4x6 and 6x4  $D_h=4.8$ mm), using R134a as the working fluid, and considering mass velocity from 150 up to  $750 \text{ kg.m}^{-2}.\text{s}^{-1}$ . They divided their results into four different flow regimes: intermittent flow, wavy flow, annular flow, and dispersed flow. Figure I.6 presents the comparison between the map for adiabatic air-water two-phase flow in round tubes and the flow pattern map for convective condensation of R134a. The symbols in figure I.6 represent the experimental data in adiabatic water-air flow and dotted or full line are transition lines obtained in condensation case. From this study, it was noted that it is important to take into account the phase-change effect to develop a reliable flow pattern map. Indeed, the same flow regimes can be observed for the same range of mass velocity, however the transition lines are different. It is noted that authors divided wavy flow into two different types: discrete wavy where wave amplitude is small and disperse wave where wave amplitude is higher. No experimental data was found above the transition from discrete to disperse waves zones. Moreover, all experimental points corresponding to an annular pattern highlighted "discrete waves" when the working fluid was the refrigerant. Therefore, the transition lines for adiabatic and condensation configurations are totally different.

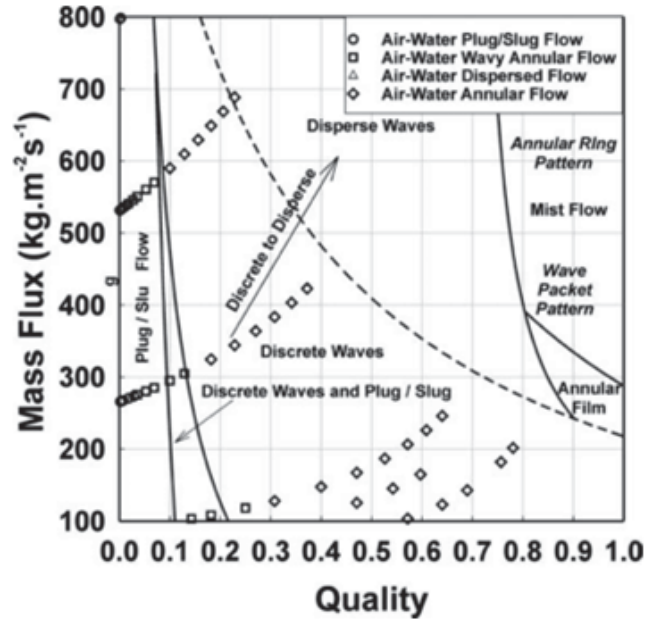


Figure I.6: Comparison between flow pattern maps for adiabatic water-air flow and condensation flow of R134a inside 4.91mm hydraulic diameter tube [2].

Coleman and Garimella also analyzed the effect of tube shape on condensation flow pattern map. For example the intermittent regime was found to be larger in round tubes than in square and rectangular tubes when the mass velocity is low, while it is approximately the same whatever is the cross-section shape when the mass velocity is high. That can be explained considering that at low mass velocity the surface tension force is the dominant force and is different in square and rectangular tubes in comparison to the round tubes. At high mass fluxes, the shear stress becomes the dominant one, therefore the difference due to surface tension force is no more significant.

Other studies of flow regimes are available in the literature, such as the one of Dobson and Chato [26] for condensation of different refrigerants inside mini tube from 3.1 to 7.04 mm or the one of Cavalini et al. [27] for condensation of R134a, R125, R32, R410A and R236ea inside 8mm hydraulic diameter tubes. The mass velocities during these tests varied from  $100 \text{ kg.m}^{-2}.\text{s}^{-1}$  to  $750 \text{ kg.m}^{-2}.\text{s}^{-1}$ . However no general flow pattern map was proposed.

### Gravity's effect

Some studies have been conducted with conventional tubes that allow studying the effect of gravity on ground by varying the tube inclination. Ghajar et al. [9] presented recently a study of water-air two-phase flow inside a 12.7 mm hydraulic diameter polycarbonate tube and a 12.5 mm diameter stainless steel round tube. The gas and liquid

flow rates were varied from 0.001 to 0.2 kg/min and from 1 to 10 kg/min, respectively. The range of inclination angles was from 0 to 90°. The effect of inclination angles on the flow pattern map is reported on Figure I.7.

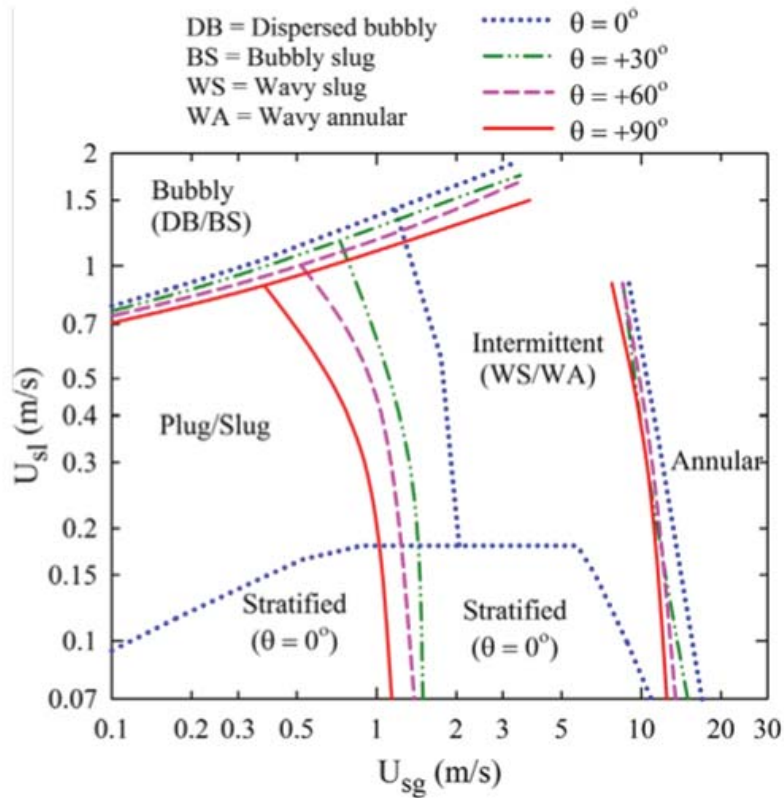


Figure I.7: Effect of tube inclination on flow pattern map for water-air flow in a 12.7 mm hydraulic diameter tube [9].

From this study, it can be concluded that the main effect of the inclination change is on the transition between intermittent and slug/plug flow that shifts to lower gas velocity. The annular and bubbly flows are less sensible to the inclination change.

Another recent experimental study is the one of Lips and Meyer [28] who studied convective condensation of R134a inside a copper tube of 8.38 mm inner diameter. Two glass windows were inserted in the setup, upstream and downstream the copper section. Visualizations of the flow patterns have been performed for inclinations from -90° (vertical downwards flow) to +90° (vertical upwards flow). They found that at a mass velocity of  $300 \text{ kg}\cdot\text{m}^{-2}\cdot\text{s}^{-1}$  the flow is insensitive to the inclination angle and more and more annular as the vapor quality is increased. On the contrary, for low vapor qualities the flow is highly sensitive to the inclination angle: stratification occurs for slightly downward flow while intermittent flow appears for higher inclination angle.

Therefore at this mass velocity, we can observe the effect of gravity on flow regime. They also performed experiments for a constant vapor quality of 0.5 and for different mass velocity. For low mass velocity, the flow regime depends on the inclination angle while at high mass velocity the flow pattern becomes annular and independent on tube orientation. However no flow pattern map depending on inclination angle has been developed.

### I.1.3 Pressure drop of condensation two-phase flow inside conventional and mini tubes

Pressure drop is an important parameter for designing a heat exchanger. In two-phase flow, this pressure drop is a complex function that can be calculated as the sum of gravitational pressure drop, momentum pressure drop and friction pressure drop. Because of the complexity of the pressure drop, authors usually choose a focusing parameter.

Two of the main models for frictional pressure drop, namely homogeneous and separated flow models, are briefly described hereafter.

#### Homogeneous flow model

In this model developed for adiabatic flow, it is supposed that the liquid phase and the gas phase have the same velocity. The frictional pressure drop equation is the Darcy equation which uses Blasius relation to evaluate the friction factor from the average mixture properties :

$$f_{TP} = 0.079/Re_{TP}^{-0.25} \quad (\text{I.1.3.1})$$

Where  $Re_{TP} = G_{TP}D_h/\mu_{TP}$  is the two-phase Reynolds number,  $f_{TP}$  is the friction coefficient,  $G_{TP}$  is the mass velocity and  $D_h$  is the hydraulic diameter.

The equivalent viscosity of the two-phase mixture can be evaluate for instance by Mac Adams et al. law:

$$\mu_{TP}^{-1} = x\mu_V^{-1} + (1-x)\mu_L^{-1} \quad (\text{I.1.3.2})$$

Where  $x$  is the vapor quality and  $\mu_L$  and  $\mu_V$  are the liquid and vapor dynamic viscosities, respectively.

The two-phase frictional pressure drop is then:

$$\Delta p = \frac{2f_{TP}G_{TP}^2l}{\rho_{TP}} \quad (\text{I.1.3.3})$$

With  $l$  is the pipe length.

This homogeneous model is accurate for density ratio between the two phases lower than 10 and mass velocity lower than  $2000 \text{ kg.m}^{-2}.\text{s}^{-1}$  [29].

### Separated flow models

Lockhart and Martinelli [30] carried out many investigations to develop their theory based on separate flow model. Their model is based on experimental data obtained with circular pipes of diameter ranging from 1.48mm to 25.83mm and using two-phase mixture constituted by air with benzene, kerosene, water and several oils. There are two principal assumptions : the statistic pressure drops for both liquid and vapor are the same regardless the flow pattern maps and the pipe volume is always occupied by liquid and gas flows.

Based on these assumptions and experimental database, the pressure gradient in the two-phase flow can be written as a function of the pressure gradient corresponding to a single-phase liquid flow:

$$\left(\frac{dp}{dx}\right)_{TP} = \Phi_L^2 \left(\frac{dp}{dx}\right)_L \quad (\text{I.1.3.4})$$

The two-phase multiplier  $\Phi_L^2$  can be evaluated from following equation:

$$\Phi_L^2 = 1 + \frac{c}{X} + \frac{1}{X^2} \quad (\text{I.1.3.5})$$

Where  $X = \sqrt{\left(\frac{dp}{dx}\right)_L / \left(q \frac{dp}{dx}\right)_V}$

The value of  $c$  depends on flow regime and is ranging from 5 to 20.

Another correlation of pressure drop in two-phase flow widely used is the Friedel [31] one. This is often considered as the most accurate model to determine the pressure drop of two-phase flow. This correlation has been developed based on 16000 measured data for a wide range of tube diameter (bigger than 4mm) and for air-water mixture, air-oil mixture and R12 refrigerant. This model takes into account the effect of gravity, surface tension and total mass flux via Weber number. The Friedel model for two-phase multiplier can be written as:

$$\Phi_{Lo} = E + \frac{3.24FH}{Fr^{0.45}We^{0.035}} \quad (\text{I.1.3.6})$$

Where the Froude and Weber numbers are respectively  $Fr = \frac{G_m^2}{gD_h\rho_m}$  and  $We = \frac{G_m^2 D_h}{\rho_m \sigma}$ ;  $\sigma$  is the surface tension. The dimensionless parameters F, H and E are defined as:

$$E = (1 - x)^2 + x^2 \frac{\rho_L f_{V_o}}{\rho_V f_{L_o}} \quad (\text{I.1.3.7})$$

$$F = x^{0.78}(1 - x)^{0.224} \quad (\text{I.1.3.8})$$

$$H = \left(\frac{\rho_L}{\rho_V}\right)^{0.91} \left(\frac{\mu_V}{\mu_L}\right)^{0.19} \left(1 - \frac{\mu_V}{\mu_L}\right)^{0.7} \quad (\text{I.1.3.9})$$

$f_{L_o}$  and  $f_{V_o}$  can be calculated from the single-phase friction correlation of Blasius based on liquid Reynolds number and vapor Reynolds number:

$$f_{L_o} = 0.079/Re_{L_o}^{0.25} \quad \text{and} \quad f_{V_o} = 0.079/Re_{V_o}^{0.25} \quad (\text{I.1.3.10})$$

with  $Re_{L_o} = GD_h/\mu_L$  and  $Re_{V_o} = GD_h/\mu_V$

The pressure gradient for a liquid single-phase flow is:

$$\left(\frac{dp}{dx}\right)_{L_o} = \frac{2f_{L_o}G^2\nu_L}{D_h} \quad (\text{I.1.3.11})$$

where  $\nu_L$  is the liquid specific volume ( $m^3/kg$ ).

More recently, Mikielwicz et al. [32] investigated the pressure drop of HFE-7000 and HFE-7100 during flow condensation inside 2.3 mm inner diameter tube. They found that an increase of the mass flux or a decrease of the saturation temperature leads to an increase of the pressure drop. They compared also experimental data to existing correlations; the Muller-Steinhagen [33] and Fronk and Garimella [34] models are found to be the most accurate.

Meyer et al. [35] presented an investigation of gravitational effect on two-phase pressure drop during condensation in inclined tube. The investigation has been done inside a 8.38 mm hydraulic diameter tube with the refrigerant R134a and for vapor qualities ranging from 0.1 to 0.9. The mass flux has been varied from 100 to 400  $kg.m^{-2}.s^{-1}$ . Experimental data have been measured at saturation temperature of  $30^\circ C$ ,  $40^\circ C$  and  $50^\circ C$  with inclination angle from  $-90^\circ$  (downward flow) to  $+90^\circ$  (upward flow). Figure I.8 presents the evolution of pressure drop at saturation temperature of  $30^\circ C$  for different inclination angles and mass fluxes. For high mass flux and vapor quality, the effect of gravity on pressure drop is not prominent due to the dominance of shear stress. The authors also concluded that the pressure drop is reduced when the saturation temperature increases, and that increasing mass flux and vapor quality lead the pressure drop to increase.

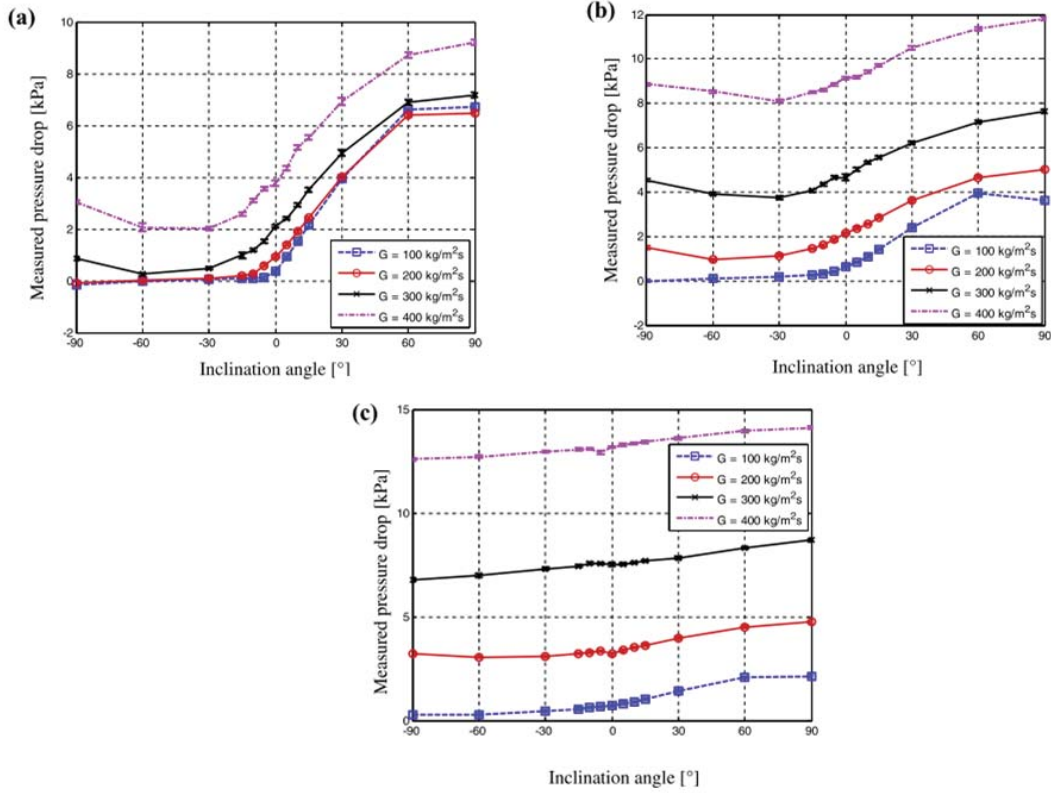


Figure I.8: Effect of inclination angles on pressure drop at different mass fluxes and vapor qualities of a)0.25 b)0.5 and c)0.75 at saturation temperature of  $30^{\circ}\text{C}$

For the reader who is interested in two-phase pressure drop modeling in mini-tubes, several other models are available in the literature, among which one can cite : Del Col et al. [36], Muller Steinhagen [33], Fronk and Garimella [34] (models for different fluids), Mishima and Hibiki [37] (for rectangular and circular channel), Zhang and Webb [38] (for multi-port), ...

#### I.1.4 Heat transfer of condensation inside conventional and mini channels

In a two-phase thermal management system, the heat transfer coefficient is one of the most important term to evaluate its performance. The heat transfer coefficient is defined as:

$$h = \frac{\varphi}{\Delta T} \quad (\text{I.1.4.1})$$

where

$\varphi$  is the heat flux ( $\text{W}\cdot\text{m}^{-2}$ )

$h$  is the heat transfer coefficient ( $W.m^{-2}.K^{-1}$ )

$\Delta T$  is the temperature difference between the solid wall and the surrounding fluid (K)

The heat transfer coefficient is very often correlated to the dimensionless Nusselt number (Nu). This dimensionless number has been established by Wilhelm Nusselt and represents the ratio between the fluid temperature gradient at the wall and the "apparent" temperature gradient defined as the wall-to-fluid temperature difference divided by the characteristic length of the considered problem. The Nusselt number is then expressed as:

$$Nu = \frac{hL_c}{\lambda} \quad (I.1.4.2)$$

where  $L_c$  is the characteristic length and  $\lambda$  is the thermal conductivity of the fluid.

Investigations on heat transfer can be divided into experimental, empirical or semi-empirical and numerical studies. Hereafter a review about heat transfer coefficient studies inside conventional and mini tubes with different shapes, mass fluxes and gravity's effect is proposed.

In the case of two-phase heat transfer in a conventional tube, the most efficient flow regimes are annular and stratified flows. Therefore, the investigations of heat transfer coefficient were mainly associated to these flow regimes. Some common correlations for the heat transfer coefficient are presented hereafter.

### Shah's Correlation [39]:

One of the most popular model for calculating the heat transfer coefficient was proposed by Shah [39]. In his paper, he presented a simple dimensionless correlation to predict heat transfer coefficients during condensation inside tubes. This correlation was established from a great number of experimental data obtained with different working fluids in horizontal, vertical, and inclined tubes having diameters ranging from 7mm to 40mm. The experiments were carried out considering vapor velocities from 3 to 300 m/s, vapor qualities from 0 to 1, mass flux from 10.83 to 210.55  $kg.m^{-2}.s^{-1}$ , heat flux from 158 to 1893 000  $W/m^2$ , reduced pressure from 0.002 to 0.44, liquid Reynolds numbers from 100 to 63000 and liquid Prandtl numbers from 1 to 13. The correlation of heat transfer coefficient proposed by Shah thanks to this set of data can be written as:

$$h = h_{Lo}[(1 - x)^{0.8} + \frac{3.8x^{0.76}(1 - x)^{0.04}}{Pr^{0.38}}] \quad (I.1.4.3)$$

Where  $h_{Lo}$  is evaluated assuming the fluid is in the liquid state using the Dittus-Boelter equation:

$$h_{Lo} = 0.023 Re_L^{0.8} Pr_L^{0.3} \lambda_L / D_h \quad (\text{I.1.4.4})$$

**Tang's correlation [40]:**

Tang [40] proposed a simple correlation which is an extension of Shah's correlation [39] applicable for reduced pressure ranging from 0.2 to 0.53 and mass velocity ranging from 300 to 810  $kg.m^{-2}.s^{-1}$ . This correlation is valid for annular flow only:

$$\frac{hD_h}{\lambda_L} = 0.023 Re_L^{0.8} Pr_L^{0.4} [1 + 4.863 (\frac{-x \ln(p_r)}{1-x})^{0.836}] \quad (\text{I.1.4.5})$$

**Hajal, Thome and Cavallini's correlation [10]:**

Thome et al.[10] developed a heat transfer model for condensation inside horizontal, plain tubes based on flow regimes. They included also effect of liquid-vapor interfacial roughness on heat transfer. The model predicts local heat transfer coefficients in condensation configuration based on following flow regimes: annular, intermittent, stratified-wavy, fully stratified and mist flow. This model was compared with experimental data from nine independent research laboratories obtained with 15 different fluids (R-11, R-12, R-22, R-32, R-113, R-125, R-134a, R-236ea, a R-32/R-125 near-azeotrope, R-404A, R-410A, propane, n-butane, iso-butane and propylene). Experiments were performed within the following conditions: mass velocities from 24 to 1022  $kg.m^{-2}.s^{-1}$ , vapor qualities from 0.03 to 0.97 and tube internal diameters from 3.1 to 21.4 mm. The convective condensation heat transfer coefficient for annular, intermittent and mist regime can be calculated by:

$$h = c.Re_L^n Pr_L^m \frac{\lambda_L}{\delta} f_i \quad (\text{I.1.4.6})$$

In this equation, c, n and m are empirical constants that were determined from the heat transfer database; the best fitting was obtained with: c=0.003, n=0.74 and m=0.5.  $\delta$  is the thickness of the liquid film;  $f_i$  is an *interfacial roughness correction factor*:

$$f_i = 1 + (\frac{u_V}{u_L})^{1/2} (\frac{(\rho_L - \rho_V)g\delta^2}{\sigma})^{1/4} \quad (\text{I.1.4.7})$$

where  $u_V$  and  $u_L$  are vapor and liquid velocities, respectively. They can be evaluated as below:

$$u_V = \frac{Gx}{\rho_V \alpha} \quad (\text{I.1.4.8})$$

$$u_L = \frac{G(1-x)}{\rho_L(1-\alpha)} \quad (\text{I.1.4.9})$$

where  $\alpha$  is the void fraction.

The Reynolds number can be determined as follows:

$$Re_L = \frac{4G(1-x)\delta}{\mu_L(1-\alpha)} \quad (\text{I.1.4.10})$$

The film thickness in annular, intermittent and mist flow can be evaluated by:

$$\delta = \frac{D_h}{2}(1 - \sqrt{\alpha}) \quad (\text{I.1.4.11})$$

The void fraction is expressed as:

$$\alpha = \frac{\alpha_{Hm} - \alpha_{RA}}{\ln(\alpha_{Hm}/\alpha_{RA})} \quad (\text{I.1.4.12})$$

where  $\alpha_{Hm}$  is the homogeneous void fraction that can be calculated by:

$$\alpha_{Hm} = \left(1 + \frac{1-x}{x}\right) \left(\frac{\rho_V}{\rho_L}\right) \quad (\text{I.1.4.13})$$

$\alpha_{RA}$  is the non homogeneous void fraction that can be evaluated by Rouhani-Axelsson's law as:

$$\alpha_{RA} = \frac{x}{\rho_V} \left( [1 + 0.12(1-x)] \left[ \frac{x}{\rho_V} + \frac{1-x}{\rho_L} \right] + \frac{1.18(1-x)[g\sigma(\rho_L - \rho_V)]^{0.25}}{G\rho_L^{0.5}} \right)^{-1} \quad (\text{I.1.4.14})$$

It can be noticed that the liquid film thickness appears as an important parameter in this correlation to determine the heat transfer coefficient. More details on the model can be found in [10]. They presented then a comparison of model results with the data of other authors obtained with different refrigerants. Comparison of actual model with experimental results are reported on figure I.9 . It is noted that about 85% of the experimental data are well predicted with a discrepancy less than 20%; it confirms the reliability of the model.

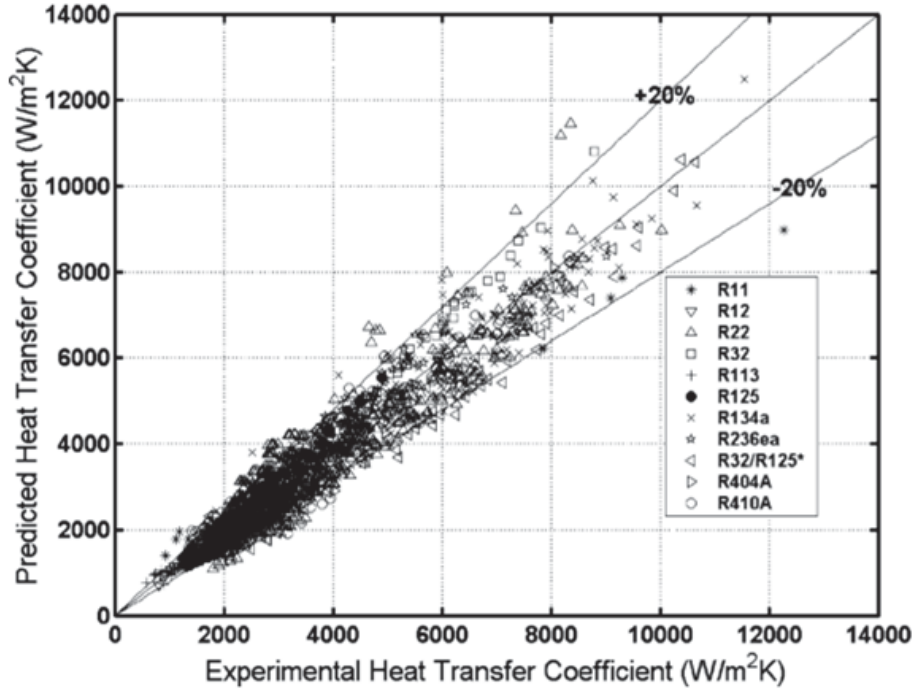


Figure I.9: A comparison of actual model of Hajal et al. with experimental results of eleven different refrigerants [10].

### Cavallini's Correlation [41]:

Cavallini et al. [41] presented a model for annular regime inside horizontal smooth tube with complete condensation process in normal gravity. This model was built from experimental results available in literature in order to design condensers for the air conditioning and refrigeration industry. A particularity of the proposed model is that it takes into account the entrainment of small liquid droplets in the vapor core. This model can be used for condensation of halogenated refrigerants inside tube with internal diameter  $D_h > 3mm$ , at reduced pressure lower than 0.75 and liquid-to-vapor density ratio greater than 4.

$$J_V = \frac{x \cdot G}{(g \cdot D_h \cdot \rho_V \cdot (\rho_L - \rho_V))^{0.5}} \quad (\text{I.1.4.15})$$

$$X_{tt} = (\mu_L / \mu_V)^{0.1} \cdot ((\rho_L / \rho_V)^{0.5} \cdot [(1 - x) / x]^{0.9}) \quad (\text{I.1.4.16})$$

The following model, valid only for annular flow, can be applied if dimensionless vapor velocity  $J_V > 2.5$ :

$$h = \rho_L \cdot c_{pL} \cdot (\tau / \rho_L)^{0.5} / T^+ \quad (\text{I.1.4.17})$$

$$T^+ = \delta^+ \cdot Pr_L \quad \delta^+ \leq 5 \quad (\text{I.1.4.18})$$

$$T^+ = 5 \cdot \{ Pr_L + \ln[1 + Pr_L \cdot (\delta^+ / 5 - 1)] \} \quad 5 < \delta^+ < 30 \quad (\text{I.1.4.19})$$

$$T^+ = 5 \cdot \{ Pr_L + \ln(1 + 5 \cdot Pr_L) + 0.495 \ln(\delta^+ / 30) \} \quad \delta^+ \geq 30 \quad (\text{I.1.4.20})$$

$$\delta^+ = (Re_L / 2)^{0.5} \quad \text{for } Re_L \leq 1145 \quad (\text{I.1.4.21})$$

$$\delta^+ = 0.0504 Re_L^{7/8} \quad \text{for } Re_L \geq 1145 \quad \text{where } Re_L = G(x - 1) D_h / \mu_L \quad (\text{I.1.4.22})$$

$$\text{With } \delta^+ = \frac{\delta \cdot u_\tau \cdot \rho_L}{\mu_L} \quad \text{with } u_\tau = (\tau / \rho_L)^{1/2} \quad (\text{I.1.4.23})$$

$$\tau = \left( \frac{dp}{dz} \right)_f \cdot \frac{D_h}{4} \quad (\text{I.1.4.24})$$

$$\left( \frac{dp}{dz} \right)_f = \Phi_{LO}^2 \cdot \left( \frac{dp}{dz} \right)_{f,LO} = \Phi_{LO}^2 \cdot f_{LO} \cdot G^2 / (D_h \cdot \rho_L) \quad (\text{I.1.4.25})$$

$$\Phi_{LO}^2 = E + (1.262 FH) / (We^{0.1458}) \quad (\text{I.1.4.26})$$

$$E = (1 - x)^2 + x^2 \frac{\rho_L \cdot f_{VO}}{\rho_V \cdot f_{LO}} \quad F = x^{0.66978} \quad (\text{I.1.4.27})$$

$$H = (\rho_L / \rho_V)^{0.3278} (\mu_V / \mu_L)^{-1.181} (1 - \mu_V / \mu_L)^{3.477} \quad We = G^2 \cdot D_h \quad (\text{I.1.4.28})$$

$$f_{LO} = 0.046 [G \cdot D_h / \mu_L]^{0.2} \quad f_{VO} = 0.046 [G \cdot D_h / \mu_V]^{0.2} \quad GD_h / \mu > 2000 \quad (\text{I.1.4.29})$$

$$f_{LO} = 16 / [G \cdot D_h / \mu_L] \quad f_{VO} = 16 / [G \cdot D_h / \mu_V] \quad GD_h / \mu < 2000 \quad (\text{I.1.4.30})$$

In another paper, Cavallini et al. [11] extended the model of condensation heat transfer coefficient to the case of smooth horizontal tubes of internal diameter smaller than 3 mm. This model was obtained by using data from their own experimental investigations for both heat transfer and pressure drop. The experiments were conducted with various refrigerants (R134a, R125, R32, R410A, R236ea) and for mass velocity varying from 100 to 750  $kg \cdot m^{-2} \cdot s^{-1}$ . It was considered that for a vapor velocity greater than a critical value, the heat transfer coefficient does not depend of the wall-to-saturation temperature difference  $\Delta T$ , whereas it depends on for low vapor velocities. The transition value of the dimensionless vapor velocity between  $\Delta T$ -independent and  $\Delta T$ -dependent zones is expressed as:

$$J_V^T = [(7.5 / (4.3X1.111_t + 1))^{-3} + C_T^{-3}]^{-1/3} \quad (\text{I.1.4.31})$$

Where  $C_T = 1.6$  for hydrocarbons and  $C_T = 2.6$  for other refrigerants.

For  $\Delta T$ -independent flow regime with  $J_V > J_V^T$ :

$$h_A = h_{Lo}[1 + 1.128x^{0.8170}(\rho_L/\rho_V)^{0.2363}(1 - \mu_V/\mu_L)^{2.144}Pr_L^{-0.100}] \quad (I.1.4.32)$$

For  $\Delta T$ -dependent flow regime for  $J_V \leq J_V^T$ :

$$h_D = [h_A(J_V^T/J_G)^{0.8} - h_{strat}](J_G/J_G^T) + h_{strat} \quad (I.1.4.33)$$

With:

$$h_{Lo} = 0.023Re_{Lo}^{0.8}Pr_L^{0.4}\lambda_L/D_h \quad (I.1.4.34)$$

and

$$h_{strat} = 0.725[1+0.741[(1-x)/x]^{0.3321}]^{-1} \cdot [\lambda_L^3 \rho_L (\rho_L - \rho_V) g h_{LV} / (\mu_L D_h \Delta T)]^{0.25} + (1-x)^{0.087} \alpha_{Lo} \quad (I.1.4.35)$$

The authors presented a comparison of their model with 425 data points taking from 18 different investigations. The experimental results were obtained during condensation inside mini and conventional tube from 3 to 17 mm in diameter and for large range of mass velocity from 30 to 800  $kg.m^{-2}.s^{-1}$  with various working fluid (HCFCs, HFCs, HCs, carbon dioxide, ammonia, and water). Figure I.10 presented an application of actual model to HFC pure fluids and an azeotropic mixture. The model is considered to well predict the heat transfer coefficient with the exception of ammonia.

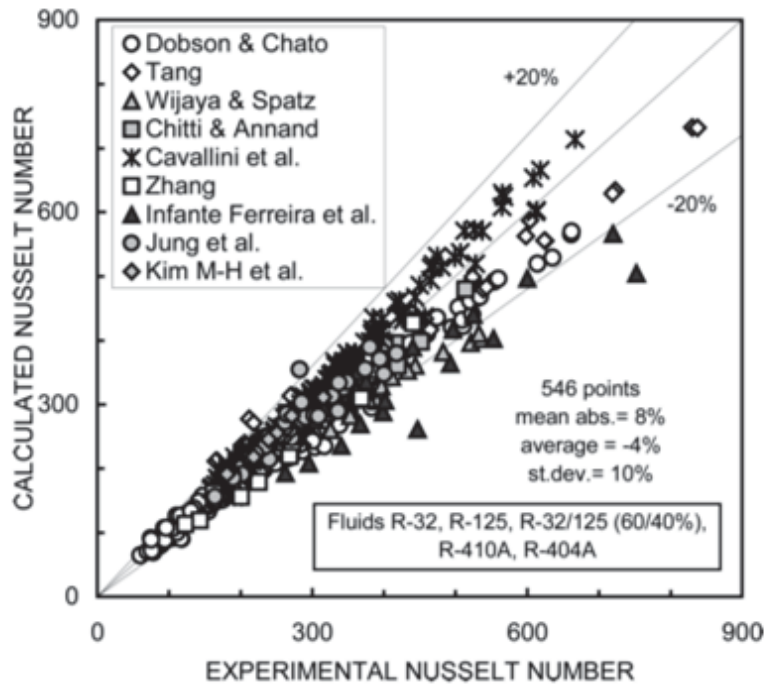


Figure I.10: Application of the Cavallini et al. model to HFC pure fluids and an azeotropic mixture [11]

The heat transfer coefficient during condensation inside 2mm hydraulic diameter was experimentally measured by Yan and Lin [42]. They compared their experimental results to previous ones obtained inside a 8 mm hydraulic diameter tube. From this study, it is highlighted that the average heat transfer coefficient inside the smallest tube is about 10% higher than inside the bigger pipe.

Del Col and al. [43] presented the effect of tube shape on heat transfer coefficient. They measured the condensation heat transfer coefficient inside a single square-cross section minichannel of 1.18 mm hydraulic diameter and compared them to the ones previously measured in a circular minichannel with the same dimension. Experimental data were recorded with R134a as the working fluid, at saturation temperature of  $40^{\circ}C$  and for mass velocity ranging between 200 and  $800 \text{ kg}\cdot\text{m}^{-2}\cdot\text{s}^{-1}$ . At  $200 \text{ kg}\cdot\text{m}^{-2}\cdot\text{s}^{-1}$ , the heat transfer coefficient in the square cross-section channel is higher than the one measured in the circular mini tube by 20-30%. At higher mass velocity, the heat transfer coefficients measured in the two channels are approximately the same. At low mass velocity, the effect of surface tension becomes greater and inside square mini tube, due to the corner's effect, the surface tension pulls the liquid out to corners reducing the average thermal resistance in the cross section and thus enhancing the heat transfer.

Other models of heat transfer dedicated to the annular and stratified flow are available in literature, among which one can cite Akers [44], Dobson and Chato [45], Moser and Web [46]. It is also highlighted that the heat transfer law is not applicable for all tube range and all working fluid as well as tube shape.

### Gravity's effect

Gravity has an important role in two-phase systems. The heat transfers in two phase flow with condensation depend mostly on gravity and shear stress for big pipe and also on surface tension for small diameter tube. There are some available studies about effect of gravity in this tube diameter range. Hereafter, a short review of gravity effect on condensation heat transfer is realized.

Lips and Meyer [28] investigated the effect of gravity on heat transfer coefficient by inclining smooth tube at different angles. The experimental tests were performed with R134a in a 8.38 mm inner diameter tube.

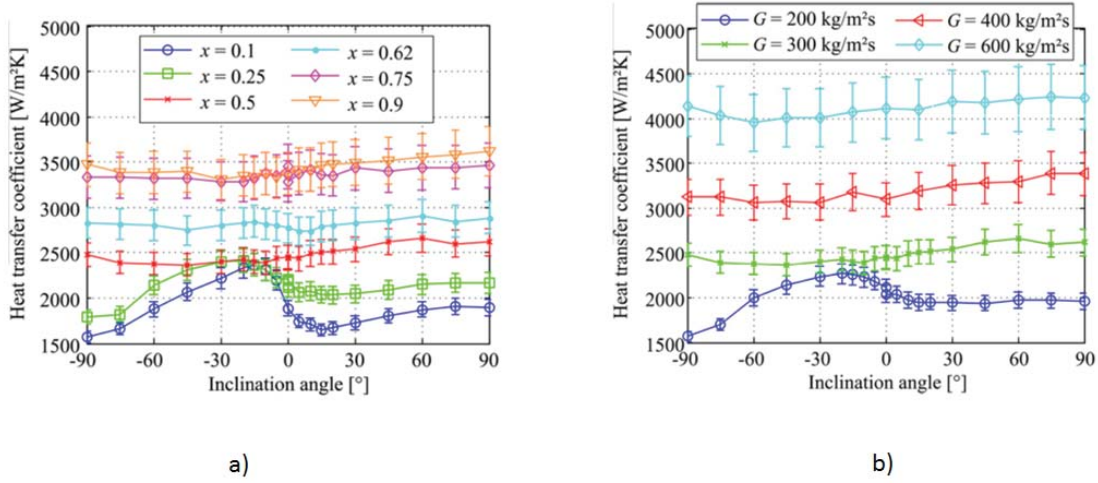


Figure I.11: Inclination effect on heat transfer coefficient for a) different vapor qualities at a constant mass velocity of  $300 \text{ kg.m}^{-2}.\text{s}^{-1}$  b) different mass velocities at a constant vapor quality of 0.5

Figure I.11a shows the heat transfer coefficient versus inclination angles for different vapor qualities at a constant mass velocity of  $300 \text{ kg.m}^{-2}.\text{s}^{-1}$ . Figure I.11b presented the heat transfer coefficient versus inclination angles for different mass velocities at a constant vapor quality of 0.5. At high mass velocity and high vapor quality, there is no effect of inclination angle or of gravity in general. However at low mass velocity and low vapor quality, the effect of inclination angle is observed. An optimum inclination angle between  $-15^\circ$  and  $-30^\circ$  was found (corresponding to a downward flow) for which the heat transfer coefficient is the highest, while an inclination angle of  $15^\circ$  leads to the lowest heat transfer coefficient.

In a recent paper, Del Col et al. [47] presented the effect of gravity on condensation of two HFC refrigerants inside a single square cross-section minichannel by varying the channel orientation. The local heat transfer coefficient during condensation of R134a and R32 were measured in horizontal ( $0^\circ$ ), downward flow and upward flow configurations with various inclination angles from  $15^\circ$  to  $90^\circ$  inside a 1.23 mm hydraulic diameter tube with mass fluxes ranging from 100 to  $390 \text{ kg.m}^{-2}.\text{s}^{-1}$ . It was noted that the inclination effect on the heat transfer coefficient can be observed at vapor qualities less than about 0.6 and mass velocities lower than a critical value depending on working fluids ( $150 \text{ kgm}^{-2}.\text{s}^{-1}$  for R134a and  $200 \text{ kgm}^{-2}.\text{s}^{-1}$  for R32).

Therefore, from the works presented above, the effect of gravity on heat transfer coefficient has been experimentally determined and is found to play an important role at low mass fluxes and low vapor qualities for both conventional and mini channels. Depending on the working fluid and tube dimensions, the critical vapor quality and mass velocity are different. However these studies have been performed on ground

where the gravity effect always exists, therefore it is interesting to analyze more deeply the heat transfer coefficient trend according to gravity level.

In a recent paper in 2013, Lee et al. [12] made experimental and theoretical investigations of annular flow condensation in microgravity. They used FC-72 as working fluid and the experiments were carried out in parabolic flights which provides a microgravity period of 15s to 20s ( $< 1.10^{-4}g$ ). They used two test sections for these studies, one for measuring the heat transfer coefficient and the second for visualization. To measure the heat transfer coefficient, they used stainless steel tube with a 7.12 mm internal diameter and 0.41 mm wall thickness. The cooling fluid was counter-current water. Mass velocity was ranging from  $129 \text{ kg.m}^{-2}.s^{-1}$  to  $340.5 \text{ kg.m}^{-2}.s^{-1}$  with inlet pressure from 1.137 to 1.263 bar. The cooling fluid mass velocity was ranging from 86.7 to  $321.4 \text{ kg.m}^{-2}.s^{-1}$ . The water inlet temperature was from 24.4 to  $27.4 \text{ }^\circ\text{C}$ . The second test section was used for visualization of condensation outside tube. Figure I.12 presents the two test modules employed to perform tests in microgravity.

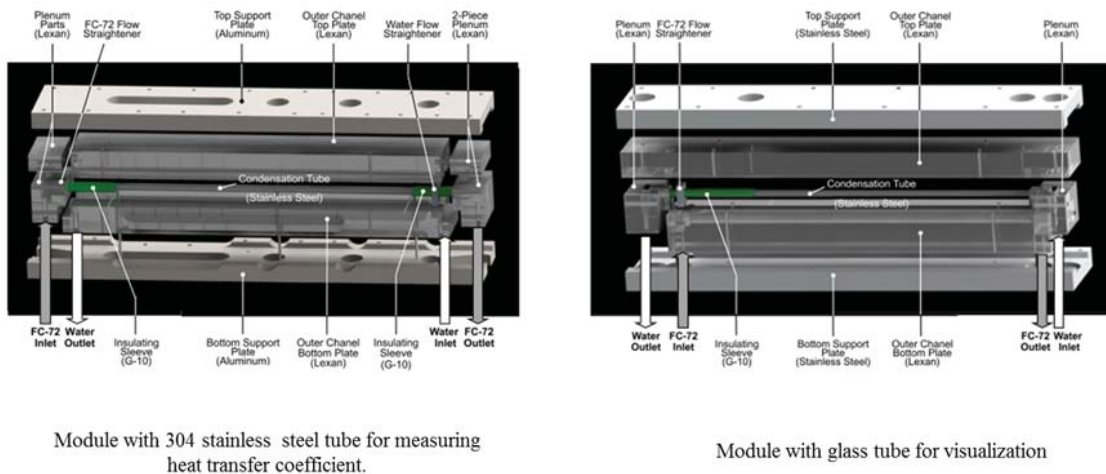


Figure I.12: The two test sections used by Lee et al. [12] to analyze convective condensation in microgravity condition.

The local heat transfer coefficients were then measured. Figure I.13 presents the local heat transfer coefficient during convective condensation at a mass velocity of  $264.1 \text{ kg.m}^{-2}.s^{-1}$  at different positions from the inlet versus time. It is pointed out that at the different positions the heat transfer coefficient decreases during microgravity period.

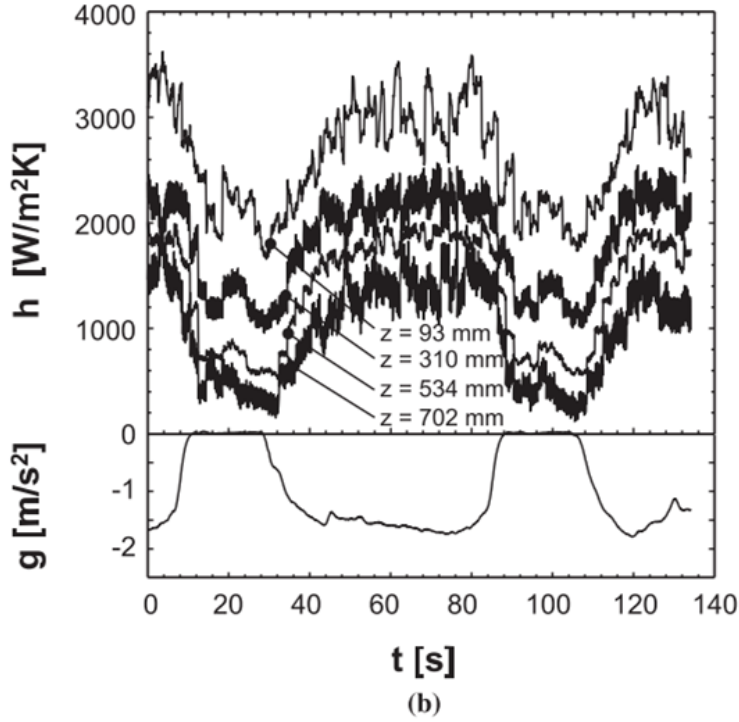


Figure I.13: Variation of condensation heat transfer at four axial locations during gravity changes corresponding to two microgravity parabolas for  $G = 264.1 \text{ kg.m}^{-2}.\text{s}^{-1}$  and inlet vapor quality of 0.73 at different positions.

They also proposed a model to calculate the heat transfer coefficient based on the control volume method. This microgravity model was developed from the formulation of Kim and Mudawar [48] (which is a model for annular flow condensation in small channels) and of Park et al. [49].

The local heat transfer coefficient in microgravity was expressed as:

$$h = \frac{\frac{\delta}{\lambda_f}}{\left[ \int_0^1 \left( 1 + \frac{Pr_f}{Pr_{f,T}} \cdot \frac{\varepsilon_m}{\nu_f} \right)^{-1} d\left(\frac{y}{\delta}\right) \right]} \quad (\text{I.1.4.36})$$

Where  $\delta$  is the average film thickness and  $\lambda_f$  is the liquid thermal conductivity.

$\varepsilon_m$  is eddy momentum diffusivity and could be evaluated by following formulation:

$$\frac{\varepsilon_m}{\nu_f} = \frac{-1}{2} + \frac{1}{2} \sqrt{1 + 4.K^2.y^{+2} \cdot [1 - \exp(-\sqrt{\frac{\tau}{\tau_w}} \frac{y^+}{A^+})]^2 \frac{\tau}{\tau_w} \left(1 - \frac{y^+}{\delta^+}\right)^{0.1}} \quad (\text{I.1.4.37})$$

Where  $y^+ = yu^*/\nu_f$ ;  $\delta^+ = \delta u^*/\nu_f$  with  $u^* = \sqrt{\tau_w/\rho_f}$ ;  
 $A^+ = 26[1 + 30.18\mu_f\rho_f^{-0.5}\tau_w^{-1.5}(dP/dz)]^{-1}$  and Von-Karman constant  $K=0.4$ . Finally,

the turbulent Prandtl number is expressed as:

$$Pr_{f,T} = 1.4 \exp\left(-15 \frac{y^+}{\delta^+}\right) + 0.66 \quad (\text{I.1.4.38})$$

where  $Pr_f$  is Prandtl number of the fluid and  $\tau_{wall}$  is the shear stress at the wall.

A comparison between the model and the experimental data was carried out. It was pointed out that the mean absolute errors was ranging from 10.3% to 26.1%.

To our knowledge, there is no other study of effect of gravity level on convective condensation in this tube dimension range.

In conclusion, in this range of tube dimension, there are many investigations about heat transfer coefficient during convective condensation. However most of them have been conducted on ground and at high mass velocity (higher than  $100 \text{ kg.m}^{-2}.\text{s}^{-1}$ ). It is highlighted that for given working fluid, tube dimension and cross-section shape, the effect of gravity was only observed at low mass velocity and low vapor quality. The critical vapor quality and mass velocity to determine the gravity-independent zone depend of each studied case. In the other hand, it is noted that the local heat transfer coefficient for convective condensation inside mini-tube in microgravity condition decreases in comparison of the one obtained in normal gravity. However, studies of convective condensation in microgravity condition inside mini and conventional tubes are still rare.

## I.2 Convective condensation inside micro channel

When the tube diameter becomes small compare to the capillary length, the surface tension becomes dominant compare to the gravitational force and this property can be used to simulate micro-gravity on ground. The two phase flow observed in micro tube can be divided into: annular flow, transitional regime, elongated bubble, spherical bubble. There is no stratified flow observed in this tube range both in high and low mass fluxes, it confirms the negligible value of gravitational force. Hereafter a review of condensation studies inside micro tube for flow pattern maps, pressure drop and heat transfer coefficient will be presented.

### I.2.1 Two phase flow pattern map in micro tube

There are fewer studies of two phase flow inside micro tube than inside conventional or mini tubes. In a study of Choi et al. [13], a flow of water and nitrogen gas inside rectangular micro channels of  $510 \times 470 \mu\text{m}^2$ ,  $608 \times 410 \mu\text{m}^2$ ,  $501 \times 237 \mu\text{m}^2$  and  $503 \times 85 \mu\text{m}^2$  with aspect ratio of 0.92, 0.67, 0.47 and 0.16 respectively was observed with superficial liquid velocity and superficial vapor velocity ranges between 0.06 to 1 m/s

and 0.06-71 m/s respectively. Authors divided the flow patterns observed into: bubble flow, transitional flow and liquid ring flows. The figure below presents the two phase flow observed in their tests at superficial liquid velocity of 0.2 m/s and at different superficial gas velocity. From figure I.14, it is noted that at a constant superficial liquid velocity as increasing the superficial vapor velocity the bubble length increases also until the transition regime occurs. However, they didn't propose any flow pattern map in this study.

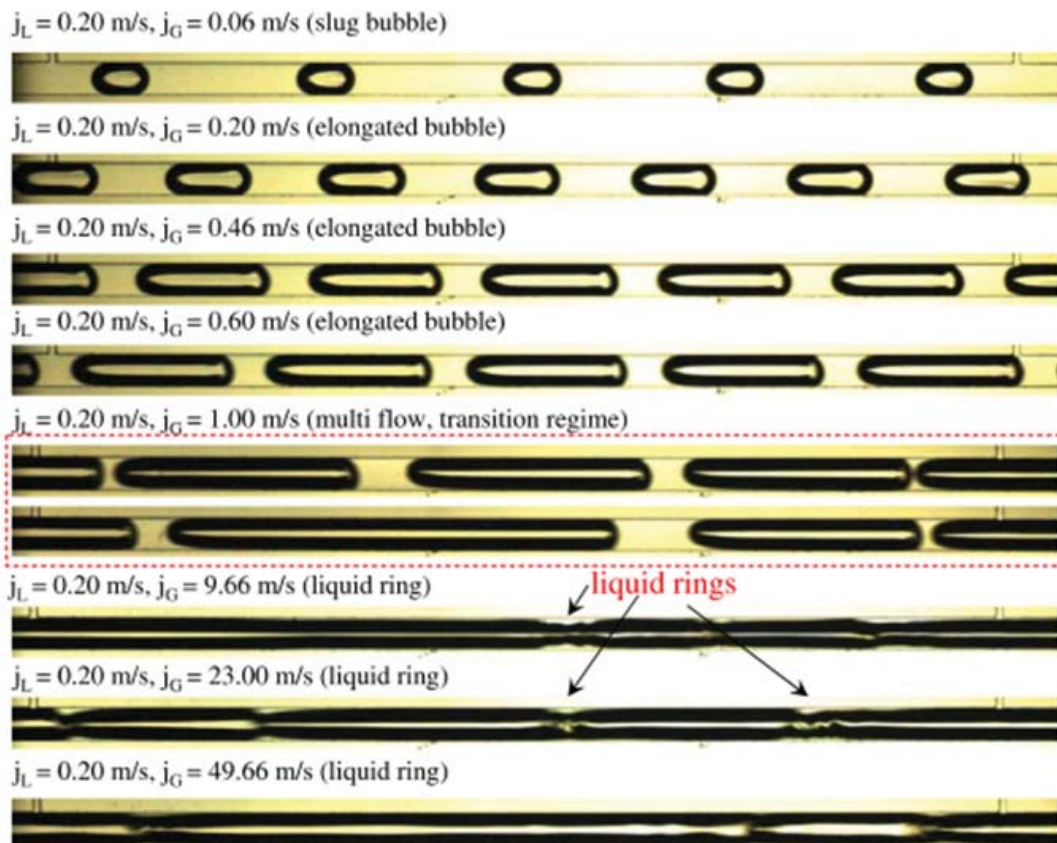


Figure I.14: The effect of superficial gas velocity on flow patterns of two phase flow inside  $510 \times 470 \mu m^2$  [13].

In other study of Sur and Liu [50] of adiabatic water-air two phase flow inside circular micro tube of 100, 180 and  $324 \mu m$ . They divided the flow patterns into: spherical bubble, elongated bubble, ring and annular flows. They established different flow pattern maps for different tube size. The figure I.15 presents the flow pattern maps obtained at different tube sizes where flows named bubbly, slug correspond to spherical bubble and elongated bubble. It is noted that as reducing the tube diameter, the regime transition from annular to ring flows or from ring to slug flows occurs at

higher superficial gas velocity. It is as the result of competition between surface tension and frictional force.

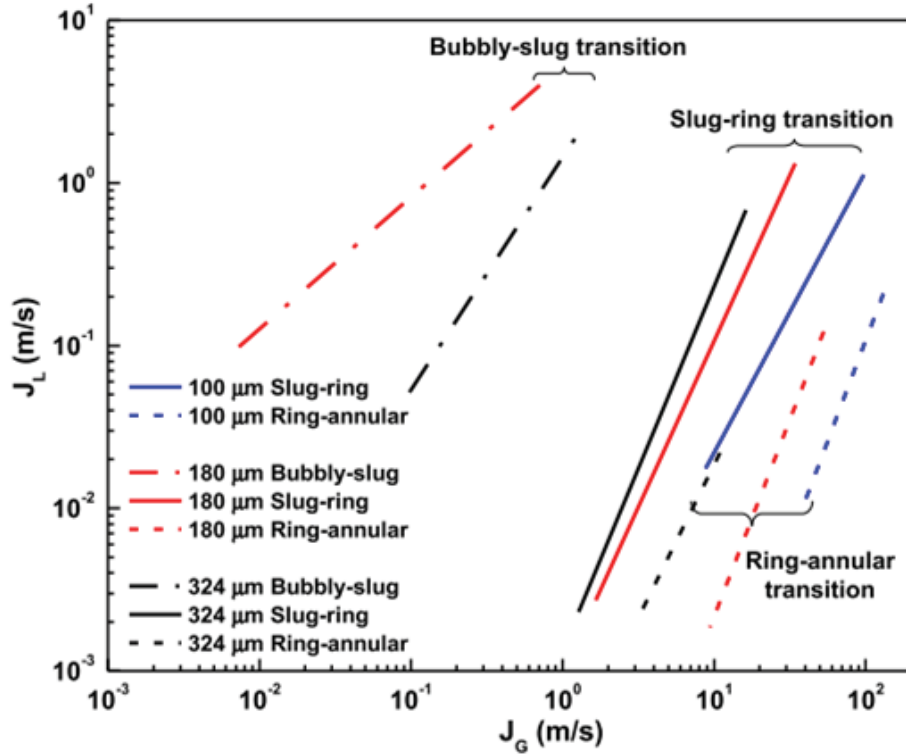


Figure I.15: The effect of superficial gas velocity on flow patterns of two phase flow inside  $510 \times 470 \mu m^2$

There are other investigations such as: Chung and Kaiwaji [51], Cubaud and Ho [52], Xu [53] for adiabatic two phase flow mostly in water-air inside micro tube from 20 to 600  $\mu m$  of different shapes. The same flow patterns were observed in these studies. However in these studies, the two phase change was not taken into account. In the following part an investigation of condensation inside micro tube will be presented.

Among many flow pattern investigation in convective condensation inside micro tube, Kim et al. [48] performed many tests of convective condensation of FC-72 inside parallel square tube of 1 mm hydraulic diameter. The range of mass velocity is from 67 to 367  $kg.m^{-2}.s^{-1}$  with saturation temperature from 57 to 62<sup>0</sup> C. They compared the experimental results with flow pattern maps of previous study of water-air adiabatic flow with approximately same hydraulic diameter of Chung and Kawaji [51] and Triplett [54] and concluded that the flow transition boundaries were coherent to these two previous studied.

At lower mass velocities where the viscous effect compared to tension force is neg-

ligible, investigation is still modest. The structures observed are more axisymmetric. Odaymet and Louahlia-Gualous [55] presented the flow regimes encountered in the adiabatic flow (water-air) where the hydraulic diameter is  $305 \mu\text{m}$  for single square micro-channel with a mass velocity ranging from 14 to  $31 \text{ kg.m}^{-2}.\text{s}^{-1}$ . Médéric et al. performed [56] the condensation of n-pentane inside  $0.54 \text{ mm}$  circular tube at low mass velocities from  $3.5 \text{ kg.m}^{-2}.\text{s}^{-1}$  to  $15 \text{ kg.m}^{-2}.\text{s}^{-1}$ . Water is used as coolant. At the beginning of the two-phase flow, an annular regime can be observed inside of the tube [56], [14]. Along the position, vapor velocity decreases, it causes ripples to form on the liquid-vapor surface, leading to the formation of collars. Eventually, the collars grow to form a bridge [14]. The relative size of the gap released as a result of liquid bridge defines slug, plug, and bubble regimes [56]. Fig. I.18 show the flow patterns often encountered in a capillary tube. In a large tube, the bridge is not observed because of dominant gravitational force on the liquid film. In addition, in the case of small-diameter tubes, the instability occurs due mainly to capillary blocking where the liquid film bridges the tube to form a plug or a slug. They found the regime transition occurs at a critical value of vapor velocity.

In a recent study, El Achkar [14] study the flow pattern maps of in-tube condensation of n-pentane and HFE-7000 in a miniature square section ( $553 \times 675 \mu\text{m}^2$ ) with mass fluxes range between 3.1 to  $12 \text{ kg.m}^{-2}.\text{s}^{-1}$  for HFE-7000 and of 1.8 up to  $22 \text{ kg.m}^{-2}.\text{s}^{-1}$  for n-pentane with air conditioner as secondary fluid. They classified the flow regimes encountered into 2 groups: annular zone and intermittent zone (spherical bubble and elongated bubble). In annular zone, liquid collars were observed. Figure I.16 presented some observed two phase flow regimes during condensation of n-pentane at  $5 \text{ kg.m}^{-2}.\text{s}^{-1}$  inside square micro tube.

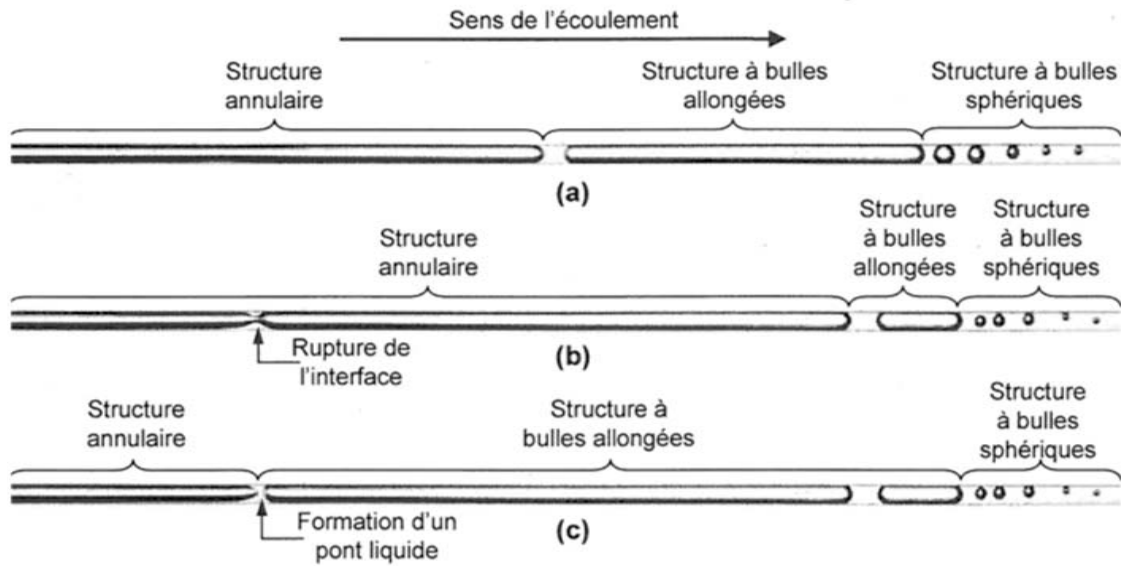


Figure I.16: Structure of the different flow patterns encountered during the condensation process in a square cross-section micro-channel with n-pentane working fluid at  $5 \text{ kg.m}^{-2}.\text{s}^{-1}$  with  $22.62^{\circ} \text{ C}$  conditioning air temperature in three different moments: (a)  $t=0 \text{ ms}$ ; (b)  $t=50 \text{ ms}$ ; (c)  $t=51 \text{ ms}$  [14]

From this study, it was highlighted that with respective working fluid, for a given tube diameter, in the range of mass velocities studied, the size of liquid collar increase quickly at the end of the annular zone to form liquid bridges. The position of this liquid formation which delimitate the end of the annular zone and the beginning of elongated bubble is observed at a same value of average vapor velocity. The average vapor velocity is estimated assuming that the void fraction at the location of formation of liquid bridge is equal to 0.81 for the square section tube (Garimella [57]). The interesting point is that these value remains the same in the entire range of mass velocity studied. The fact that a unique value of vapor velocity allows to predict the position of the transition between annular regime and intermittent regime whatever the mass flow rate value where observed with the two fluids studied ; n-pentane and HFE-7000. Of course this critical value depends on the working fluid.

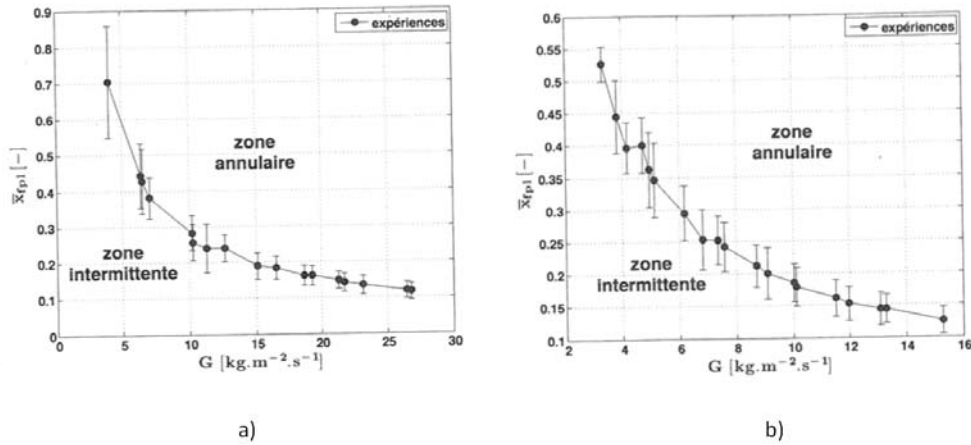


Figure I.17: Evolution of average vapor quality at the location of formation of liquid bridge according to the mass velocity for a) HFE-7000 flow at 23.13°C conditioning temperature b) n-pentane flow at 22.67°C air conditioning temperature [14].

It is pointed out that the instability of two phase interface was experimentally observed. The instability of the liquid-vapor interface appear in the first development of the liquid film (at very high value of the quality) the observed wave increases and creates solitary waves which form liquid collar. This collar continues to grow until they form a liquid bridge which generate the transition between annular and plug flow regimes. Many studies about this type of two phase flow instability has been investigated, mostly inside micro scale channels. In general, they proposed criterion for flow transitions. Rabas and Minard [58] suggested two forms of flow instabilities occurring inside horizontal tubes with complete condensation. The two forms are distinguished by a transition Froude number. It is suggested that the first instability results from the low vapor flow rate associated with a stratified exit condition and from vapor flowing into the tube exit, which causes condensate chugging or water hammer instability. The second instability results from a high vapor flow rate, which produces an inadequate distribution of the vapor and blockage of the tube exit, in turn causing large sub-cooled condensate temperature variations.

In another study, Duclaux et al.[15] studied experimentally and theoretically the effect of gravity on the capillary instabilities in tubes. They investigated the motion of silicone oils and glycerol liquid film with tube radius ranging from 150  $\mu\text{m}$  to 1.5 mm. From experimental investigation, they found that the instability only occurs if  $h_o/R_o > 0.3(R_o/a)^2$ , where  $a$  is the capillary length,  $h_o$  is liquid film and  $R_o$  is tube radius and  $a$  is the capillary length.

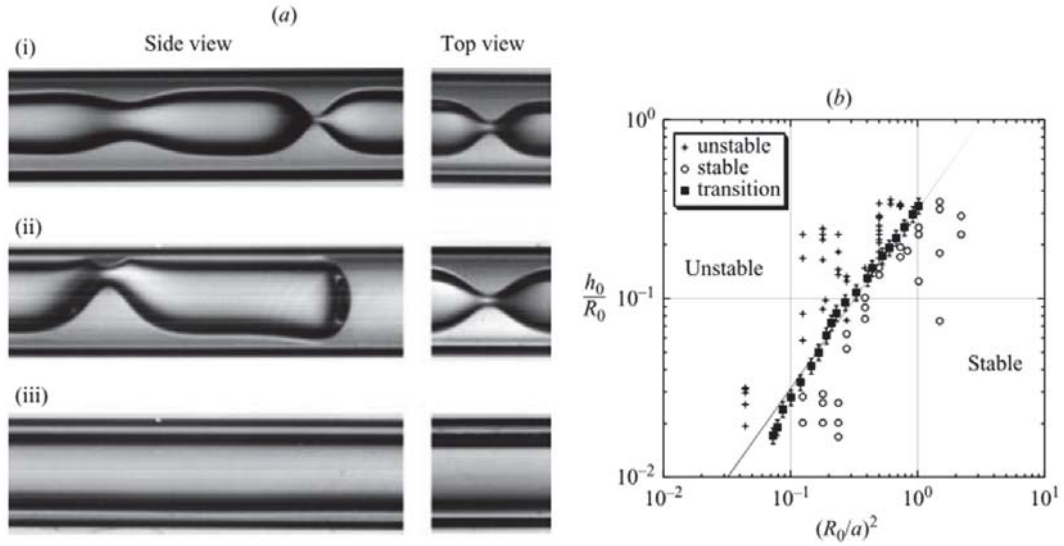


Figure I.18: The experimental results of instability of the motion of silicon oils and glycerol inside micro tube [15].

Concerning model of instability study resulted by the dynamics of the viscous liquid film and static stability of the collar film in cylindrical capillaries, there are some available study such as Gauglitz and Radke [59] of adiabatic micro tube, Teng et al. [60] in a thermosyphon condenser, Tabatabai and Faghri [61] inside two phase flow in horizontal micro channels. It was pointed out that at high relative vapor velocities, hydrodynamic force was responsible for this instability. And on the other hand, at low relative vapor velocities, surface tension, the hydro-dynamic force and the vapor-liquid density ratio were responsible for interface instability in capillary tubes. Furthermore, in comparing between these two cases, it was highlighted that at high vapor velocity, the vapor-liquid is often more irregular because of the facility break-up disturbance waves due to a high hydrodynamic interfacial force. Additionally, interface liquid bridges are maintained by buoyant motion of the vapor bubbles.

Numerically in another study, Miscevic et al.[62] [63] proposed a model for condensation in cylindrical capillaries by considering two phases in this model. The model was formulated by the continuity equations and the conservation of momentum equations for the liquid and vapor phases with an approximation of small slope of interface, with assumption of uniform pressure distribution in each cross-section of liquid phase and vapor phase and with the phase change. The thermal balance was established in considering that the exchange between the working fluid and coolant is purely radial and transfers is purely conductive in liquid films. They succeed to simulate the instationary and stationary flow observed by Méderic et al.[56] . The dominant effects of this type of flow, which are characterized by dimensionless numbers  $Ca$  (capillary number) and  $Bo$  (boiling number), representing the competition between the capillary, viscous and

phase-change effects. Finally the result is analyzed based on four dimensionless numbers capillary number, boiling number, the density ratio of the phases and the liquid Reynolds number.

## I.2.2 Pressure drop of two phase flow in micro tube

In section above, a general investigation about two phase flow pressure drop has been done. The most common and most used correlations are the one of Lockhart and Martinelli [30] and Friedel [31] one; however these correlations have been developed inside large tube. It is highlighted that the pressure drop are mainly depend on flow regime which result of forces balance between viscous, inertia and capillary forces. Therefore common correlations sometimes failed to predict the pressure drop inside micro tube.

In a paper, Mudawar and Kim [49] proposed a universal approach to predict the pressure drop inside mini-micro tube based on 7115 pressure drop data points from 36 different sources for both adiabatic and condensing flow. The model was built on Lockhart and Martinelli model in modifying the constant  $c$ . Whose values are ranging from 5 to 20 for conventional tube with a dimensionless groups in order to capture small dimension's effect, different working fluids and flow parameters. The two phase pressure drop of two phase flow can be calculated as:

$$\left(\frac{dp}{dx}\right)_{TP} = \Phi_L^2 \left(\frac{dp}{dx}\right)_L \quad (\text{I.2.2.1})$$

With  $\Phi_L$  is two phase friction multiplier that can be evaluated as:

$$\Phi_L^2 = 1 + \frac{c}{X} + \frac{c}{X^2} \quad (\text{I.2.2.2})$$

With:  $X^2 = \frac{(dp/dz)_L}{(dp/dz)_V}$  and :  $\left(\frac{dp}{dx}\right)_L = \frac{2f_L G^2 (1-x)^2 \nu_L}{D_h}$  and  $\left(\frac{dp}{dx}\right)_V = \frac{2f_V G^2 x^2 \nu_V}{D_h}$

With  $f_k$  can be determined as:

$$f_k = 16Re_k^{-1} \text{ for } Re < 2000$$

$$f_k = 0.079Re_k^{-0.25} \text{ for } 2000 \leq Re < 20000$$

$$f_k = 0.046Re_k^{-0.2} \text{ for } Re \geq 20000$$

For laminar flow in rectangular pipe:

$$f_k Re_k = 24(1 - 1.3553\beta + 1.9467\beta^2 - 1.7012\beta^3 + 0.9564\beta^4 - 0.2537\beta^5)$$

With  $\beta$  is channel aspect ratio and  $k$  is noted for vapor or liquid phase and Reynolds numbers of each phase can be evaluated as:  $Re_L = \frac{G(1-x)D_h}{\mu_L}$  and  $Re_V = \frac{GxD_h}{\mu_V}$  The

constant  $C$  can be determined as following:

$$\text{If } Re_L > 2000 \text{ and } Re_V > 2000 : C = 0.39 Re_{Lo}^{0.03} Su_{Vo}^{0.10} \left(\frac{\rho_L}{\rho_V}\right)^{0.35}$$

$$\text{If } Re_L \leq 2000 \text{ and } Re_V < 2000 : C = 8.7 \times 10^{-4} Re_{Lo}^{0.17} Su_{Vo}^{0.50} \left(\frac{\rho_L}{\rho_V}\right)^{0.14}$$

$$\text{If } Re_L < 2000 \text{ and } Re_V \leq 2000 : C = 0.0015 Re_{Lo}^{0.59} Su_{Vo}^{0.19} \left(\frac{\rho_L}{\rho_V}\right)^{0.36}$$

$$\text{If } Re_L < 2000 \text{ and } Re_V < 2000 : C = 3.5 \times 10^{-4} Re_{Lo}^{0.44} Su_{Vo}^{0.50} \left(\frac{\rho_L}{\rho_V}\right)^{0.48}$$

$$\text{With } Re_{Lo} = \frac{GD_h}{\mu_L} \text{ and } Re_{Lo} = \frac{\rho_V \sigma D_h}{\mu_V^2}$$

This model is then compared to experimental data. An agreement has been found with a deviation less than 27%.

### I.2.3 Heat transfer coefficient inside micro tube

Heat transfer during convective condensation inside micro tube have been taken the attention and studied since many years. These investigations are realized in order to improve their performance and design more effective and more compact thermal exchanger. Hereafter a review of heat transfer coefficient inside single or multiple micro tube of different dimensions and shapes will be presented.

#### Koyama's Correlation [64]:

Koyama et al.[64] investigated experimentally the local characteristics of pressure drop and heat transfer for the condensation of pure refrigerant R134a in two kinds of 865 mm long multi-port extruded tubes; one with eight channels in 1.11 mm hydraulic diameter and the second with 19 channels in 0.80 mm hydraulic diameter. Mass fluxes extend over a range between 100 to 700  $kg.m^{-2}.s^{-1}$ . Using the Haraguchi et al. approach [65] proposed for in-tube condensation, Koyama proposed a tentative correlation that has better agreement with the experimental data. In this correlation, both effects of the forced convection and free convection are taken into account. The correlation on heat transfer coefficient initially developed for conventional tube of 8.4 mm I.D has been modified in order to fit experimental data obtained for such a tubes with the following approach.

The Nusselt number is:

$$Nu = (Nu_F^2 + Nu_B^2)^{1/2} \quad (I.2.3.1)$$

Where  $Nu_F$  and  $Nu_B$  are respectively Nusselt number of forced convection condensation term and of gravity controlled convection condensation term. And they are

calculated by:

$$Nu_F = 0.0152(1 + 0.6Pr_L^{0.8})\left(\frac{\phi_V}{X_{tt}}\right)Re_L^{0.77} \quad (I.2.3.2)$$

Where:

$$\phi_V^2 = 1 + 21(1 - e^{-0.319})X_{tt} + X_{tt}^2 \quad (I.2.3.3)$$

And

$$Nu_B = 0.725H(\alpha)\left(\frac{GaPr_L}{Ph}\right)^{1/4} \quad (I.2.3.4)$$

Where:

$$H(\alpha) = \alpha + \{10[(1 - \alpha)^{0.1} - 1] + 1.7x10^{-4}Re_{Lo}\}\sqrt{\alpha}(1 - \sqrt{\alpha}) \quad (I.2.3.5)$$

With Ga is Galileo number, Ph is phase change number,  $\alpha$  is void fraction.

$$\alpha = \left[ 1 + \frac{\rho_V}{\rho_L} \left( \frac{1-x}{x} \right) \left( 0.4 + 0.6 \sqrt{\frac{\frac{\rho_L}{\rho_V} + 0.4 \frac{1-x}{x}}{1 + 0.4 \frac{1-x}{x}}} \right) \right]^{-1} \quad (I.2.3.6)$$

#### Bandhauer's model [66]:

Bandhauer and all presented a model for predicting heat transfer during condensation of R134a refrigerant in horizontal microchannels. Heat transfer coefficient measurements were conducted inside three circular microchannels of 0.506mm, 0.761mm and 1.524mm over the mass flux ranging from 150 to 750  $kg.m^{-2}.s^{-1}$ . The proposed empirical model was based on these experimental results. The Bandhauer's model employed the pressure drop model of Agarwal [67] to define the turbulence parameter as below:

$$u^+ = \frac{u}{u^*} \quad (I.2.3.7)$$

$$R^+ = \frac{\rho_L R u^*}{\mu_L} \quad (I.2.3.8)$$

Where R is tube's radius and  $u^*$  is friction velocity which is determined as:

$$u^* = \sqrt{\frac{\tau_i}{\rho_L}} \quad (I.2.3.9)$$

The dimensionless turbulence temperature is evaluated by:

$$T_+ = \frac{\rho_L c_{pL} u^*}{\dot{q}} \quad (\text{I.2.3.10})$$

Where  $\dot{q}$  is the heat flux. The heat transfer coefficient is calculated as formulation below:

$$h = \frac{\rho_L c_{pL} u^*}{T_+} \quad (\text{I.2.3.11})$$

The inter-facial shear stress can be evaluated as following:

$$\tau_i = \left(\frac{\Delta p}{L}\right) \frac{D_h}{4} \quad (\text{I.2.3.12})$$

$$\left(\frac{\Delta p}{L}\right) = \frac{1}{2} f_i \frac{G_{tot}^2 x^2}{\rho_V \alpha^{2.5} D_h} \quad (\text{I.2.3.13})$$

The void fraction can be determined by following expression:

$$\alpha = [1 + \left(\frac{1-x}{x}\right)^{0.74} \left(\frac{\rho_V}{\rho_L}\right)^{0.65} \left(\frac{\mu_L}{\mu_V}\right)^{0.13}]^{-1} \quad (\text{I.2.3.14})$$

The interfacial friction factor is:

$$f_i = f_L A \chi^a Re_L^b \psi^c \quad (\text{I.2.3.15})$$

The parameter Martinelli can be determined as:

$$\chi = \left[\frac{(dp/dz)_L}{(dp/dz)_V}\right]^{1/2} \quad (\text{I.2.3.16})$$

Where the Reynolds number of liquid and vapor phases can be determined as:

$$Re_L = \frac{G_{tot} D_h (1-x)}{\mu_L (1-\sqrt{\alpha})} \quad (\text{I.2.3.17})$$

$$Re_V = \frac{G_{tot} D_h x}{\mu_L \sqrt{\alpha}} \quad (\text{I.2.3.18})$$

With A, a, b, c which are friction factors depend on liquid Reynolds number:

- If  $Re_L < 2100$ :  $A=1.308 \times 10^{-3}$ ;  $a=0.427$ ;  $b=0.930$  and  $c=-0.121$ .

- If  $Re_L > 3400$ :  $A=25.64 \times 10^{-3}$ ;  $a=0.532$ ;  $b=-0.327$  and  $c=0.021$ .

Where the friction factor  $f$  can be evaluated as:  $f=64/Re$  if  $Re < 2100$  and  $f=0.316 Re^{-0.25}$  if  $Re > 3400$ . For transition regime, it is calculated at the values of mass velocities corresponding to the limitation of laminar and turbulent regimes and a linear interpolation between this two limitations is done. The surface tension can be determined as:

$$\psi = \frac{j_L \mu_L}{\sigma} \quad (\text{I.2.3.19})$$

Where  $j_L$  is liquid velocity:

$$j_L = \frac{G_{tot}(1-x)}{\rho_L(1-\alpha)} \quad (\text{I.2.3.20})$$

The dimensionless temperature is defined as following formulation:

- For  $Re_L < 2100$

$$T^+ = 5Pr_L + 5\ln\left[1 + Pr_L\left(\frac{\delta^+}{5} - 1\right)\right] \quad (\text{I.2.3.21})$$

- For  $Re_L \leq 2100$

$$T^+ = 5Pr_L + 5\ln(5Pr_L + 1) + \int_{30}^{\delta^+} \frac{dy^+}{\left(\frac{1}{Pr_L} - 1\right) + \frac{y^+}{5}\left(1 - \frac{y^+}{R^+}\right)} \quad (\text{I.2.3.22})$$

The dimensionless liquid film thickness is written as:

$$\delta^+ = \frac{\rho_L \delta u^*}{\mu_L} \quad (\text{I.2.3.23})$$

$$\delta = (1 - \sqrt{\alpha}) \frac{D_h}{2} \quad (\text{I.2.3.24})$$

This model based on experimental data at high mass velocity was developed by considering the analysis of turbulent film liquid or shear stress is the dominant force. The surface tension was not taken in to account therefore inside micro tube or at low mass velocity where the surface tension becomes important, this model couldn't predict well the heat transfer coefficient.

**Akhil Agarwal's Correlation [16], [17]:**

In a recent papers, Akhil Agarwal et al. [16], [17] studied heat transfer coefficients in six non-circular horizontal micro-channels with hydraulic diameter ranging from 0.424mm to 0.839 mm of different shapes during condensation of R134a working fluid. The experimental investigation was carried out with the following mass flux range :  $150 \text{ kg.m}^{-2}.\text{s}^{-1} < G < 750 \text{ kg.m}^{-2}.\text{s}^{-1}$ . The channel shapes studied were barrel-shaped, N-shaped, rectangular, square, triangular extruded tubes, and a channel with a W-shaped corrugated insert that yielded triangular micro-channels. Fig. I.19 presents channel shapes and number of channels studied by Akhil Agarwa et al.

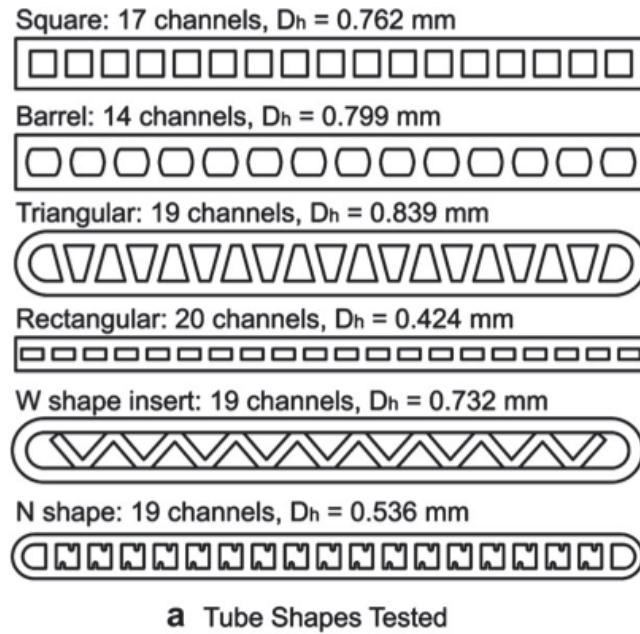


Figure I.19: Test section schematic and micro-channel shapes used by Akhil Agarwal et al.[16], [17].

They proposed a model for heat transfer below:

$$Nu = 0.00345 Re_{mix}^{0.9} \left( \frac{\mu_V \cdot l_V}{\lambda_V \cdot (T_{sat} - T_w)} \right)^{1/3} \quad (\text{I.2.3.25})$$

Where:  $Re_{mix}$ : is Reynold number mixture of vapor and liquid:

$$Re_{mix} = \frac{G \cdot D_h}{\mu_{mix}} \quad (\text{I.2.3.26})$$

With:

$$\mu_{mix} = \left( \frac{x}{\mu_V} + \frac{1-x}{\mu_L} \right)^{-1} \quad (\text{I.2.3.27})$$

While many studies presented above have proposed correlations, others attempt to validate them. Shin and Kim [68] [69] performed many experimental measurement of heat transfer coefficient during condensation inside a micro tube. Tests were carried out with R134a working fluid inside circular sections of 0.493, 0.691 and 1.067mm hydraulic diameter and square sections of 0.494, 0.658 and 0.972 mm with mass velocity of 200, 400, 600  $kg.m^{-2}.s^{-1}$  and flux density rang of 5 to 20  $kW.m^{-2}$ . They compared then their experimental results to the correlation of Shah [39] and Akers [70]. The Shah's correlation was developed during condensation for mini channels from 7 mm to 40 mm and mass velocity ranging from 200 to 600  $kg.m^{-2}.s^{-1}$ . They found that at low mass velocities, Shah's correlation underestimates experimental results. However at high mass velocity, this model overestimates the Nusselt number. For Akers's correlation [70] which predicts well many studies during condensation inside very small tube diameter ([71]-[72]). In this study they compared also experimental results inside circular and square tubes at the same dimension. They found that at low mass velocity, the effect of surface tension can be observed when the heat transfer coefficient inside square tube is higher than inside circular tube. This effect reduces at higher mass velocity. In the other hand, inside smaller tube, the heat transfer coefficient is higher due to the effect of higher capillary force.

There are other comparison of experimental results with many available models such as: Park et al. [73], [49]... In these investigations, it is shown that the heat transfer coefficient law inside micro tube is not the same behavior inside mini and conventional tubes. Moreover, the result inside non-circular tube section is different to the one inside circular test section due to the different effect of surface tension. Therefore the heat transfer law inside circular tube is not applicable for non circular tube.

### I.3 Conclusion

This chapter presents a review of flow pattern maps, pressure drop and heat transfer coefficient during condensation inside conventional and mini channels where the gravity plays an important role and inside micro-channel where the gravity is negligible. It is highlighted that the heat transfer coefficient, pressure drop are correlated with flow patterns especially to liquid film distribution. In some correlations for predicting heat transfer coefficient, film thickness is an important parameter. However very few investigations of heat transfer coefficient and condensation film thickness simultaneously during condensation has been performed. This review shows also that inside conventional and mini tube, at high mass flux and for some vapor qualities and tube dimension (whose values depending on working fluid), the effect of gravity is not observed due to the dominance of shear stress both on heat transfer coefficient, pressure drop and flow patterns. However, very few studies investigate the evolution of these important aspects for different level of gravity. Not only a lack of information about

---

experimental measurements of heat transfer coefficient and film thickness but also the condensation inside mini tube at low mass flux is really rare. In this context, this thesis is dedicated to study the heat transfer coefficient and flow pattern map especially liquid film thickness evolution inside mini tube at low mass fluxes under the effect of gravity.

## Chapter II

# Opening model for condensation's instabilities in a micro-channel

The interface liquid-vapor's instability has been studied more recently, it helps to determine the regime transition. Many experimental investigations were performed in micro-gravity condition or in micro-gravity simulation on ground. However the corresponding development of a model of a two-phase flow has been still modest. In knowing that the heat transfer coefficient is a function of flow pattern, therefore, it is interesting to develop a model that can simulate and predict the two phase-flow which is supposed to be annular in these conditions. Moreover, El Achkar et al. [14] who investigated experimentally the convective condensation of HFE-7000 and n-pentane inside a micro tube both in square tube of  $0.553 \mu m$  hydraulic diameter and multi-circular tube of  $0.56 \mu m$  hydraulic diameter to simulate micro gravity on ground with air conditioner as secondary fluid. They found that in square tube, the transition regime between annular and intermittent occurs at the same vapor velocity for each working fluid and independently to mass velocity. These values correspond to  $0.73$  and  $0.43 m.s^{-1}$  for n-pentane and HFE-7000 respectively. However the surface tension effect will not be the same in different micro channel configurations. Therefore the transition regime between annular and intermittent inside circular micro tube is predicted at the same vapor velocity for working fluid and independently to mass velocity however being different value found in square tube. This chapter will present an opening physical model based on experimental results of condensation inside micro tube. In the first part of this chapter, some experimental results of flow regime with transition regime inside circular tube will be exploited. Finally, an opening numerical model will be presented.

## II.1 Investigation of convective condensation inside condenser multi-channels

The experimental study of convective condensation of n-pentane working fluid has been carried out inside multi-channel of 4 horizontal circular micro tube by Georges El Achkar [14]. Conditioned air is used as secondary fluid. The tube's hydraulic diameter is  $560 \mu\text{m}$  and the distance between them is  $1 \text{ cm}$ . The range of mass velocity is from  $5.45$  to  $22.5 \text{ kg.m}^{-2}.\text{s}^{-1}$ . More experimental details had been described in [14]. The figure below shows the experimental condenser's installation for this study with  $\delta = 1 \text{ cm}$  and the flow structure inside four condensers when the total mass flow rate is equal to  $5.45 \text{ kg.m}^{-2}.\text{s}^{-1}$  obtained by a high speed camera working at a frequency of  $1000 \text{ Hz}$ . Figure II.1 presents the schema of condenser during condensation tests and figure II.2 presents the two phase flow configuration obtained at total mass velocity of  $5.45 \text{ kg.m}^{-2}.\text{s}^{-1}$  and for flux density of  $3970 \text{ W.m}^{-2}$ .

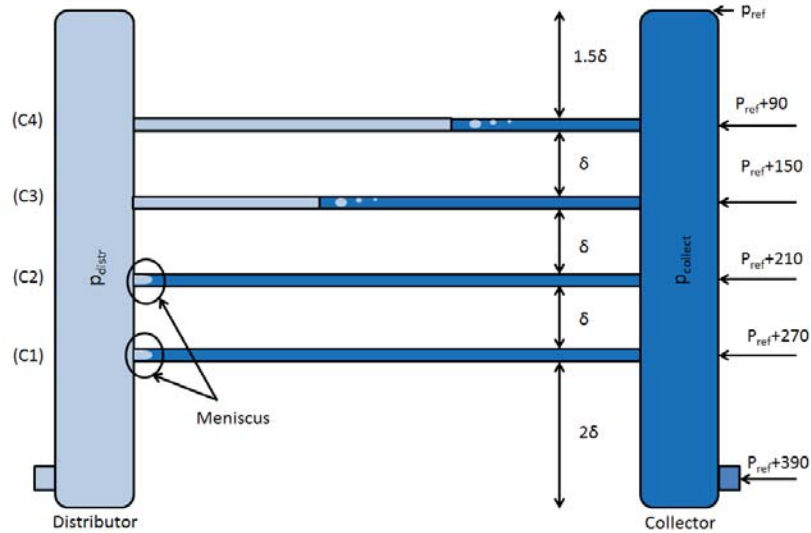


Figure II.1: The schema of condenser installation during test with n-pentane working fluid and an obtained flow regime inside 4 condensers for total mass velocity of  $5.45 \text{ kg.m}^{-2}.\text{s}^{-1}$  and for flux density of  $3970 \text{ W.m}^{-2}$  [14].

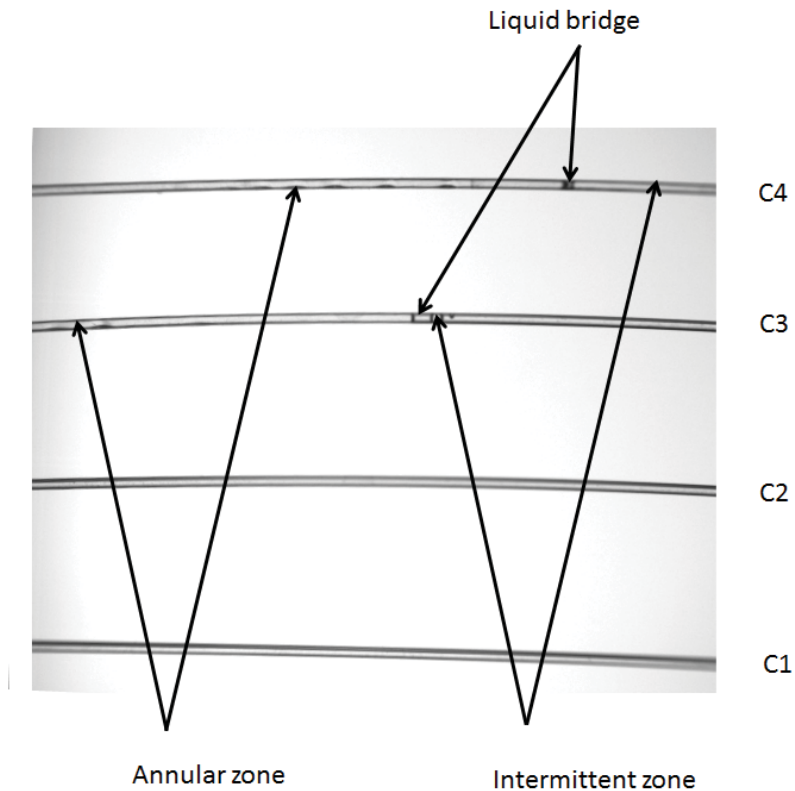


Figure II.2: Flow distribution inside 4 condensers for total mass velocity of  $5.45 \text{ kg.m}^{-2}.s^{-1}$  and for flux density of  $3970 \text{ W.m}^{-2}$  recorded by high speed camera recorded by El Achkar et al. [14].

In this study, El Achkar et al. [14] presented some results of liquid bridge formation such as: the position of liquid bridge formation and the deducted mass velocity in each condenser. No information about flow transition regime was given as it was done in square tube. In order to estimate the critical vapor velocity at liquid bridge, an image processing of video obtained by Georges El Achkar has been done.

In order to study the interface's evolution, it is necessary to determine the distribution of liquid-vapor phases inside tube. Therefore, a specific program has been developed thanks to Matlab software to performe image processing of all experimental data. The two-phase distribution in each tube has been investigated separately at different mass velocity.

All raw images acquired by high speed camera had been recorded at different grey levels from 0 to 255. These photos have been then first interpolated ; in order to use the information contained in gray level and then converted to binary image relatively to a chosen threshold value. Therefore the vapor and liquid zones have been detected.

More details about image processing could be found in chapter 3 of this thesis. The axial position of waves are then determined. As it can be observed also in figure II.2, when liquid collar collapse the liquid bridge creates a barrier for the vapor flow. The liquid bridge is then pushed by the vapor flow. A sudden increase of the collar speed is then observed when the liquid collar becomes a liquid bridge. This property is used to detect the axial position of liquid bridge formation. This position reveals also the transition regime location between annular and intermittent flows. Therefore, the axial position of liquid collar versus time has been studied and analyzed through this processing image. The figure II.3a) shows the collar liquid's evolution and position during experiment of condensation of n-pentane working fluid at mass velocity of  $4.3 \text{ kg.m}^{-2}.s^{-1}$  in condenser C3. The green, red and blue waves have been observed from its creation until its collapse and their positions with time have been presented in figure II.3b) of the same colors.

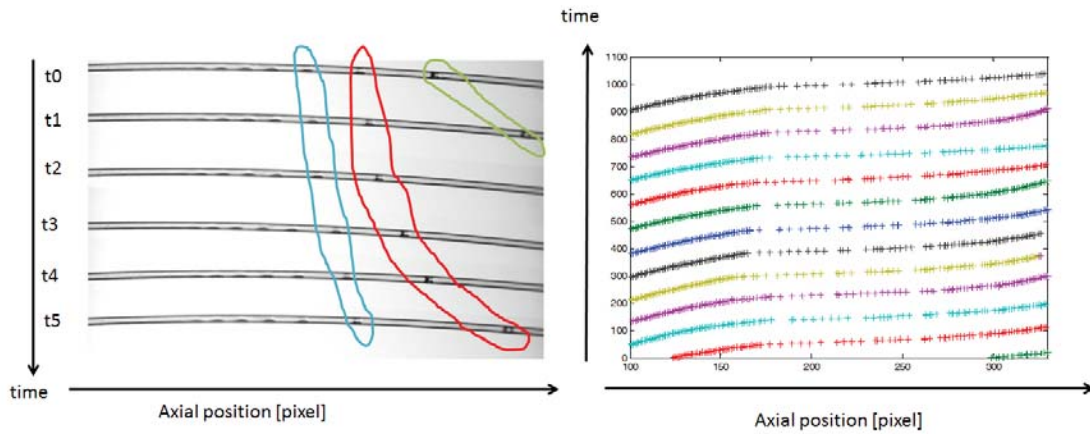


Figure II.3: Flow distribution inside 4 condensers with mass velocity of  $5.45 \text{ kg.m}^{-2}.s^{-1}$  and for flux density of  $3970 \text{ W.m}^{-2}$  recorded by high speed camera and wave's position evolution versus time obtained from image processing program.

From axial position's evolution and frequency of acquisition, the value of the wave's velocity can be determined. Figure II.3 shows waves move slowly at the beginning and accelerate (around the axial position equal to 175) when collars start to collapse and achieve its maximum velocity when the transition between annular and intermittent occurs and the bubble then detaches from annular zone. This phenomena has been observed for all other tests. We considered the maximum wave velocity is the critical velocity when the flow transition occurs. Figure II.4 presents the vapor velocity while liquid bridge appears versus vapor quality ranging from 1 to  $7 \text{ kg.m}^{-2}.s^{-1}$  and for a flux density of  $3970 \text{ W.m}^{-2}$ .

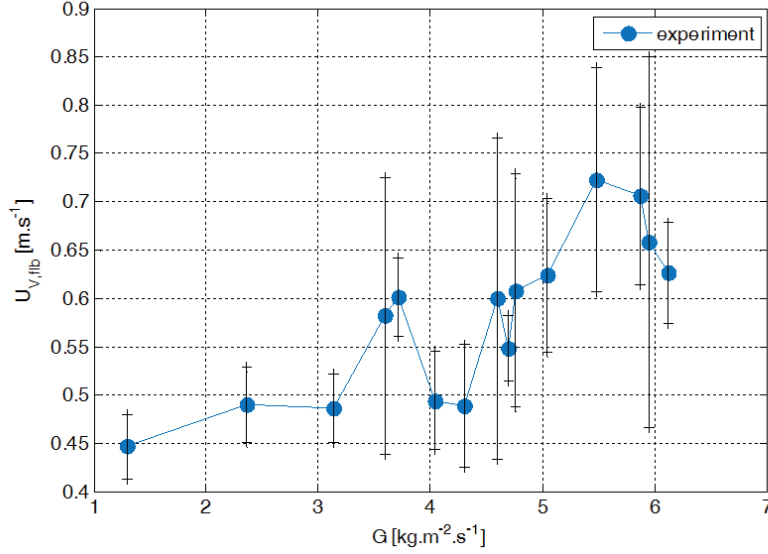


Figure II.4: Evolution of average vapor velocity while liquid bridge arrives for n-pentane working fluid and flux density of  $3970 \text{ W.m}^{-2}$  [experimental data measured by El Achkar et al.[14] at Laplace laboratory, University of Paul Sabatier].

From figure II.4, we note that the velocity of liquid formation is quasi-constant. The transition between annular and intermittent flow occurs at a vapor velocity of about  $0.5790 \text{ m.s}^{-1}$  with a standard deviation of 14.5%. However, this standard deviation is quite high. Regarding the graph, one could highlight a slight increase in vapor velocity at the moment of liquid plug formation as a function of mass flux. In comparison with results from previous work by El Achkar [30] during convective condensation inside a square single tube for the same working fluid (n-pentane) and the same hydraulic diameter, it is highlighted that inside a circular tube the regime transition occurs at a lower mass flux. Indeed, in the square cross-section channel as previously indicated, the vapor velocity  $U_{V,flb}$  was  $0.73 \text{ m.s}^{-1}$ , i.e. 26% higher than for the circular tube. This can be explained by considering the capillary effect, which is more important in a square cross-section channel due to the presence of corners. Hereafter, an attempt to build a two-phase flow model during convective condensation at microgravity conditions is presented in order to be able to predict the regime transition.

## II.2 One dimensional two-fluid model

In this section, an attempt to model the two-phase flow involved during condensation at low mass flux at microgravity conditions or in a micro channel will be presented. The approach is based on the modeling of two incompressible vapor and liquid flows separated by a liquid-vapor interface. The 1D two-fluid model is then derived from area

averaging over the channel cross section of the resultant equations. The profile of the main quantities are then obtained and depend only on the primary flow direction (i.e axial axis of the tube).

### II.2.1 Geometric configuration

The geometric configuration considered, the assumptions and the boundary conditions imposed are those used in the experimental study of El Achkar et al.[14] and are schematized in figure II.5.

The channel, has a circular cross-section with an external diameter  $D_{ext}$ . The area of the internal cross section is noted  $A_t$ , with an internal diameter  $D_h$ . A mass flow of saturated vapor is fixed at the inlet to the tube. Then in contact with the cool wall of the pipe, the vapor condenses and a film of liquid forms. Its thickness varies with the quality, which is itself dependent on the axial position. Experimentally, this type of flow structure is found in a micro-gravity environment or in micro channel or inside a vertical tube. In both cases, the flow can be taken to be axisymmetric.

Conductive heat transfers through the wall are assumed to be purely radial, corresponding to the commonest situation, where the wall is thermally thin. The channel is cooled by a fluid at temperature  $T_{out}$ , which remains constant all along the channel, with a convective heat transfer coefficient  $h_{ext}$  between the outer wall and the coolant that also remains uniform and constant.

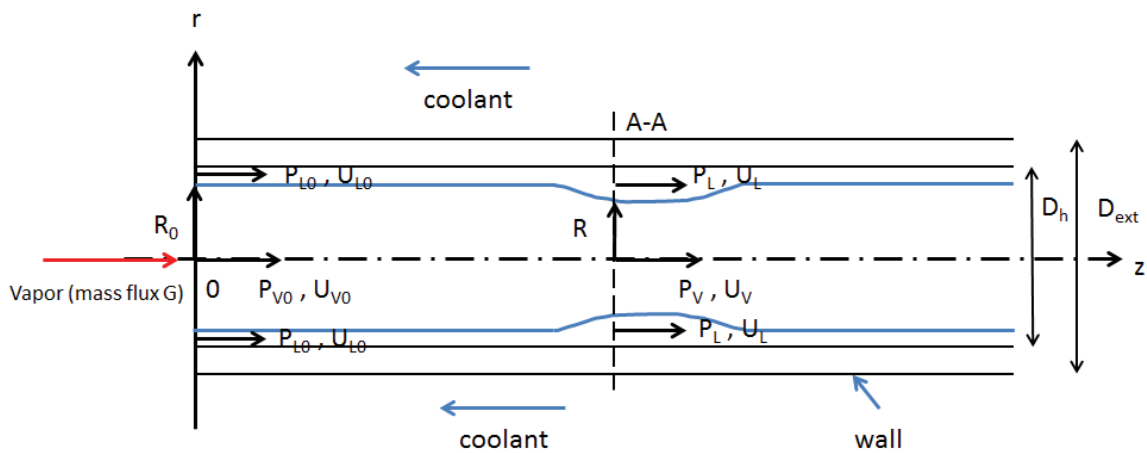


Figure II.5: Geometrical configuration studied. The cooling is ensure by a flow of cold fluid at a constant temperature and with a constant external heat transfer coefficient over the whole length of the channel. Flow is assumed to be axisymmetric.

The modeling approach developed here describes the liquid and vapor phases separately where  $X=[\alpha(z, t), U_L(z, t), U_V(z, t), P_L(z, t), P_V(z, t)]$  are unknowns depending on time and position for one-dimensional model.  $U_L(z, t), U_V(z, t), P_L(z, t), P_V(z, t)$  are for each phase the average over a cross-section of the fluid velocity  $\vec{v}_k(\vec{x}, t)$  and pressure  $p_k(\vec{x}, t)$  local fields.

We use in an equivalent way either the vapor core radius  $R(z, t)$  or the void fraction  $\alpha(z, t)$  in the cross-section which can be evaluated as formulation below:

$$\alpha(z, t) = \frac{\pi R(z, t)^2}{A_t} = \frac{R(z, t)^2}{D_h^2/4} \quad (\text{II.2.1.1})$$

where  $D_h$  is the hydraulic diameter of the tube.

The boundary conditions can be found at the inlet of studied zone are named  $X_0 = [\alpha(z=0), \alpha'(z=0), U_L(z=0), U_V(z=0), P_L(z=0), P_V(z=0)]$ .

## II.2.2 1D model

The continuity equations for the liquid and vapor phases can be written, respectively, as:

$$\frac{\partial}{\partial t}(\rho_L(1-\alpha)) + \frac{\partial}{\partial z}(\rho_L U_L(1-\alpha)) = -\frac{\Gamma_{m,L}}{A_t} \quad (\text{II.2.2.1})$$

$$\frac{\partial}{\partial t}(\rho_V\alpha) + \frac{\partial}{\partial z}(\rho_V U_V\alpha) = -\frac{\Gamma_{m,V}}{A_t} \quad (\text{II.2.2.2})$$

At the interface, the continuity of the fluxes of mass gives:

$$\Gamma_{m,L} + \Gamma_{m,V} = 0 \quad (\text{II.2.2.3})$$

The equations for the conservation of momentum in each phase in axial direction are written as:

$$\frac{\partial}{\partial t}(\rho_L(1-\alpha)U_L) + \frac{\partial}{\partial z}(\rho_L\xi_L U_L^2(1-\alpha)) = -\frac{\partial}{\partial z}(P_L(1-\alpha)) - p_{I,L} \frac{\partial \alpha}{\partial z} - \frac{\mathcal{P}_t \tau_W}{A_t} + \frac{\mathcal{P}_I \tau_{I,L}}{A_t} - \frac{\Gamma_{mv,L}}{A_t} \quad (\text{II.2.2.4})$$

$$\frac{\partial}{\partial t}(\rho_V\alpha U_V) + \frac{\partial}{\partial z}(\rho_V\xi_V U_V^2\alpha) = -\frac{\partial}{\partial z}(P_V\alpha) + p_{I,V} \frac{\partial \alpha}{\partial z} + \frac{\mathcal{P}_I \tau_{I,V}}{A_t} - \frac{\Gamma_{mv,V}}{A_t} \quad (\text{II.2.2.5})$$

Where the coefficients  $\xi_k$  represent the ratio between the mean of the square of the velocity and the square of the mean velocity in a cross-section. Assuming a second

order profile,  $\xi_k$  are equal to  $4/3$ . The table II.1 presents all interfacial terms.

Term	Interpretation	Units	Definition from local variables
$\Gamma_{m,k}(z, t)$	Mass flow rate through the interface $\Sigma, I$ by unit length	$kg \times s^{-1} \times m^{-1}$	$\Gamma_{m,k} = \lim_{\Delta z \rightarrow 0} \frac{1}{\Delta z} \int_{\Sigma, I} \rho_k (\vec{u}_k - \vec{u}_\Sigma) \cdot \vec{n}_k dS$ (II.2.2.6)
$\Gamma_{mv,k}(z, t)$	Momentum flow rate through the interface $\Sigma, I$ by unit length (horizontal component)	$kg \times s^{-2}$	$\Gamma_{mv,k} = \lim_{\Delta z \rightarrow 0} \frac{1}{\Delta z} \int_{\Sigma, I} \rho_k \vec{u}_k \cdot \vec{e}_z (\vec{u}_k - \vec{u}_\Sigma) \cdot \vec{n}_k dS$ (II.2.2.7)
$p_{I,k}(z, t)$	The interface pressure	Pa	$\frac{\partial A_k}{\partial z} p_{I,k} = \lim_{\Delta z \rightarrow 0} \frac{1}{\Delta z} \int_{\Sigma, I} p_k \vec{n}_k \cdot \vec{e}_z dS$ (II.2.2.8)
$\tau_{I,k}(z, t)$	The interface shear stress	Pa	$\mathcal{P}_I \tau_{I,k} = \lim_{\Delta z \rightarrow 0} \frac{1}{\Delta z} \int_{\Sigma, I} (\underline{\tau} \cdot \vec{n}_k) \cdot \vec{e}_z dS$ (II.2.2.9)

Table II.1: Definition of the model's interface variables and source terms.

At the interface, we have:

$$\frac{\Gamma_{mv,V}}{A_t} + \frac{\Gamma_{mv,L}}{A_t} - (\tau_{I,V} + \tau_{I,\ell}) \frac{\mathcal{P}_I}{A_t} - p_{I,V} \frac{\partial \alpha}{\partial z} + p_{I,V} \frac{\partial \alpha}{\partial z} + \sigma \mathcal{C} \frac{\mathcal{P}_I}{A_t} + \frac{\partial \sigma}{\partial z} \frac{\mathcal{P}_I}{A_t} = 0 \quad (\text{II.2.2.10})$$

The last term is the superficial tension term where  $\sigma$  is the surface tension and  $\mathcal{C}(z, t)$  is the curvature which is expressed using the two following radii  $R_1(z, t)$  and  $R_2(z, t)$ :

$$\frac{1}{R_1} = \frac{1}{R_t \cdot [\alpha + (\frac{Rt}{2} \alpha')^2]^{1/2}} = \frac{1}{R[1 + R'^2]^{1/2}} \quad (\text{II.2.2.11})$$

$$\frac{1}{R_2} = \frac{R_t [\frac{\alpha'}{2} - \alpha \cdot \alpha'']}{2 \cdot [\alpha + (\frac{Rt}{2} \cdot \alpha')^2]^{3/2}} = \frac{R''}{(1 + R'^2)^{3/2}} \quad (\text{II.2.2.12})$$

### II.2.3 Additional assumptions and closure laws

These four equations from equation II.2.2.1, II.2.2.2, II.2.2.4, II.2.2.5 will be employed to determine the two phase flow interface and energy balance will be added. The five selected unknowns are void fraction in order to determine the liquid film thickness, the mean velocities and pressures in vapor and liquid phases. However, there are also other parameters which are not yet known such as the interfacial terms in table II.1. Therefore it is necessary to add some hypothesis :

- The annular regime in micro gravity condition is considered. So the pressure distribution in each cross section can be supposed to be uniform for both phases i.e.  $P_V = p_{I,V}$  and  $P_L = p_{I,L}$ .
- The rate of condensation is too low to induce a significant influence of the momentum flow rate through the interface.
- The interfacial shear stress of liquid and vapor phase is mainly due to the tangential component of the force (the normal terms are neglected) respect the balance force at the interface, therefore considering that the surface tension is constant we have:  $\tau_{I,L} = -\tau_{I,V} = \tau_I$  with  $\tau_I$  chosen positive when the vapor leads the liquid.
- The accumulation of energy in the liquid and in the wall are neglected compared to the radial heat transfer which is limited by the external convection. An energy balance at the interface gives thus:

$$\Gamma_{m,L} = \Gamma = -\frac{2\pi R_t h_{ext}(T_{sat} - T_f)}{l_v} \quad (\text{II.2.3.1})$$

where  $T_{sat}$  and  $T_f$  are saturation temperature of working fluid and secondary fluid temperature at experimental investigation. Both temperature are known and supposed to be uniform. By convention the sign of  $\Gamma$  is negative for condensation.

- From study of Miscevic et al. ([63],[62]), the characterization time of  $\rho_L(1 - \alpha)U_L$  and  $\rho_V\alpha U_V$  at momentum equation is very rapid in comparing to characterization time of interfacial evolution. Therefore, these acceleration terms are considered to be negligible.

Finally, the simple equations are presented as below with only one equation of time evolution:

$$\frac{\partial \alpha}{\partial t} = -\frac{\Gamma}{\rho_L A_t} + \frac{\partial}{\partial z}(U_L(1 - \alpha)) \quad (\text{II.2.3.2})$$

$$\frac{\partial}{\partial z}(U_V \alpha) + \frac{\partial}{\partial z}(U_L(1 - \alpha)) + \frac{\Gamma}{A_t} \left( \frac{1}{\rho_V} - \frac{1}{\rho_L} \right) = 0 \quad (\text{II.2.3.3})$$

$$\frac{\partial}{\partial z}(\rho_L \xi_L U_L^2 (1 - \alpha)) + (1 - \alpha) \frac{\partial P_L}{\partial z} + \frac{2\tau_W}{R_t} - \frac{2R\tau_I}{R_t^2} = 0 \quad (\text{II.2.3.4})$$

$$\frac{\partial}{\partial z}(\rho_V \xi_V U_V^2 \alpha) + \alpha \frac{\partial P_V}{\partial z} + \frac{2R\tau_I}{R_t^2} = 0 \quad (\text{II.2.3.5})$$

$$p_V - p_L - \sigma \left( \frac{1}{R_1} + \frac{1}{R_2} \right) = 0 \quad (\text{II.2.3.6})$$

### Friction laws (closure equations)

$\tau_W$  and  $\tau_I$  are wall and interface shear stress coefficients that need to be evaluated to close equation system above. For Poiseuille flow assumption of liquid phase, the wall shear stress is defined as:

$$\tau_W = \frac{16}{Re_L} \frac{1}{2} \rho_L U_L^2 \quad (\text{II.2.3.7})$$

where Reynold number of liquid phase can be evaluated by:

$$Re_L = \frac{\rho_L U_L D_{h,L}}{\mu_L} \quad (\text{II.2.3.8})$$

with  $D_{h,L}$  is hydraulic diameter of liquid film and it can be calculated as:

$$D_{h,L} = \frac{4S}{P} = \frac{4\pi(Rt^2 - R^2)}{2\pi(Rt + R)} = 2(Rt - R) \quad (\text{II.2.3.9})$$

The interface shear stress coefficient is a complicated function of vapor, liquid mass velocities. However in annular case, the vapor velocity is much higher than the liquid one, therefore the interfacial shear stress coefficient can be evaluated as vapor shear stress with the velocity at interface is equal to:  $U_V - 2U_L$  obtained by the continuity of liquid and vapor velocities at the interface.

$$\tau_I = \frac{16}{Re_{I,V}} \frac{1}{2} \rho_V (U_V - 2U_L)^2 \quad (\text{II.2.3.10})$$

where Reynold number of liquid phase can be evaluated by:

$$Re_{I,V} = \frac{\rho_V (U_V - 2U_L) D_{h,V}}{\mu_V} \quad (\text{II.2.3.11})$$

With  $D_{h,V}=2R$  is hydraulic diameter of vapor phase.

Therefore, the equations system has a temporal equation for void fraction evolution versus time II.2.3.2 and four spatial equations II.2.3.3- II.2.3.6 for evaluating liquid, vapor velocities and pressures. Due to the complicated equation of two phase flow, the dimensional equations are employed for final resolution.

### II.2.4 Boundary and initial conditions

Boundary conditions  $X_0$  at the inlet and the initial void fraction profile have to be evaluated to solve the system of equations. In order to avoid the initial conditions being too far from the condensation configuration, the boundary conditions at the inlet of studied zone has been imposed considering a two-phase flow with an uniform liquid film. In the case of low mass flux, the two-phase flow is proposed to be laminar and the velocity profiles correspond to that of Poiseuille flow in both phases (see figure II.6):

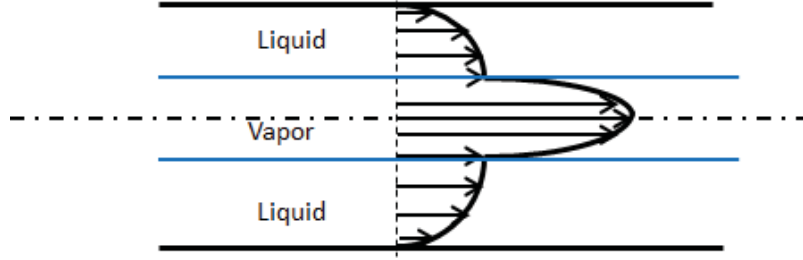


Figure II.6: Vapor and liquid velocities' profiles assumed for this model.

Therefore  $u_V$  and  $u_L$ , the local vapor and liquid velocities are function of radius position:

$$u_V(r) = a_1 r^2 + b_1 r + c_1 \quad (\text{II.2.4.1})$$

$$u_L(r) = a_2 r^2 + b_2 r + c_2 \quad (\text{II.2.4.2})$$

with  $a_1, b_1, c_1, a_2, b_2, c_2$  are constants which are determined using the following relations:

$$u_L(r = R_t) = 0 \quad (\text{II.2.4.3})$$

$$\frac{\partial u_V}{\partial r}(r = 0) = 0 \quad (\text{II.2.4.4})$$

$$u_V(r = R) = u_L(r = R) \quad (\text{II.2.4.5})$$

$$\mu_V \frac{\partial u_V}{\partial r}(r = R) = \mu_L \frac{\partial u_L}{\partial r}(r = R) \quad (\text{II.2.4.6})$$

$$U_{L,0} = \frac{1}{A_L} \int_{r=R}^{r=R_t} u_L(r) r dr d\theta \quad (\text{II.2.4.7})$$

$$U_{V,0} = \frac{1}{A_V} \int_{r=0}^{r=R} u_V(r) r dr d\theta \quad (\text{II.2.4.8})$$

On the other hand, the balance force at the interface has been noted with Laplace equation at the interface. An assumption for annular perfectly smooth at the beginning of studied domain before the appearance of instability has been done. Thus the boundary conditions at interface liquid vapor can be written as:

$$\frac{\partial p_V}{\partial z}(r = R) = \frac{\partial p_L}{\partial z}(r = R) \tag{II.2.4.9}$$

By using Navier Stokes in supposing the vapor and liquid velocities depending only on radius and its gradient is in z for momentum we have:

$$\frac{\partial p_V}{\partial z}(r = R) = \mu_V \frac{1}{R} \frac{\partial}{\partial r} \left( r \frac{\partial u_V}{\partial r} \right) (r = R) \tag{II.2.4.10}$$

$$\frac{\partial p_L}{\partial z}(r = R) = \mu_L \frac{1}{R} \frac{\partial}{\partial r} \left( r \frac{\partial u_V}{\partial r} \right) (r = R) \tag{II.2.4.11}$$

Therefore the system equation of 7 unknowns:  $a_1, b_1, c_1, a_2, b_2, c_2$  and  $R$  has been determined with 7 equations from II.2.4.3 to II.2.4.9 as presented above. An explicit algorithm has been developed thanks to Matlab to determine the boundary conditions. The table below presents the solution obtained with these boundary condition at different average vapor and liquid velocity. The average vapor velocity is supposed to be very high in comparing to the one of liquid one that corresponds to annular very thin film thickness. For a 3mm diameter tube we have the boundary conditions as below:

$U_L(1 - \alpha)$	$U_V\alpha$	$\alpha$	$P_v[Pa]$	$P_L[Pa]$	$\alpha'$
5e-6	0.5	0.9827	124540	124532.33	0
5 e-4	0.5	0.8492	124540	124531.75	0
5 e-4	1.	0.8886	124540	124531.94	0

Table II.2: Boundary condition found with all assumptions above.

From the table II.2, we found that with the average vapor velocity is much higher than the liquid one the vapor core is greater due to higher interface friction force. These results of average liquid and vapor velocities, void fraction and liquid as well as vapor and liquid pressure are employed as boundary condition at the inlet of studied domain.

### II.2.5 Numerical solution

While the system equation is closed and the boundary condition has been determined, the equation can be solved. From equation II.2.3.2 to II.2.3.6, it is important to note

that the value of unknowns at node  $i+1$  can be evaluated by other values at previous positions or previous time. Therefore, it is important to determine the partial and temporal drifts of all terms. The finite volume has been employed and the evaluation of drift can be written as:

$$\frac{\partial f(z_i, t)}{\partial z} = \frac{f(z_{i+1/2}, t) - f(z_{i-1/2}, t)}{\Delta z} \quad (\text{II.2.5.1})$$

With  $f$  is source term. And for temporal partial term can be estimated as:

$$\frac{\partial \alpha(z, t_n)}{\partial t} = \frac{\alpha(z, t_{n+1}) - \alpha(z, t_n)}{\Delta t} \quad (\text{II.2.5.2})$$

Therefore, all unknown term can be evaluated from these system equations. The figure below presents the approximation of the partial drift of all source terms at a node  $i$ .

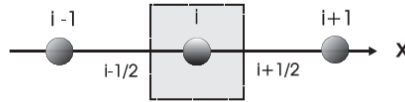


Figure II.7: Finite volume of uni-dimension around node  $i$ .

To solve the system equation, it is necessary to imposed an initial condition profile. From temporal equation, the spatial void fraction profile has to be known. At the first time, the interface profile is perfectly uniform what happens before instability occurs. Therefore, void fraction is uniform along a small domain corresponding to studied zone. The axial profiles of average liquid and vapor velocities and pressures can be found from equations II.2.3.3 II.2.3.6. The figure below presents the profiles obtained with assumption of uniform interface.

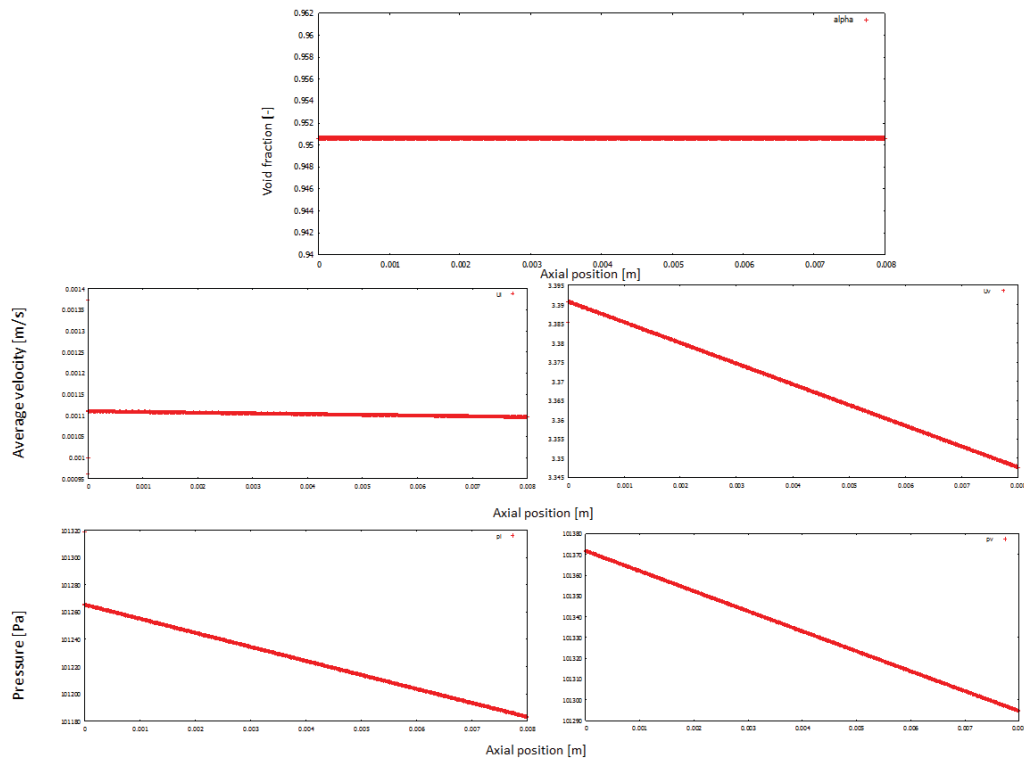


Figure II.8: The axial profiles obtained with the assumption of annular uniform profile of interface.

Due to friction stress, the velocity and pressure decrease along axial position. While boundary and initial conditions are determined, the evolution of these parameters during time can be determined by the equation system from II.2.3.2 to II.2.3.6. To solve the equation system, the volume finite method was employed.

While the initial and boundary conditions are determined, the evolution of all parameters could be evaluated via finite volume method employed. The figure II.9 presents the algorithm to solve these equations:

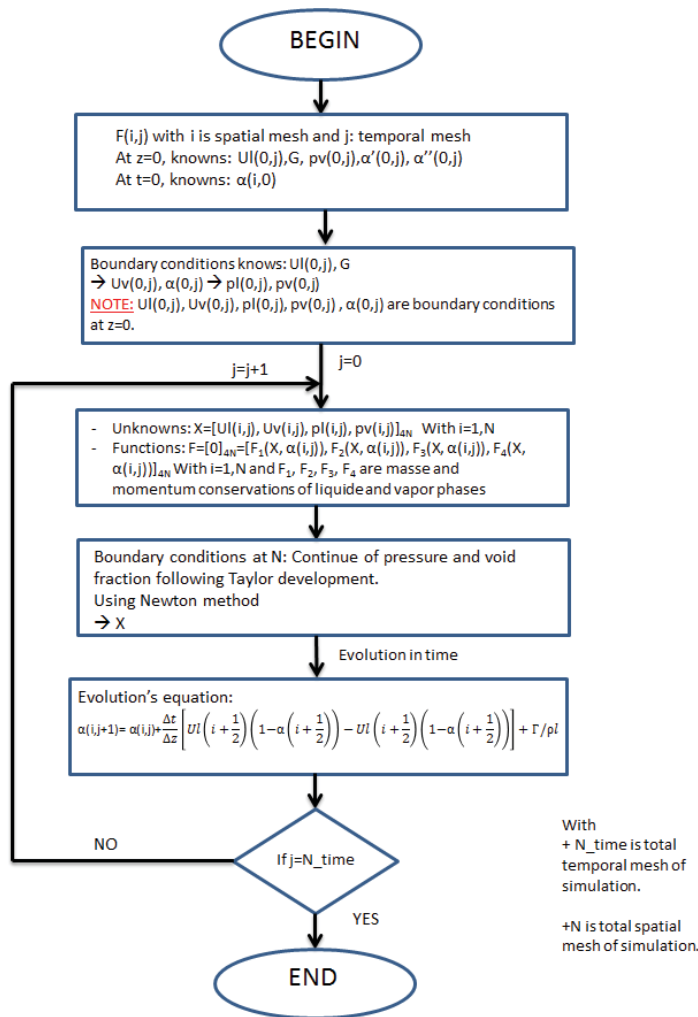


Figure II.9: Algorithm employed to determine the evolution of all parameters during time.

The equation system is closed and then numerically developed. Using Fortran, big data packet has been created and thank to this algorithm, the evolution of these parameters versus time has been determined. During simulation period, the difficulty of convergence has been encountered. Therefore, a campaign of linear analysis of instabilities has been performed to understand where the instability comes from.

### II.2.6 Analyses of linear stability

In mathematics, the linear stability analysis is used to study to the stability of steady-state solutions of differential equations under small perturbations of initial conditions. The principle of the linear stability analysis for a system of partial differential equations

assumed that the vector of solutions  $\vec{S}(z, t)$  is the sum of a steady-state solution  $\vec{S}_0(z)$  disturbed by an infinitesimal quantity named  $\vec{s}(z, t)$ . The partial differential system of equations governing the dynamics of the perturbation is then deduced assuming the second order terms (and greater) are negligible. As a consequence, the perturbed system is linear and then a study based on the eigen values and the dispersion relation inform us if the perturbation will be damped or amplified i. e. the state state solution  $\vec{S}_0(z)$  is stable or not.

Here, the determined unknowns of five equation's system above are:  $\alpha$ ,  $U_L$ ,  $U_V$ ,  $p_L$ ,  $p_V$ . Due to the complexity of the complete equations system, the linear analysis has been performed for different simplified forms of the system of equations. The most simple case corresponds to a two-phase flow without phase change where the surface tension and friction force are negligible. A steady-state solution is then to an infinite uniform liquid film with a homogeneous velocities and pressures. Therefore the studied vectors are:

$$S(z, t) = \begin{pmatrix} \alpha_0(z, t) \\ U_L(z, t) \\ U_V(z, t) \\ P_L(z, t) \\ P_V(z, t) \end{pmatrix} \quad (II.2.6.1)$$

$$S_0 = \begin{pmatrix} \alpha_0 \\ U_{L0} \\ U_{V0} \\ P_{L0} \\ P_{V0} \end{pmatrix} \quad (II.2.6.2)$$

$$\tilde{s}(z, t) = \begin{pmatrix} \tilde{\alpha}(z, t) \\ \tilde{u}_L(z, t) \\ \tilde{u}_V(z, t) \\ \tilde{p}_L(z, t) \\ \tilde{p}_V(z, t) \end{pmatrix} \quad (II.2.6.3)$$

and the governing equations from the general model become:

$$\frac{\partial \alpha}{\partial t} = \frac{\partial}{\partial z}(U_L(1 - \alpha)) \quad (II.2.6.4)$$

$$\frac{\partial}{\partial z}(U_L(1 - \alpha)) = 0 \quad (II.2.6.5)$$

$$\frac{\partial}{\partial z}(\rho_L \xi_L U_L^2 (1 - \alpha)) + (1 - \alpha) \frac{\partial P_L}{\partial z} = 0 \quad (II.2.6.6)$$

$$\frac{\partial U_V \alpha}{\partial t} + \frac{\partial}{\partial z}(\rho_V \xi_V U_V^2 \alpha) + \alpha \frac{\partial P_V}{\partial z} = 0 \quad (II.2.6.7)$$

$$p_V - p_L = 0 \quad (II.2.6.8)$$

After the linearisation process and the application of the Fourier transform<sup>1</sup> (assuming an infinite liquid film), we found for each value of the wave length  $k$  :

---

<sup>1</sup>the Fourier transform is define as  $\bar{s}(k, t) = \int_{z=-\infty}^{z=+\infty} \tilde{s}(z, t) e^{-ikz} dz$  where  $k$  is the wave length.

$$\left\{ \begin{array}{l} \frac{\partial \bar{\alpha}(k,t)}{\partial t} = \frac{1}{2} \frac{[-U_{L0}^2 \rho_L \xi_L \alpha_0 - (1-\alpha_0) \rho_V U_{V0}^2 \xi_V] ik \bar{\alpha}(z,t)}{\rho_V U_{V0} \xi_V (1-\alpha_0) + \rho_L U_{L0} \xi_L \alpha_0} \\ \bar{u}_L(k,t) = \frac{\rho_V \alpha_0 \bar{\alpha}(z,t)}{2(\rho_V U_{V0} \xi_V (1-\alpha_0) + 2\rho_L U_{L0} \xi_L \alpha_0)} \left[ \frac{\xi_L U_{L0}^2}{1-\alpha_0} + \frac{\rho_V \xi_V U_{V0}^2}{\rho_L \alpha_0} - \frac{2\rho_V U_{V0} \xi_V (U_{V0} - U_{L0})}{\rho_L \alpha_0} \right] \\ \bar{u}_V(k,t) = -\frac{((U_{V0} - U_{L0}) \bar{\alpha}(z,t) + (1-\alpha_0) \bar{u}_L(z,t))}{\alpha_0} \\ \bar{P}_V(k,t) = \bar{P}_L(k,t) \end{array} \right. \quad (\text{II.2.6.9})$$

As a consequence, solving this system of ordinary equations, we found that the perturbation  $\tilde{s}(z,t)$  is given by:

$$\tilde{s}(z,t) = \int_{k=-\infty}^{k=+\infty} C e^{\omega t} e^{ikz} dk \quad (\text{II.2.6.10})$$

where the pulse is given by :

$$\omega = \frac{1}{2} \frac{[-U_{L0}^2 \rho_L \xi_L \alpha_0 - (1-\alpha_0) \rho_V U_{V0}^2 \xi_V] ik}{\rho_V U_{V0} \xi_V (1-\alpha_0) + \rho_L U_{L0} \xi_L \alpha_0}$$

Here  $\omega_r$  the real part of  $\omega$  is equal to zero. So that we couldn't conclude if the system equation is stable<sup>2</sup>.

An extension of this first study is achieved adding the liquid inertia. The following equation was considered instead of the equation II.2.6.5:

$$\frac{\partial U_l(1-\alpha)}{\partial t} + \frac{\partial}{\partial z} (\rho_L \xi_L U_L^2 (1-\alpha)) + (1-\alpha) \frac{\partial P_L}{\partial z} = 0 \quad (\text{II.2.6.11})$$

Then, this time, the characteristic polynomial is:

$$\omega^2 + 2\omega ik \left( \frac{\rho_V U_{v0}(1-\alpha_0)}{\rho_L(1-\alpha_0) + \rho_V(1-\alpha_0)} \right) - k^2 \left( \frac{\rho_V U_{v0}^2(1-\alpha_0)}{\rho_L(1-\alpha_0) + \rho_V(1-\alpha_0)} \right) = 0 \quad (\text{II.2.6.12})$$

As a consequence, the dispersion relation  $\omega_r = f(k)$  is given by:

$$\omega_r = \frac{k}{\rho_L \alpha_0 + \rho_V (1-\alpha_0)} (\rho_V \rho_L \alpha_0 (1-\alpha_0) (U_{V0} - U_{L0})^2)^{1/2} \quad (\text{II.2.6.13})$$

2

$\omega_r$	$> 0$	$< 0$	$= 0$
Solution	Unstable	Stable	Couldn't determine

We found that the real part of the growth rate is always positive therefore the model is always unstable in this case. This situation is similar to the one of Kelvin Helmholtz's instability where two fluids flow at different velocities. Indeed, the real part of Kelvin Helmholtz from literature is written as below:

$$\omega_r = \frac{k}{\rho_L + \rho_V} (\rho_v \rho_L (U_{V0} - U_{L0})^2)^{1/2} \quad (\text{II.2.6.14})$$

Comparing these two equations, we found that the Kelvin Helmholtz studied in free surface (in general for clouds, the ocean...) are very similar. The confinement effect is taken into account in our case.

## II.3 Conclusion

Experimental results for the transition between annular flow and intermittent flow inside round micro tube was obtained. Based on these experimental results, an instable liquid-vapor interface was observed just after the onset of the liquid film. This instability grows and leads to liquid collars formation. These collars are carried by the flow and collapse to produce liquid bridges. This leads to the transition regime from annular to intermittent flow. Moreover this transition regime is always observed around the same critical value of vapor velocity independently of the mass velocity. In order to better understand the mechanism of this kind of instability, an investigation of the liquid film dynamics inside mini micro tube at microgravity was performed. A two-fluid model of the annular flow was built with many assumptions based on previous study and experimental observations. The first attempt of resolution by finite volume and using Fortran language was established. However, the simulation results were drastically limited by a lot of numerical stability problem especially due to the surface tension terms which are highly sensitive to the inlet boundary conditions. In order to (i) study intrinsic liquid film stability and (ii) distinguish the numerical instability from the physical instability, a linear stability analysis was performed. Particularly some steady-state solutions with a stable interface were sought. However, for the studied cases, the results of the linear analysis of stability reveal that the liquid film is unconditionally unstable or that we couldn't conclude on the dynamics. So as the linear analyzes do not allow concluding, the efforts must focus on the numerical part. In order to increase the knowledge on microgravity convective condensation, experimental data are essential. They will allow first characterizing liquid flow regime and heat transfer and secondly validating numerical model. One can then expect to be able in the future to predict heat transfer and flow regime for different fluids and boundaries conditions. To address these needs, a condensation test section has been built and will be presented in next chapter.

## Chapter III

# Measurements of condensation inside a mini-channel during parabolic flights

In recent decades, the convective condensation has been extensively studied primarily in conventional channels ( $> 8$  mm). Many correlations were developed to predict the heat transfer coefficient, pressure drop and flow pattern maps [28, 47]. In this range of dimensions, the effect of gravity, shear stress and inertia are dominant, surface tension effect is generally considered negligible.

More recently, due to the growing interest in miniature devices, attention has focused on micro-channels having a hydraulic diameter of about 1 mm or less [56, 14, 43]. By this way, the surface tension force becomes more important compared to gravitational one. Therefore the competition between surface tension force and shear stress determines the two phase flow regime in such low diameter condenser. This is also one way to simulate the micro-gravity on ground.

For intermediate diameters which are of considerable industrial interest, most studies involve high mass velocities where shear stress is dominant compared to gravitational effect. For low mass velocities, available models are rarer and highly sensitive to the relative roles of gravitational, interfacial and inertial forces. There is a lack of information about the role of these forces in intermediate channel. However, due to the demand for two-phase heat transfer systems to cool electronics of future satellites (communications, Earth observation) and also power electronic in commercial flights, the knowledge of condensation flows in microgravity conditions at low mass velocities is an important issue.

As flow pattern manages heat transfer and pressure drop, flow visualization, heat transfer coefficient and pressure drop measurements should be studied at the same configuration. There are some studies concerning both visualization and thermal measurements but they are still modest.

In this context, an investigation of convective condensation in a tube having a circular cross section of hydraulic diameter 3.38 mm which includes both heat transfer coefficient, pressure drop measurement and visualization of flow structures (with liquid film thickness measurement) has been conducted, in normal and microgravity environment. In this case, with HFE-7000 as the working fluid, the capillary length is:

$$L_{cap} = \sqrt{\frac{\sigma}{(\rho_L - \rho_V)g}} = 0.96mm \quad (\text{III.0.0.1})$$

Where  $L_{cap}$  is capillary length,  $\sigma$  is surface tension of working fluid,  $\rho_L$  and  $\rho_V$  are liquid and vapor densities of fluid respectively and  $g$  is gravitational acceleration.

The section used is more than 3.3 times bigger than the capillary length, therefore two phase flow regime and heat and mass transfer will be influenced by the gravity level (normal gravity or micro gravity). In order to design a test section which is able to catch the desired parameters with the accuracy needed, some primary studies and validation tests have been conducted. One of the main challenges is also to make sure that the loop can work not only on ground but also during parabolic flight where the micro-gravity period is quite short. On the other hand, after validation phase condensation test with HFE-7000 as working fluid and water as coolant has been performed at micro gravity thank to parabolic flights. Some experimental results have been exploited and compared the ones at normal gravity condition. All these experimental results will be presented hereafter.

## III.1 Preparation for parabolic flight experiment

To build an adequate condenser test section, some important points must be reminded. Firstly, as the determination of the internal heat transfer coefficient is obtained thanks to an enthalpy balance on the secondary fluid and the determination of temperature difference between wall and saturation temperature, the accuracy on these quantities must be well controlled. Consequently in order to get significant temperature difference between wall and saturation temperature the external heat transfer coefficient must be much higher than the internal one. That implies that the wall temperature is close to the water one, therefore subcooling between wall and saturation temperature becomes high enough to have a good accuracy on the heat transfer coefficient determination. An accurate measurement of pressure drop is also required to have precise knowledge of saturation temperature in whole test section. In the coolant side the water temperature must be homogeneous. For tube material, thermal resistance of the channel wall and axial conduction should be low in order to control the exchange. These points will be developed in this chapter.

In the next part, specific considerations regarding the preparation of the loop to the constraints imposed by parabolic flight are detailed. Among these, particular attention is paid on the thermal response time of the loop in order to get the possibility to reach steady-state regime before the end of the twenty seconds of microgravity environment available during each parabola of the plane.

### III.1.1 Micro-gravity simulation

Before starting the conception for test section, available micro-gravity platforms would be described to understand why parabolic flight experiment is the one used to achieve our aim.

To have a long and stable duration of micro-gravity, International space station (ISS) is the best choice. However, carrying out some experiments in this platform is quite expensive and it requires a lot of safety conditions. It is why some others micro-gravity simulation platforms are created for checking apparatus firstly.

There are three common platforms to simulate microgravity on ground: drop tower, sounding rockets and parabolic flights. Drop tower is a long conduct in which micro-gravity is reached during free fall. With this systems the microgravity duration is quite short and for the operators it is impossible to manually access to the experiment. The microgravity time depends on the length of the conduct, for example the 105 m German drop tower in Bremen (ZARM) gives the possibility to simulate the microgravity for 4.72 s. Like drop towers, with sounding rockets the experiments can be controlled, but not be accessed manually by operators. They are sub-orbital carrier and they provide 180 to 780 s of reduced gravity.

To avoid this disadvantage, parabolic flights are used. They allow to achieve approximately 20 s of micro-gravity. The period before and after the micro-gravity period are periods of hyper-gravity due to the parabola maneuver. Due to the fact that the duration of micro-gravity is only 20s, experiments should be designed to ensure that stable condition can be reach in this quite short period. However, during the parabolas many experimental set-ups and operators can access in the flight, this is the largest advantage of this simulation platform. It is why many scientists choose this method.

### **III.1.2 Condenser length design**

The goal of this study is to investigate the convective condensation in low and intermediate mass velocity (below  $200 \text{ kg.m}^{-2}.\text{s}^{-1}$ ) inside a mini channel for which gravitational force on ground cannot be neglected in comparison with surface tension and inertial ones.

The idea is to measure heat transfer coefficient and pressure drop simultaneously to flow visualization in the whole range of vapor quality. It is why the necessary length to obtain the complete convective condensation is calculated at mass velocity of  $200 \text{ kg.m}^{-2}.\text{s}^{-1}$  which is the highest one. In this calculation, conditions on the coolant are expected to be the same in the whole experimental loop.

One of important points regarding condenser conception is to check that the external heat transfer coefficient is much higher than the internal one to be accurate in the determination of internal heat transfer. Due to the high thermal conductivity of copper tube, the wall resistance can be neglected. So internal wall temperature would be very close to water temperature and heat transfer are mainly governed by internal heat transfer coefficient. The Working fluid, HFE-7000, enters in the test section about  $10^\circ\text{C}$  super-heated and exits at liquid state. Assuming these assumptions, an evaluation of the condenser length is performed. The exchange configuration can be described as below:

$T_{sat}$ [°C]	$P_{sat}$ [bar]	$h_{V,inlet}$ [kJ/kg]	$h_{L,out}$ [kJ/kg]	$\Delta h$ [kJ/kg]	$l_v$ [kJ/kg]	$Q_{de-sh}$ [W]	$Q_{cond}$ [W]
45	1.48	393.9	255.09	138.81	129.14	17.56	234.50

Table III.1: Exchange parameters at mass flux of  $200 \text{ kg.m}^{-2}.\text{s}^{-1}$  for a tube of 3mm hydraulic diameter.

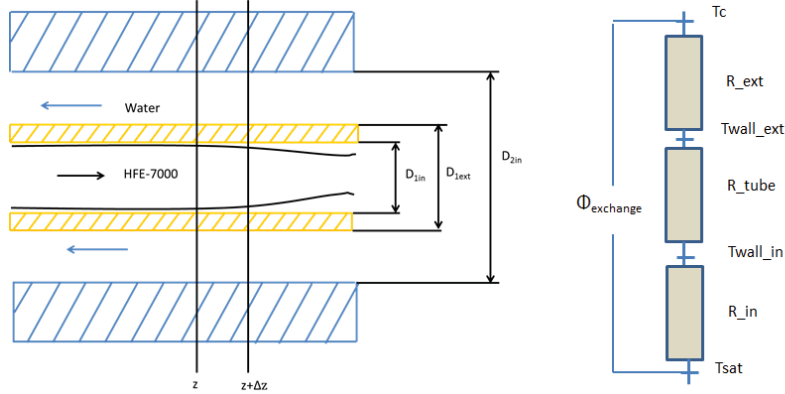


Figure III.1: Configuration of a the studied domain between  $z$  and  $z+\Delta z$  with working fluid and secondary fluid in counter-current.

The table III.1 allows to deduce power exchange at mass velocity of  $200 \text{ kg.m}^{-2}.\text{s}^{-1}$ .

Moreover, by using Cavallini's correlation [11] for condensation in horizontal circular tube, the condensation heat transfer coefficient can be evaluated. The heat balance in a small domain between  $z$  and  $z + \Delta z$  is:

$$\alpha_{in} \cdot (T_{sat} - T_w) \cdot \pi \cdot D_{1in} \cdot \Delta z = \dot{m}_c \cdot c_p \cdot (T_c(z + \Delta z) - T_c(z)) \quad (\text{III.1.2.1})$$

On the other hand, by using thermal balance in refrigerant side, quality variation,  $\Delta x$ , is deduced :

$$\alpha_{in} \cdot (T_{sat} - T_w) \cdot \pi \cdot D_{1in} \cdot \Delta z = \Delta x \cdot l_v \cdot \dot{m}_{ref} \quad (\text{III.1.2.2})$$

Assuming that the external heat transfer coefficient is the dominant one, the external thermal resistance can be neglected. The thermal wall resistance and internal thermal resistance are calculated by:

$$R_w = \ln\left(\frac{D_{ext}}{D_{1in}}\right) / (\lambda_{copper} \cdot 2 \cdot \pi \cdot \Delta L) \quad (\text{III.1.2.3})$$

$$R_{in} = \frac{1}{\alpha \cdot \pi \cdot D_{1in} \cdot \Delta z} \quad (\text{III.1.2.4})$$

Through calculation, the wall resistance is calculated to confirm that thermal resistance of the copper wall is negligible in comparison to the internal one. The refrigerant mass flow rate can be determined from mass velocity as following:

$$\dot{m}_{ref} = G \cdot \pi \cdot \frac{D_{in}^2}{4} \tag{III.1.2.5}$$

In the aim that the conception allows the external heat transfer coefficient is much higher than the condensation one, the wall temperature will be very close to the coolant one. By using these equations we have the table below of necessary length at 45°C of saturation temperature, in both super-heated of 10°C or saturation state. The water mass flow rate is 0.003 kg.h<sup>-1</sup> for HFE-7000 working fluid:

$T_{sat}$ [°C]	$\Delta T_{sh}$ [°C]	$Q_{de-sh}$ [W]	$Q_{cond}$ [W]	L[m] at $T_{c,inlet}$ =22°C	L[m] at $T_{c,inlet}$ =20°C	L[m] at $T_{c,inlet}$ =25°C
45	0	0	234.50	1.03	0.82	1.87
45	10	12.28	234.50	1.08	0.87	1.92

Table III.2: The necessary length if vapor quality at the outlet is 0.

We found that the heat exchange for complete condensation for HFE-7000 working fluid at mass velocity of 200 kg.m<sup>-2</sup>.s<sup>-1</sup> and saturation temperature of 45°C is 234.5 W for a tube of 3mm internal diameter.

The necessary length is shapely reduced by increasing the temperature difference between the refrigerant and the coolant. An exchange length of approximately 0.8 meter is chosen, expecting the coolant temperature at the inlet is about 20°C.

### III.1.3 Characteristic time evaluation

One other important point that should be studied is the characteristic time of the loop. As mentioned above, for each parabola, only 20 seconds of microgravity are available, thus some studies have been performed to make sure that the loop can achieve the steady state in 20s. Only components involving a liquid vapor interface are supposed to potentially affect significantly the response time. So the response time of the test section and the evaporator are evaluated in the following.

#### a) Time response of the condenser

Assuming that the conductance of copper wall is very high because of its high thermal conductivity, we obtain the following equation system for copper and water

sides by using thermal balance in each part :

$$\rho_w c_{p,w} \frac{D_{1ext}^2 - D_{1in}^2}{4} \frac{\partial T_w}{\partial t} = \alpha_{cond} D_{1in} (T_{sat} - T_w) - \alpha_c D_{1ext} (T_w - T_c) \quad (III.1.3.1)$$

$$\rho_c c_{p,c} \frac{D_{2in}^2 - D_{1ext}^2}{4} \frac{\partial T_c}{\partial t} = \alpha_c D_{1ext} (T_w - T_c) - c_{p,c} \frac{\dot{m}_c}{\pi} \frac{\partial T_c}{\partial z} \quad (III.1.3.2)$$

In this configuration, the water condition is supposed to be constant, only the condensation heat transfer coefficient changes when microgravity condition is imposed. Results of response time are obtained for different water condition and variation of refrigerant heat transfer coefficient.

Simulation results below show the reaction of wall temperature when the internal heat exchange suddenly changes.

The internal heat transfer coefficient is from 1000 to 3000  $W.m^{-2}.K^{-1}$  and the water heat transfer coefficient is from 1000 to 4000  $W.m^{-2}.K^{-1}$  for different cases of exchange.

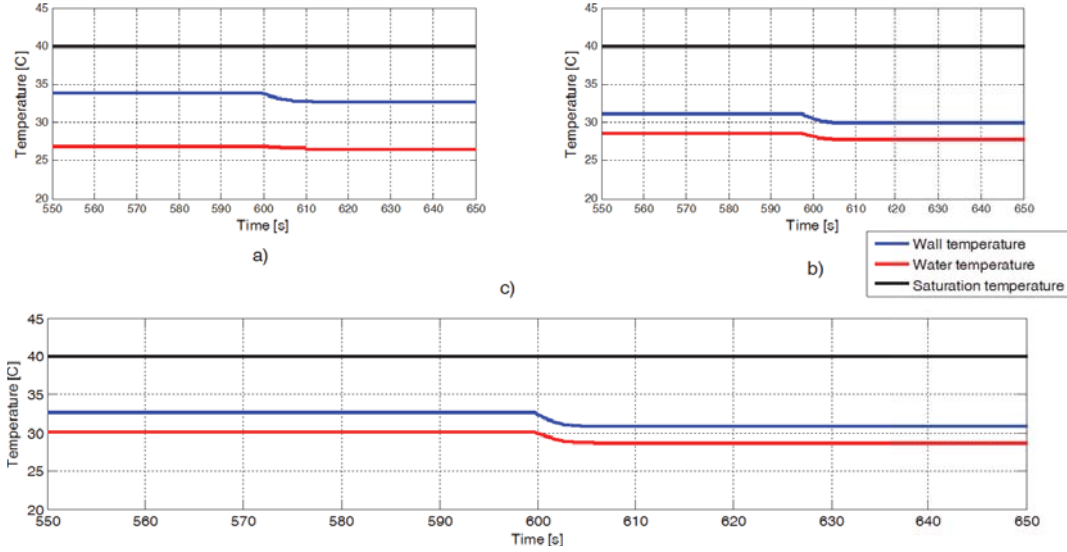


Figure III.2: Response time at different test conditions a) Internal heat transfer coefficient variations from 2000 to 1500  $Wm^{-2}K^{-1}$  with external heat exchange of 1000  $Wm^{-2}K^{-1}$ . b) Internal heat transfer coefficient variations from 2000 to 1500  $Wm^{-2}K^{-1}$  with external heat exchange of 4000  $Wm^{-2}K^{-1}$ . c) Internal heat transfer coefficient variations from 3000 to 2000  $Wm^{-2}K^{-1}$  with external heat exchange of 5000  $Wm^{-2}K^{-1}$ .

These results have been obtained for a same coolant mass flow rate of  $0.014 \text{ kg.s}^{-1}$  at saturation temperature of  $40^\circ\text{C}$  and water temperature at the inlet of  $24^\circ\text{C}$ . We found that even for low water heat transfer coefficient, the maximum response time is 17s. This result shows that the response time is lower than the micro gravity period. The test section will be stable if others parts of the loop are already stable.

**a) Time response of the evaporator**

In order to reduce the response time, all parts of the loop must be weakly affected by changes in gravity level, it is why a stirring magnetic evaporator available at ULB (Université Libre Bruxelles) is employed. Depending on the speed of the rotating mixer, competition between centrifugal force and gravitational force affect more or less the liquid vapor distribution inside the evaporator.

To determine the order of magnitude of the velocity that is necessary to keep a constant liquid distribution whatever is the gravity, the interface within the evaporator is simulated. A domain between  $z$  and  $z+\Delta z$  is used to calculate the shape of the liquid-vapor interface :

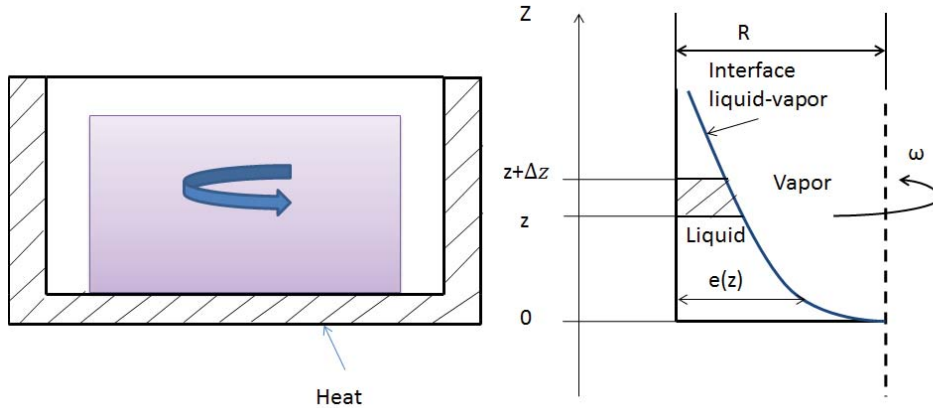


Figure III.3: Configuration of liquid-vapor interface of stirring magnetic machine

The evaporator is of total surface  $A_{tot}$ . The studied domain between  $z$  and  $z+\Delta z$  is considered in stationary regime. Mass conservation and momentum equation for liquid phase allow obtaining :

$$\frac{\partial}{\partial z}(\rho_L U_L(z)\pi(R^2 - (R - e(z))^2)) + (\Gamma A_{total}) = 0 \tag{III.1.3.3}$$

$$\frac{\partial}{\partial z}(U_L^2(z)(R^2 - (R - e(z))^2)) + \frac{\Gamma A_{total} U_{Liz}}{\rho_L \pi} \quad (\text{III.1.3.4})$$

$$= -g(R^2 - (R - e(z))^2) - \frac{1}{4\rho_L} \frac{\partial(p_i(z)(R^2 - (R - e(z))^2)}{\partial z} \quad (\text{III.1.3.5})$$

$$+ \frac{\omega^2}{2} \frac{\partial(R - e(z))^2(R^2 - (R - e(z))^2)}{\partial z} - \frac{\omega^2}{4} \frac{\partial(R^4 - (R - e(z))^4)}{\partial z} \quad (\text{III.1.3.6})$$

$$+ p_i(z) \frac{2}{\rho_L} (R - e(z)) \frac{\partial e(z)}{\partial z} - \tau_i(z) (R - e(z)) \frac{2}{\rho_L} - \tau_w(z) \frac{2}{\rho_L \pi} \quad (\text{III.1.3.7})$$

With  $U_L$ ,  $U_L^2$  are average velocity and square of velocity of liquid,  $e$  is liquid film thickness,  $\Gamma$  is the rate of phase change,  $p_i$ ,  $\tau_i$  and  $U_{Liz}$  are interfacial pressure, shear stress and liquid velocity and  $\tau_w$  is shear stress at the wall. The model is obtained at assumption of uniform pressure distribution over a cross section. More detail about this model can be found in Annex.

The dimensions (given by the supplier) are:  $D=90$  mm;  $H=18$  mm. We achieve the profile of liquid vapor interface at different rotated velocity. In order to reduce the response time of the evaporator, the interface must keep the same shape in normal gravity, micro-gravity and hyper-gravity. The influence of the rotating speed values at the same full rate of 0.4 via interface liquid vapor simulation obtained from system equation, is presented in figure III.4.

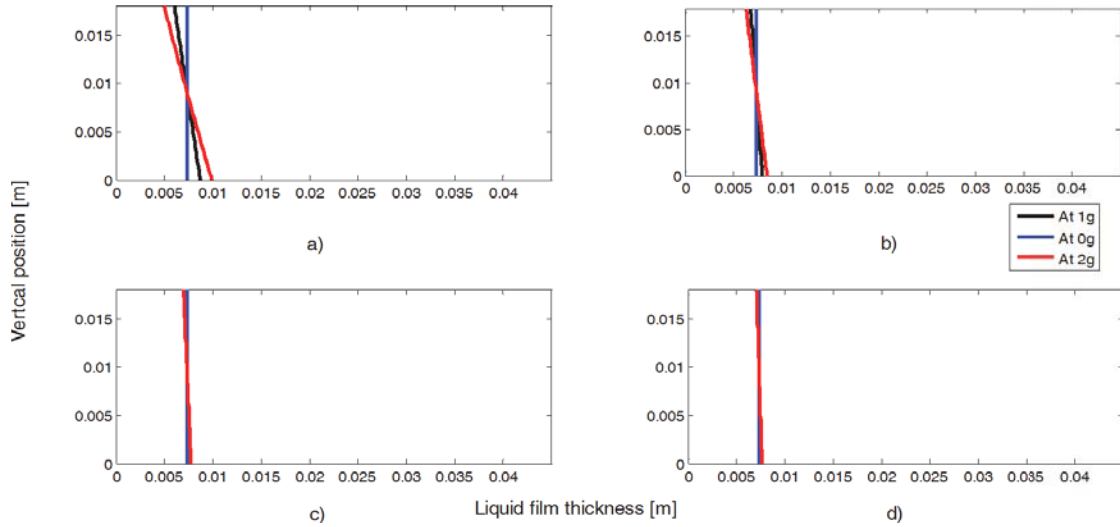


Figure III.4: Shape of the liquid-vapor interface in the evaporator for a constant filling ratio of 0.4 and for various speed of rotation : a)  $N=400$  rpm b)  $N=600$  rpm c)  $N=1000$  rpm d)  $N=1200$  rpm

The simulation has also been done for different filling ratio. We found that the

rotated velocity must be at least 600 rpm to have a stable interface in the range of gravity level encountered during parabolic flight. This value corresponds to the maximum capacity of the agitator available at ULB.

### III.1.4 Consideration for an accurate determination of the HTC in the condenser

To obtain accurate measurement of the internal heat transfer coefficient, a numerical specific study using commercial software Fluent has been done before designing the test section. Its results will show the effect of external heat transfer and of the number and positions of thermocouples on the accuracy of the HTC. It is why this step is a primary step that affects all the final test section design.

Because of the limitations of electric power consumption and weight on flights, only few measurement instruments could be installed in the final test section. Therefore this step will also allow optimizing the number of sensors. A sub-section of 100 mm long has been studied, shown in figure III.5

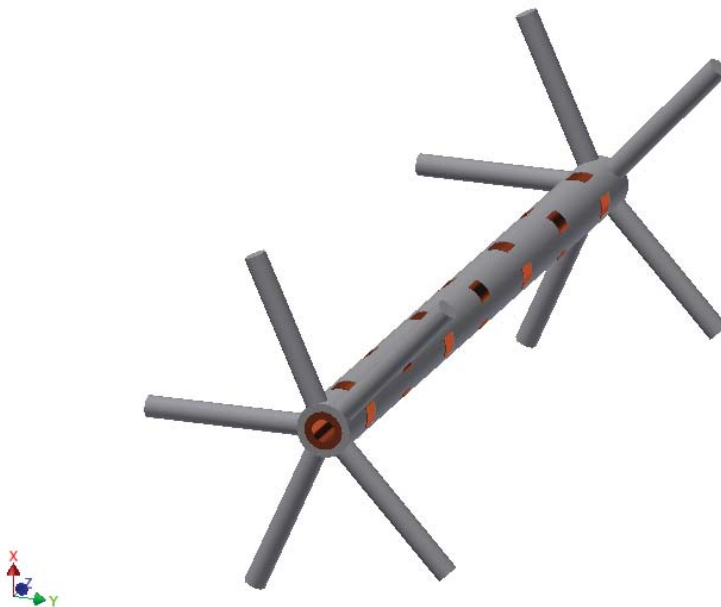


Figure III.5: The configuration of simulated 100mm heat exchange with water in grey and copper in red.

The external tube material that contains the coolant is lexan. Lexan has been chosen for its low thermal conductivity in order to avoid heat loss to environment. The five

arms at the inlet and the outlet represent five water distributors; in real conception, five holes are used to realise the water entrance. Five water distributors are needed at the inlet and at the outlet to avoid boundary effect. If there is only one or two water distributors, the exchange will be very high at the inlet and the outlet because of the boundary effect thus wall temperature at these positions would be out of trend of general profile and the quasi-local heat transfer coefficient will be difficult to evaluate in a sub section. The distance between these holes are enough to avoid any mechanical fragility of fabrication.

The copper external wall has been machined to have a specific geometry that allows the water circulating and makes this circulation more turbulent as proposed by Del Col et al. in previous studies [11]. Thanks to that, a precise measurement of the mean temperature of the water can be obtained with a themocouple. This geometry also allows increasing the external heat transfers. In the simulations the dimensions of copper tube and lexan tube are the same of the ones used in experiments. The figure III.6 shows the water circulation and the machined external surface of the copper tube.



Figure III.6: Water circulation (in grey) and copper tube design (in red) of 100mm segment of the condenser.

The boundary conditions imposed for the calculation are the following :

- mass flow rate and temperature are fixed at the inlet of the five water distributors.
- for copper part, internal heat transfer coefficient and temperature inside are imposed at saturation temperature of 40°C.
- Simulations are performed for different values of inner heat transfer coefficient ranging from 1000 to 5000  $W.m^{-2}.s^{-1}$ .

The simulations are done using Ansys Fluent software. Different meshes and methods of resolution have been tested to check the relevance of the results. Heat balance in water

part and in copper part has been checked. The figure III.7 presents the temperature distribution both in water and copper in one case of simulation.

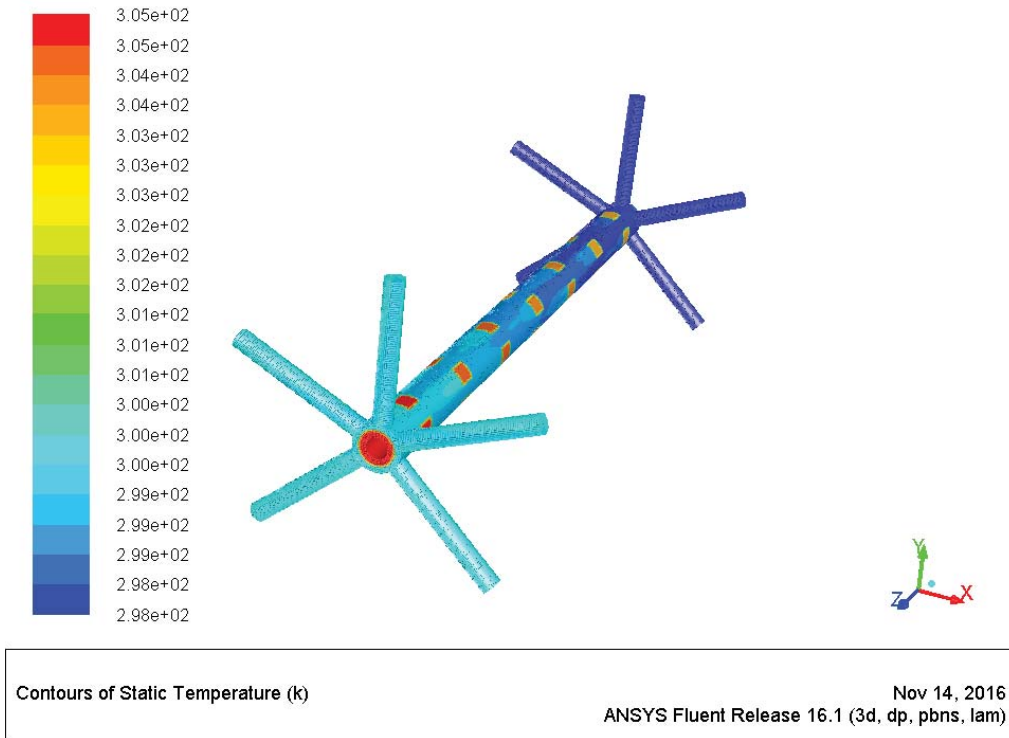


Figure III.7: The temperature distribution when inner heat transfer coefficient is  $5000 \text{ W.m}^{-2}.\text{K}^{-1}$  and a temperature of  $40^\circ\text{C}$  inside tube equivalent  $T_{sat}$ ; water temperature and mass flow rate at the inlet of  $25^\circ\text{C}$  and  $0.8 \text{ m.s}^{-1}$ .

From figure III.8 representing the temperature field in the cross section at the inlet, middle and at the outlet respectively, it can be seen that the wall temperature is very homogeneous. Therefore thermocouple can be installed anywhere in the radial direction ; on the other hand, the error of inner wall temperature measurement due to the position can also be corrected if precise position of thermocouple is known by using the drop temperature calculated from thermal conductivity and thermocouple position.

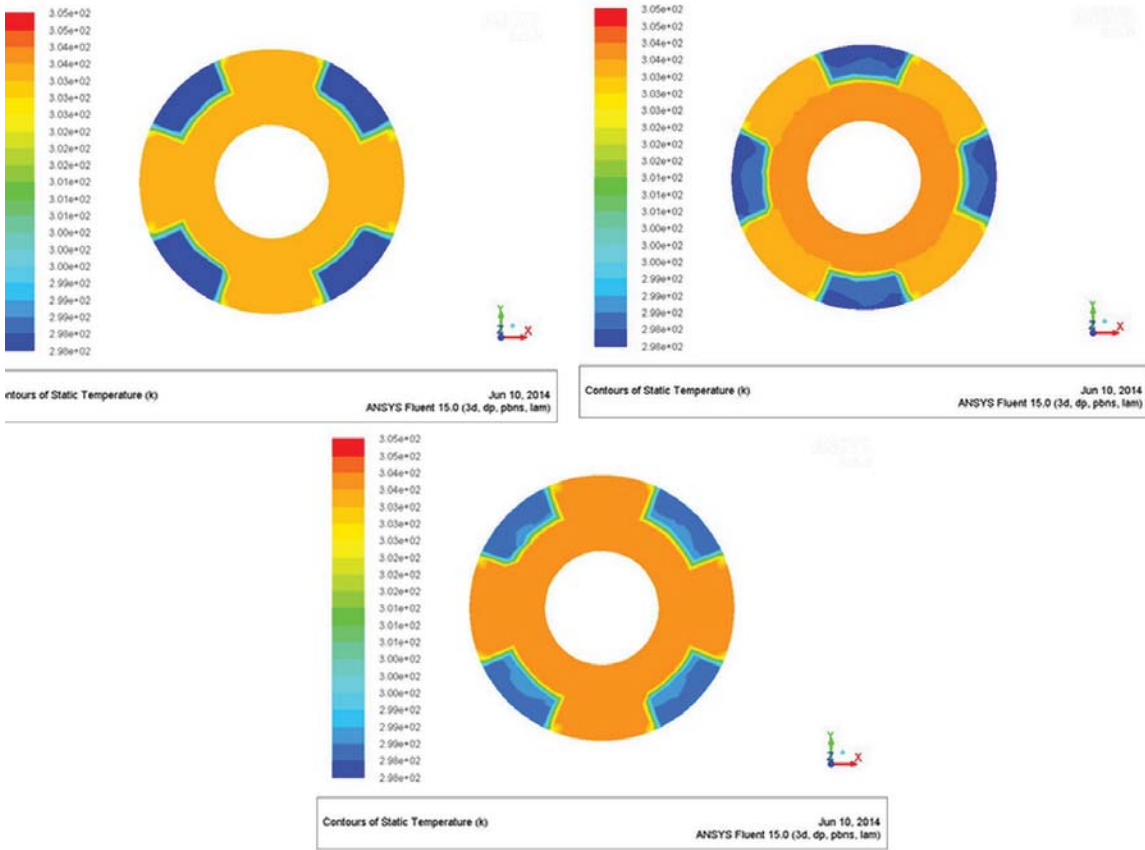


Figure III.8: Temperature field in the cross section at the inlet, middle and at the outlet

Moreover the heat transfer coefficient is evaluated from the enthalpy balance on the water and the mean temperature difference between saturation temperature and wall temperature. Mean wall temperature can be accurately evaluated at 3 fin positions with 6 thermocouples. For each position 1 couple of thermocouple are used. Figure below III.9 represents the 3 axis positions where the wall temperature is measured by thermocouples installed:

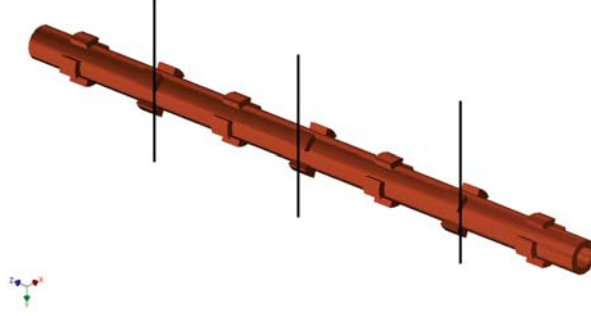


Figure III.9: Position of fins where the temperature are measured for the calculation of heat transfer coefficient.

The first and last fins are not used because at these positions the water distributor parts will be installed and so it will be difficult to install some thermocouples on the wall at these positions. Therefore second, fourth and sixth fins have been selected to install wall temperature sensors.

The heat transfer coefficient is then evaluated as:

$$\alpha_{inlet} = \frac{Q}{\Delta T_{sub} S} \quad (III.1.4.1)$$

Where  $\alpha_{in}$  is heat transfer coefficient calculated, Q is heat power exchange between refrigerant and coolant,  $S = \pi D_{in} L$  with L is tube length is internal surface. The  $\Delta T_{sub}$  is the subcooling i.e. the temperature difference between saturation value and wall temperature. This temperature difference is evaluated by the used of logarithmic mean temperature difference or mean temperature difference from 6 temperature measurements. From these two quantities, the inner heat transfer coefficient can be evaluated. The log mean temperature difference is expressed as:

$$\Delta T_{log} = \frac{\Delta T_A - \Delta T_B}{\ln \Delta T_A - \ln \Delta T_B} \quad (III.1.4.2)$$

Where:  $\Delta T_A = T_{sat} - T_{in}$  and  $\Delta T_B = T_{sat} - T_{out}$

Another way to estimate the subcooling is to consider the mean temperature difference in the middle of subsection:

$$\Delta T_{mean} = T_{sat} - T_{mean} \quad (III.1.4.3)$$

Where:  $T_{mean} = mean(T_{fin,middle})$

Where the saturation temperature is estimated at each position thanks to a linear interpolation based on the measurement of inlet pressure and pressure drop.

We can find the error between heat transfer coefficients calculated and the imposed one in boundary condition. The table below shows the heat transfer coefficient evaluated while the imposed one is  $3000 \text{ W.m}^{-2}.\text{K}^{-1}$  by using different copper temperature measured at different fins position by difference evaluation mean temperature difference.

Fins position	$Q$ [W]	$\Delta T$ [K]	$\alpha_{in}$ [ $\text{W.m}^{-2}.\text{K}^{-1}$ ]	error[%]
first and seventh fins	29.54	10.54 by equation III.1.4.2	2974.85	0.84
second and sixth fins	29.54	10.53 by equation III.1.4.2	2975.61	0.81
fourth fins	29.54	10.53 by equation III.1.4.3	2976.71	0.78

We can note that whatever is the temperature used the error remains very small. Thus because of the limitation in the number of thermocouples that can be installed in wall, only two couples of thermocouples are installed in the fins at 20.5 mm from inlet and outlet (in upper and lower parts) or in the second and sixth fins and one couple of thermocouples in the fourth fin (in the median horizontal plan).

Numerical simulations have been performed for two other values of heat transfer coefficient (1000 and  $5000 \text{ W.m}^{-2}.\text{K}^{-1}$ ). The table III.3 presents the error for the different imposed heat transfer coefficients by using logarithmic mean temperature difference.

$\alpha_{imposed}$ [ $\text{W.m}^{-2}.\text{K}^{-1}$ ]	$Q$ [W]	$\Delta T_{log}$ [K]	$\alpha_{in}$ [ $\text{W.m}^{-2}.\text{K}^{-1}$ ]	error[%]
1000	12.34	13.14	996.3	0.37
3000	29.54	10.53	2975.61	0.81
5000	40.96	8.79	4928.95	1.22

Table III.3: Comparison of inner heat transfer coefficient imposed and the calculated one for different values.

The errors are very small, so it confirms the two methods used are accurate. The heat transfer coefficient can be calculated using equation III.1.4.1 with heat rate calculating by:

$$Q = \dot{m}_c c_p (T_{c,out} - T_{c,inlet}) \tag{III.1.4.4}$$

Two thermocouples are installed at water inlet and outlet to have mean water temperature that gives precise coolant properties. Furthermore, a thermopile is also installed to have a precise temperature difference measurement between the outlet and inlet. The mass flow rates of water and refrigerant are measured by different flow meters that will be detailed in the following. These results of simulation are primary step for final condenser's conception. The external wall will be machined with the geometry chosen for the simulation. The wall thermocouple positions have been chosen and the water distributors at the inlet and outlet will be built as the simulation one. For the next step, the conception of the test section and the boundary effect respecting the primary result of simulation will be presented hereafter.

## **III.2 Concept of condenser for condensation experiments**

As mentioned in the first part of this chapter, the conception of condenser has to follow a certain number of requirements in order to obtain a condenser that can be used both on ground and in parabolic flights. Furthermore, the results of CFD simulation in previous section have been used to choose a geometry and the measurement locations that allow to determine heat transfer coefficient with a required accuracy. Therefore, the design and fabrication of the test section following these criteria will be presented.

### **III.2.1 Test section for parabolic flight experiments**

Firstly, according the results of CFD simulations reported in previous section, the external copper wall will be machined to create turbulence in the water flow in order to increase external heat transfer coefficient and to obtain a precise value of the mean temperature of water in the inlet and outlet cross sections. Thermocouples will be installed in copper fin to get a precise value of the wall temperature. Moreover with such a high value of external heat transfer coefficient, the temperature difference between wall and refrigerant will increase and reduce the error of its measurement and so on the heat transfer coefficient.

On the other hand, to minimize error in wall temperature measurement due to temperature sensor position, high wall thermal conductivity must be considered. Copper is then chosen and leads to high radial conductive conductance. To reduce axial conduction wall thickness is reduced to its minimum value i.e. 1mm. With very small diameter (5mm external) in comparing to length (about 1.0m), the copper tube is very delicate and fragile. Thus the heat exchange part is divided into two parts: the first part with 3 sub-sections of 100 mm length and the second part with 2 sub-sections of 128 mm length. This division make manufacturing of the tube easier.

Figure III.10 shows the sketch of a sub-section of 128 mm length and its realization. Copper test tube's diameter measurement is realized with a Keyence electron microscope. The internal tube diameter is found to be  $3.38\text{mm} \pm 20 \mu\text{m}$  with a mean roughness of  $0.4\mu\text{m}$ .

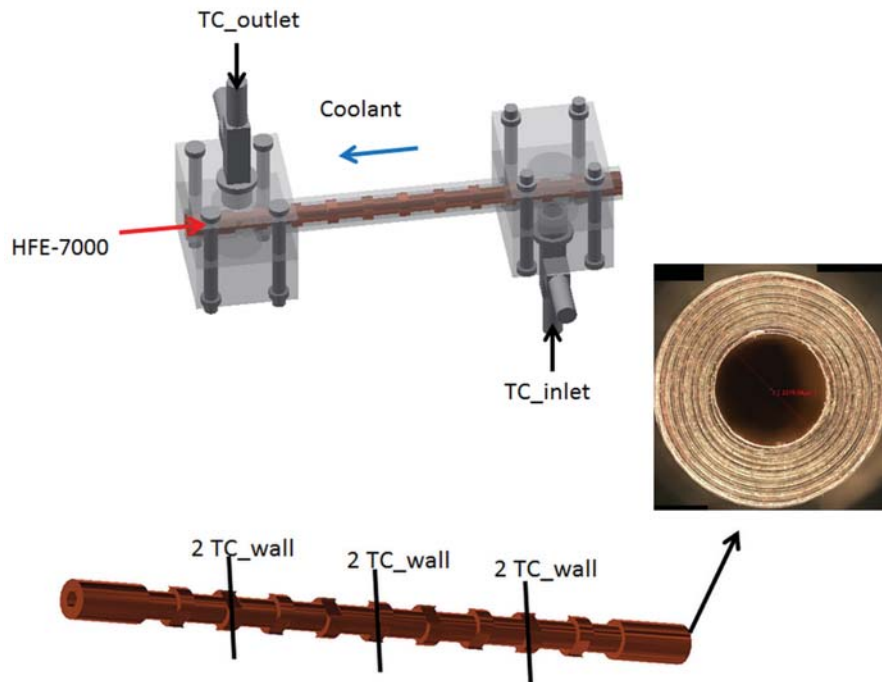


Figure III.10: The sketch of a subsection of 128 mm length for the heat exchange and picture of the machined copper tube.

Another objectif of the test section is to allow the visualization of the two-phase flow in order to have information both on heat performance and on flow regime. To achieve this objective a glass window is placed between the two copper heat exchangers.

Finally the test section is composed of 3 parts with two copper heat exchangers and a glass tube in the middle as presented in figure III.11.

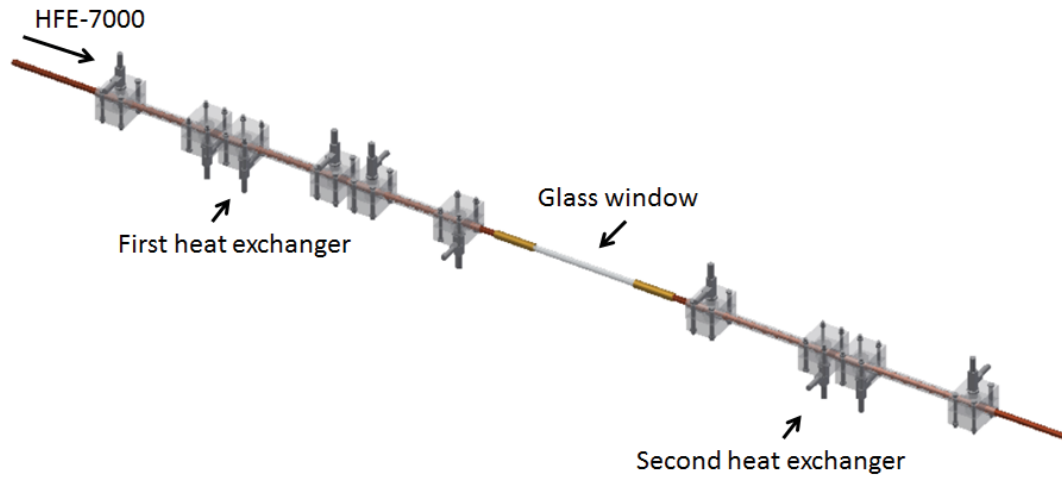


Figure III.11: Whole test section designed for both on ground and parabolic flight experiments.

In order to measure quasi-local heat transfer coefficient the first copper heat exchanger has been divided in 3 sub-sections (sectors) of 100 mm exchange length. In the same way, the second copper heat exchanger has 2 sub-sections of 128 mm exchange length. These two exchangers are connected with the adiabatic section in (glass tube) of 200mm in length.

To summarize, in order to evaluate the heat transfer coefficient, 6 temperature sensors are installed in copper wall at 0.6 mm from internal wall in a hole of 0.7 mm in diameter. Saturation temperature is deduced from pressure measurement at the inlet and pressure drop between inlet and outlet of the whole test section. It has to be noticed that between two copper sub-sections is a copper adiabatic part where the boundary effect can affect the measurement. So axial conduction, should be studied. This investigation has been done and is presented in the following.

### III.2.2 Boundary effects

As mentioned before, axial condition at the border of each sub-sector heat exchanger must be studied. CFD analysis was employed to investigate this heat exchange between two different sub-sections. The geometry studied in this case is half of a condenser of 100 mm exchange length due to its symmetry as shown in figure III.12.

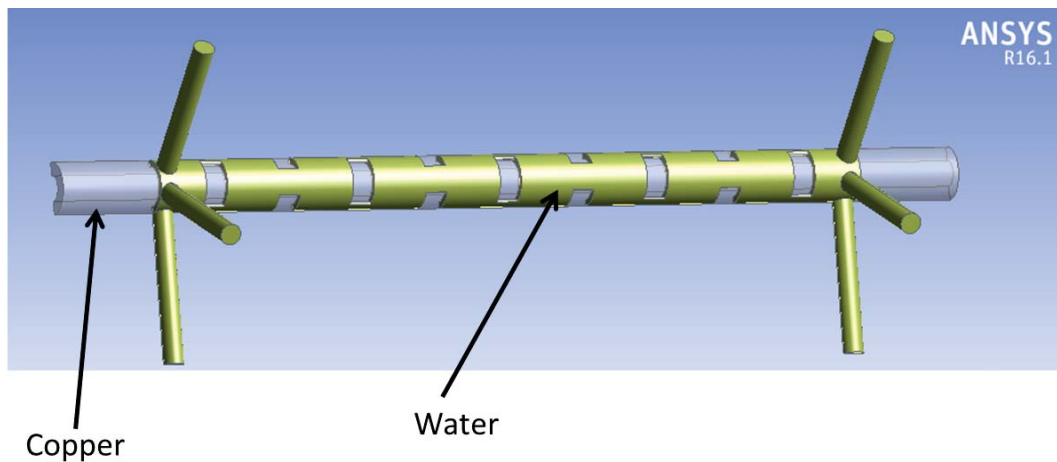


Figure III.12: The geometry of a sub-section of 100 mm heat exchange used for Fluent simulation

This geometry corresponds to the final experimental sub-section used in final tests. Five water distributors are simulated as the holes for entering coolant. The two copper parts downstream and upstream of the sub-section are not in contact with water. This study will investigate the boundary effect as well as axial conduction that can effect the heat transfer result.

For the boundary conditions of water part, water temperature and water mass flow rate are imposed at the inlet. For the copper part, the inner wall temperature corresponding to saturation temperature and heat transfer coefficient are imposed. Different simulations with various inner heat transfer coefficient, water conditions; number of mesh in the domains and models are done. The table III.4 shows all the simulations done, for imposed heat transfer coefficient ranging from  $500$  to  $8000 \text{ W.m}^{-2}.\text{K}^{-1}$ .

$\alpha_{imposed}$ [ $W.m^{-2}.K^{-1}$ ]	Laminar		Turbulent		$T_{c,inlet}$	
	3M elts	5M elts	3M elts	5M elts	20°C	30°C
8000				x	x	
7000				x	x	
6000				x	x	
5000	x	x	x	x	x	x
4000				x	x	
3000				x	x	
2500				x	x	
2000				x	x	
850	x	x		x	x	x
500				x	x	

Table III.4: CFD analysis with different simulation cases was performed.

All possible conditions are simulated for both high and small heat transfer coefficient (i.e. at  $5000 Wm^{-2}K^{-1}$  and at  $850 Wm^{-2}K^{-1}$  respectively). These results are to investigate the effect of number of meshes, sub-cool temperatures and different models (laminar or turbulent). On the other hands, all range of heat transfer coefficients from 500 to  $8000 Wm^{-2}K^{-1}$  covering the range of experimental results have been considered for a same condition to quantify the axial heat conduction.

Figure III.13 shows the temperature profiles of the wall and the coolant as well as the saturation temperature. The zone between two black lines are the heat exchange zone. Because of axial conduction, we observe some differences between wall temperature and saturation temperature in the non-exchange copper part of the sub-section:

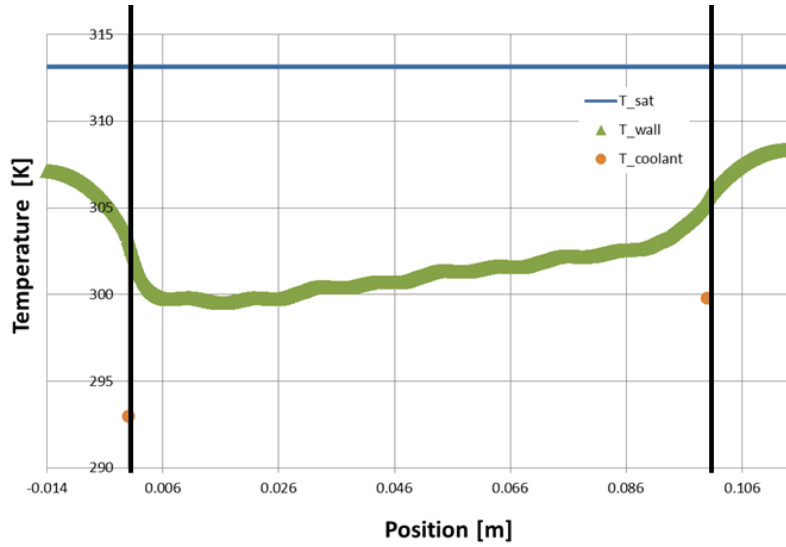


Figure III.13: Temperature profiles of the wall and the water for a heat transfer coefficient of  $6000 \text{ W.m}^{-2}.\text{K}^{-1}$  and a saturation temperature of  $40^\circ\text{C}$ , 5 million meshes and inlet water temperature of  $20^\circ\text{C}$ . The temperature gradients in the wall at the entrance and exit of the heat exchanger (upstream and downstream of the black lines) show that axial heat conduction is present and is not symmetrical. This effect must be taken into account to evaluate the heat transfer coefficient.

To investigate the effect of the number of meshes and of the method of resolution, some simulations have been done for different values of heat transfer coefficient. The tables III.5 and III.6 show the results of heat transfer coefficient calculated for two different values of imposed heat transfer coefficient :

- Imposed heat transfer coefficient of  $850 \text{ W.m}^{-2}.\text{K}^{-1}$ , water temperature at the inlet of  $20^\circ\text{C}$  and water velocity of  $0.1 \text{ m.s}^{-1}$ .

Studied case	Q [W]	$\Delta T_{log}$ [K]	$\Delta T_{mean}$ [K]	$HTC_{log}$	error %
Laminar with 3 millions of elements and FIRST order resolution	10.08	18.04	18.03	1051.98	23.76
Laminar with 3 millions of elements and with SECOND order resolution	9.81	17.59	17.57	1049.79	23.5

Table III.5: Simulation results of CFD for imposed heat transfer coefficient of  $850 \text{ W.m}^{-2}.\text{K}^{-1}$  with different numbers of meshes.

- Imposed heat transfer coefficient of  $5000 \text{ W.m}^{-2}.\text{K}^{-1}$ , water temperature at the inlet of  $20^\circ\text{C}$  and water velocity of  $0.1 \text{ m.s}^{-1}$

Studied case	Q [W]	$\Delta T_{log}$ [K]	$\Delta T_{mean}$ [K]	$HTC_{log}$	error %
Laminar with THREE millions of elements and first order resolution	37.50	12.36	12.28	5717.21	14.34
Laminar with FIVE millions of elements and with first order resolution	34.66	11.55	11.37	5652	13.05

Table III.6: Simulation results of CFD for imposed heat transfer coefficient of  $5000 \text{ W.m}^{-2}.\text{K}^{-1}$  with different numbers of meshes.

From these results, we found that the heat transfer coefficient calculated is not depending of resolution method.

Furthermore, other simulations have been done to study the effect of water inlet temperature. Tables III.7 and III.8 show the results of heat transfer coefficient calculated considering two different imposed heat transfer coefficient.

- Imposed heat transfer coefficient of  $850 \text{ W.m}^{-2}.\text{K}^{-1}$  with turbulent method, 5 millions of elements and first order resolution

Studied case	Q [W]	$\Delta T_{log}$ [K]	$\Delta T_{mean}$ [K]	$HTC_{log}$	error %
at $T_{c,inlet} = 20^\circ\text{C}$	10.16	18.18	18.16	1052.97	23.9
at $T_{c,inlet} = 25^\circ\text{C}$	5.08	9.09	9.08	1052.97	23.9

Table III.7: Simulation results of CFD for imposed heat transfer coefficient of  $850 \text{ W.m}^{-2}.\text{K}^{-1}$  with different water temperature at the inlet.

- Imposed heat transfer coefficient of  $5000 \text{ W.m}^{-2}.\text{K}^{-1}$  with turbulent method, 5 millions of elements and first order resolution

Studied case	Q [W]	$\Delta T_{log}$ [K]	$\Delta T_{mean}$ [K]	$HTC_{log}$	error %
at $T_{c,inlet} = 20^{\circ}\text{C}$	38.62	12.70	12.63	5726	14.52
at $T_{c,inlet} = 30^{\circ}\text{C}$	19.31	6.35	6.32	5762.05	14.52

Table III.8: Simulation results of CFD for imposed heat transfer coefficient of  $5000 \text{ W.m}^{-2}.\text{K}^{-1}$  with different water temperature at the inlet.

We found that the coolant temperature doesn't affect results on heat transfer coefficient. Higher calculated heat transfer coefficient than the imposed ones are obtained. These situations weren't observed in the previous simulations where only the exchange zone of a subsector was considered ; with the latter approach the errors between the imposed heat transfer and the calculated one were below 1%.

Condensation heat flux can be corrected by eliminate the axial conduction as following:

$$Q_{cond} = Q - Q_{axial,inlet} + Q_{axial,out} \tag{III.2.2.1}$$

With axial flux can be calculated by:

$$Q_{axial} = -\lambda_w \cdot A_w \cdot \left(\frac{\partial T_w}{\partial z}\right)_{z=z_{inlet,or,outlet}} \tag{III.2.2.2}$$

With:  $\frac{\partial T_w}{\partial z}$  is gradient of wall temperature at zone of axial effect. It is estimated at the border of the exchange part (black lines) in figure above. And surface of copper wall is deduced from:

$$A_w = \pi(D_{ext}^2 - D_{in}^2)/4/2 \text{ (m}^2\text{) considering half of the tube.}$$

Thus the evaluated heat transfer coefficient can be corrected as following:

$$\alpha_{in} = \frac{Q_{cond}}{\Delta T \cdot A} \tag{III.2.2.3}$$

The two tables below present the axial heat which depends on subcool temperature at different imposed heat transfer coefficient.

$HTC_{imposed}$ [ $W.m^{-2}.K^{-1}$ ]	500	850	2000	3000	4000	5000	6000	7000	8000
$HTC_{cal}$ [ $W.m^{-2}.K^{-1}$ ]	627	1053	2401	3521	4636	5726	6805	7877	8944
$Q_{axial}$ [W]	1.17	1.79	3.24	3.91	4.42	4.61	4.48	4.49	5.03
$Q_{axial}/(\Delta T_{log}.A_{tube})$ [ $W.m^{-2}.K^{-1}$ ]	116	185	376	496	608	683	776	885	907

Table III.9: Axial heat flux obtained from simulation results for subsection of 100 mm length

Where  $A_{tube} = \pi D_h L$  is the cross-section area and  $\Delta T_{log}$  is logarithmic mean temperature difference between the saturation and the wall ones. The heat transfer coefficient evaluated without considering the axial flux. Finally axial flux has been calculated as  $Q_{axial} = Q_{axial,inlet} - Q_{axial,out}$ .

In the experimental configuration, only external heat exchange is known and independent to water boundary conditions. To reduce error induced by axial heat conduction, an approximation is done based on numerical simulation results for both 100mm and 128 mm heat exchange sub-sector. Figures III.14 show the trend of  $Q_{axial}/(\Delta T_{log}.A_{tube})$  in function of calculated heat transfer coefficient.

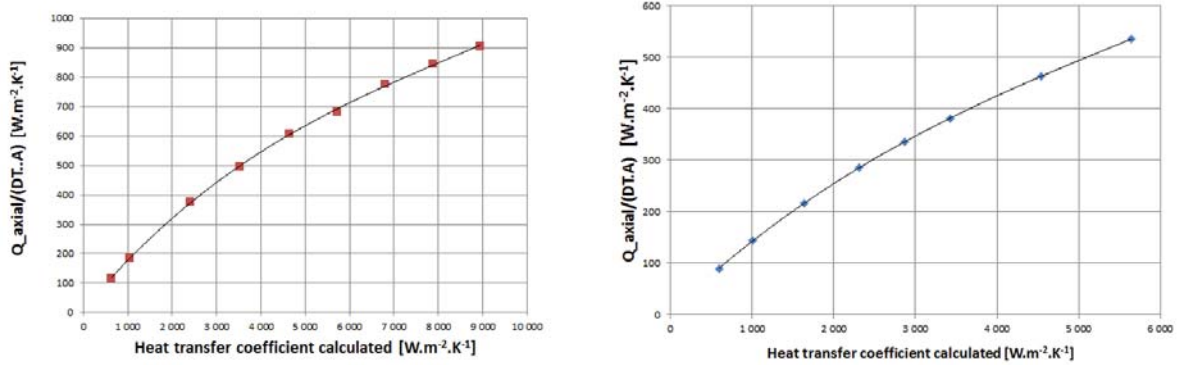


Figure III.14: Trend of  $Q_{axial}/(\Delta T_{log}.A_{tube})$  as a function of calculated heat transfer coefficient in the exchange zone for a) 100 mm length sub-sector and b) 128 mm length sub-sector.

For the 100mm exchange length sub-sector, the following law is deduced from this trend:

$$Q_{axial} = f1(HTC_{cal}).\Delta T_{log}.A_{tube} \quad (III.2.2.4)$$

With:

$$f1(x) = 5.528E-10.x^3 - 1.394E-5.x^2 + 0.1811x + 9.3284 \quad (III.2.2.5)$$

The same investigation has been done for exchange length of 128 mm. The various cases tested are presented in table III.10 at water velocity of  $0.1 \text{ ms}^{-1}$ .

$HTC_{imposed} [W.m^{-2}.K^{-1}]$	Turbulent 5 elts	$T_{water,inlet} [^{\circ}C] = 20^{\circ}C$
8000	x	x
7000	x	x
6000	x	x
5000	x	x
4000	x	x
3000	x	x
2500	x	x
2000	x	x
850	x	x
500	x	x

Table III.10: Various cases tested for simulation of a sector of 128mm length.

Using the same analysis method for exchange length of 100mm, for exchange length of 128mm the axial conduction is evaluated as:

$$Q_{axial} = f2(HTC_{cal}).\Delta T_{log}.A_{tube} \quad (III.2.2.6)$$

with

$$f2(x) = 8.627E-10.x^3 - 1.502E-5.x^2 + 1.502E-1.x + 5.103 \quad (III.2.2.7)$$

By using these corrections, the corrected heat transfer coefficients become:

- For L=100mm

$HTC_{imposed}$ [ $W.m^{-2}.K^{-1}$ ]	500	850	2000	3000	4000	5000	6000	7000	8000
$HTC_{cal}$ [ $W.m^{-2}.K^{-1}$ ]	627	1053	2401	3521	4636	5726	6805	7877	8944
$Q$ [W]	6.3	10.2	20.7	27.8	33.7	38.6	42.8	46.4	5.0
$Q_{axial,cal}$ [W]	1.17	1.79	3.24	3.91	4.42	4.61	4.88	4.98	5.03
$HTC_{cor}$ [ $W.m^{-2}.K^{-1}$ ]	509	868	2030	3031	4032	5033	6035	7036	8034
error %	1.88	2.08	1.48	1.05	0.79	0.66	0.58	0.51	0.43

Table III.11: Heat transfer coefficient evaluated with axial correction for 100mm length.

- For the exchange length of 128mm the evaluated heat transfer coefficients become:

$HTC_{imposed}$ [ $W.m^{-2}.K^{-1}$ ]	500	850	1400	2000	2500	3000	4000	5000
$HTC_{cal}$ [ $W.m^{-2}.K^{-1}$ ]	598	1006	1637	2314	2873	3429	4536	5644
$Q$ [W]	7.3	11.5	17.0	21.8	25.1	27.9	32.4	35.9
$Q_{axial,cal}$ [W]	1.1	1.65	2.25	2.69	2.93	3.1	3.31	3.4
$HTC_{cor}$ [ $W.m^{-2}.K^{-1}$ ]	508	863	1421	2029	2537	3047	4073	5108
error %	1.55	1.54	1.49	1.43	1.48	1.55	1.83	2.16

Table III.12: Heat transfer coefficient evaluated with axial correction for 128mm length.

The error in both case is from 0 to 2% confirming that the correction of heat exchange by axial conduction is a good way to correct the heat transfer coefficient. These calculations will be used to improve the data reduction later.

### III.2.3 Calibration of test section

The test section has been machined to obtain external wall following the previous design in the mechanics department of Laboratory of Phase Change Heat Transfer of Padova, Italy. Pressure sensors are installed at the inlet and outlet of the test section to measure both absolute pressure and pressure drop in the test section. Six thermocouples are installed at 3 positions in the wall of the copper tube as presented above.

They are located at from the inner surface 0.7mm at 20.5 mm from the inlet and outlet, and in the middle. The mixer of water is also installed before water enters and exits to homogenize the coolant. The exchanger works in counter current configuration.

After that, the test section has been installed into the loop already available in Padova for some preliminary validation tests. The figure below shows the test rig scheme in Laboratory of Phase Change Heat Transfer of Padova, Italy:

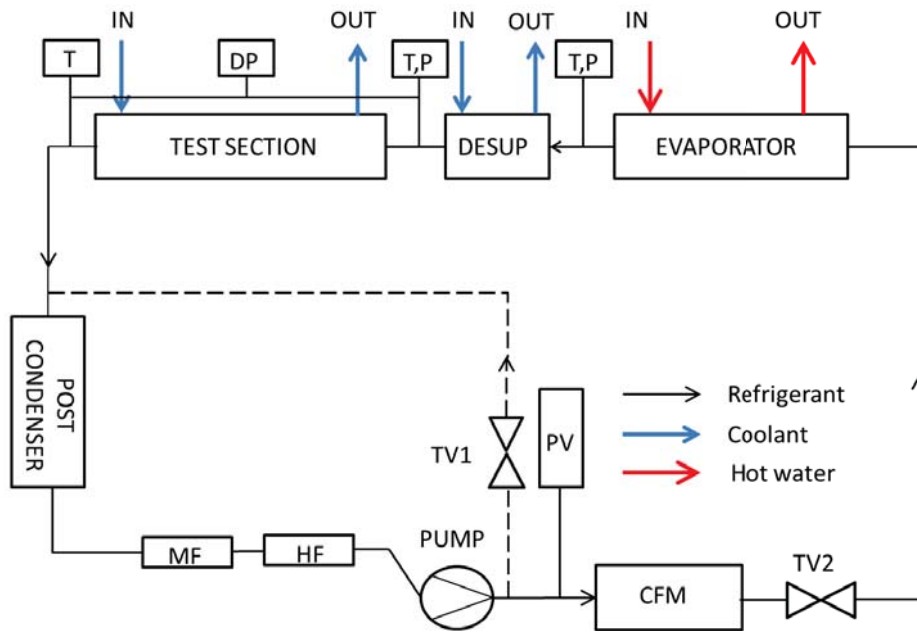


Figure III.15: Experimental loop used to validate the test section in Padova university: FD (filter drier); PV (pressure vessel); CFM (Coriolis-effect mass flow meter); TV (throttling valve); MF (mechanical filter); HF (Dehumidifier); P (relative pressure transducer); DP (differential pressure transducer); T(thermocouple).

Two water loops are dedicated to cool the refrigerant in the test section. The first one cools the first three sub-sections. As the flows are in counter current the water outlet of the third sub-section is the water inlet of water of the second sub-section and the outlet of the second sub-section is the inlet of the first sub-section. The second water loop cools the fourth and the fifth sub-sections; the water outlet of the fifth sub-section is the water inlet of the fourth sub-section. Each water loop is composed of a regulating valve and a flow meter.

Except the test section part, this apparatus is composed of the primary loop of refrigerant and three water loops to set refrigerant condition upstream and downstream of the test section. The subcooled refrigerant passes through a filter and a drier and

is then sent to gear pump. It is then pumped through the Coriolis flow meter (CFM) into an evaporator where the fluid is heated, vaporized and superheated. At the evaporator exit, the temperature and pressure are measured. A desuperheater is installed upstream of test section in order to cool down the refrigerant until it reaches the desired state at the inlet of the test section.

The refrigerant then enters the test section. Its temperature and pressure are measured in the adiabatic sector upstream of the test section. At the outlet of test section, the temperature is also measured. A differential pressure sensor is installed to measure pressure drop between the ends of the test section. The loop closes in the post condenser where refrigerant is condensed and subcooled.

Figure III.16 shows the test section installed in test rig at Padova university:

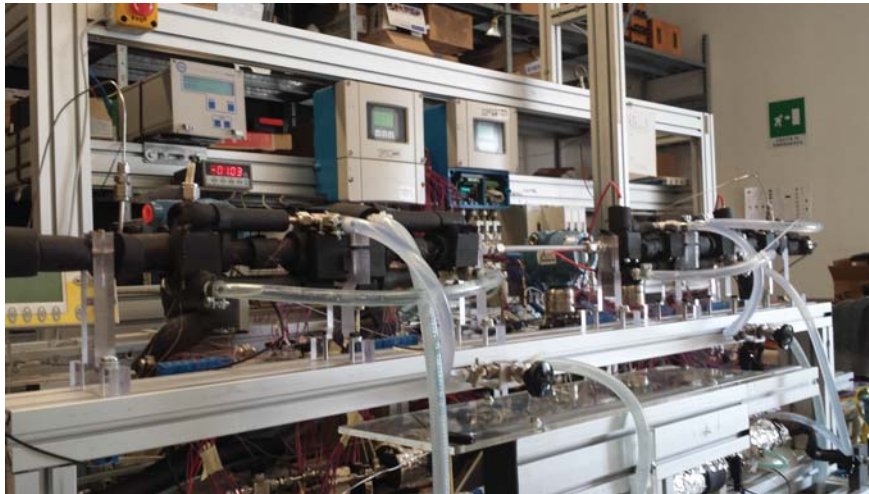


Figure III.16: The condensation test section installed in the experimental test rig of Padova university.

When the test section is installed in the loop, a calibration procedure is required before carrying out primary tests on ground.

The calibration procedure of the apparatus is performed in order to have the desired accuracy of the measurements. All temperature sensors are home-made of type T Copper-Constantan. Firstly, on-site calibration of thermocouples installed in the wall and in the water channel is performed. This on-site calibration is carried out by water circulation under the constant and adiabatic condition at high mass flow rate. To avoid heat losses, vacuum is maintained inside channel. Temperature calibration is performed by using two calibrated thermistors Pt100 located in the test section at water inlet and outlet. The thermistors are coupled with Hart Scientific Super Thermometer II 1890; this instrument can reach an uncertainty down to  $0.002^{\circ}C$  on measured temperature.

A correction function of each thermocouple is obtained from this calibration procedure. Wall and water temperatures measured by thermocouples before and after calibration are presented in figure III.17. Each measurement is the mean of 50 readings taken during 50s in stationary condition. The range of variation after on-site calibration is equal to 0.08K.

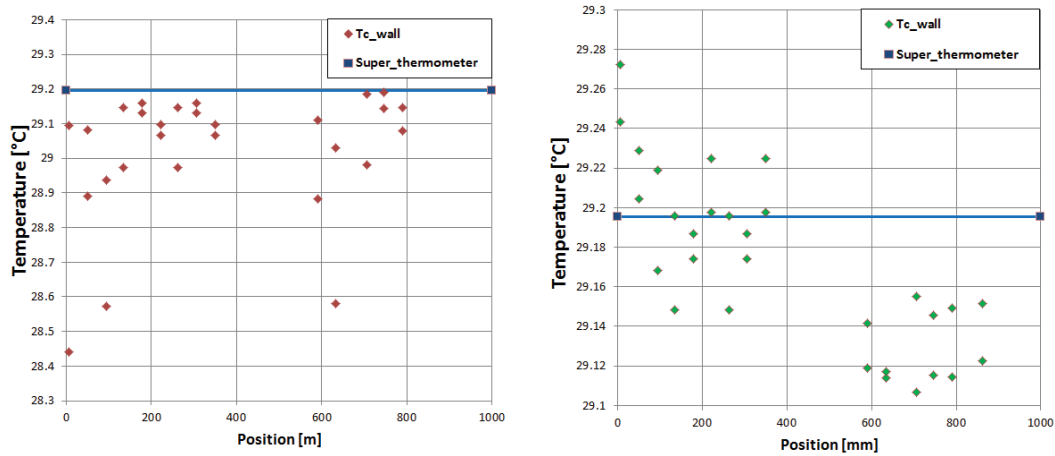


Figure III.17: Wall temperatures before and after calibration

Before performing some experimental tests, water heat losses in each sub-sector are investigated. These heat losses are expected to be small thanks to the isolation thermal insulation used. This investigation is carried out with water circulation at desired mass flow rate at different temperature. The temperature difference of the water between the outlet and inlet and the water mass flow rate are measured the heat dissipation to environment can thus be deduced. Finally, heat dissipation is found as a function of temperature difference between water and ambient one. Figure III.18 shows heat losses in second and third sub-sectors.

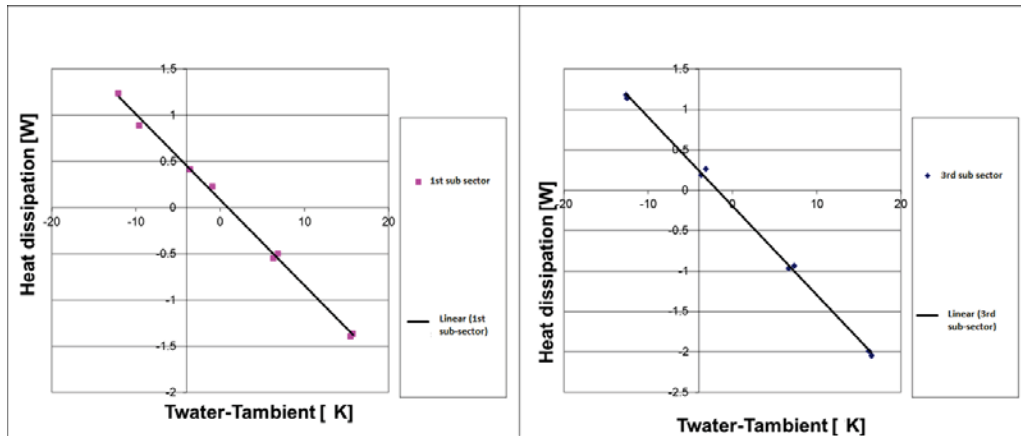


Figure III.18: Heat dissipation to the environment measured at a) second and b) third sub-sections.

As the calibration is done, the heat balance can be realized. R134a which is a very common and well known fluid, is used to realize these first condensation tests. These tests are performed considering superheated vapor at the inlet and subcooled liquid at the outlet of the test section. The figure III.19 shows the temperature profile of water, wall and refrigerant:

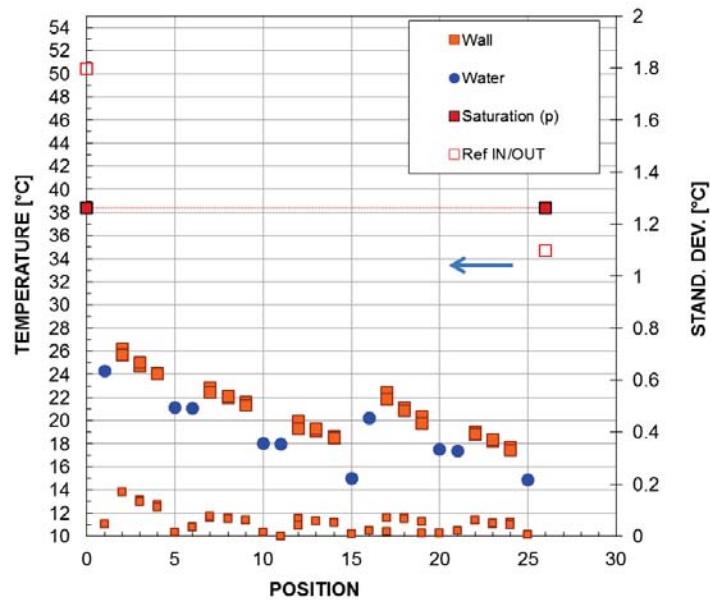


Figure III.19: All temperature profiles in test section.

The refrigerant enters the test section at superheated vapor state with an inlet pressure of 9.74 bar and exits the test section at 34.7°C. The table III.13 refers the heat balance in the test section :

$G [kg.m^{-2}.s^{-1}]$	$Q_{c1s}$ [W]	$Q_{c2s}$ [W]	$Q_{c3s}$ [W]	$Q_{c4s}$ [W]	$Q_{c5s}$ [W]	$Q_{ctot}$ [W]	$Q_{ref}$ [W]	error %
201.09	70.0	65.3	65.2	57.3	52.2	310.1	330.8	-6.2

Table III.13: Heat balance verification of water and refrigerant.

Where  $Q_{ctot} = Q_{c1s} + Q_{c2s} + Q_{c3s} + Q_{c4s} + Q_{c5s}$  is heat exchange measured in water side from first to fifth sectors. And  $Q_{ref} = (h_{ref,inlet} - h_{ref,out})\dot{m}_{ref}$  measured from refrigerant side by temperature and pressure measured at the inlet and outlet of the whole test section.

We found that the wall temperature is very close to water temperature and it confirms our conception. More details in tests validation and heat balance can be found in [74]. After the test section has been fully tested, it has been sent to the in Université Libre de Bruxelles in order to prepare the experimental investigation in parabolic flight.

### III.3 Experimental investigation of condensation in parabolic flights

After all calibration and verification of the test section have been done, the test section was sent to Université Libre de Bruxelles where the rig is built to have a complete specific loop dedicated for parabolic flights experiment.

#### III.3.1 Experimental apparatus

The experimental facility used in this investigation has been designed to measure detailed average heat transfer as well as to visualize simultaneously the flow pattern using a high speed camera during parabolic flight experiments. The schema III.20 shows the experimental loop used in parabolic flight.

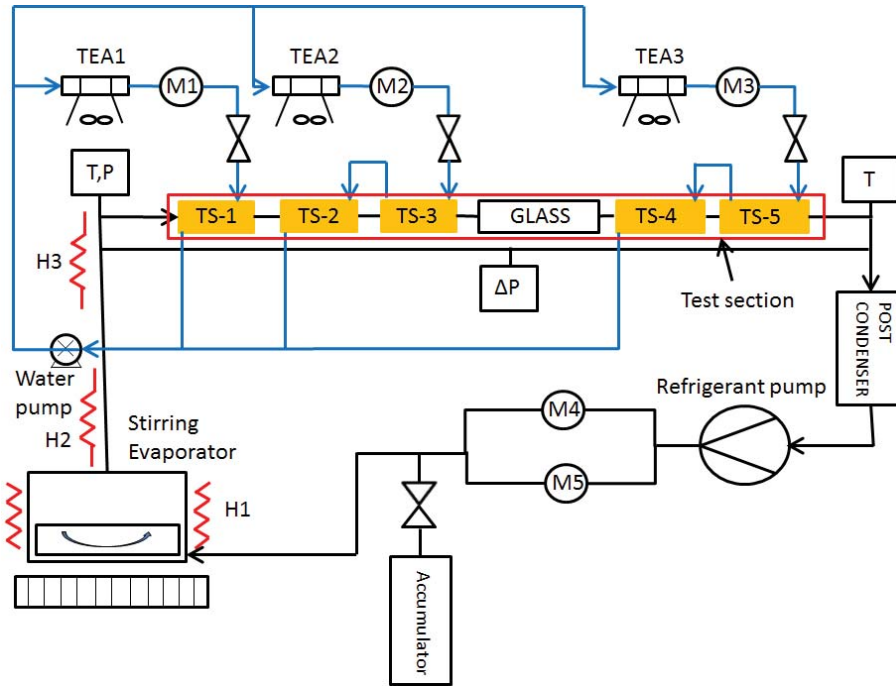


Figure III.20: Schema of the final loop for condensation tests used in parabolic flights.

The schema above describes the final apparatus with two principle loops: the primary refrigerant loop and the coolant water loop. The working fluid exits the test section and flows to post condenser, which is a fan coil, to condense the possible flow of remaining vapor and subcool the liquid. The fluid is then pumped by a gear pump. Upstream of the pump, two refrigerant flow meters are installed in parallel, working on two different mass flow rate ranges. The mass flow meter, named as M4 in schema, has a working range between 0.75 and 15 mL/min and operates on a thermal through-flow measuring principle; the second one, named as M5, is a turbine mass flow meter and works on a higher range of mass flow rates, between 10 to 100 mL/min. Then the working fluid is heated in a stirrer magnetic evaporator. Superheated vapor is obtained by two electrical heaters (H2 and H3) attached to the tube walls before reaching the inlet of the test section.

The experimental test section is as previously described, composed of two heat exchangers in copper and a visualization window in glass. At the inlet of the test section, the local pressure and temperature of the superheated vapor are measured by an absolute pressure transducer ranging from 0 to 2 bar and a T-type thermocouple. Then the fluid is condensed in the different exchangers completely or partially by using water as coolant. At the outlet the fluid temperature is measured by a T-type thermocouple and the pressure is determined by inlet refrigerant pressure and pressure drop measured by a differential pressure transducer ranging from 0 to 150 mbar.

The water loop has 3 sub-circuits in parallel as presented in figure III.20. Each sub-circuit consists of an air cooled thermoelectrical water-cooling assembly (TEA), a turbine flowmeter ranging 10-100 mL/min and a regulating valve. The aim of the first sub-circuit is to reject heat from first sub-section in copper; the second one is for second and third sub-sections and the third one is for the fifth and fourth sub-sections. At the inlet and outlet of each water sub-circuit, the temperatures and temperature difference between water outlet and inlet are measured by T-type thermocouple and a thermopile. In each sub-circuit, the water and the refrigerant flows are in counter-current. In this test section, the first sub section works as a desuperheater.

Regarding the visualization system, an optical bench is installed on an optical table of 600 x 400  $mm^2$ . This system is composed of a telecentric backlight, three LED light sources (LZ1-00R200 provide by Led engine company) emitting a monochromatic red light around 662nm, a ground glass, two mirrors and a high speed camera (CL600x2 provided by optronic company) as presented in figure III.21. The system can work in two different configurations i.e. local view and global view. Concerning the local visualization, the collimated light sent by the telecentric backlight is passed on the visualization section of the test section by one mirror. The light sent through the test cell is then redirected by another mirror and captured by the objective of the camera of a focal length of 100 mm and achieving a view zone of about 6.5 x 16.2  $mm^2$ . Concerning the global view, the light issued from the LED sources transmitted through a ground glass to obtain a uniform distribution of light and lights up the whole transparent visualization part. The light is then reflected through a mirror in the direction of the camera. The camera objective has a focal length of 35 mm and achieves a view zone of about 6.5 x 150  $mm^2$ .

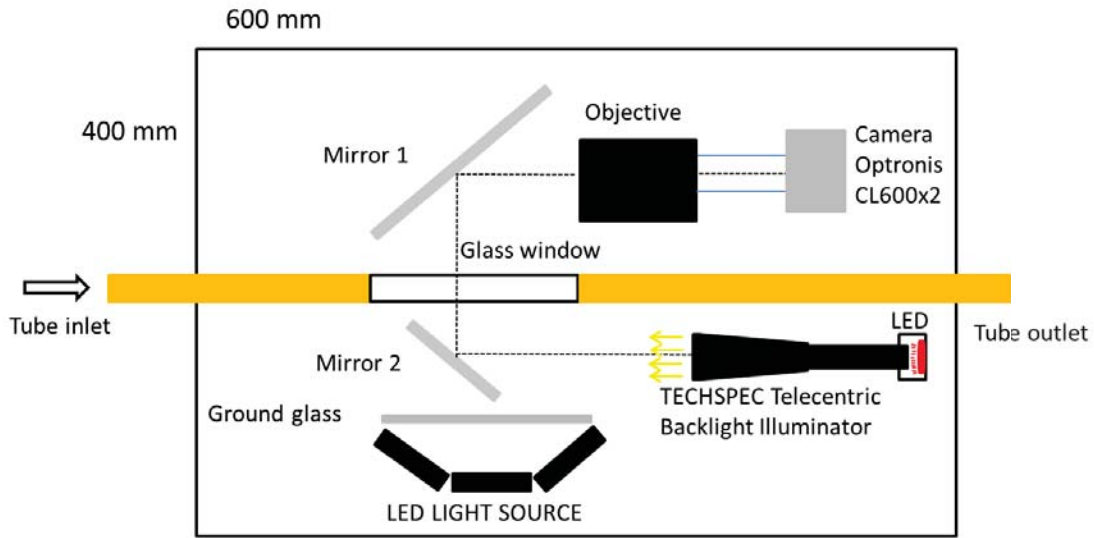


Figure III.21: The schema of final loop used in parabolic flights

The refrigerant used in the experiment is HFE-7000. Its low saturation temperature at ambient pressure respect some safety requirements in flight. Firstly, the leak of the loop has been checked. To be sure that non-condensable gases are not present, the fluid is degased thanks to an auxiliary system and then charged into the loop. To avoid any risk of introducing non-condensable gases in the refrigerant loop the inside pressure is fixed at higher value than the atmospheric one. Nevertheless, between two experiments or during night, the pressure inside the loop can decrease strongly and fall below the ambient value. To avoid this configuration a damping accumulator is connected to the circuit and used to pressurize the experimental loop to avoid air entering the refrigerant circuit.

Other primary point is to calibrate all thermocouples and thermopile in new loop. The same procedure as described previously has been done before the apparatus is mounted in the plane.

Figures III.22 and III.23 are pictures of the experimental apparatus ready for the flight. The experimental data are recorded continuously with a time step of 2.7 s.

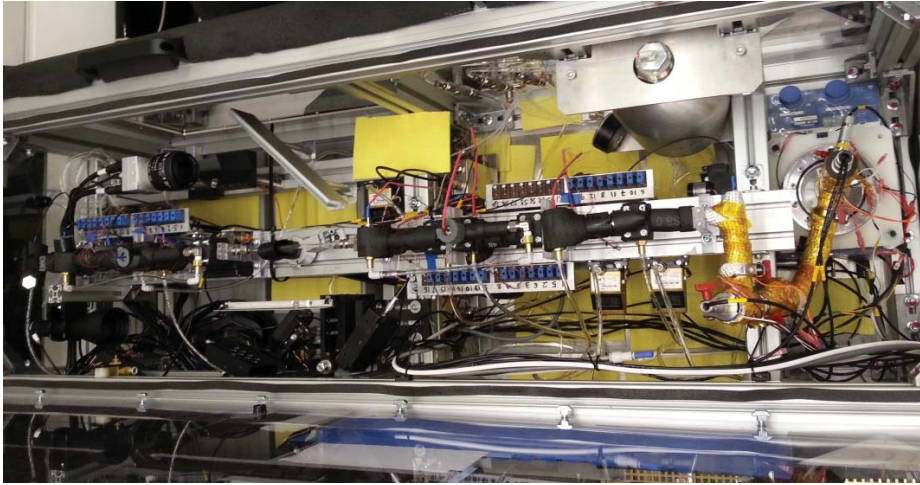


Figure III.22: Picture of the test section installed into the loop and ready for flight



Figure III.23: Experimental facility installed and ready to operate in the plane.

### III.3.2 Experimental procedure

During condensation experiments, the working fluid HFE-7000 has to enter the test section of 3.38 mm hydraulic diameter in superheated vapor state. The temperature and pressure at the inlet measured by a T-type thermocouple and an absolute pressure transducer are used to determine the thermodynamic state of the working fluid at the

inlet. In each sub-sector, a quasi-local heat transfer coefficient can be determined from the measurement of wall temperature, water temperature difference between the outlet and inlet of each sub-sectors and water mass flow rate. The flow regime is also obtained via direct visualization through the glass window.

In a parabolic campaign, three days of flights are available to realize microgravity experiments. A typical day of tests is composed of a three hours of flight during which 31 parabolas maneuvers are performed. Parabolas are grouped by group of five consecutive parabola. In each group the duration of break between two consecutive parabola is around 1 or 2 minutes ; between two consecutive groups of 5 parabolas a break of 5-8 minutes is allowed. Each parabola consists of 22 seconds of hyper gravity at 1.8g announced by the term "pull-up", followed by 20 seconds of microgravity at  $0\pm 0.05g$  and closed by 22 seconds of hypergravity of 1.8g announced by the term "pull-out".

Due to the low duration of microgravity compare to the response time of the loop to reach steady state when parameters are modified, only specific tests can be achieved in quasi-stable state conditions. For this reason, to avoid to lose microgravity period, mass flow rate of the refrigerant and of the water are kept constant during one group of parabolas. The only parameter than can be modified in such short time between two consecutive parabolas is the inlet water temperature. This parameter is frequently used to set the vapor quality in the glass tube. All data acquisition are collected every 2.7 seconds. The following section presents the results obtained for both heat transfer coefficient and flow pattern in microgravity condition.

### **III.3.3 Experimental results of heat transfer coefficient**

#### **III.3.3.1 Analysis of the transient effect**

The figure III.24 shows the configuration of the condenser with HFE-7000 as the working fluid and water as the coolant. The data reduction will be determined by studying the domain between  $z$  and  $z+\Delta z$ . The objective of this section is to analyze the unsteady terms compared to the steady ones. Quantification of unsteady terms will allow us to select the experimental data that can be used to determine the heat transfer coefficient.

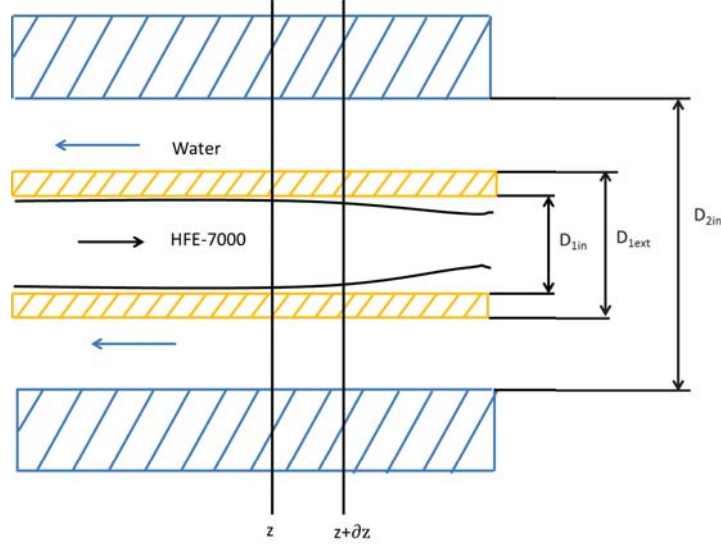


Figure III.24: Configuration of experimental test section.

Assuming that the internal wall temperature is equal to external one because the copper thermal resistance is negligible, the complete heat balance on the water side and the copper wall can be written respectively as following:

- For water:

$$\rho_c c_{p,c} \frac{\partial T_c(z, t)}{\partial t} A_c \Delta z = \alpha_c P_c \Delta z (T_w(z, t) - T_c(z, t)) + Q_{exchange} \quad (\text{III.3.3.1})$$

- For copper wall:

$$\rho_w c_{p,w} \frac{\partial T_w(z, t)}{\partial t} A_w \Delta z = \alpha_{cond} P_{in} \Delta z (T_{sat}(z, t) - T_w(z, t)) - \alpha_c P_c \Delta z (T_w(z, t) - T_c(z, t)) \quad (\text{III.3.3.2})$$

Where  $T_c$ ,  $T_w$  are coolant and wall temperatures.

Where  $Q_{exchange}$  can be calculated by:

$$Q_{exchange} = \dot{m}_c c_{p,c} (T_c(z) - T_c(z + \Delta z)) - q_{losse} - q_{axial} \quad (\text{III.3.3.3})$$

Combining these equations, the final equation can be formulated as below:

$$\alpha_{cond} P_{in} \Delta z (T_{sat}(z, t) - T_w(z, t)) = \rho_c c_c \frac{\partial T_c(z, t)}{\partial t} A_c \Delta z + \rho_w c_{p,w} \frac{\partial T_w(z, t)}{\partial t} A_w \Delta z - Q_{exchange} \quad (\text{III.3.3.4})$$

On the refrigerant side, considering a homogenous mixture of liquid and vapor, the thermal balance appears as:

$$\frac{\partial H(z, t)}{\partial t} A_{in} \Delta z = \dot{m}_{ref}(h(z, t) - h(z + \Delta z, t)) - \alpha_{cond} P_{in} \Delta z (T_{sat}(z, t) - T_w(z, t)) \quad (\text{III.3.3.5})$$

Where H is enthalpy per unit volume of a homogenous two-phase mixture:

$$H = h_L(1 - \epsilon)\rho_L + h_V\epsilon\rho_V \quad (\text{III.3.3.6})$$

Where  $\epsilon$  is the void fraction. By replacing the condensation heat transfer coefficient below, we have:

$$\begin{aligned} \frac{\partial H(z, t)}{\partial t} A_{in} \Delta z = & \dot{m}_{ref}(h(z, t) - h(z + \Delta z, t)) - \rho_c c_c \frac{\partial T_c(z, t)}{\partial t} A_c \Delta z \\ & - \rho_w c_w \frac{\partial T_w}{\partial t} A_w \Delta z + Q_{exchange} \end{aligned}$$

and extracting the enthalpy term at  $z + \Delta z$  is:

$$h(z + \Delta z, t) = h(z, t) - \frac{Q_{exchange}}{\dot{m}_{ref}} - \frac{\frac{\partial H(z, t)}{\partial t} A_{in} \Delta z + \rho_c c_c \frac{\partial T_c(z, t)}{\Delta t} A_c \Delta z + \rho_w c_w \frac{\partial T_w(z, t)}{\partial t} A_w \Delta z}{\dot{m}_{ref}} \quad (\text{III.3.3.7})$$

In steady state conditions, the terms depending on the time can be neglected and the final equations to determine the heat transfer coefficient and vapor quality become:

$$\alpha_{cond} = \frac{Q_{exchange}}{P_{in} \Delta z (T_{sat} - T_w(z, t))} \quad (\text{III.3.3.8})$$

$$h(z + \Delta z, t) = h(z, t) - \frac{Q_{exchange}}{\dot{m}_{ref}} \quad (\text{III.3.3.9})$$

$$x(z) = \frac{h(z) - h(z + \Delta z)}{h_v(z) - h_l(z)} \quad (\text{III.3.3.10})$$

Where  $\dot{m}_c c_{p,c}(T_c(z, t) - T_c(z + \Delta z, t))$  is the local heat flux received in water side that can be calculated in each subsection by means of water mass flow rate and the temperature difference measured by thermopiles.  $q_{losse}$  is a function of temperature difference between water temperature and ambient temperature.  $q_{axial}$  is axial conduction which can be evaluated for both 100mm exchange length sub-section and 128m exchange length sub-section by numerical simulation. Comparing the terms in non-stationary equations, the effect of the unsteady term on the heat transfer coefficient

and enthalpy can be analyzed. The maximum of unsteady terms is at the moment the level of gravity changes suddenly. For each parabola analysis, the unsteady state term and the steady state are compared and if this ratio is higher than 10% on the last 5s of parabola, the data are discarded.

### **III.3.3.2 Heat transfer coefficients**

In each subsection, the local saturation temperature can be evaluated by assuming a linear pressure variation between the inlet and outlet. Therefore, the heat transfer coefficient can be determined by the equation III.3.3.8 above with the subcooling calculated by mean or logarithmic mean temperature difference.

Using the data reduction above, the heat transfer coefficient is evaluated at each parabola. The condensation tests have been performed using HFE-7000 as the working fluid, with mass velocity ranging from 70 to 170  $kg.m^{-2}.s^{-1}$  and saturation temperature between 44.2°C and 47°C. Some tests at the same working conditions have been done several times to check the repeatability of thermal dynamic. Moreover, some data at normal gravity condition are collected during long break between two parabolas at the same working condition to be sure that there is no slow drift of the conditions which would modify the values obtained in the so-called "stationary regime" obtained in few seconds.

Figures III.25 and ?? refer the experimental heat transfer coefficients for normal and microgravity conditions at different mass velocities of 70, 100, 150  $kg.m^{-2}.s^{-1}$ ; at these mass velocities there is a decrease of the condensation heat transfer performance during microgravity. Whatever the mass flow rate value is, the heat transfer difference between normal gravity and microgravity is increased at lower quality values.

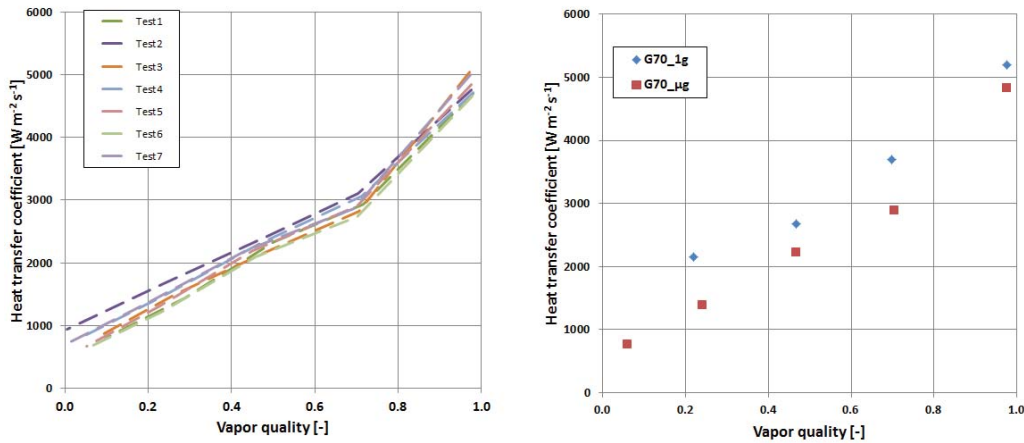


Figure III.25: Quasi local heat transfer coefficient as a function of vapor quality for a mass velocity of  $70 \text{ kg}\cdot\text{m}^{-2}\cdot\text{s}^{-1}$ : - left: the same experiment repeated 6 times in microgravity condition. - Right: gravity effect.

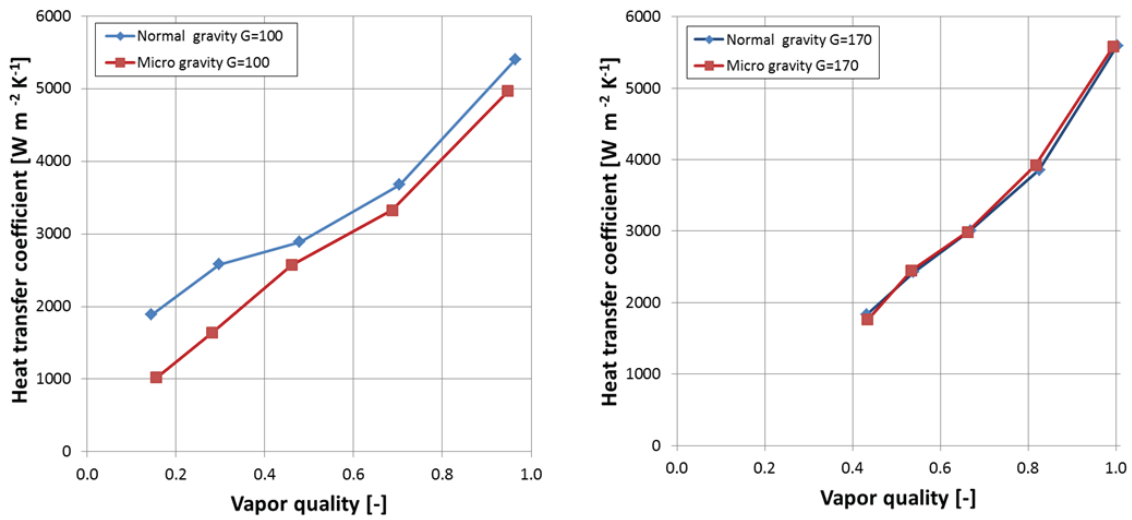


Figure III.26: Heat transfer coefficient trends in microgravity and normal gravity conditions and for mass velocity of 100 and  $170 \text{ kg}\cdot\text{m}^{-2}\cdot\text{s}^{-1}$ .

Moreover figure III.27 shows the ratio of the experimental heat transfer coefficient in microgravity to the one in normal gravity conditions at vapor quality of 0.8, 0.6 and 0.4.

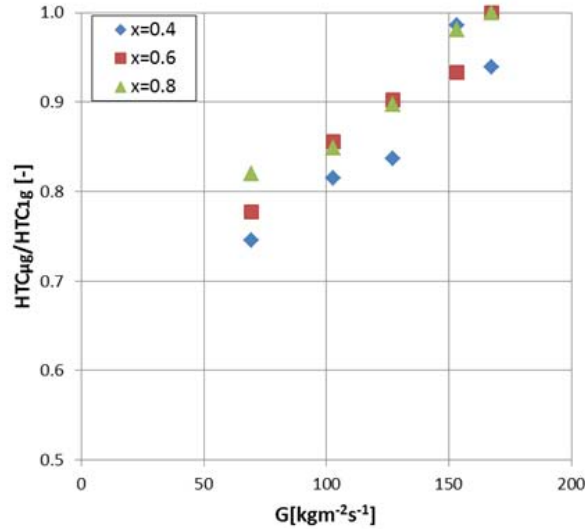


Figure III.27: Ratio of the experimental heat transfer coefficient in microgravity and in normal gravity conditions for HFE-7000 working fluid at the different mass velocities ranging from 70 to 175  $\text{kg}\cdot\text{m}^{-2}\cdot\text{s}^{-1}$  and vapor qualities of 0.8, 0.6 and 0.4.

At  $G=170 \text{ kg}\cdot\text{m}^{-2}\cdot\text{s}^{-1}$  the ratio is almost constant and close to 1 at  $x=0.8$  and 0.6. However at  $x=0.4$  the ratio becomes smaller and reach 0.95. At  $G=150 \text{ kg}\cdot\text{m}^{-2}\cdot\text{s}^{-1}$  the ratio at  $x=0.8$  is also close to 1 but at  $x=0.6$  the ratio goes down to 0.9. Considering  $G=130 \text{ kg}\cdot\text{m}^{-2}\cdot\text{s}^{-1}$  the decrease between the two heat transfer coefficients is about 10%, for vapor qualities of 0.8 and 0.6, but for vapor quality of 0.4 the ratio reaches only 0.82. For mass velocities of  $100 \text{ kg}\cdot\text{m}^{-2}\cdot\text{s}^{-1}$  the decrease of the heat transfer coefficient ranges between 15% and 20%. Considering mass velocity of  $70 \text{ kg}\cdot\text{m}^{-2}\cdot\text{s}^{-1}$ , this decrease is between 15% and 25%. An important thing we can observe is at the same mass velocity at higher vapor quality the heat transfer coefficient decrease less and at the same vapor quality at higher mass velocity the diminution is smaller. This means that the effect of gravity depends on the working conditions, and specifically from the mass velocity and the vapor quality.

### III.3.4 Investigation of flow pattern

The heat transfer coefficient and flow pattern are correlated. So to understand the heat transfer mechanism, it is necessary to analyze the flow pattern as well as liquid film thickness variation.

Figures III.28 and III.29 show sequential images of the condensing HFE-7000 during normal gravity and microgravity conditions in the adiabatic glass tube installed between the two heat exchangers of the test section at mass velocity equal to 170

$kg.m^{-2}.s^{-1}$  and  $70 kg.m^{-2}.s^{-1}$  respectively. For each test condition there are three images in normal gravity, named 1, 2, 3 on the left and three ones in microgravity condition, named 4, 5, 6 on the right; the images in normal gravity have been recorded before the pull-out phase of the parabola. They were taken by the high speed camera at 200 Hz in local view configuration.

For  $G=170 kg.m^{-2}.s^{-1}$ , during normal gravity, the film thickness is slightly observed on the bottom and sometimes on the top; the flow pattern inside glass tube is in the transition between annular and stratified wavy. In microgravity the film on the top of the tube appears thicker and the flow regime is more axisymmetric; however the flow pattern does not change significantly. In both microgravity and normal gravity conditions, the condensed film is distributed along the internal wall tube. In this case, we can conclude that at such mass velocity the shear stress has an important role and gravity effects are reduced.

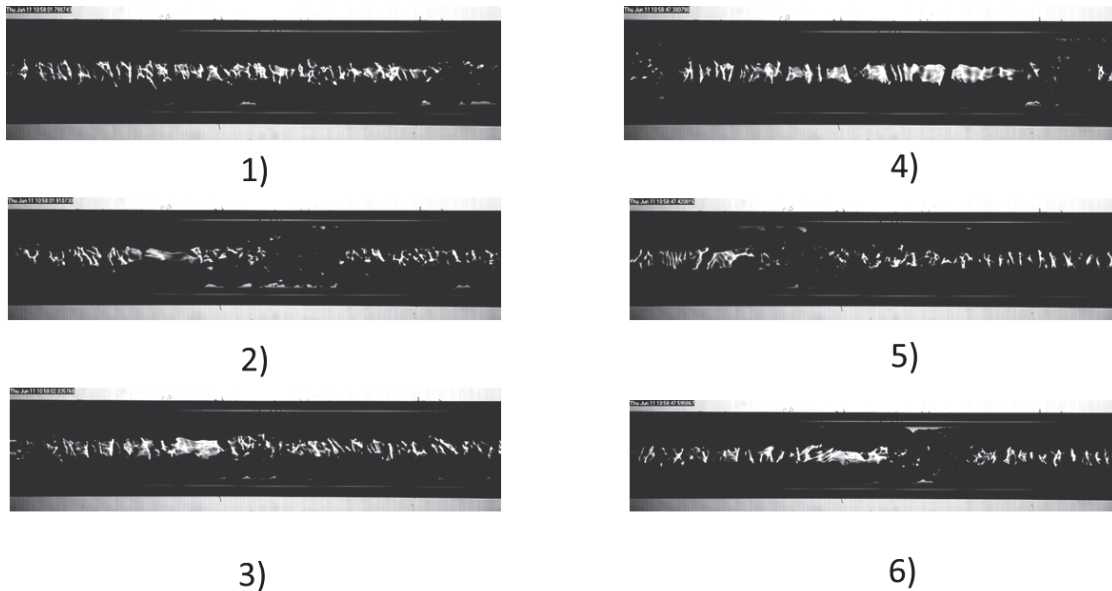


Figure III.28: Flow pattern observed during condensation of HFE-7000 in normal (1,2,3) and microgravity (4,5,6) conditions at  $G=170 kg.m^{-2}.s^{-1}$  and  $x=0.64$ .

Recorded video of condensation flow regime in glass tube have been recorded at a lower mass velocity of  $70 kg.m^{-2}.s^{-1}$  and a quality  $x=0.32$ . At such mass velocity, the effect of all force terms in momentum balance such as gravity, surface tension and shear stress must be considered. In figure III.29, the images named 1, 2, 3 are recorded in normal gravity and 4, 5, 6 are recorded in microgravity. We can note that, in normal gravity, the film is thicker on the bottom of the tube and not visible on the top; here the gravity plays an important role to drain the condensed liquid on the lower part

of the tube, creating a pool. In microgravity the liquid film is propagated along the internal circumference of the tube under the effects of surface tension and shear stress.

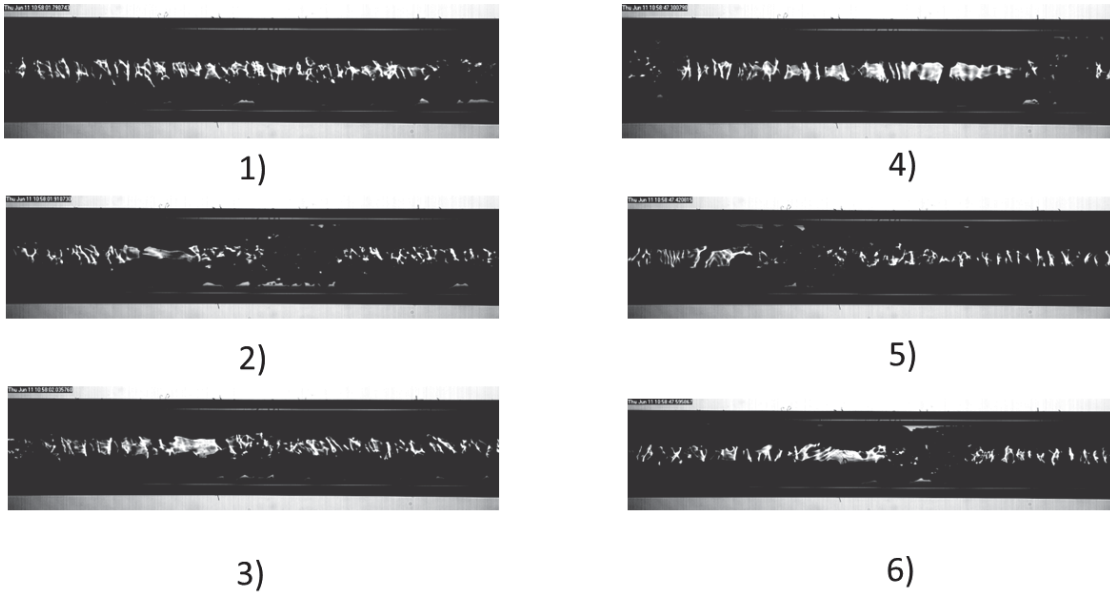


Figure III.29: Flow pattern observed during condensation of HFE-7000 in normal (1,2,3) and microgravity conditions (4,5,6) at  $G=70 \text{ kg.m}^{-2}.s^{-1}$  and  $x=0.32$ .

Regarding the thermal and flow pattern results, the gravity plays an important role at low mass velocity which is, for HFE-7000 at approximately atmospheric pressure under  $150 \text{ kg.m}^{-2}.s^{-1}$ . At these low mass fluxes, the heat transfer coefficient depends on the gravity level due to the important change of liquid film thickness distribution around the periphery of the tube.

The reduction of heat transfer coefficient when microgravity is reduced for the range of mass velocity from  $70 \text{ kg.m}^{-2}.s^{-1}$  to  $170 \text{ kg.m}^{-2}.s^{-1}$ , can be explained as follows: at Earth's gravity level, as the condensate film thickness at the bottom is thicker than on the top (knowing that the exchange for smaller film thickness is higher than for a thicker one) the heat transfer coefficient on the top is higher than the one at the bottom part. In microgravity condition, the surface tension and shear stress lead the film thickness to be axisymmetric around the tube. But as the local heat transfer coefficient is inversely proportional to the liquid film thickness, it is better to have small liquid film thickness in a small region and higher value on other part than an homogeneous value of the liquid film thickness all around the periphery of the internal wall.

These modifications of liquid film distribution in normal gravity and microgravity can be observed also on the wall temperature profile: when the film thickness becomes thinner, the film resistance is smaller and the wall temperature is reduced. Figure III.30 presents the wall temperatures measured in three different positions in the 3rd sub-sector (the one just before the glass tube). In the inlet and outlet fins the wall temperatures are measured at the bottom and on the top. We can observe the temperature difference modification between two thermocouples at the same position; in middle position, the thermocouples are installed in the median horizontal plan of the fin so that the temperature difference variation of these two thermocouples is less. At the inlet and outlet fins, it can also be observed that in normal and hyper gravity the temperature at the top is higher than the one at the bottom and this difference decreases when gravity is reduced; this is because the liquid film in microgravity distributes more uniformly on the tube wall while during normal gravity and hyper gravity conditions the film thickness at the bottom is thicker than the top one.

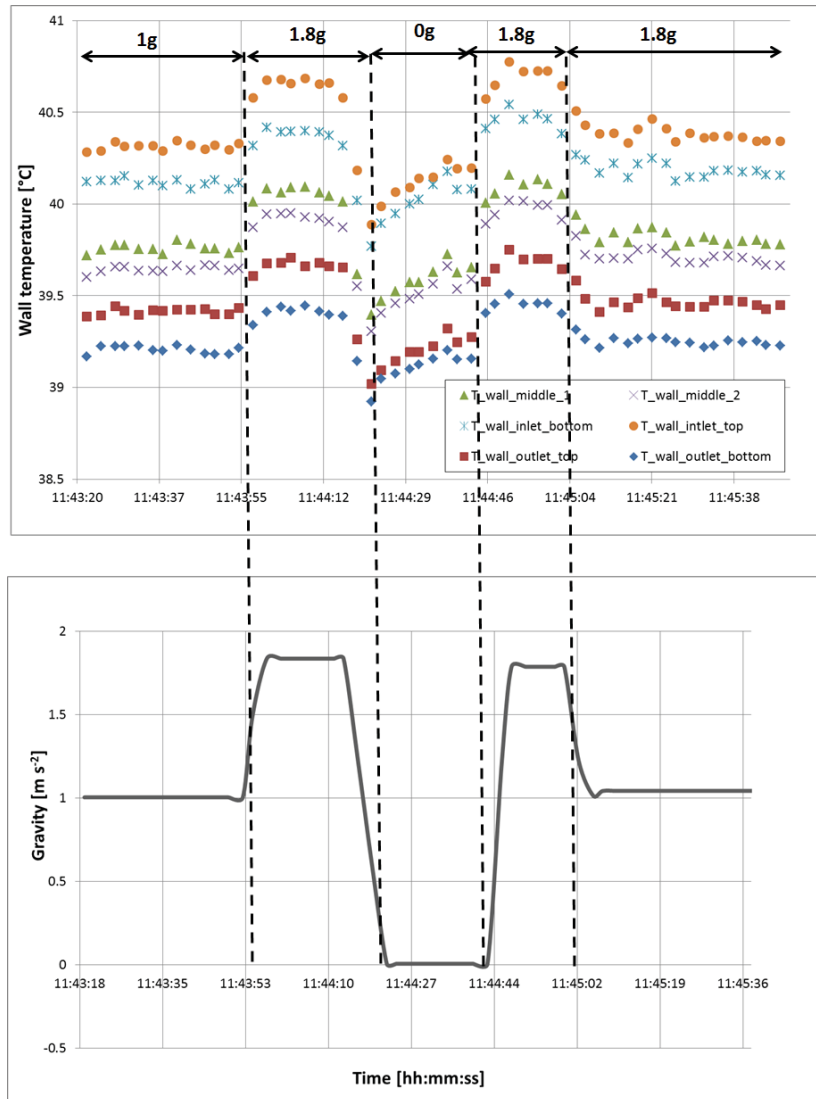


Figure III.30: Evolution of the wall temperatures in the third sub-sector (immediately upstream the glass tube) during parabolic flight at three different positions for  $G=70 \text{ kg}\cdot\text{m}^{-2}\cdot\text{s}^{-1}$ .

### III.3.5 Film thickness measurement analysis

#### III.3.5.1 Ray tracing method and calibration curve

The heat transfer coefficient and film thickness are correlated and the knowledge of the film thickness is an important parameter to validate models. However the measurement of this parameter is so difficult that no experimental data exist for condensation. This investigation is the first step to measure simultaneously the heat transfer coefficient and film thickness received from video acquisition by Camera Optronis CL600x2. The

consecutive images have been captured at frequency of 200 Hz or 1500 Hz.

The dimensions of borosilicate tube are 3.4 mm inner diameter and 6 mm outer diameter. The fluid used is HFE-7000. The parabolas chosen for heat transfer coefficient analysis are collected simultaneously with the camera in the close view configuration. The focal length of the camera lens is 100 mm with an aperture of 25 mm. These parameters are important and must be taken into account into the ray tracing propagation modeling detailed hereafter

First, some images sequences are acquired from the video recordings. The seen film thickness can be detected, but to convert this apparent film thickness to the real one, it is necessary to apply a correction due to the distortion induced by tube curvature. In literature, different methods [75], [76] are developed for film thickness measurement to analyze the flow distribution. Here a ray tracing optical method [56] is used to determine the calibration curve and also the minimum film thickness that can be measured. Figure III.31 shows the schema of optical system that has been simulated.

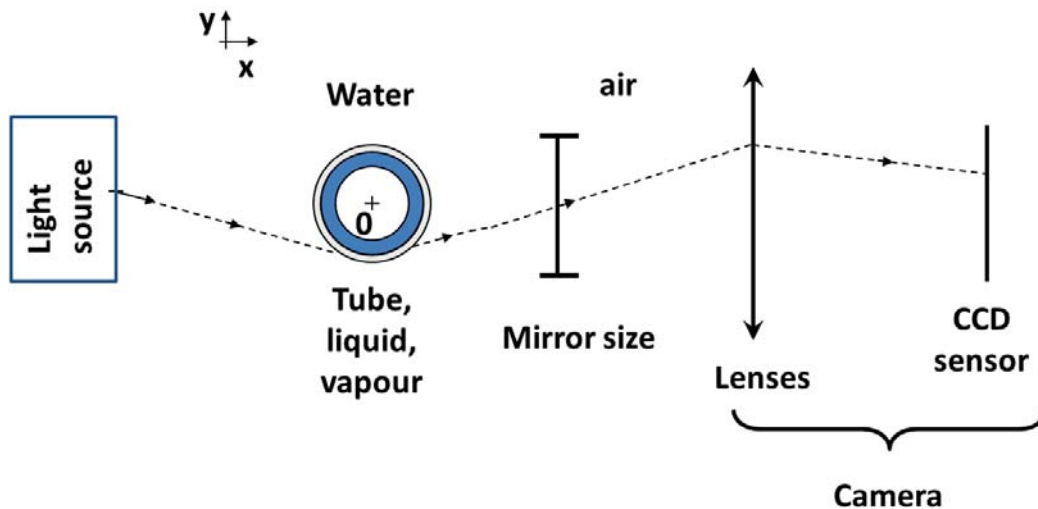


Figure III.31: The optical configuration employed for ray tracing simulation

The optical modeling developed considers a two dimensional pattern. The light source used is considered as a parallel light source. The film thickness is considered to remain at inner tube with a cylindrical shape (we will see later that this assumption is not so strong). The vapor is in the core of the channel. All the condenser's dimensions and camera characteristics are well known. The refractive index of the working fluid HFE-7000 (for both vapor and liquid), and the one of the pipe material are taken into account. The collimated light source is represented by 30 000 uniform rays dis-

tributed over the whole height of the tube. The ray number can be increased to have more accuracy in local analysis, especially for thin film thickness. The ray propagation from the light source to the receiver of the camera follows the geometric optical theory (Descartes laws). At the interface of two different environments, the ray trajectory is broken down into a successive points between two straight light propagations by considering the reflective index is homogenous in each medium. Fig.III.32 presents the ray propagation to determine the path of the light rays from parallel light source to receiver of the camera.

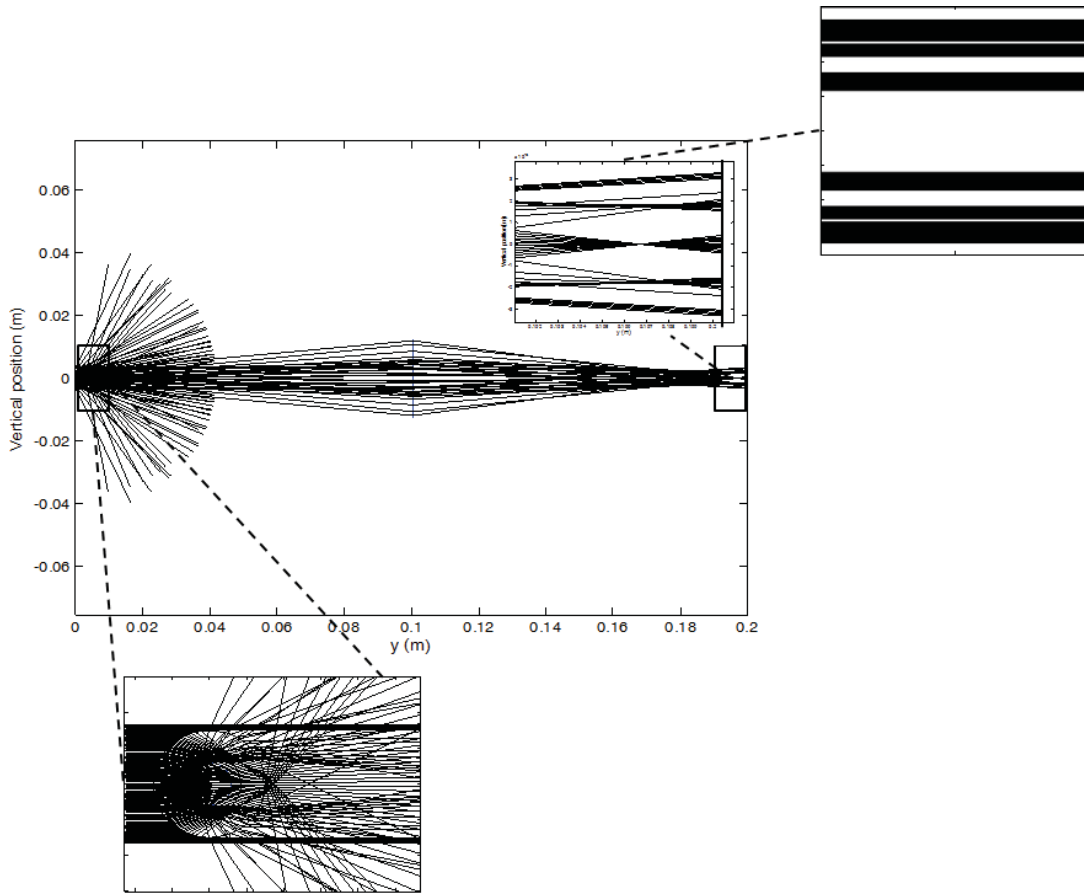


Figure III.32: Ray propagation from parallel light source to the camera receiver and reconstructed image on the camera.

The aim of this investigation is to determine the impact of the curvature of the tube on the liquid film thickness determination. When the light rays exit the external tube wall, the one which can reach the camera lens are extended. The impact point with this lens is determined and Gauss approximation theory for thin lens is used to determine the new ray direction at lens exit. Finally, the ray trajectory reach the CCD

receiver. The number of rays received by CDD sensor is then converted to grey level. The calculation is repeated for all the source's light rays, for all the geometric shapes (various film thicknesses) and for different position (screen positions).

Before the reconstruction of image received by the camera at each imposed liquid film thickness, the position of the camera lens has to be fixed in order to have the exact same disposition as in the real case. Also the experimental image obtained by high speed camera when the tube is full of liquid is compared to the reconstructed image calculated by ray tracing method at the same condition to adjust the exact distance. Figures III.33 presents the image obtained in this optical configuration. From the top to the bottom of the image we can observe first in grey color the air at the top of the tube wall. The first border encountered between grey and black part represents the external border of the tube wall. Below a small grey region (i.e line) is produced by a reflection on the internal wall of the light crossing the tube wall. If we remove this light the resulting large black part represents the tube wall thickness modified by the optical distortion induced by the circular shape of the tube. Below this black part, the shadowgraph configuration can lead, depending on the optical configuration, either to a large white part centered on the middle of the tube, corresponding to the liquid medium or like here, to a large white part where two large black bands can be observed. These black bands are induced by aperture limitation of the camera lenses. As the aperture of the objective is always reduced when we are closed to the border of the image the thickness of these black bands increase with the distance from the center of the image. These phenomenon can be easily observed on the experimental image. The aperture of the optical system is here induced by the lenses of the camera but also by the mirror used to reflect the line. The effect of mirror has been studied with a mirror of 29 mm height and placed at 152 mm from the tube and we observed that the mirror reduces the aperture diameter of the receiver. To obtain the exact value of the aperture diameter the comparison between calculated image and observed image when the tube is full of liquid is also used.

It is highlight that only two parameters are used to get the optical properties of the optical system : the diameter of the lens that collects the light and the distance between the tube and the camera. The first one affects the thickness of the black bands present in the so-called "liquid area", the second one changes the position of the internal wall. The fact that the black bands are well positioned, that the small grey line in the tube wall exist and is placed at the exact position, with the same thickness that in the experimental image can not be adjust. Combining these observations with the fact that the values of the two parameters used to adjust the optical configuration are coherent with the experimental optical configuration lead to conclude that the coherence of two images validates the ray tracing method.

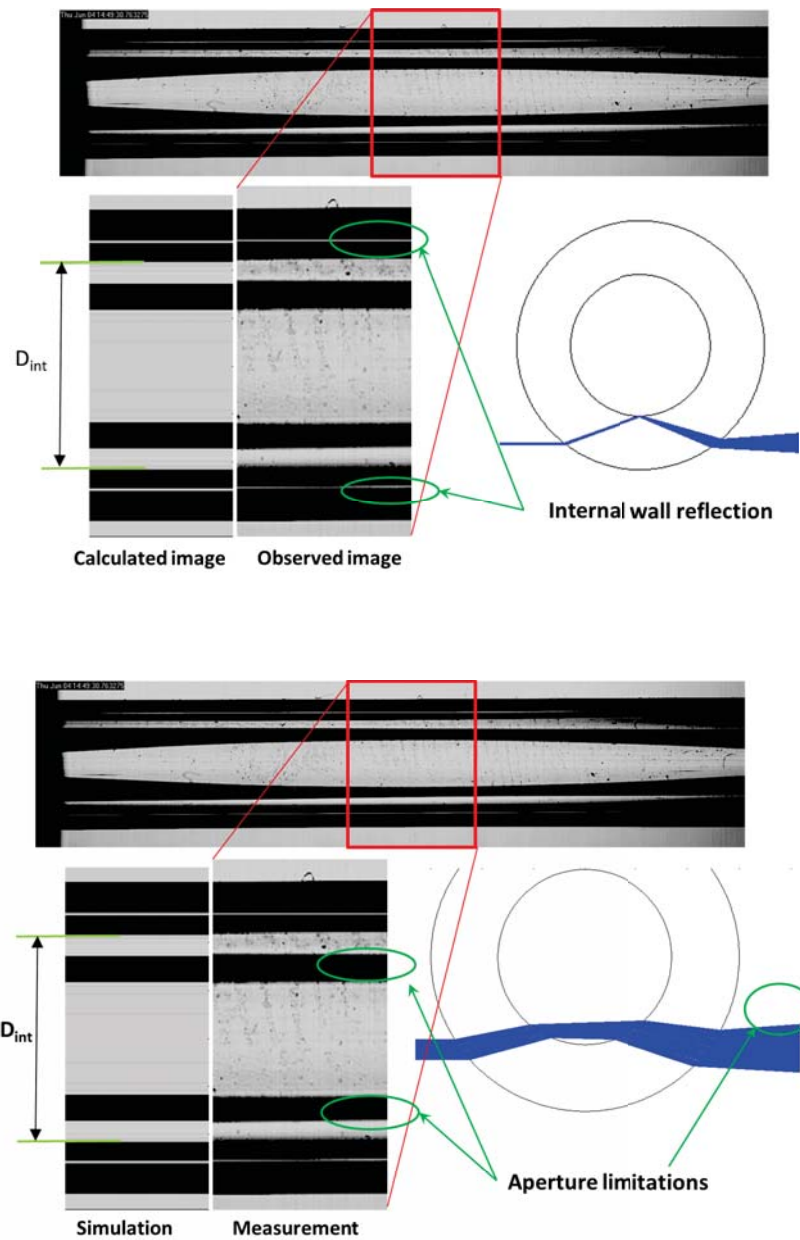


Figure III.33: Photo recorded with the tube full of liquid compared to the simulation one by ray tracing method.

As only the middle part of the image is quite homogeneous, calibration deduced from both optical model and experimental data will concern only this part of the image.

On the other hand, the effect of light source has been investigated by simulating the parallel light source and divergent source of  $1^\circ$ . This value corresponds to the order

of magnitude of the divergence obtained with the telecentric objective. The difference between the two light sources doesn't affect the calibration results.

The final calibration curve is reported in figure III.34. A linear trend between the apparent liquid film thickness on the image and the liquid film thickness inside the tube is obtained. It's also important to note that with a cylindrical tube in shadowgraph configuration the liquid film can not be seen below a threshold value. Regarding the optical configuration used the detection threshold value is here  $106.5 \mu\text{m}$ . So all the liquid film thinner that  $106.5 \mu\text{m}$  can not be seen on the camera.

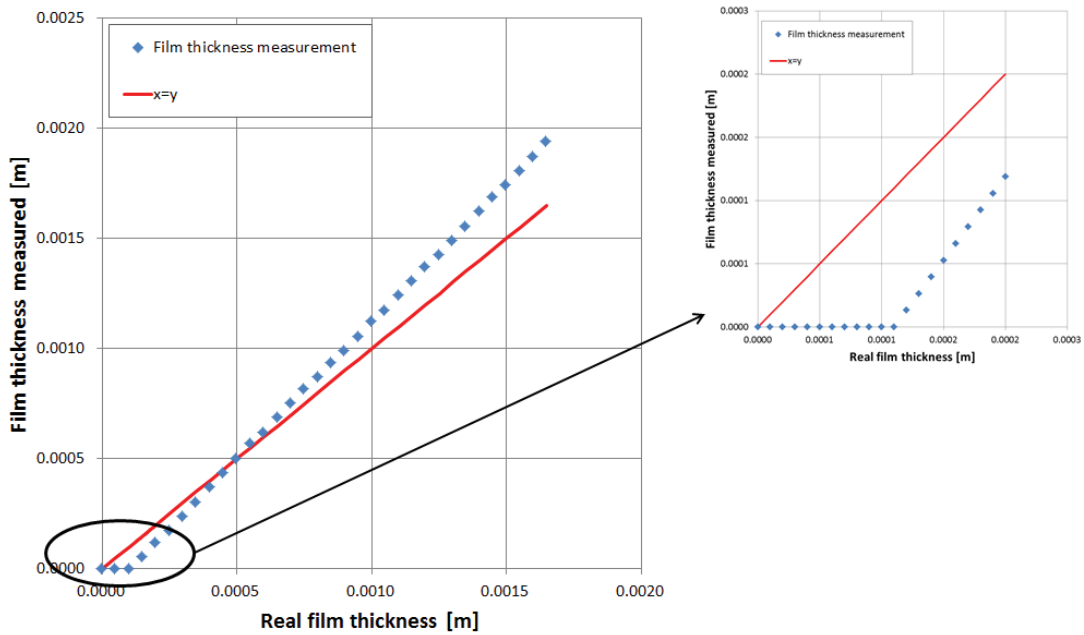


Figure III.34: Calibration curve obtained by the ray tracing method correlating the apparent (or seen) film thickness acquired by the camera to the real film thickness.

Now the calibration curve is obtained, the real liquid film thickness can be deduced from the apparent one determined from recorded video.

### III.3.5.2 Gravity effect on flow regime and film thickness

The flow regime in convective condensation is one of important field to study heat transfer coefficient and pressure drop. Thanks to the film thickness knowledge some convective condensation phenomena could be explained and understood. From the camera recording at frequency 200 or 1500 Hz, some image sequences are acquired. To analyze these images in order to catch the liquid-vapor interface profile and determine apparent film thickness, a post-processing procedure with Matlab is used. Fig. III.35

shows the original image and the image obtained after post processing. This image is obtained at a mass flux of  $100 \text{ kg.m}^{-2}.s^{-1}$  and vapor quality of 0.34. In order to check the proper operation of the algorithm the grey region are colored according to the following convention : liquid region are colored in blue, liquid contours are surrounded in green, the other grey zone are colored in red. By this way, we can see that the liquid film is well detected and apparent liquid film thickness can be easily determined.

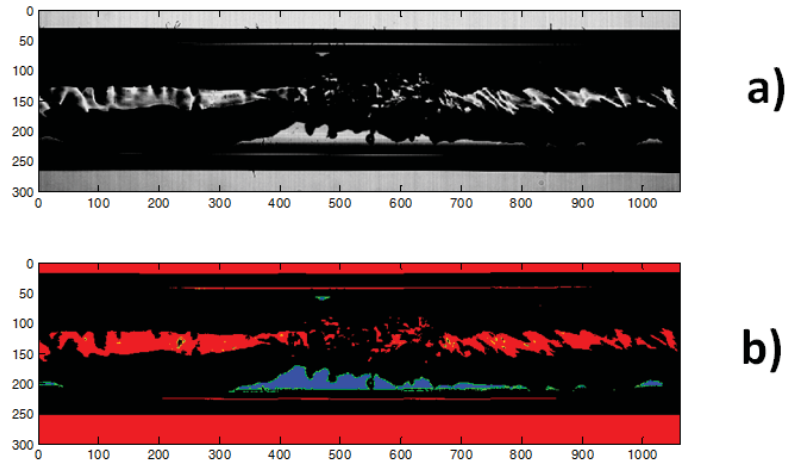


Figure III.35: Original image a) and b) post-processed image using Matlab tool where liquid region is in blue and liquid contours are in green.

On the other hands, from the data reduction presented previously by selecting the stable parabolas employed for heat transfer coefficient analysis we can create a table summarizing the conditions reach by HFE-7000 when it flows inside the adiabatic glass tube :

Vapor quality reported in this table is the vapor quality at the outlet of the third sub-section (the one installed immediately upstream of the glass window). The heat transfer coefficient reduction reported in this table is the reduction average in the heat transfer coefficient in this sub-section.

From these data it appears roughly that the heat transfer coefficient is reduced during microgravity from 3% to 13% depending on the mass velocity and vapor quality. At low mass velocity and low vapor quality, the effect of microgravity on heat transfer coefficient is more significant than at high mass velocity and high vapor quality; these result are in agreement with other research ([35], [47]).

To explain this phenomenon, a statistic analysis of liquid film is done for the same parabolas chosen for heat transfer coefficient analysis. Firstly, the flow regime obtained

$G [kg.m^{-2}.s^{-1}]$	$x_{1g} [-]$	$x_{\mu g} [-]$	% HTC reduction due to $\mu g$
170	0.64	0.64	0.67
150	0.53	0.53	3.57
130	0.47	0.47	8.22
100	0.34	0.34	13.92
70	0.24	0.30	10.79
70	0.32	0.34	15.21

Table III.14: Two phase condition inside adiabatic glass tube.

is most annular wavy, even if sometimes there is liquid film appearing on the bottom corresponding to the transition between wavy annular and stratified flow (especially at low mass velocities).

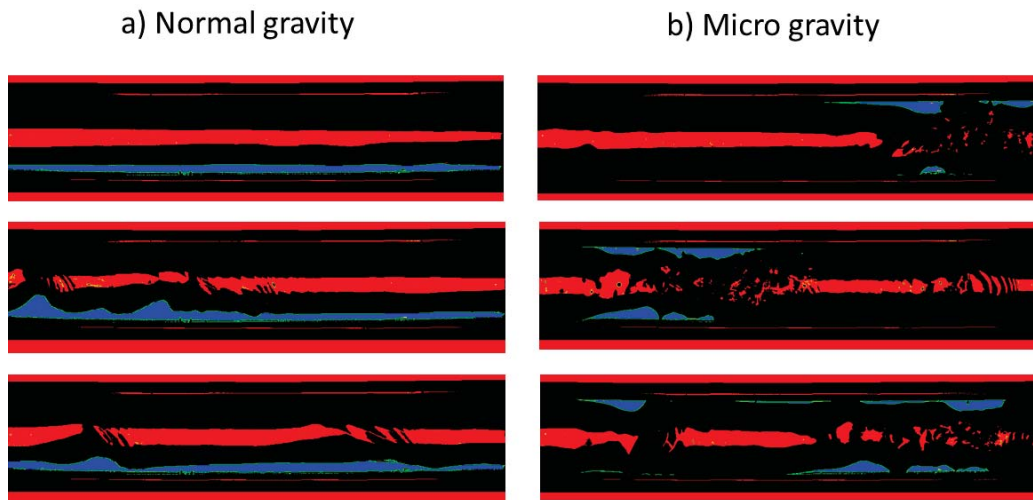


Figure III.36: Flow regimes obtained in a) Normal gravity and b) Microgravity at mass velocity of  $70 kg.m^{-2}.s^{-1}$  and vapor quality of 0.24.

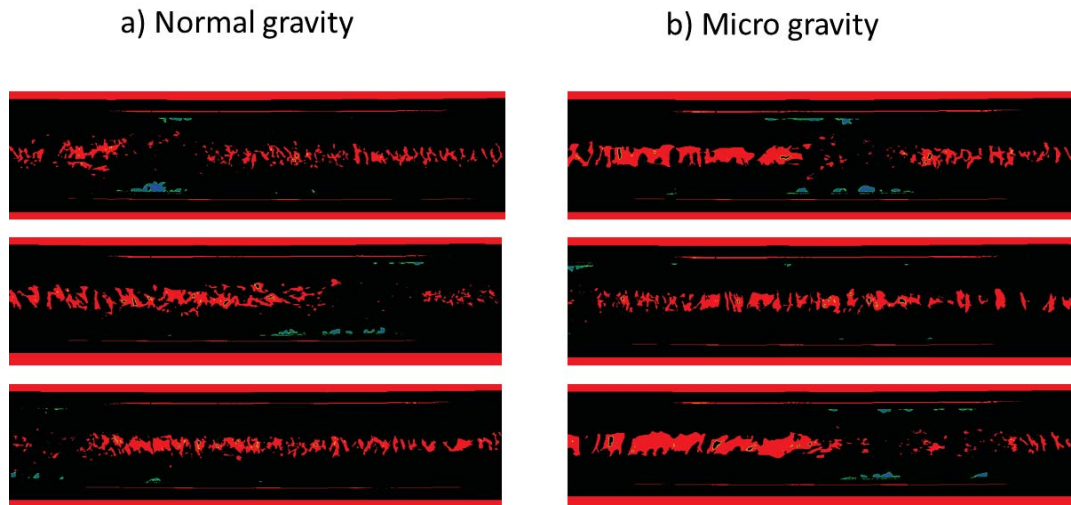


Figure III.37: Flow regimes obtained at a) Normal gravity and b) Microgravity at mass velocity of  $170 \text{ kg.m}^{-2}.\text{s}^{-1}$  and vapor quality of 0.64.

Figures III.36 and III.37 show the time evolution of liquid film thickness (i.e the wave height profile) at the middle of the images during normal gravity for mass velocity of  $70 \text{ kg.m}^{-2}.\text{s}^{-1}$  and vapor quality of 0.24 and at mass velocity of  $170 \text{ kg.m}^{-2}.\text{s}^{-1}$  with a vapor quality of 0.64. The same remark as for the previous section about flow pattern evolution can be done. However, to have a quantitative comparison, the variation of film thickness on the top and bottom during normal and micro-gravity is explored.

After post processing, the sequence of images is converted to apparent film thickness in pixel. When the detected zone is done, the film thickness can be calculated as the difference between two boundaries of liquid shape at the same position. The figure III.38 shows an example of the apparent film thickness profile.

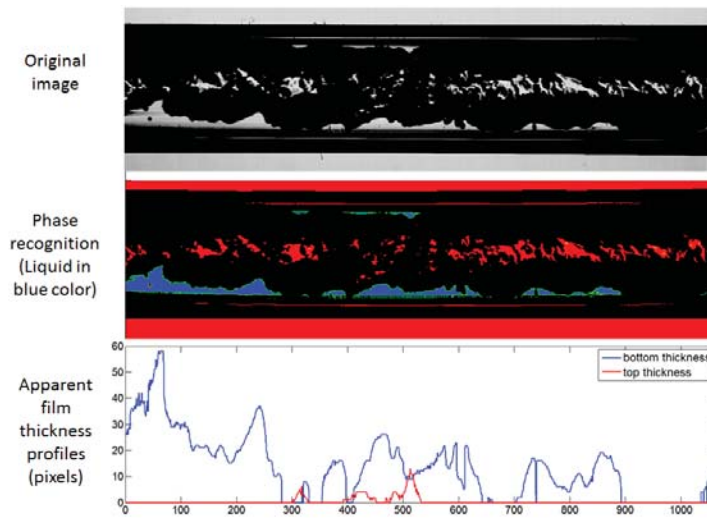


Figure III.38: Example of image processing to obtain the apparent film thickness variation (in pixel) in normal gravity.

While the apparent film thickness in pixel is obtained the actual film thickness in metric is obtain knowing the magnification coefficient ( $25.862\mu m/pixel$ ). This coefficient can be easily evaluated knowing the distance between the two external tube walls and the real external tube diameter. As mention in last section thanks to the calibration curve, the real liquid film thickness (inside the tube) can be determined. A question remains when no liquid film can be detected by the camera. Indeed, according to the calibration curve in this situation, the liquid film thickness is below the threshold value ( $106\mu m$ ). In order to evaluate consequences induced by this lack of information, two extreme ways are considered to convert the apparent film thickness to the real one. In one case each time this situation is encountered the real film thickness is chosen equal to the threshold value, in the other case, each time no liquid film can be detected the real liquid film thickness is chosen equal to zero. Figure III.39 presents the real film thickness with these two methods for a mass velocity of  $70 kg.m^{-2}.s^{-1}$  and a vapor quality of 0.24.

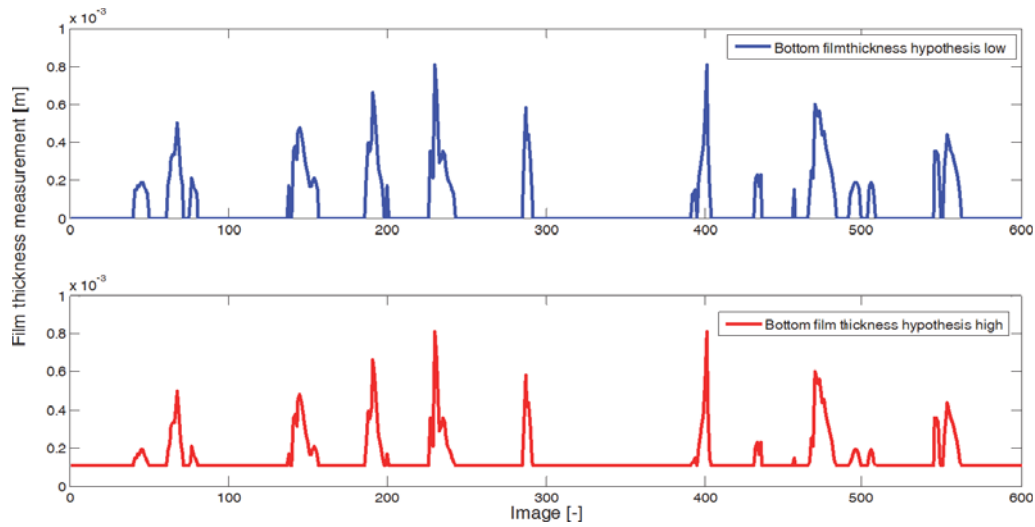


Figure III.39: Profiles of liquid film thickness considering the two extreme values for the non-detectable liquid film thickness in micro gravity condition at  $G=70 \text{ kg}\cdot\text{m}^{-2}\cdot\text{s}^{-1}$  and  $x=0.30$ .

Using these two methods, the average film thicknesses evaluated are  $146.73\mu\text{m}$  and  $63.99\mu\text{m}$ , respectively. We can note that these two extreme values are very different for this flow regime constituted by small waves.

The mean film thickness measurement is compared at the same mass velocity and different vapor quality or at different mass velocity and different vapor quality to explain the evolution of heat transfer coefficient. The figure III.40 shows the evolution of bottom and top film thickness at mass velocity of  $70 \text{ kg}\cdot\text{m}^{-2}\cdot\text{s}^{-1}$  at different vapor quality.

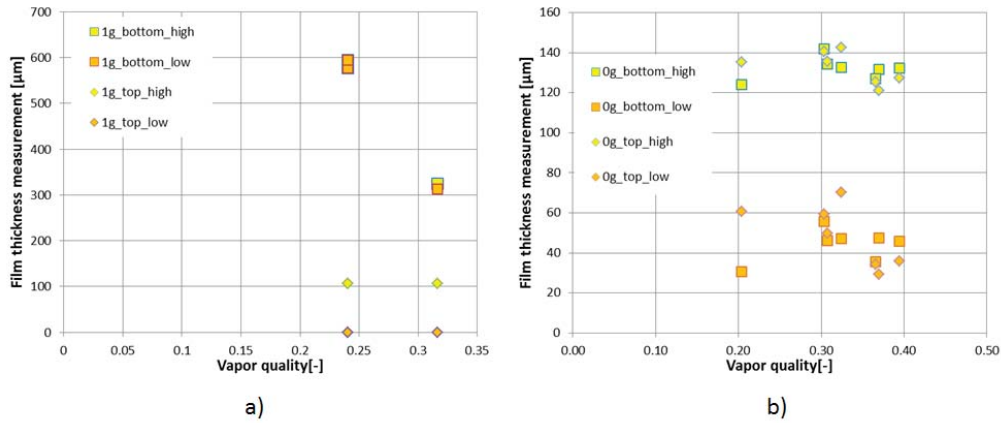


Figure III.40: Top and bottom film thicknesses evolution for different vapor qualities and at mass velocity of  $70 \text{ kg}\cdot\text{m}^{-2}\cdot\text{s}^{-1}$  a) In gravity condition and b) In microgravity condition.

From this figure we found that in normal gravity the liquid film thickness on the top is invisible; the bottom film thickness decreases with increasing vapor quality and the two boundaries of bottom film thickness are very close because the number of event with invisible liquid film is very small. So the mean value is not affected by the assumption done about these rare events. In microgravity condition, the two extreme values of the film thickness (using high and low values for invisible liquid film) at the top and bottom are very close because at microgravity the film is more axisymmetric. The in homogeneity of film thickness in this range of vapor quality at this mass velocity in microgravity is small and only about 8% maximum in film thickness measurement. In the other hands, can note that the two extreme values of the film thickness should be very different in the case of small liquid waves.

Otherwise, the whole film thickness evolution at different vapor qualities and different mass velocities is exploited. Figure III.41 shows the film thickness's evolution for different mass velocity ranging from 70 to 170 and vapor quality ranging from 0.2 to 0.6.

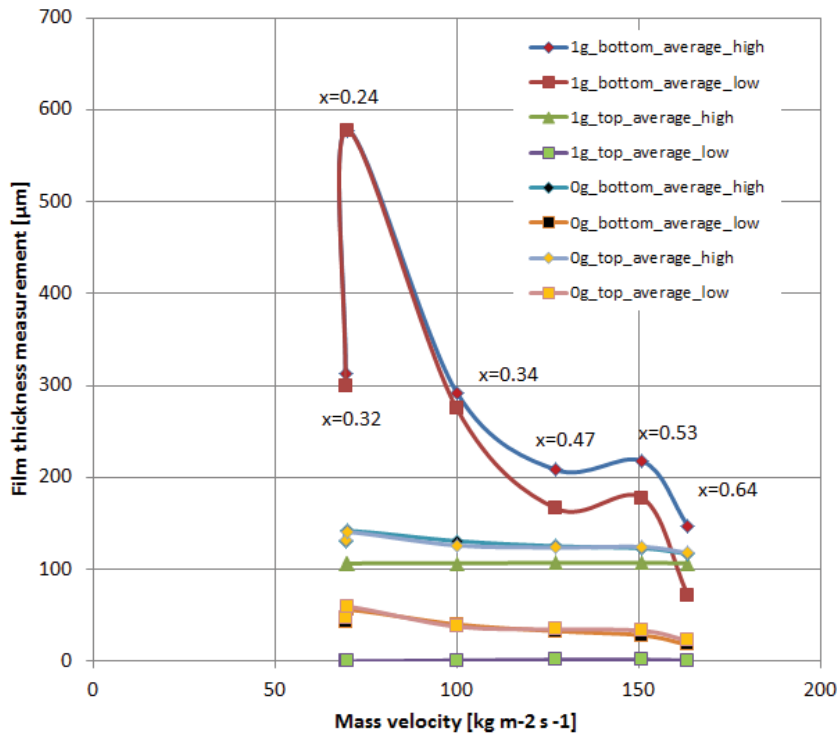


Figure III.41: Evolution of film thickness at the bottom and on the top in normal gravity and microgravity for different mass velocities and vapor qualities.

Firstly, in microgravity an increase of the mass velocity leads to increase of the vapor quality in glass tube while the film thickness decreases. Secondary, in normal gravity, the film thickness at the top is always smaller than at the bottom and the difference is quite high except for  $G=170 \text{ kg.m}^{-2}.\text{s}^{-1}$  where the top and bottom boundaries have a common part. It's also interesting to note that, as observed in the previous figure for  $G = 70 \text{ kg.m}^{-2}.\text{s}^{-1}$  the film thickness at the bottom of the tube in normal gravity grows from  $300 \mu\text{m}$  to  $580 \mu\text{m}$  when the vapor quality change respectively from 0.32 to 0.24 whereas in microgravity the evolutions of the film thickness are very small for the same conditions.

This figure confirms the evolution observed on heat transfer coefficient when microgravity period starts. At low mass velocity and low vapor quality the film thickness changes a lot during the transition between normal and micro gravity and normal gravity from invisible film thickness on the top and high film thickness on the bottom to annular regime with axisymmetric film; at higher mass velocity and higher vapor quality, changes induced by modification of the gravity level are strongly attenuated.

In other words, the film thickness is an important parameter for heat transfer coef-

ficient, it is why the heat transfer coefficient at low mass velocity and low vapor quality is more sensible to gravity than at high mass velocity and high vapor quality.

To highlight the correlation between heat transfer coefficient and film thickness measurement, the figure below presents the film thickness as a function of the heat transfer coefficient:

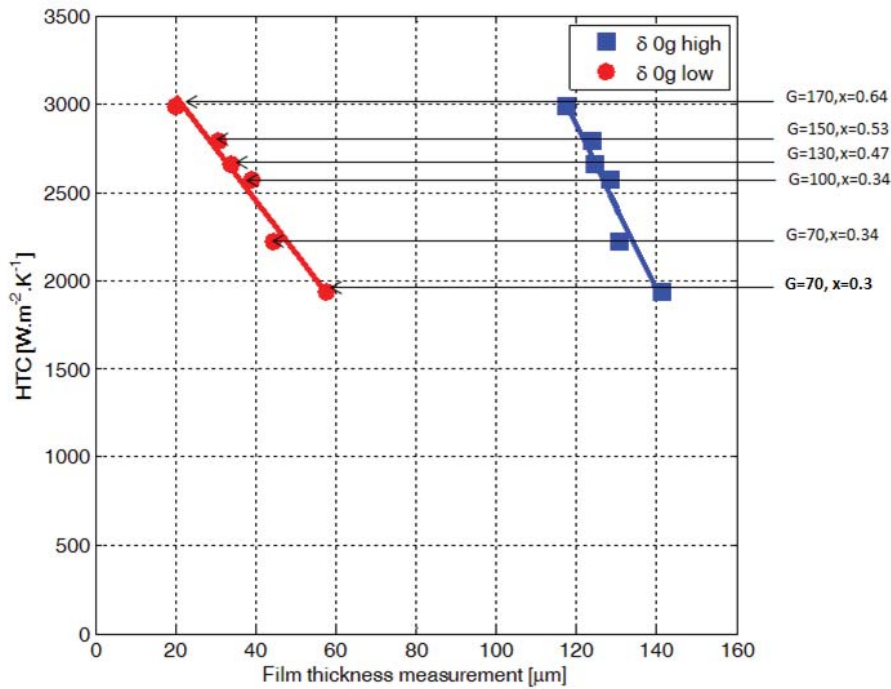


Figure III.42: Film thickness as a function of heat transfer coefficient for different mass velocity in microgravity condition with two assumptions about invisible film thickness: For the "low" hypothesis when the film thickness is not visible, its value is set to 0. For the "high" hypothesis the thickness of invisible film is set to 106.5  $\mu m$  corresponding to the minimum value that can be detected.

We found that the extreme values of these film thicknesses are a function of heat transfer coefficient at different mass velocity and vapor quality. It confirms the correlation between the film thickness measurement and heat transfer coefficient. However the real film thickness is difficult to evaluate in this case where the waves height are small in comparison to the value of detection threshold. It is necessary to improve the film thickness measurement method. A white light interferometer which can detect liquid film thickness between 0.5  $\mu m$  and 160  $\mu m$  has been used to complete data for real film thickness measurement. Unfortunately the available integration time (0.5  $\mu s$ )

was too low comparing to the dynamic variation of liquid film thickness to catch their value. As it would be detailed in the next chapter if the film thickness variation is too high during the integration time, the interferences will overlap and cancel each other out. Improvement of this integration time is planed for the next measurements presented in the following chapter.

At low mass velocity, Nusselt number is usually proposed to be equal to 1. Assuming this hypothesis a mean equivalent liquid film thickness can be calculated from the average heat transfer coefficient measured (at the third sector that is upstream of glass tube):

$$\delta_{equiv} = \frac{D_{in}}{2} (1 - \exp(-2\lambda_L / (h_{meas} D_{in}))) \tag{III.3.5.1}$$

The result is presented in the figure hereafter:

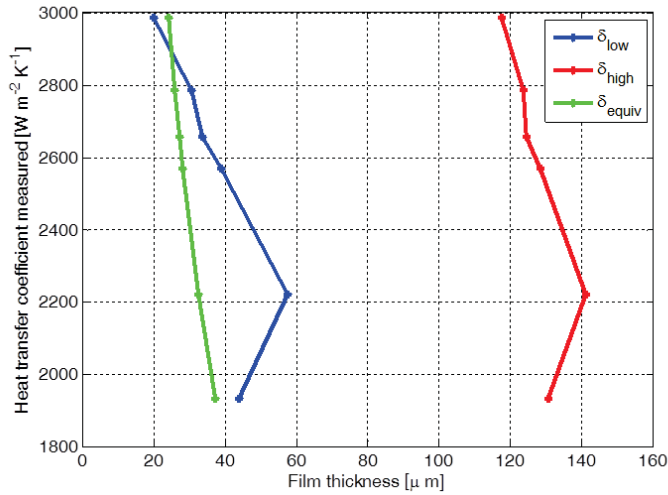


Figure III.43: Heat transfer coefficient as a function of the measured average film thickness or the calculated film thickness

We can note that for the highest heat transfer coefficient (corresponding to the highest mass velocity when the waves are quite small), the average film thickness is in between the two boundary curves. For lower heat transfer coefficients (and thus lower mass velocities, involving greater wave amplitudes), the average film thickness is smaller than the thickness calculated assuming the low hypothesis. This observation can be explained by the demonstration below.

When the film thickness is thin compared to the internal diameter, the equivalent film thickness can be calculated as:

$$\delta_{equiv} = \frac{\lambda}{h_{meas}} \quad (III.3.5.2)$$

Where  $h_{meas}$  is deduced from the equation:

$$\Phi = h_{meas}S(T_w - T_{sat}) \quad (III.3.5.3)$$

With  $\Phi$  the heat power is deduced from heat balance in secondary fluid in the third sector.

Therefore:

$$\Phi = \frac{\lambda}{\delta_{equiv}}S(T_w - T_{sat}) \quad (III.3.5.4)$$

In order to compare  $\delta_{equiv}$  to the mean value of the measured film thickness, an attempt to calculate heat power deduced from the dynamics of film is proposed. Assuming a constant internal wall temperature, the heat power is linked to the instantaneous heat transfer coefficient by:

$$\Phi = \frac{1}{T} \int_0^T \int_0^L h_{in}(t, z)(T_w - T_{sat})P_{in}dzdt \quad (III.3.5.5)$$

Where  $L, P_{in}$  are the length and perimeter of the third sector.  
with  $\langle h_{in}(t) \rangle = \frac{1}{L} \int_0^L h_{in}(t, z)dz$

$$\Phi = \frac{1}{T} \int_0^T \langle h_{in}(t) \rangle (T_w - T_{sat})S_{in}dt \quad (III.3.5.6)$$

Therefore:

$$\Phi = \langle h_{in} \rangle (T_w - T_{sat})S_{in} \quad (III.3.5.7)$$

Assuming the exchange is purely conductive in the liquid film, the local heat transfer is linked to the film thickness by:

$$h(z, t) = \frac{\lambda}{\delta(z, t)} \quad (III.3.5.8)$$

Finally:

$$\Phi = \lambda \left\langle \frac{1}{\delta} \right\rangle S (T_w - T_{sat}) \quad (III.3.5.9)$$

From equation III.3.5.9 and III.3.5.4 we deduce:

$$\delta_{equiv} = \frac{1}{\left\langle \frac{1}{\delta} \right\rangle} \quad (III.3.5.10)$$

Therefore  $\delta_{equiv}$  is different from  $\langle \delta \rangle$ .

For example the figure III.44 shows that in some situations when  $\delta$  is small, the  $\frac{1}{\delta}$  is greater than  $\frac{1}{\delta}$  even with low hypothesis. Indeed the figure presents that the equivalent film thickness can be smaller than the mean film thickness at low hypothesis, which is compatible with result obtained in the figure III.43.

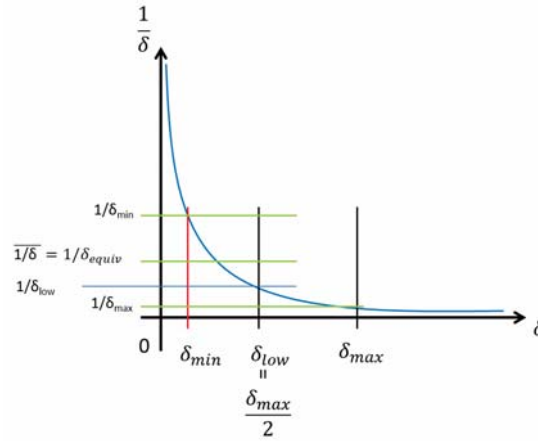


Figure III.44: Illustration of the difference between  $\overline{\frac{1}{\delta}}$  and  $\frac{1}{\delta}$  according to the value of  $\delta$

Therefore, it is important to note that the knowledge of the mean film thickness is not the relevant information to obtain the heat transfer coefficient. Temporal evolution of the film thickness is essential and the dynamic of waves is a key-point to be able to predict the heat transfer.

### III.4 Conclusion

In this chapter, the condensation test section of 3.4mm in diameter as well as the apparatus dedicated for both experiments on-ground and in parabolic flights were presented. The test section is composed of 2 copper heat exchangers for the heat transfer measurement and an adiabatic glass tube for the two-phase flow visualization in different conditions. For the condensation tests, the investigation has been performed for mass

fluxes from  $70 \text{ kg.m}^{-2}.\text{s}^{-1}$  to  $175 \text{ kg.m}^{-2}.\text{s}^{-1}$ . The flow regime and condensate film thickness were determined using the video acquired with the high speed camera. On the other hands, the heat transfer coefficient was also evaluated thanks to the various sensors implemented in the loop.

- The data reduction for heat transfer coefficient measurement was developed. The evolution of heat transfer coefficient in normal gravity and microgravity has been determined. The same conclusion as Mudawar et al. [12] was found the heat transfer coefficient is reduced during microgravity. On the other hands, at high mass fluxes and high vapor qualities, the effect of gravity on heat transfer coefficient is not significant in comparison to the case of for low mass fluxes and low vapor qualities.
- For low mass velocity and low vapor quality the flow regime changes a lot during micro gravity in comparison to the one in normal gravity. The two phase-flow which is in transition between stratified wavy flow or annular wavy flow with invisible film thickness on the top and high film thickness at the bottom in normal gravity becomes annular and axisymmetric in microgravity. At higher mass velocity and higher vapor quality, the two-phase flow remains always annular. This explains why the heat transfer coefficient changes a lot at low mass velocity and low vapor quality.
- A specific procedure to determine film thickness by ray tracing method was developed. By comparing the images recorded by high speed camera and the one received by simulation of ray tracing in the same condition, the ray tracing method simulation was validated. Therefore the extreme values of the film thickness measurement depending on assumption were found. However the real film thickness is difficult to evaluate in these experimental tests due to its invisibility under a threshold value both at normal and micro gravity conditions.

To finish this chapter, a comparison between the heat transfer coefficient and the two extremal values of the film thickness was presented.

## Chapter IV

# Set-up and measurement protocol on the vertical down stream sapphire test section on-ground

One of the shortcomings of the first test section, used to investigate the effect of gravity on convective condensation described in the previous chapter, is the absence of simultaneous measurements of heat transfer, flow visualization and film thickness along the tube. Therefore this chapter is presenting a method to evaluate the condensation heat transfer coefficient, flow pattern and film thickness of convective condensation inside a vertical sapphire mini-tube. The aim is not only to compare to the results of convective condensation in micro-gravity condition but also to set up a primary step for the conception of new test section that could be used in the next parabolic flight campaign with the mid-term objective of developing measurement techniques that can be used on ISS (International Space Station). So, this investigation aims to produce data and models that will be used for spatial and ground applications.

Sapphire has been chosen as tube's material because of its high thermal conductivity that allows to enhanced radial heat transfer and its transparency that permits the flow visualization. The dimensions of the test section are the same than those used for the parabolic flight test-section campaign with an inner diameter of 3.4 mm and an outer diameter of 6 mm. The working fluid is HFE-7000. Its low saturation pressure at ambient temperature allows working with this transparent material securely. The tube has been installed vertically in order to have an axisymmetric configuration of the liquid-vapor flow as the one obtained at micro-gravity conditions. The one meter length of the tube allows a complete convective condensation for mass velocity lower than  $50 \text{ kg.m}^{-2}.\text{s}^{-1}$ . The secondary fluid is forced air flow.

In this chapter, a detailed description of the experimental apparatus is carried out. Furthermore, the experimental procedure developed for the calibration of the apparatus, and the determination of both external and internal heat transfer coefficients

will be presented. Finally experimental results with simultaneous measurement of film thickness and heat transfer coefficient will be analysed before concluding and highlighting some perspectives about these measurement techniques.

## IV.1 Experimental apparatus

### IV.1.1 Description

The experimental assembly comprises an inlet tank, a controlled temperature chamber at the outlet of this tank (electrical resistance wire), a valve system, a sapphire test section placed vertically, an air-conditioner, a post condenser, a flow meter, an outlet tank to control the outlet temperature and pressure, a pump to return the fluid back to the inlet tank, two thermostatic bathes to control the fluid condition at inlet and outlet and a high speed camera, an infrared camera, an interferometer for recording data. The scheme of the apparatus is reported in figure IV.1

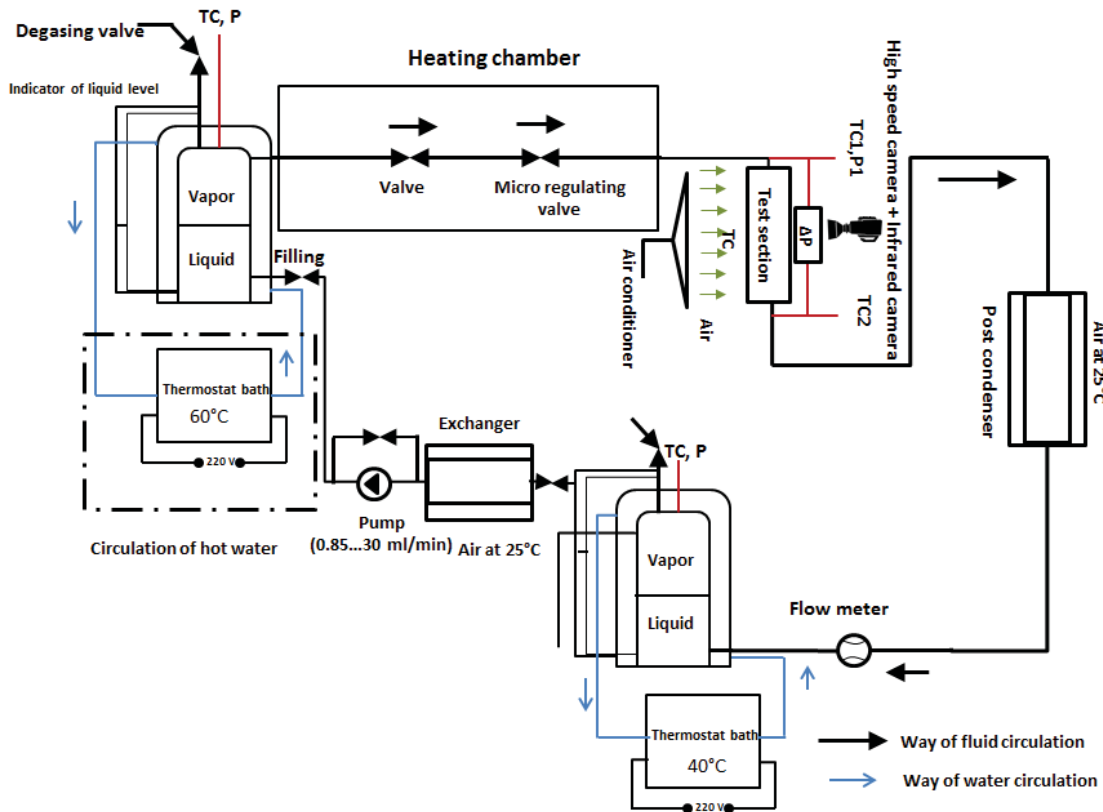


Figure IV.1: Scheme of complete loop test used for this investigation.

The inlet and outlet reservoirs consist of two coaxial cylinders of different diameters. The internal cylinder contains the refrigerant. In the annular cavity between the two cylinders, a circulation of water with a temperature regulated by thermostatic bath is imposed. The Fisher Scientific thermostatic baths used can impose water temperature up to 80°C. In these tanks a two-phase thermal equilibrium of the refrigerant at saturation temperature equal to the set point temperature of the water is assumed. By this way, the water temperature imposes the saturation temperature and so pressure of refrigerant inside the tank. The pressure difference between the inlet and outlet is thus fixed and it imposes the refrigerant mass flow rate. There are three connections with valves in each reservoir containing the refrigerant. The first one located at the lower lateral surface of the reservoir and serves for filling or emptying the refrigerant. The second one, at the top of reservoir, is used for degassing the refrigerant. The third one is installed in upper lateral surface of the reservoir for feeding the refrigerant vapor for the test section.

At the exit of the inlet tank a precision valve is used to fix a precise value of the mass flow rate of refrigerant. Its orifice diameter is 1.42 mm and this valve can create a pressure drop up to 0.8 bar. There is also a stainless steel quarter turn Instrument Plug valve before this valve to close the circulation in order to avoid the break of micro-valve which can occur while applying too much force to close this valve.

To avoid condensation of the vapor coming from inlet reservoir, temperature of the tube between the outlet of the inlet tank and the inlet of the test section is adjusted by electrical heating wires controlled by electrical tension provided by a PID control. This allows setting the state of fluid as super heated vapor at the inlet of test section. Two thermocouples are installed in metallic wall upstream and downstream the regulating valve in order to control the tube temperature. Then the refrigerant at super heated vapor state enter in the vertical test-section. The vapor of working fluid is then condensed with the help of air-conditioner giving a homogeneous air circulation perpendicular to the tube axis. The air velocity is about 3.2 m/s and can be produce at ambient temperature or at about 12-15°C when the air conditioning system is powered on.

At the outlet of test section, the post-condenser made of stainless steel serpentine is placed to condense all the vapor going out of test section. A Coriolis flow meter is installed just downstream to measure the mass flow rate with a precision +/-0.2%. The outlet tank is used to stock the refrigerant before pumping it to inlet tank. The control of the pressure in the inlet and outlet reservoirs allows the refrigerant mass flow rate to be imposed. Picture of the whole test rig is presented in figure IV.2

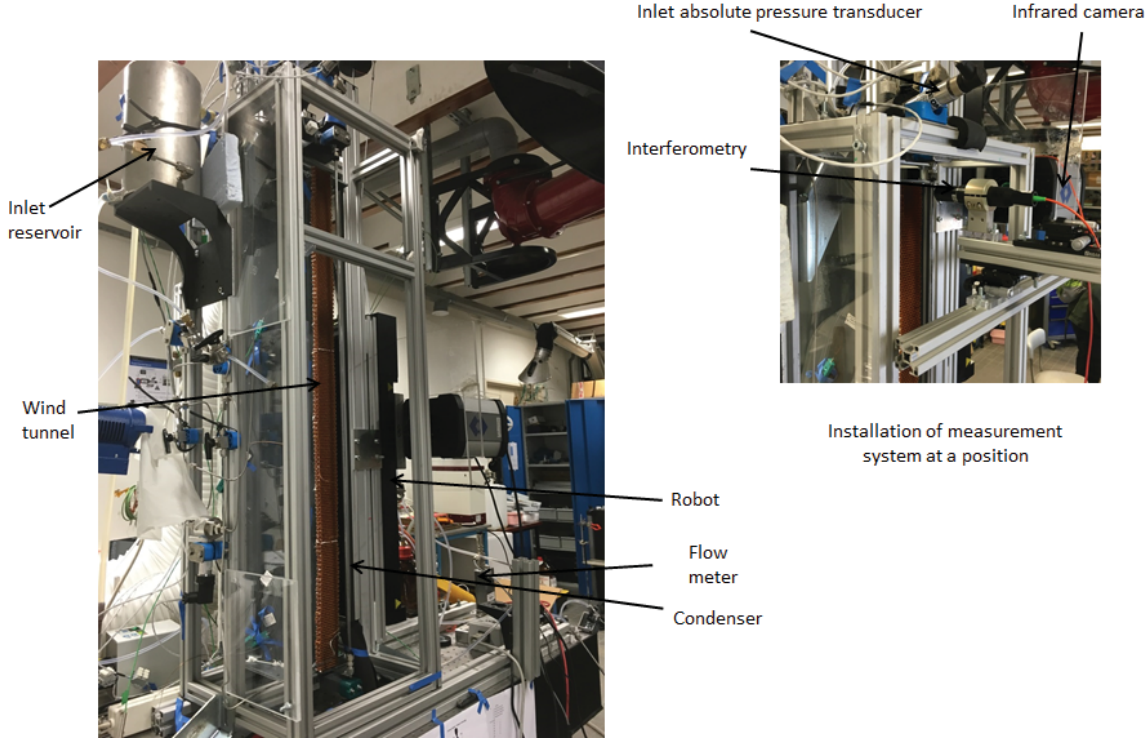


Figure IV.2: The real complete apparatus built at the laboratory.

The secondary fluid is air provided by an air conditioner of type "MCM230B" with a cooling power of 6700W and a mass flow rate of 1170  $m^3/h$ . Figure IV.3 presents the secondary fluid source.



Figure IV.3: The air-conditionner conduct for the secondary fluid

At the exit of the air conditioner, the air transport is provided by two flexible plastic ducts of a maximum length of 1 m and a diameter of 150 mm. At the end of each duct, a specific air distributor has been fabricated with different air deflector, bee lines and cross section reduction to achieve an almost high velocity homogeneous air flow along the sapphire tube. A hot wire anemometer has been employed to measure the air velocity at different tube's position during the distributor conception in order to obtain the best homogeneous air velocity. The result obtained will be presented in the section dedicated to the external air heat exchange calibration (figure 31). Six thermocouples have been also installed close to the tube to have precise air temperature measurement in order to determine external heat transfer coefficient.

In order to scan precisely all the length of the tube with the infrared camera, a motorised translation stage is used. This M-IMS300V Metric Vertical Linear stage offers 300 mm vertical travel length and a precise vertical motion with a typical accuracy of  $0.3 \mu\text{m}$  for loads up to 400 N. As the tube length (1 meter) is longer than the travel distance of the motorised translation stage (300 mm) a specific system has been developed to move the robot (i.e the support of the motorised translation stage). First the robot is placed so that the camera can visualize the inlet of the tube. Then the motorised translation stage is used to move the infrared camera precisely. When the travel distance of the translation stage is reached, a winch attaching this robot is used to move it to another position while the motorised translation stage return to its zero position. As the displacement produced by the winch is not precise, to have a precise relative movement between two winch positions, a reference object is placed in front of the tube before and after the displacement of the robot. This object is used to

remark the old and new positions is a rigid tube. This procedure is repeated twice in order to scan all the tube from the top to the bottom. Moreover, an interferometer has been installed at the same position of infrared camera by an arm fixed and attached to the translation stage. Therefore when the translation stage moves, the interferometer moves simultaneously with the infrared camera. Figure IV.4 presents the photo of the system used to move the infrared camera and interferometer.

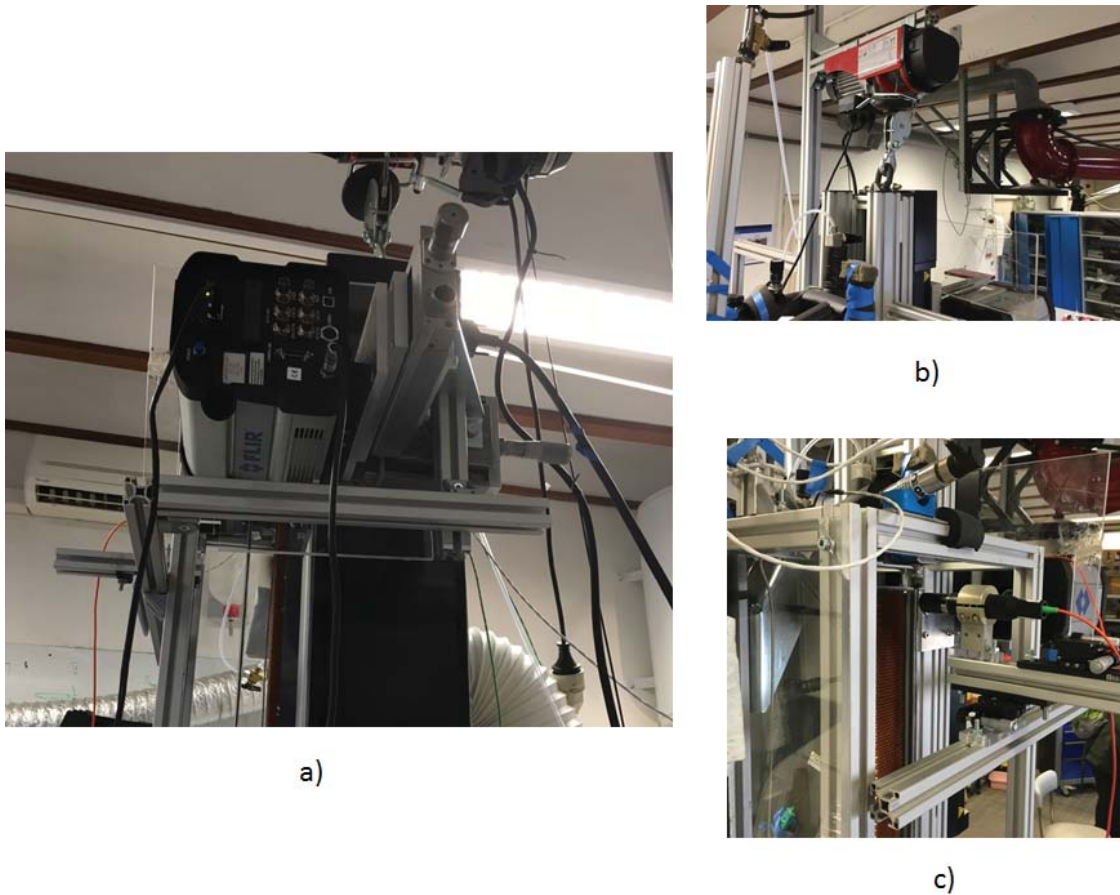


Figure IV.4: The photo presents a) The general view of robot system with the arm to fix the interferometer position b) The winch attaching the robot c) The relative position of interferometer to the infrared camera.

All parts of the loop are placed on an optic table provided by "Newport" manufacturer with threaded hole allowing to fix all components. This table is placed under four optical table support including pneumatic vibration isolators to absorb all vibrations that could come from the ground to the test section. Once all components are connected and placed on the table, the calibration procedure is performed before the experimental measurement and result analysis.

## IV.1.2 Test section and instrumentation

The test section used in the experimental set-up is a one meter length sapphire tube having an internal diameter of 3.4 mm. The length was chosen in order to achieve the complete condensation at mass velocity of  $50 \text{ kg.m}^{-2}.\text{s}^{-1}$ . The choice of sapphire material is motivated by its high thermal conductivity and its transparency. The pressure inside the tube has been tested using pressurized air and can go up to 10 bars. The inside tube roughness is about  $0.8 \mu\text{ m}$  measured by MAP instrument.

The working fluid used is HFE-7000. Its low saturation temperature at ambient pressure avoids any risk of tube break even sapphire is very rigid. On the other hand, the fluid used is the same as fluid used for parabolic flight to have a possible comparison. Moreover the low latent heat of HFE-7000 allows us to work on a wider range of mass velocity.

In the following parts some devices relative to the test section are detailed, most of the measurements are dedicated to the determination of internal heat transfer coefficient and flow pattern map by using thermal camera. Another important point is the way used to obtain the liquid film thickness. The metrology used based on white light interferometer spectrum analysis is then presented. Finally the instrumentation for the rest of the apparatus is detailed.

### IV.1.2.1 Test section

There are two thermocouples installed at the inlet and outlet of the test section. The thermocouples employed is K-type (chromel-alumel) of 0.5 mm diameter wrapped in a stainless steel sheath. All thermocouples were calibrated in the working range from  $20^{\circ}\text{C}$  to  $60^{\circ}\text{C}$  by a reference: platinum probe Pt100. After the calibration the measurement accuracy is  $0.2^{\circ}\text{C}$ . In order to ensure perfect sealing, these thermocouples are connected to the test section using sealing passages. The inlet absolute pressure is measured by a pressure transducer PXM4 of mark Omega ranging from 0 to 3.5 bars with a precision of 18 mbars. This sensor allows the determination of the saturation pressure at the entrance of the test section. Finally a differential pressure transducer of mark Omega ranging from 0 to 0.5 bar is used to determine pressure drop in the test section. To get this value the hydrostatic pressure is taken into account depending on the two phase length. By this way, thermodynamic states of refrigerant at the inlet and outlet of the test section are known.

#### IV.1.2.2 Inlet and outlet reservoir

Thermodynamic conditions in the inlet and outlet reservoirs described above are obtained thanks to a thermocouple installed in the upper part of each reservoir allowing to measure the temperature of the refrigerant. This value is also used to check the coherence with the water temperature circulating inside the annular part of the reservoir while stationary state is achieved. On the other hands, absolute pressure transducers are also installed at the top of each tank (close to the thermocouple) in order to measure refrigerant pressure. The measurement ranges are from 0 to 10 bars with a precision of 40 mbars for the entrance tank and from 0 to 4 bars with a precision of 40 mbars for the outlet tank. These measurements allow checking the purity of refrigerant inside reservoirs.

#### IV.1.2.3 Heating chamber

In order to avoid the condensation of HFE-7000 vapor before entering the test section, the metallic tube between the outlet of the inlet reservoir and the inlet of the condenser was heated by an electrical resistance wire. Therefore to control the heat loss of HFE-7000 vapor between the inlet reservoir and the inlet of the test section, two thermocouples are installed in metallic wall upstream and downstream the regulating valve (preceding the sapphire tube entrance).

#### IV.1.2.4 Air as secondary fluid

Air temperature and velocity are important parameters for heat transfer coefficient determination. The air velocity was checked in order to ensure a homogeneous air velocity distribution along the tube and thus ensure almost homogeneous external heat transfer coefficient. Therefore, six thermocouples are installed along the tube to cover all tube's length. They are placed perpendicularly to the air current and close to the condenser. The anemometer employed to measure air velocity is the AM-4204 model of mark "Fisher Scientific". This device allows to measure the air velocity and air temperature simultaneously. This hot wire anemometer works in the range from 0 to 20  $m.s^{-1}$  with a precision of 0.1  $m.s^{-1}$  and measures temperature from 0 to 50°C with a precision of 0.1°C.

#### IV.1.2.5 Mass flow rate

In order to have mass velocity, the mass flow rate of HFE-7000 is measured after the condensation(liquid state) by a Coriolis flow meter Bronkhorst ranging from 0.03 to 30  $kg.h^{-1}$ . The HFE-7000 exiting the test section is sub-cooled by a tube coil before passing through the flow meter. The precision of this instrument reaches  $\pm 0.2\%$ . This flow meter has a specific block system to avoid any effects of vibration on the measurement. This kind of Coriolis flow meter has been also used during conden-

sation experiments in parabolic flights due to its high precision.

#### **IV.1.2.6 Acquisition system**

During these experiments, Agilent data acquisition unit employed allows to connect and read all data measured by all sensors listed below:

- Fluid temperatures in the two reservoirs (2 thermocouples).
- Wall temperatures upstream and downstream regulating valve. (2 thermocouples)
- Cooling air temperatures at various vertical positions (6 thermocouples).
- Refrigerant temperatures at the inlet and outlet of the test section (2 thermocouples).
- Refrigerant absolute pressure at the inlet of the test section and in the two reservoirs.
- Pressure difference between the inlet and the outlet of the test section.
- Coriolis flow meter.

All these acquisition data are recorded by a data acquisition unit Agilent 34970A with an acquisition card of 16 ports and providing a baud rate of 115200. Thank to Keysight Connection and Agilent BenchLink Data software, all data are visualized and recorded at a frequency of 1/3 Hz.

#### **IV.1.2.7 Thermal camera**

One of the main aims of this experiment is to determine the condensation heat transfer coefficient, so sapphire wall temperature should be measured. A thermal camera has been employed to measure external wall temperature profile. As the sapphire is transparent in the wavelength range (from 3 to  $5\mu m$ ) detected by the cooled InSb sensor of the camera, infrared radiation emitted by a black paint line deposited on the external wall of the tube is used to determine the external wall temperature. The specific procedure used is detailed in a following section. The thermal camera used for these experiments of type "SC6000HS" is provided by Flir system . The characteristics of this instrument are detailed in the section where the results obtained using this thermal camera are presented.

#### IV.1.2.8 Interferometry

As mentioned above, the liquid film thickness is an important parameter that manages heat transfer coefficient. It is correlated in some models to calculate heat transfer coefficient as for example in the models of Cavalini et al [41], Bandhauer [66]...However these correlations are very rarely studied experimentally, therefore one aim of the present work is to measure film thickness to fulfill the state of the art. The interferometer employed is provided by STIL company. The STIL-DUO controller offers two simultaneous measurement technologies: the confocal chromatic and white light spectral interferometry. In our case, the interferometry technique has been chosen. One main reason for this choice holds in the ability of this metrology to detected small liquid film thickness (the minimum thickness detection value is around  $0.5\mu m$ ) and is also driven by the fact that these measurements are not influenced by small vibrations (i.e small variations between the optics and the tube). Such a property can be critical, especially regarding the case of parabolic flight experiments.

To carry out these measurements, the manufacturer offers its own software, which collects data and does the signal analysis in order to determine the thickness value, but also offers the possibility to record raw data. Due to the limitations imposed by the manufacturer apparatus, this second solution has been chosen in order to solve problems encountered with the measurements and then improve the performances of the apparatus. Figure IV.5 shows the complete STIL system.



Figure IV.5: The complete STIL DUO employed to measure liquid film thickness with two pencils: one for confocal mode and one for interferometer mode.

So let us first explain the basis of the white light interferometry measurement used.

Figure IV.6 described the principle of this metrology.

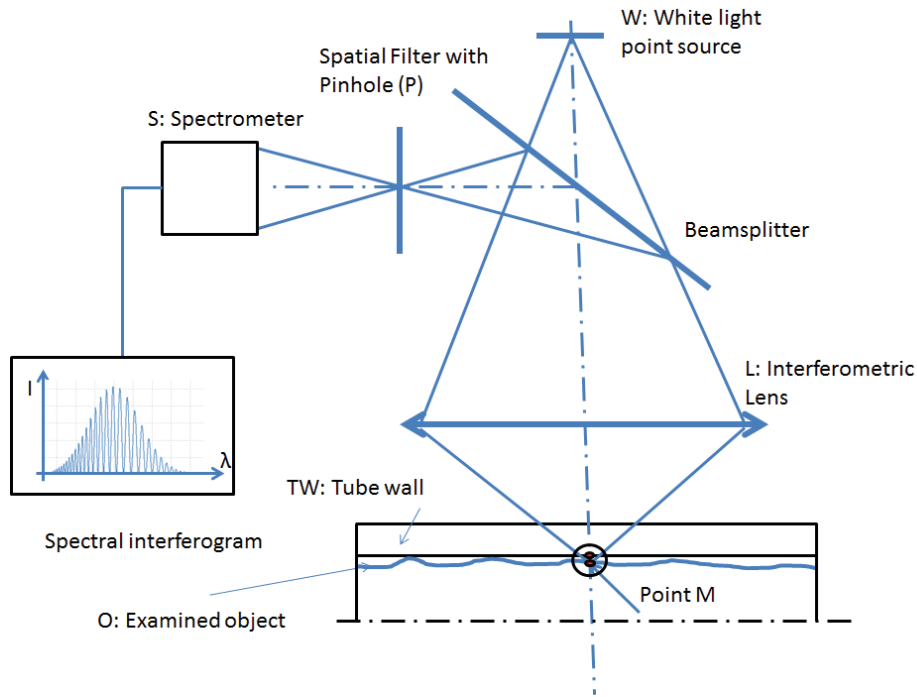


Figure IV.6: Schema illustrating the principle of white light interferometric measurement.

The light coming from white light source W is focus on the M point, thanks to a convergence lens L where the two (optical) interfaces (internal tube wall and liquid-vapor interface in our configuration) are present. Due to optical index variation between the different media, the light reaching each interface is then reflected in the opposite direction and go back to the white light source. At this M point, light reflection induced by these two interfaces looks like light emitted from two coherent sources (nearly ponctual) placed on these interfaces. Thanks to a beam splitter a part of this light coming back to the original source is deviated and focus in the point P instead of W. In order to select at this point only light reflected around the focal point M, a pinhole is placed around the point P to block all the light far from the optical axis. Thanks to this, apparent light sources placed on the interface around the M point appear more ponctual for the spectrometer which collects the light after the pinhole (P). Thus spatial coherence is maintained (or increased) between the two sources created by the two reflections on the interface around M point. White light collected by the spectrometer looks like a light providing from two coherent ponctual sources placed on the optical axis located on the two optical interface around M. As the optical path (distance multiply by the optical index) between the two apparent sources and the collector (i.e spectrometer) are not the same, interferences appear. From the spectrum analysis of the white light

collected, optical path difference can be deduced. Knowing the optical index between the two interfaces around M, the distance between them is then obtained.

So let us now explain the link between the intensity distribution gets by the spectrometer and the optical path difference in order to understand how spectrum analysis manages to determine liquid film thickness. It is well known that intensity collected from two monochromatic coherent sources is given by :

$$I(\lambda) = I_1(\lambda) + I_2(\lambda) + 2\sqrt{I_1(\lambda) \times I_2(\lambda)} \times \cos\left(\frac{2 \times \pi \delta}{\lambda}\right) \quad (\text{IV.1.2.1})$$

where  $I_1$  and  $I_2$  are the intensities from the two sources (here the two reflexions),  $\lambda$  the wavelength of the monochromatic source and  $\delta$  the path difference between the two sources. In our configuration  $\delta = n.2e$  with  $n$  the optical index of the liquid and  $e$  the liquid film thickness. Indeed compared to the light reflected on the first interface encountered around the M point, before coming back, the light reflected on the second interface must cross the liquid film twice (to go and go back). In our configuration the sources are polychromatic but thank to the spectrometer the intensities at each wavelength, (between 400 *nm* and 900 *nm*) can be determined. Actually, each point of the spectrum is an integration of the light intensity on a small bandwidth. For the spectrometer used, the bandwidth (i.e the spectral resolution of the spectrometer) is 0.6  $\mu m$ . If we consider first a configuration where  $\delta$  is small enough to assume that the cosine variation is small when the wavelength variation is equal to 0.6  $\mu m$ , then the discrete value of the spectrum intensity observed is perfectly described by equation IV.1.2.1 evaluated every 0.6  $\mu m$ . Neglecting the variation of the optical index with the wavelength (it's easier to understand the approach but it's no more complicated to take it into account), the path difference  $\delta$  can be considered constant for all the wavelengths collected. In that case, as the intensities variations of  $I_1$  and  $I_2$  change slowly with the wavelength  $\lambda$  compared to the cosine variations, by analysing the period of the cosine with the variable  $\frac{1}{\lambda}$  the path difference can be easily determined. With such an algorithm, the path difference and the liquid thickness can be calculated with nanometric resolution, typically 10nm.

Two limitations impose the maximum value of the path difference (i.e liquid film thickness). The first one is link to the spectrometer resolution. When path difference reach too high value to consider the cosine variation small compared to the wavelength variation corresponding to the resolution of the spetrometer (0.6  $\mu m$ ), as intensity obtained at each point of the spectrum is the result of the cosine integration on this bandwith, the apparent amplitude of the cosine will decrease with increasing the path difference and frequency aliasing occurs (temporal coherence limitation is reached). In the present configuration this limitation appears when the value of  $\delta$  reach 700  $\mu m$  that is to say  $n.e = 350 \mu m$ . The second limitation is related to the optic. As the distance between the two interfaces increases the limitation induced by the depth of field of the lens will make these reflexions less ponctual, which will reduce the spatial

coherence and so decrease the contrast of intensity induced by these interferences. This limitation is the first one encountered with our system. The manufacturer chooses to limit the value of the path difference at  $\delta = 280\mu\text{m}$  or  $n.e = 140\mu\text{m}$ . This limitation is associated to an arbitrary value of the signal-to-noise ratio, but depending of the situation, even with this optic higher path difference values can be detected. In order to not be restricted by this arbitrary value we chose to produce our own signal processing algorithm. Moreover, other limitations appeared in our configuration. The first one is link to the tube geometry. As the focalisation of the light must be done in the internal wall of the tube, the light must cross the asymmetric curvature of the tube in order to detect the distance between this wall and the interface. Indeed by considering a plane passing through the tube axis, the curvature of the external wall is equal to zero (the intersection between the tube and this plane is a straight line) whereas in a plane perpendicular to the tube axis the radius of curvature is the radius of the external wall. This asymmetry leads to defocus the light and reduces spatial coherence property of the optical system. The last additional limitation is induced by the kinetic of the variation of the liquid film thickness. The exposure time of the apparatus (STIL DUO) is nearly equal to the inverse of the acquisition frequency and cannot be adjusted. The maximum acquisition frequency is equal to 2000 Hz so the minimum available exposure time is equal to 0.5 ms. If the cosine variation values in equation IV.1.2.1 are too large (liquid film thickness variation are too fast) the sensor integrates time evolution of the intensity and mean value of cosine reaches zero, so interference cannot be detected. In order to overcome this limitation, the continuous halogene light source proposed by the manufacturer has been changed by a spectroscopic LED light source (Metaphaser model MP-LE1007). This system allows providing to the LED light source a current of 40A; the strobe pulse width is set to 100  $\mu\text{s}$  so the integration time is at least (intensity is not constant during this duration) five times shorter compared to the continuous halogene light source. Nevertheless in order to protect the LED from thermal destruction pulse frequency must be reduced to 100 HZ.

The advantages of this method consists an exceptional nanometric resolution of layer thickness measurement with a minimum measurable thickness about 0.5  $\mu\text{m}$ . However the main limitation is the maximum value of the measurable thickness (around 120  $\mu\text{m}$ ) and the angle of the interface which must be less than 17°.

### IV.1.3 Measurement protocol and calibration procedure

Before carrying out many tests, the apparatus has to be calibrated and many manipulations have been done to obtain a reliable apparatus.

**IV.1.3.1 Verification of vertical position of the tube**

The tube has been placed vertically with a downward flow to obtain the annular configuration as in microgravity condition. The vertical position is checked with a spirit level for the rack containing the tube. The rack is then put on a specific table with 4 air bags under to avoid any disturbance.

**IV.1.3.2 Filling and degassing**

For filling HFE-7000 to the inlet reservoir, a specific system has been built. The image below shows the system used. This system consists in a thermostated bath containing a metallic bottle full of the HFE-7000 in liquid state supplied by 3M and a connection pipe system in PFA (PerFluoroAlkoxy) with some valves. The advantage of the PFA pipe is its transparency which makes it possible to observe the state of fluid HFE-7000 inside the tube.

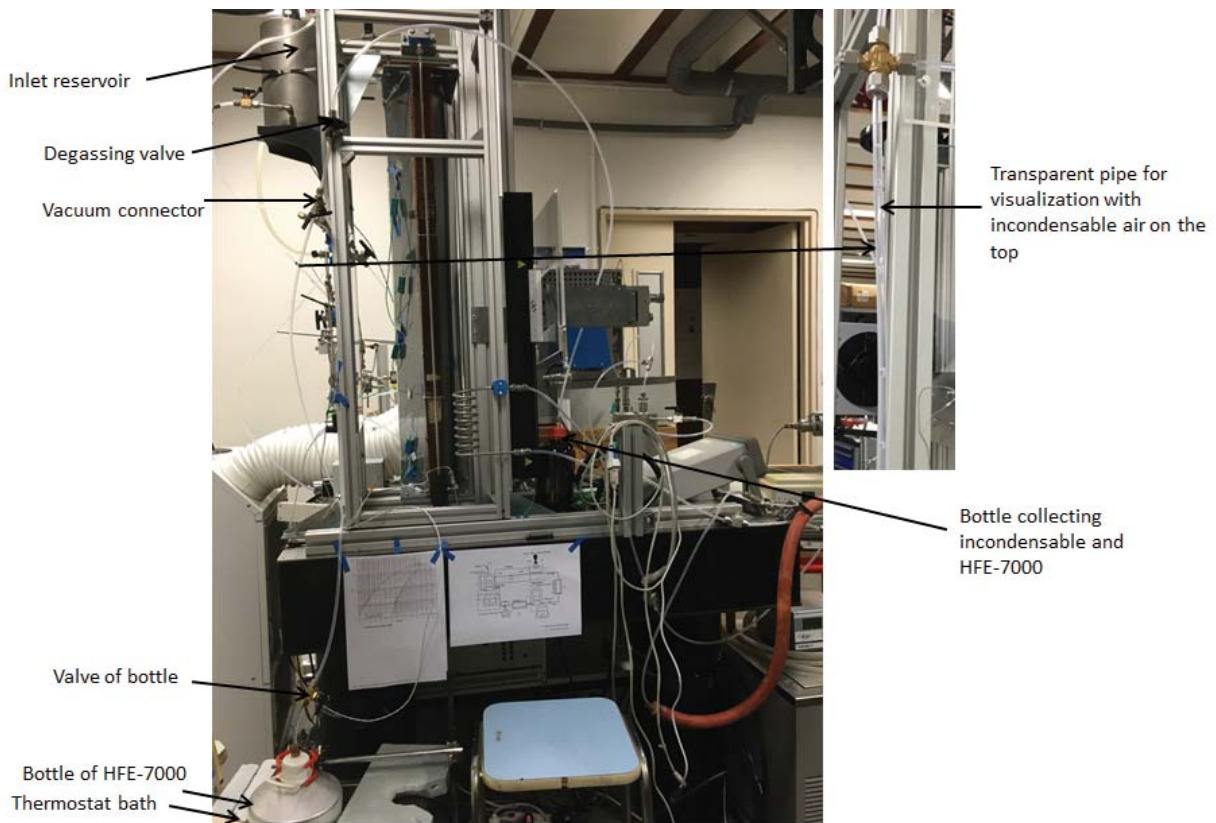


Figure IV.7: The specific system used for filling the refrigerant to inlet reservoir.

Firstly, the thermostat bath where the bottle of refrigerant in liquid state is emerged is regulated at 45°C while the valve on the top of the bottle is closed. The pressure of

HFE-7000 increases. The vapor of HFE-7000 is heavier than air therefore air will be stratified in the top of the long pipe. The non-condensable air is then evacuated by a degassing valve as shown in figure IV.7 through a glass bottle at room temperature were the vacuum was previously made. This procedure is repeated until the long pipe is full of liquid. The inlet reservoir is emptied and drawn by vacuum. The water circulating in annular part of the reservoir is regulated at 20°C during the filling phase. When HFE-7000 and the PFA tube are well degassing (i.e procedure described above has been done), the filling valve between the bottle of refrigerant and the inlet reservoir is opened. Due to the pressure difference between the two containers, the refrigerant passes through the long pipe and arrives to inlet reservoir. A level indicator indicates the level of liquid inside inlet reservoir. Following this indicator we know when the inlet reservoir is full and the filling valve is then disconnected.

HFE-7000 is a new refrigerant. Although its physical and chemical properties are given in many publications ([14],[77]), some differences appear from one publication to the other. For our experiments, the saturation properties are one of the most important parameters thus the method used for degassing allows determining the variation of the saturation pressure with temperature. The calibration procedure is presented below.

#### **IV.1.3.3 Calibration of thermocouple and absolute pressure transducer**

Before carrying out many experiments, calibration of all the instruments has to be done. Firstly all thermocouples have been calibrated by employing a Pt100 probe with an uncertainty of 0.1°C. This calibration instrument has been itself calibrated by National Calibration Instruments after some years of used in order to obtain a good uncertainty and avoid any drift of instrument than can appear over the years. The temperature range is from 10°C to 60°C to cover all working temperatures both for air cooling and the working refrigerant. In order to vary the temperature, all the temperature sensors have been put in holes made inside a copper block that is immersed in the water of a thermostat bath.

In order to avoid drift between the different pressure sensors used, all of them have been connected to the inlet thermostated two-phase reservoirs. Figure IV.8 shows the set up for the calibration. Therefore thanks to this on-site calibration the mean value of the two absolute pressure transducers is used as reference. These two sensors are the sensors P3 employed to measure inlet pressure and P4 which are the newest ones with an uncertainty of 0.018 bar for the range from 0 bars to 3.5 bars. The pressure difference between these two sensors is below 2.7 mbar for all calibration range from 1.2 to 2 bars. The sensor P1 and P2 for the inlet and outlet pressure reservoirs can then be calibrated. Figure IV.9 shows the results obtained. A linear fit was applied to link pressure with voltage. Thanks to this fitting the maximum pressure difference

between pressure reference and sensor P1 and P2 is 0.4 mbar and 3.2 mbar, respectively.

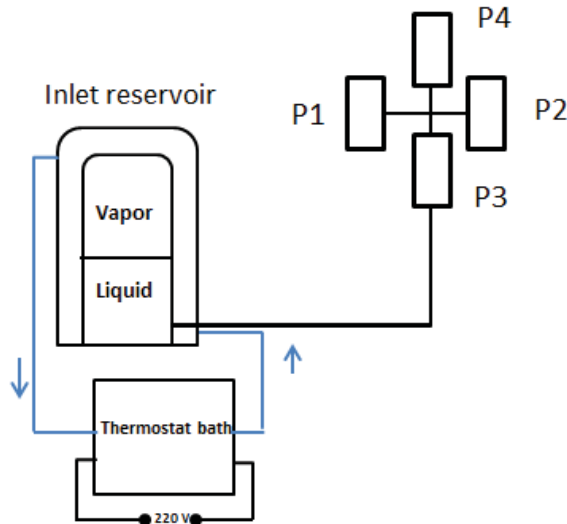


Figure IV.8: Set up used for on-site calibration of two absolute pressure transducers.

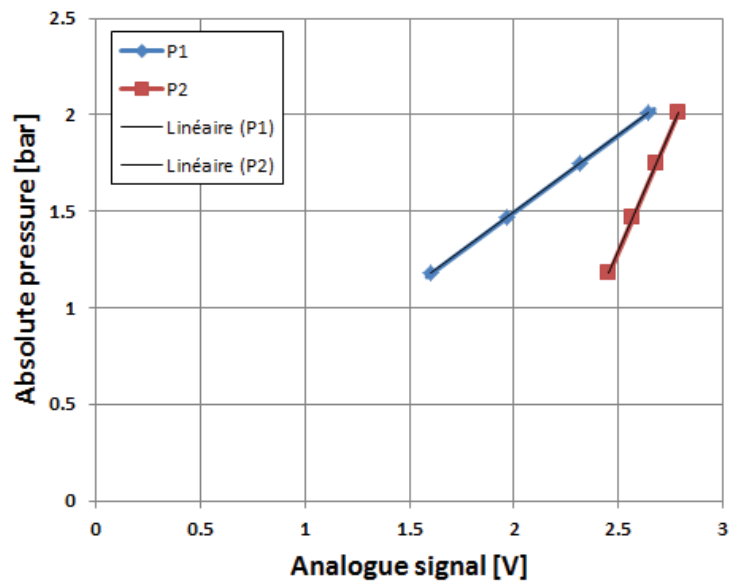


Figure IV.9: Calibration curves of P1 and P2 to convert analogue signal to absolute pressure.

**IV.1.3.4 Verification of degassing procedure and determination of the saturation curve for refrigerant HFE-7000**

After the filling of the inlet reservoir, before carrying out each experiments, an additional check on the purity of the fluid in the inlet and outlet reservoir are done. On the other hands as mentioned in subsection above, many saturation curves of HFE-7000 exist, so it is necessary to find out the saturation curve corresponding to our refrigerant. The inlet and outlet reservoirs include a number of specific instruments such as a degassing system (valve and pipe), a thermocouple, an absolute pressure transducer for refrigerant and a stable water regulator in annular part of reservoir. Figure IV.10 presents the reservoir used.

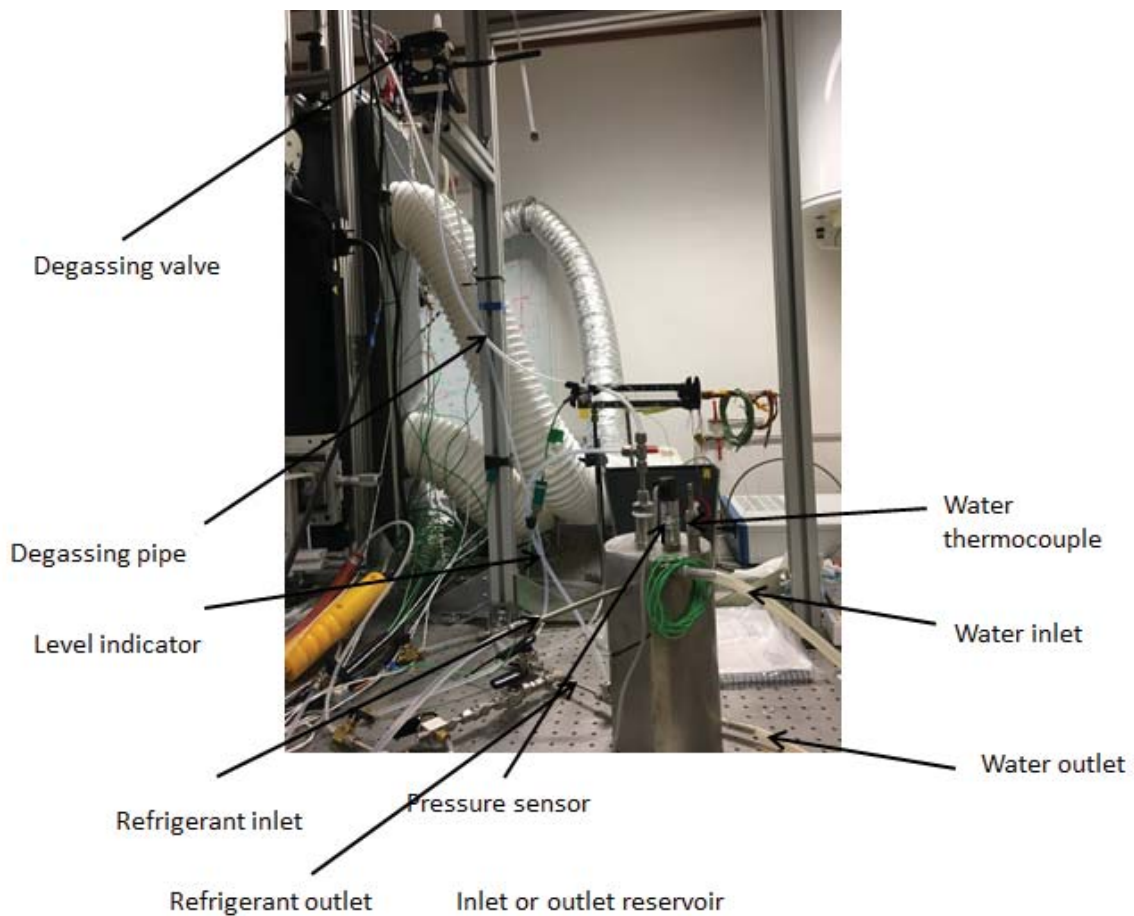


Figure IV.10: The inlet or outlet reservoir employed during tests

Two steps were carried out to check and establish the saturation properties:

- Direct visualization to check the absence of non-condensable gaz: the degassing

valve (on the top) is closed, if the fluid is well degassed, the HFE-7000 between the tank and the valve in the long degassing pipe is liquid state (no air bubble must be seen in this pipe). This degassing procedure is similar to the one used during filling of HFE-7000.

- Check of the saturation properties and establishment of a the saturation curve: When the fluid is well degassed, the degassing procedure has been continued to observe evolution of the temperature and pressure saturation in the inlet reservoir. If when this degassing procedure is done many times a stable value of the temperature and pressure in the inlet reservoir is observed, the saturation state is confirmed. By this way the saturation temperature corresponding to pressure value is measured. This calibration procedure is done at the inlet of the condenser thanks to a thermocouple and an absolute pressure transducer.

The Omega brand employed pressure transducer which was acquired most recently has a precision of 0.018 bar and a range from 0 to 3.5 bars. The thermocouple is a K-type thermocouple with 0.2K uncertainty after calibration. Even if these uncertainties are not negligible, the saturation curve established is more precise than the one we can get from the existing data given by Refprop software or 3M ready file. Indeed between these two reference databases the saturation temperature at the same atmospheric pressure achieves 2K difference. For example we found with this calibration curve that the saturation temperature is about 44.3°C at a pressure of 1.4 bar in comparison to 46°C according to 3M data and 44.35°C from [14] or 43.41°C from Refprop software. From these differences we find that the establishment of a saturation curve is necessary for all experiments in order to obtained a reliable data reduction.

Figure IV.11 shows the new saturation curve and its trend.

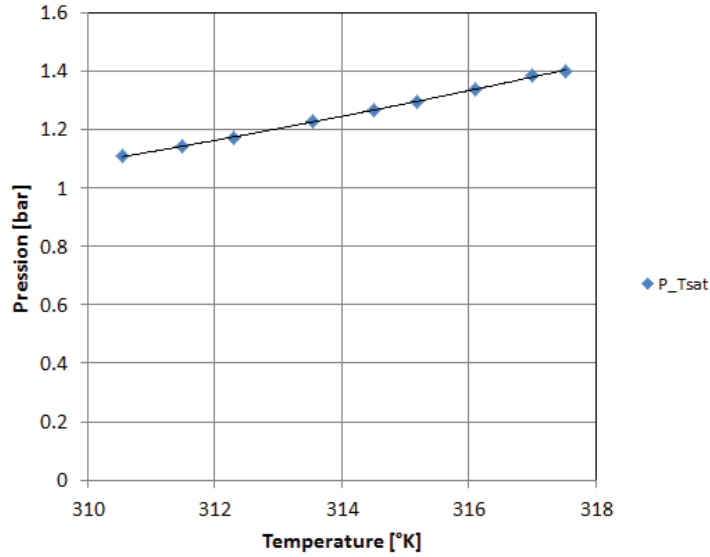


Figure IV.11: The saturation curve obtained by calibration procedure

In this range of saturation pressure and temperature the measure is good and outside this range the uncertainty will increase and this calibration couldn't be used. The saturation pressure is a function of saturation temperature as below:

$$P_{sat} = 0.0007374.T_{sat}^2 - 0.4205.T_{sat} + 60.562 \quad (\text{IV.1.3.1})$$

Where  $T_{sat}$  is expressed in Kelvin and  $P_{sat}$  in bar.

#### IV.1.3.5 First developments and analysis in order to determine wall temperature by infrared camera

Wall temperature is one of important parameter to evaluate the internal and external heat transfer coefficient. To determine the wall temperature during condensation experiments a measure procedure based on the infrared camera has been performed. The employed camera for these experiments is "SC6000HS" of "FLIR". This camera consists in a photonic matrix detector of  $640 \times 512 \text{ pixel}^2$  in an Indium antimonide (InSb) cooled down by a heat pump functioning on a Stirling cycle. The photonic sensor has an homogeneous sensibility on the spectral band between 3 and 5  $\mu\text{m}$  with a typical resolution 0,018°C (NETD) in the temperature range considered for high emissivity surface. In this spectral band, the sapphire is completely transparent which is not exactly the same for the HFE-7000. Figure IV.12 shows the infrared spectrum transmittance of HFE-7000 obtained through a tank of 60  $\mu\text{m}$  depth. An important

observation is that, at the spectral range of thermal camera corresponding to wavenumbers distributed from 2000 to 3333, most of the wavelength get a transmittance higher than 80%. Therefore it is difficult to used infrared emission from sapphire or liquid to determined wall temperature. Thus in order to measure the wall temperature a thin black paint has been deposited on the external wall of the tube in order to give this part visible with thermal camera. Radiation flux emitted by this paint will be considered at the wall temperature due to the very black thickness.

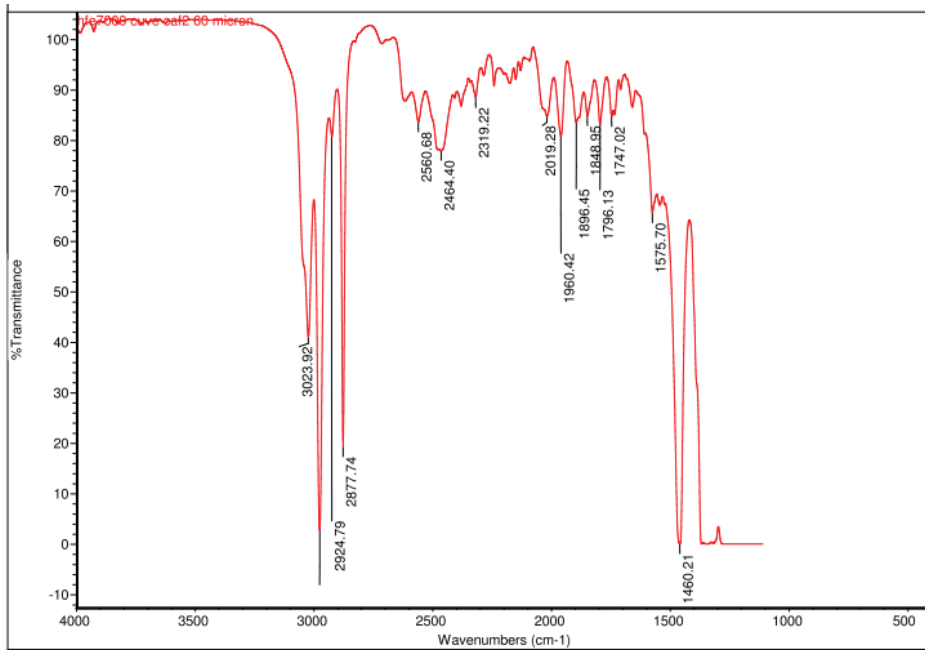


Figure IV.12: The transmittance of HFE-7000 measured for wavenumbers from 500 to 4000  $cm^{-1}$  with a depth of 60  $\mu m$  at the university Paul Sabatier, Toulouse, France by Corinne Routaboul.

A circulation of water at a known temperature has been used in order to connect radiative flux of the paint to its temperature and also to determine the sensitivity of the calibration curve obtained to numerous parameters such as ambient conditions, axial position of the camera, foccus setting of the camera... The calibration has been done for both black paint line in the center of the tube and water radiation that can be observed using the two sides around this narrow black paint line (remember that the sapphire is transparent in the bandwidth detected by the IR camera). Note that calibration of water radiation with temperature is not useful for experiment with HFE-7000, but as water is a very absorbent medium, its radiation level gives a reference value that can be used to check the high emissivity of the paint used. The two sides and black paint temperatures are considered as the same temperature that water circulating inside the

tube. The procedure can be described as:

- A water flow at a homogeneous temperature is controlled and imposed by a thermostat bath. The water temperature at inlet and outlet are measured by two thermocouples. The flow rate is high enough in order to obtain a temperature drop (typically  $0.3^{\circ}\text{C}$ ) small compared to the gap between the water and ambient temperatures. So the water temperature at each position can be evaluated by a linear interpolation from the inlet to the outlet.

- The camera is installed in order to have optical axis of infrared camera lense perpendicular to the tube one. About 40 images have been recorded at a frequency of 300 Hz. Figure IV.13 shows an example of results obtained. The intensity is calculated from these calibration images. Note that the correction of non uniformity of the different pixels gain has been done and that an internal correction has been also performed in order to homogenize the offset of different pixels of the sensor. The final intensity is then calculated using the average from all images. The detailed procedure is described in the next section.

- The calibration has been done at different days where the ambient conditions change a lot and at different position along the tube in order to evaluate and control all necessary parameters.

Note that the same procedure for set up IR camera such as the choice of working window (set of ring used behind the objectif in order to choose the magnification of the lens), exposure time (linked to the working temperature range),... has been applied for all experiments measurement later.

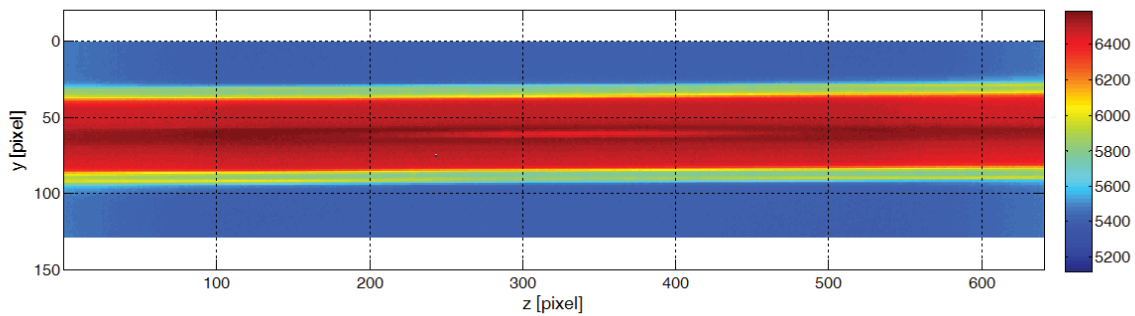


Figure IV.13: An example of the measured intensity distribution by infrared camera for a water flow at axial position from 523 mm to 584 mm and for inlet and outlet temperatures of  $34.55^{\circ}\text{C}$  and  $34.43^{\circ}\text{C}$  respectively. The ambient temperature was  $26^{\circ}\text{C}$ .

So at each condition an infrared image resulting from the averaging of 40 images is obtained. This measure allows obtaining the infrared intensity of the black paint line as well as the two sides of this line to detect water radiation in each axial position of the tube. At each column of the image (connected to the axial position) the average intensities of black paint and of water radiation have been evaluated and this procedure has been done for each position of 640 columns of the image. Finally the function linking intensity to real temperature has been determined for each column of the sensor. Note that as the tube is always placed around the same lines and that a non-uniformity correction and offset correction are done the sensitivity to the line can be neglected. This operation has been done for 6 different levels of the inlet temperature.

From these measures, at each of the 640 columns, the relation between the radiative flux received by the sensor and the real temperature has been found. An example of calibration curves obtained both for two sides and for black paint is presented in figure IV.14. The interpolation between two points of this curve has been done thank to "Hermit cubic spline" by Matlab.

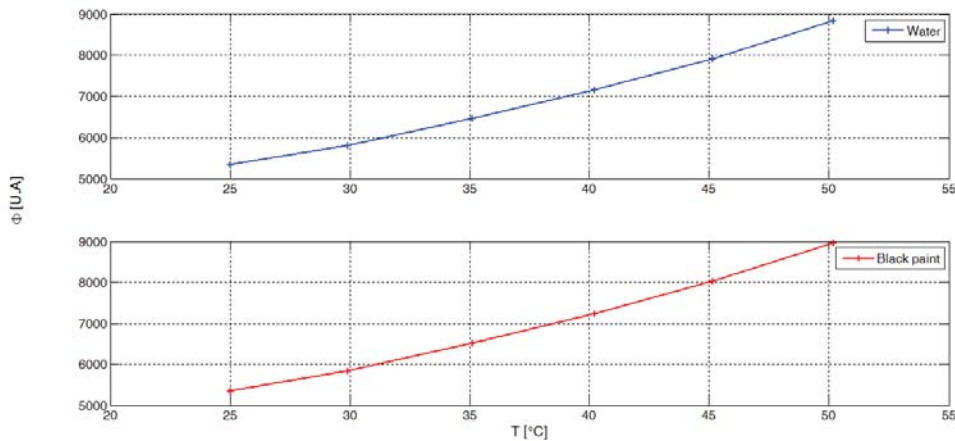


Figure IV.14: The calibration curves of water and black paint at the middle point of recorded window obtained by circulating water.

- Now let study the influence of the different parameters that can affect the measurement. In general, the radiative flux of a gray body received by the infrared camera could be described as below:

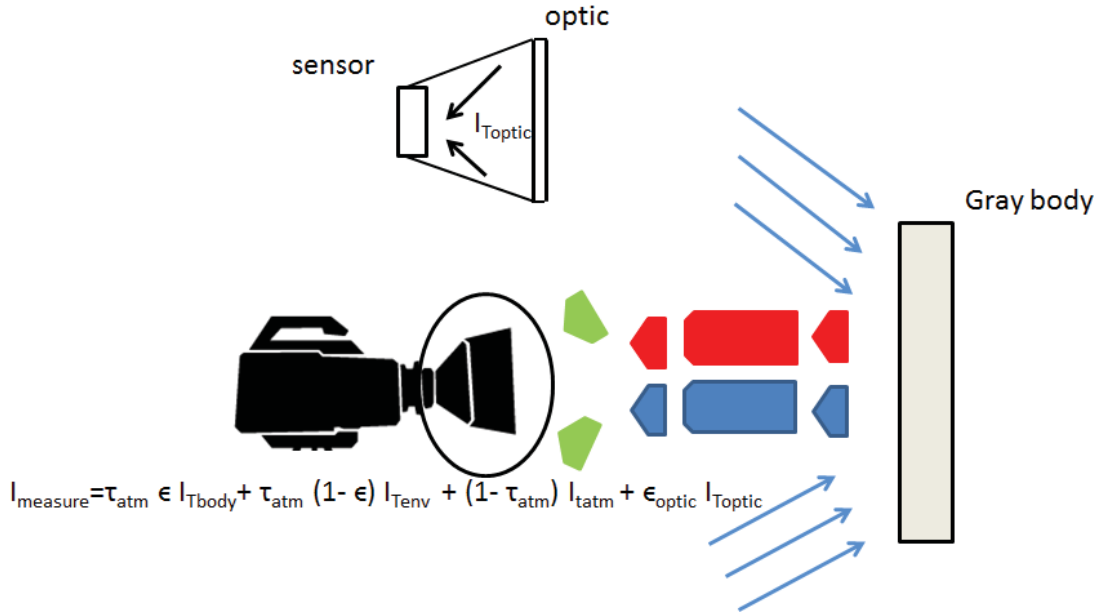


Figure IV.15: All contributions in a measured radiative flux received by the infrared camera from a gray body.

Where  $\tau_{atm} \epsilon I_{Tbody}$ ,  $\tau_{atm} (1 - \epsilon) I_{Tenv}$ ,  $(1 - \tau_{atm}) I_{Tatm}$ ,  $\epsilon_{optic} I_{Toptic}$  are corresponding to the contribution of gray body, environment and atmosphere and lens holder material respectively.

In order to avoid any effects of environment coming from long distance object, like wall radiation of the room, reflection on metallic surface..., PVC plates have been built and installed perpendicularly to lens axis and around the lens. Thanks to that the radiative environment collected by the camera is mainly created by radiation of this plates which can be considered as black body in the wavelength range concerned and so linked mainly to the air temperature of the room. As air temperature of the room is easier to determine and control than wall surface temperature of the room, a better control of ambient conditions can be done. Moreover, the camera has been worked at a short distance about 30 cm, therefore the absorption of ambient air could be considered negligible,  $\tau_{atm} = 1$ . The final equation could be rewritten as following:

$$I_{measure} = \epsilon I_{Tbody} + (1 - \epsilon) I_{Tenv} + \epsilon_{optic} I_{Toptic} \quad (IV.1.3.2)$$

From this equation the radiative flux received by the infrared camera depends on emissivity of the body (black paint here), the radiation of a black body at the same temperature, environment and radiation of the optic. As the camera lens holder find its equilibrium between cooled sensor temperature and ambient temperature of the air,

the radiative flux received by the sensor is now only due to two parameters : temperature of the object studied and air temperature of the room. So, knowing the impact of ambient air on calibration curve, all the radiative effects can be controlled and precise measurement can be obtained.

The determination of the calibration curve and the method employed to obtain the temperature profile of the external wall whatever the ambient radiative environment are presented in next section. On the other hands, the experimental procedure and data reduction are then exploited.

## IV.2 Experimental results and discussion

In this section, two important parts are presented. Firstly, the calibration procedure of wall temperature and external heat transfer coefficient. The heat transfer coefficient is measured with two different working air conditioner modes. In this part a great care has been paid to calibration with infrared camera in order to develop a measurement method of wall temperature with an uncertainty as lower as possible. Secondary, the condensation heat transfer coefficient and liquid film thickness measurements, which are the main results of this study, have been exploited.

### IV.2.1 Calibration procedure

The control of ambient effect and a check to the axis camera position dependence on temperature measurement is presented both for water and black paint zone. Three test series at three axis positions of the camera have been performed, far from the inlet to avoid any edge effects. These calibration tests have been made during two different days whose the ambient temperature changes a lot, in order to evaluate the impact of ambient radiation. Then, some results of external heat transfer coefficient with water as the working fluid and air as the secondary fluid are presented.

#### IV.2.1.1 Calibration curves for infrared camera

The infrared camera has been used in the basic mode with the pre-registered non uniformity correction called "FL50, no filter" associated to the optical configuration used. The exposure time has been chosen in order to detect temperature in the range 10°C to 50°C with a window of 128x640 *pixel*<sup>2</sup>. The calibration has been done, as described previously from the inlet to the outlet of the test section with water circulation. The inner wall temperature is then imposed by the water temperature in the vicinity of the inner wall. Due to its high absorption coefficient value (around 10<sup>3</sup>cm<sup>-1</sup>) in the infrared wavelength band, water temperature radiations collected allow to measure the liquid temperature very close to the inner wall (remember that the sapphire tube is completely transparent to the infrared radiation). To take into account the effect of

tube surface condition, and potential undesired reflection, five different positions along the tube have been recorded at the same water temperature's condition during a single day. When the flow temperature is stable, a group of 40 recorded images has been taken. Then the average radiative flux of these 40 images has been evaluated and processed. The black paint and water zones are the ones studied. An algorithm has been developed in order to detect the radiation coming from the black paint and the ones coming from the water. In the figure IV.16 the detected boundaries of each region are presented. The resolution is about 10 pixel per mm.

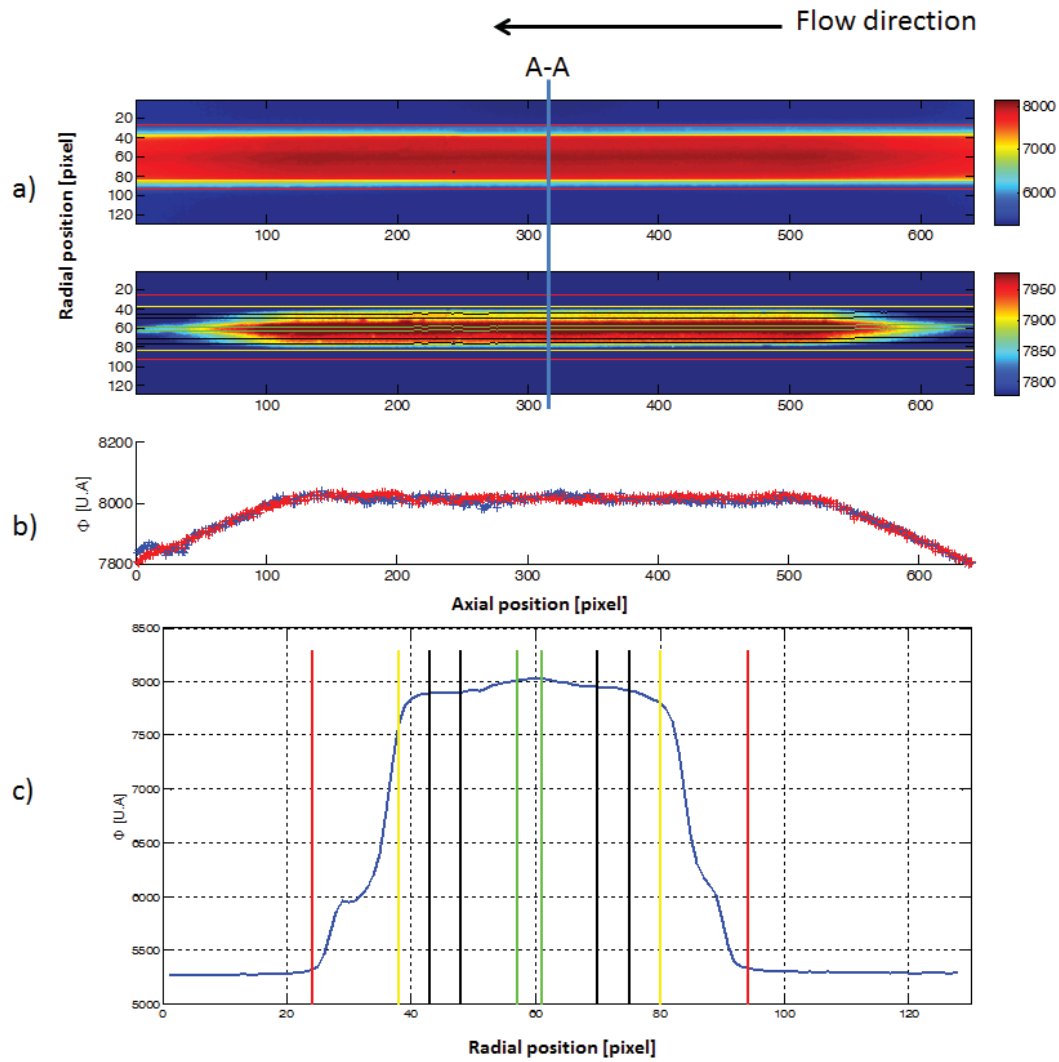


Figure IV.16: Presentation of detected zones : black paint region and water emission region. The inlet water temperature is  $45^{\circ}\text{C}$  and a temperature drop of  $0.25^{\circ}\text{C}$  from the inlet to the outlet of whole test section has been measured. Part : a) Original image recorded by infrared camera and same image with a modification of scale intensity in order to visualize the black region in the middle delimited by green lines, and water region delimited by black boundaries and sapphire internal and external walls delimited by yellow and red lines b) The two boundaries radiative flux profile of black paint region (following the two green lines) c) Radial radiative flux profile at cut A-A or in the middle of recorded window.

The figure IV.16 a) was the average of 40 original recorded images where we can find out the ambient zone outside the tube wall, the wall tube and the inside tube zone with a high radiative flux induced by both black paint line and infrared water radiative

emission. However in this image the contrast between the radiative flux of the water and the radiative flux of the paint is too small to determine these two regions. In figure IV.16 b) the scale of the color-bar level have been modified in order to magnify the contrast between the different regions inside the tube. Nevertheless, as the emissivities of the two regions are very similar it's not easy to detect the black paint line. In order to help the reader zone where the black paint in the middle has been delimited by two green lines. Their intensity is higher than other parts. The water zones chosen by the algorithm are also presented and delimited by black lines. The figure IV.16 c) presents the radiative flux at the borders of the black paint zone detected corresponding to the two green borders. We could point out that the two intensity's boundaries are very close, and confirm that the intensity received inside this green zone is really homogeneous. This verification procedure has been done for all thermal videos in order to have a good calibration curves. For each columns the mean value between the borders is saved as the intensity value corresponding to each region (paint and water). Therefore the intensity at each longitudinal pixel position has been obtained.

Figure IV.17 shows the calibration curve of these raw data at different pixel positions and different temperature tested.

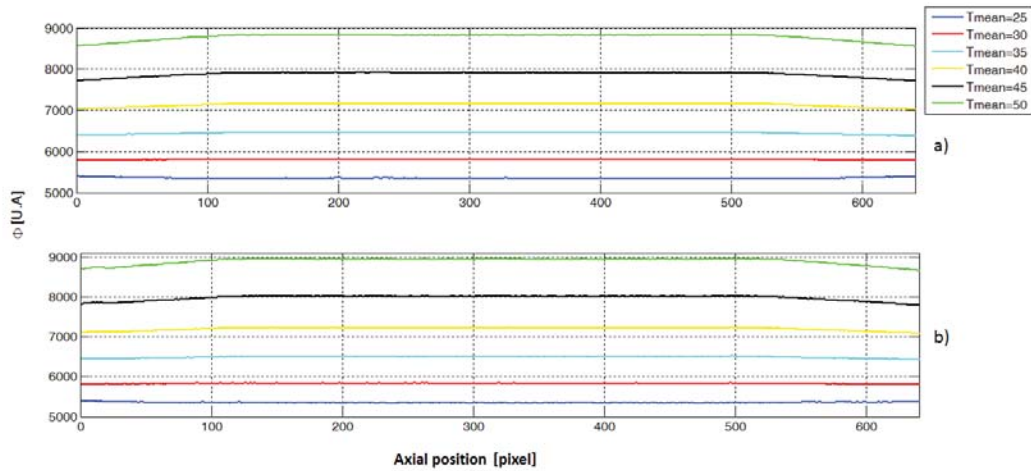


Figure IV.17: Calibration intensity trend versus position in pixel at vertical position of 523 mm (at the pixel 320 of the window) from the inlet test section for different inlet temperatures (the whole temperature drop from inlet test section to outlet test section of 0 to 0.35°C). a) Water b) Black paint zone.

By superimposing these two radiative fluxes received from water and black paint, we have figure IV.18.

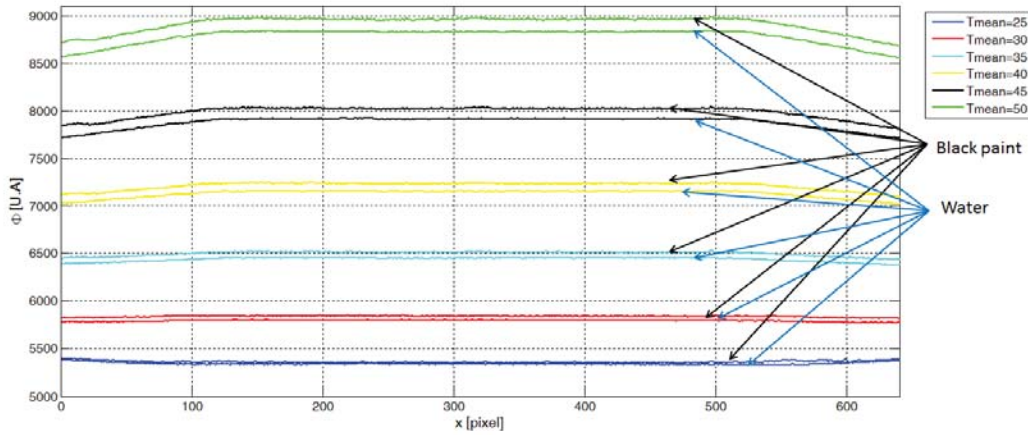


Figure IV.18: The superimposed calibration intensity trends of water and black paint versus position in pixel at vertical position of 523 mm from the inlet test section for different inlet temperatures (the whole temperature drop from inlet test section to outlet test section is less than  $0.35^{\circ}\text{C}$ ).

We can notice that the intensity of black paint is always higher than the water one and this difference increases when water temperature increases. The reason is that the black paint has a higher emissivity than the "apparent emissivity" of the water. It could be induced by optical properties of the medium but also by the fact that the two regions are not in the same focal plan of the camera. As the camera focus is realised on the paint the collected radiation from water region are behind the focal plan of the lens. On the other hands, we can observe a decrease of the intensity at the boundaries of the image. This effect is clearly induced by the focus setting. Indeed the focus of the camera on the paint is done manually by the operator and we will see hereafter that, contrary to the center of the image, the borders of the image are very sensitive to the focus setting. Therefore to eliminate this effect the studied zone is determined only from pixel 140 to pixel 500 where the intensity is homogeneous.

As the radiative flux has been determined, the temperature at each axis position given by pixel discretization has been also evaluated by linear interpolation between the inlet and the outlet of the tube. So, for each column of the image the link between the radiative flux and the temperature has been determined. Figure IV.19 presents the calibration curve at the column number 320 in camera window.

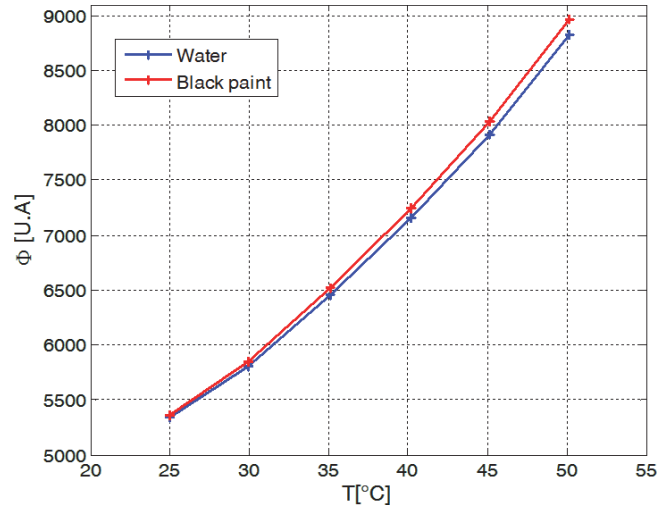


Figure IV.19: Radiative flux received versus temperature at the column number 320 in the camera window far from the inlet of test section for both water and black paint.

Now the calibration procedure has been completed for each column position of the camera image, this experimental procedure is repeated for different position of the camera along the sapphire tube axis and during different days (i.e various ambient radiative environment). The table below summarizes the various tests carried out.

Position	z=553.5 [mm]	z=623.5 [mm]	z=693.5 [mm]	z=763.5 [mm]	z=833.5 [mm]
$T_{amb} = 23^{\circ}C$ , 07th October 2015	x		x		
$T_{amb} = 26^{\circ}C$ , 16th October 2015	x	x	x	x	x
$T_{amb} = 25^{\circ}C$ , 17th November 2015	x		x		x

a) Effect of position

Many tests have been done at the same day at three different positions, at each position, the focus has been done manually, therefore the effect of position and also the effect of focus could be exploited. The three different positions are represented in the figure IV.20

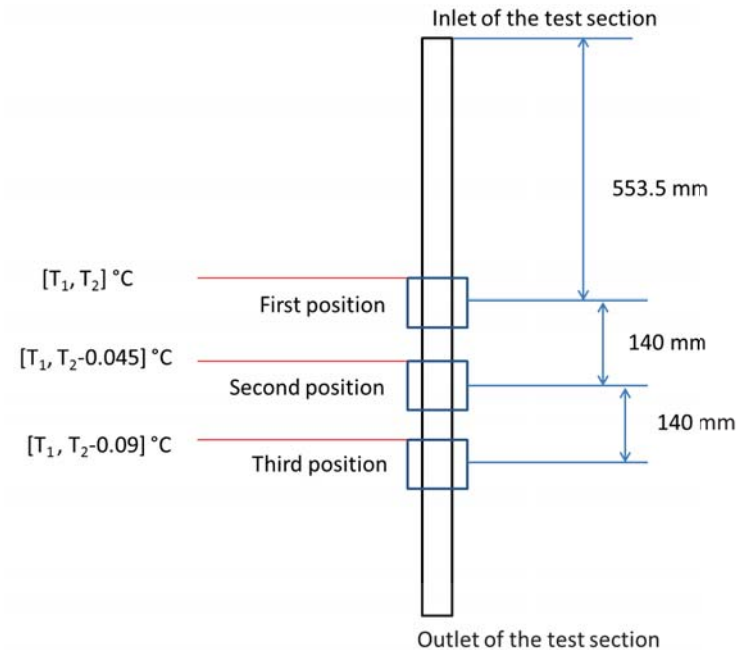


Figure IV.20: The three studied positions with the temperature drop in each case.

Figures IV.21 and IV.22 show the calibration curve at different positions, different temperatures and also different focusing for both water and paint.

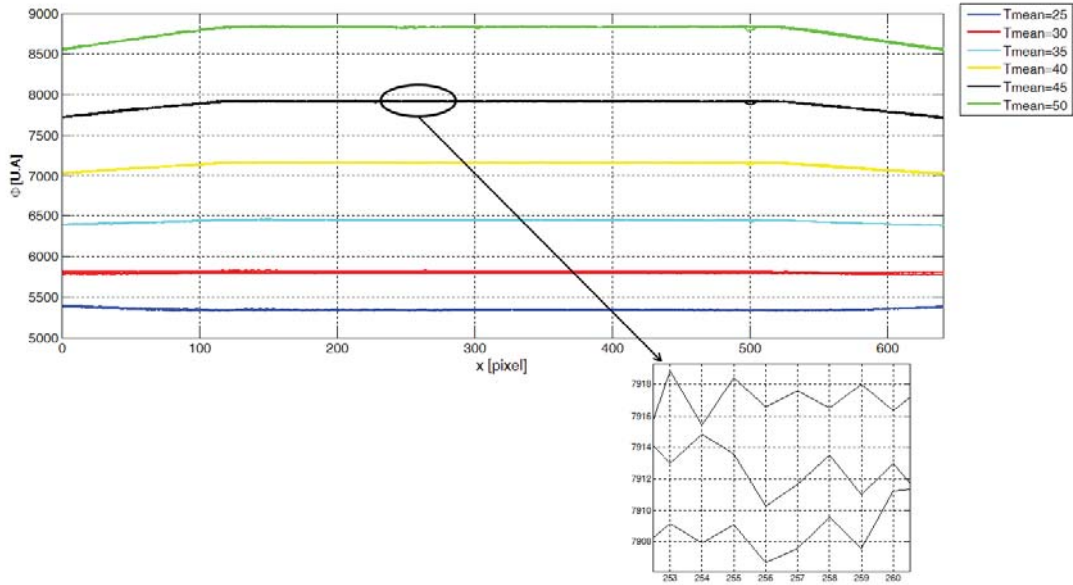


Figure IV.21: Superposition of water calibration curves for the column number 320 of the sensor matrix at three different positions described in figure above at the same inlet and outlet conditions and the same day (17th November).

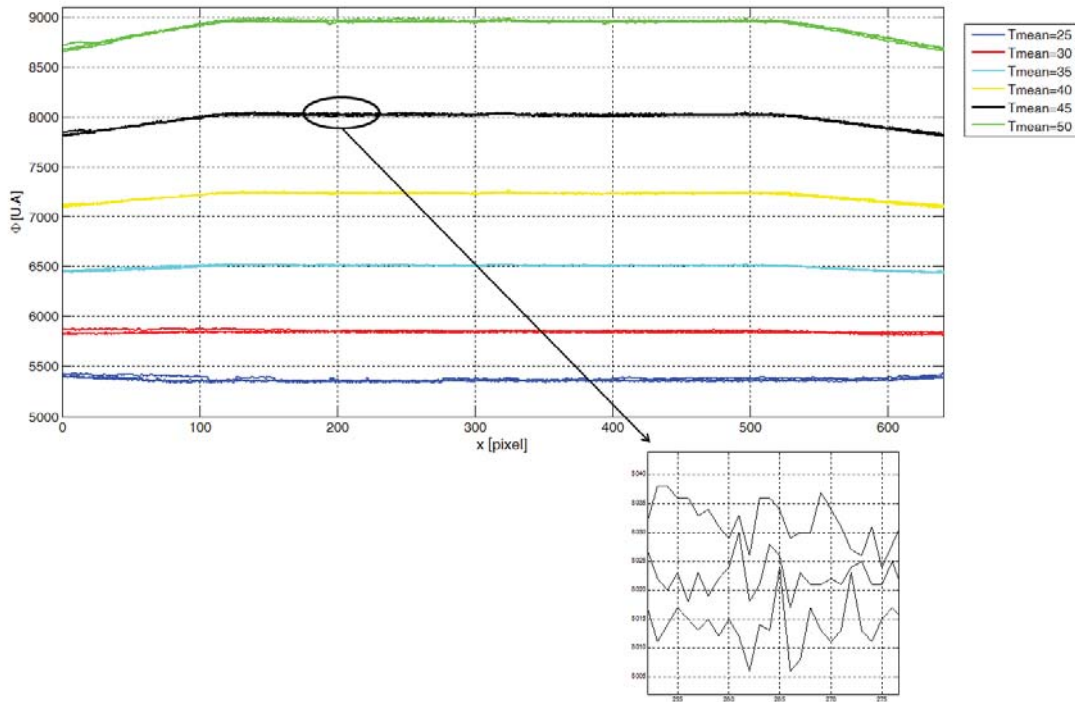


Figure IV.22: Superposition of black paint calibration curves for the column number 320 of the sensor matrix at three different positions at the same inlet and outlet conditions at three different positions described in figure above and the same day (17th November).

The temperature range studied goes from 25°C to 50°C. By using the link between intensity level and temperature obtained in the paint region for the first camera position (i.e creating a calibration curve with these data) the intensity of paint obtained at the third position can be converted to temperature. Using this conversion, temperature at the third position is found to be lower and variation between these two position goes from 0.22°C to 0.18°C when the temperature range go from 25°C to 50°C. Nevertheless as the water flows from the first to the third position its temperature decrease slightly, so its natural to find lower value at the third position. After correction of the water temperature thanks to a linear interpolation between the inlet and outlet temperatures of the tube, the real difference is found to be between 0.22°C and 0.09°C. So we can conclude that position of the camera along the axis of the tube has no impact on the calibration curve.

#### b) Effect of environment

As presented in previous section, the radiative flux received by the infrared cam-

era depends not only on the studied object itself but also on the environment around the apparatus in general. In order to evaluate the effect of radiative environment, the same procedure has been applied with two series of test for different days where the ambient temperature changes a lot. An observation of calibration curve at one position and at different ambient temperatures has to be done. Figure IV.23 presents the two calibration curves at the column number 250 of the camera sensor.

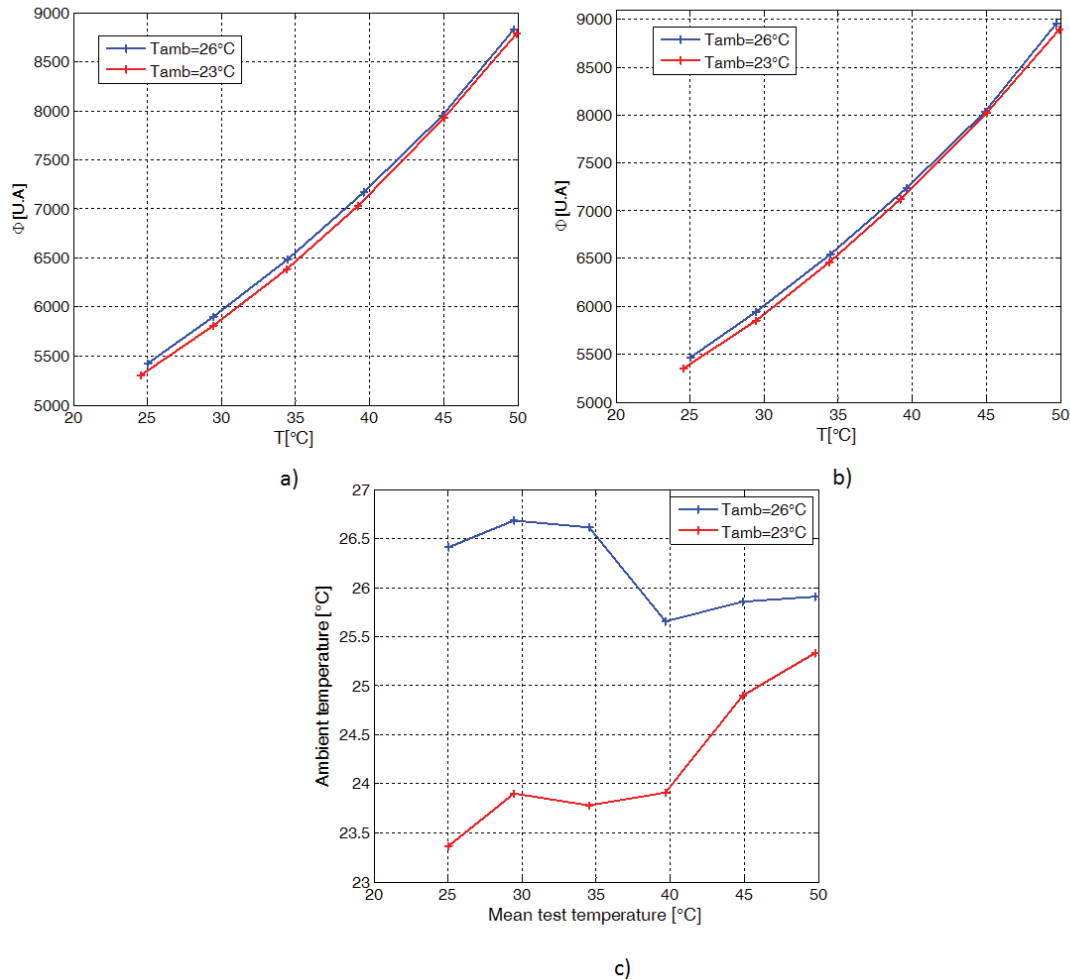


Figure IV.23: The two calibration curves at the column number 250 of the camera sensor (far from the beginning of infrared camera window) at ambient temperature of 23°C and 26°C a) For water b) For black paint c) Ambient temperature’s evolution during the two experiments.

We found that the intensity is higher for higher ambient temperature. On the other hand, the ambient temperature varied during the calibration procedure, it is why the

two curves are not perfectly parallel as expected. At the end of the experiment the two ambient temperatures are closer as seen in figure IV.23 c). We also find that by using one calibration matrix as the calibration reference, the difference between the real one and the calculated one due to the ambient deviation can reach  $0.7^{\circ}\text{C}$  at  $30^{\circ}\text{C}$  and  $0.3^{\circ}\text{C}$  at  $45^{\circ}\text{C}$ . So, at the first order the ambient temperature parameter seems to be a good way to correct the drift between the calibration curves from one day to another. As variation of ambient radiation collected by the sensor comes in addition to the radiation collected by the hot object studied (here paint), shift between two calibration curves can be assumed to be constant whatever is the object temperature (see equation (1.3.2)). The following method will then be used for all the future experiments : in order to evaluate the ambient radiative environment, at the beginning of the experiment when tube and paint are at room temperature (before vapor of HFE flows inside the tube), a set of infrared images are collected and liquid HFE temperature inside the tube (equal to ambient temperature) is recorded. This point gives the reference point to use in order to evaluate the new calibration curve that must be used for this day. The reference calibration curve which was done another day must be then shifted to this reference point as described as figure below to obtain the new calibration curve to used for the current experiment. Finally only one point measurement where temperature and radiative flux are known are needed to correct an "old" calibration curve. The validity of this technique is tested hereafter with the experiments previously described.

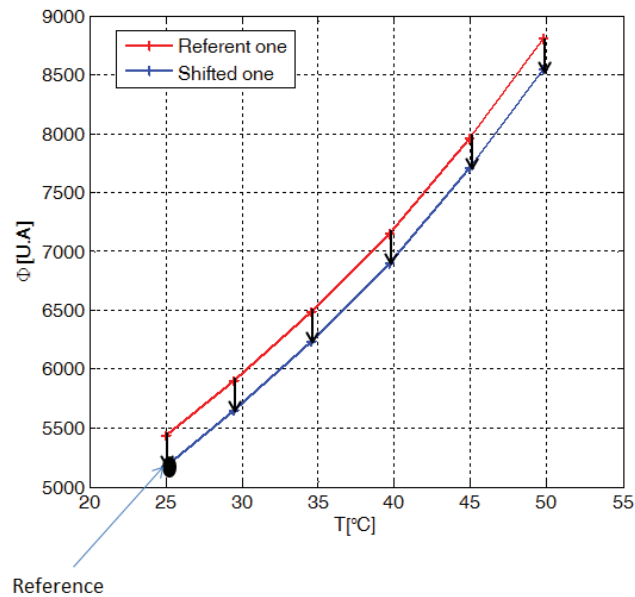


Figure IV.24: Shift of referent image by a constant at a position in infrared window.

By applying this shift both for paint and water the new calibration curves are obtained at the column number 320 of the camera sensor as following:

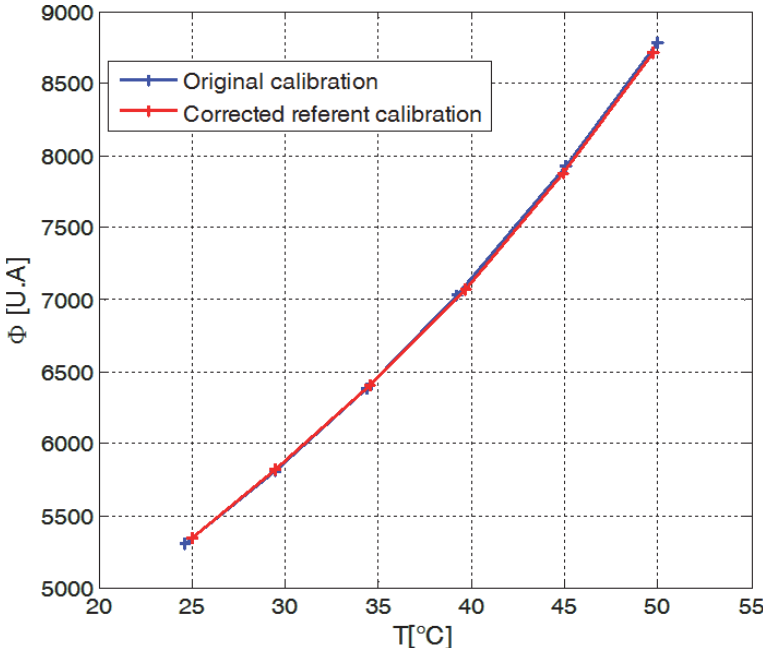


Figure IV.25: Water calibration curve at ambient temperature of 23°C and corrected water calibration from the referent one at ambient temperature of 26°C at the column number 320 of the camera sensor.

From the figure, it can be seen that with this correction, the calibration curve calculated by shifting an old calibration is close to the real one. A quantification is done to finish this procedure.

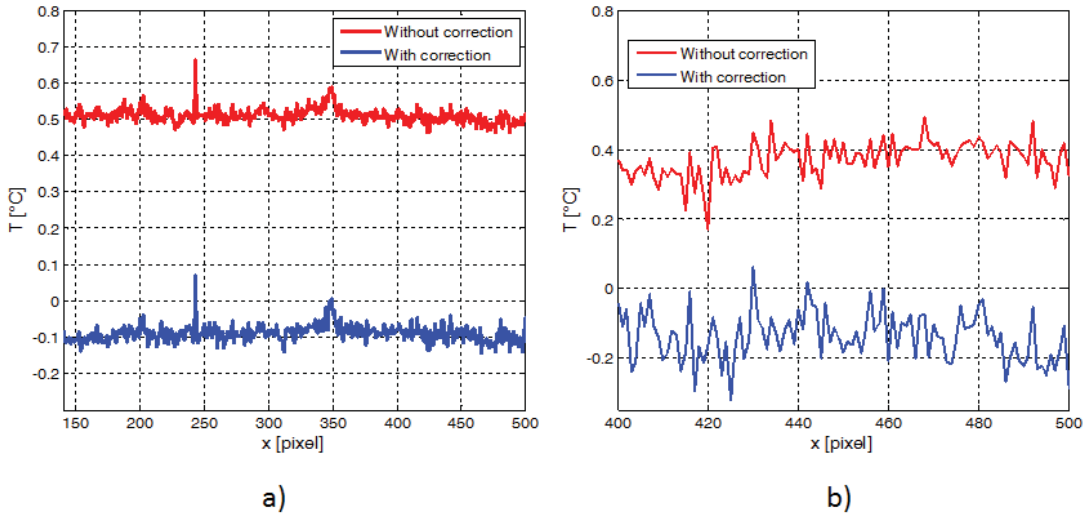


Figure IV.26: Variation of error between the real temperature and the calculating one using the referent calibration curve or by using the corrected one at the mean temperature of  $40^{\circ}\text{C}$ . a) For water b) For black paint.

From figure IV.26, we found that with water after using the corrected calibration, the absolute error goes down  $0.1^{\circ}\text{C}$  for water and  $0.2^{\circ}\text{C}$  for black paint. For the whole range of temperature, the error in general were reduced from maximum error of  $1^{\circ}\text{C}$  to maximum error of  $0.13^{\circ}\text{C}$  for water and from  $1^{\circ}\text{C}$  to  $0.20^{\circ}\text{C}$  for black paint. Therefore the correction improves clearly the results and the maximum error is evaluated to  $0.2^{\circ}\text{C}$ .

In conclusion, the infrared camera calibration procedure has been determined for both tube and paint and radiative effect linked to the environment variation has been determined and corrected. The maximum error between various experiments with the technic developed is evaluated to  $0.2^{\circ}\text{C}$ . Hereafter this technic is used in order to determined external heat transfer coefficient. This parameter is essential to determine the condensation heat transfer coefficient, which will be obtained in further measurements.

## IV.2.2 External heat transfer coefficient

While the calibration procedure has been completed, the external heat transfer coefficient measurement has to be performed. The procedure has been done with a circulation of hot water inside the sapphire tube. Water temperature at the inlet of test section is regulated by a thermostated bath at  $45^{\circ}\text{C}$ . The secondary fluid is forced air flowing perpendicularly to the tube axis coming from air conditioner. Six thermocouples are installed close to the tube to measure the air temperature and a hot wire anemometer is used to measure the air velocity. Two thermocouples are installed at the

inlet and outlet of the test section to measure water temperature. The procedure has been done for many experiments: some of them with air temperature at the same value that ambient temperature and the others with cooled air temperature (at about 12°C). These experiments were conducted for different water mass velocities. A turbine flow meter Omega with the range from 0.5 to 200 ml/min was used to measure the water mass flow rate. Figure IV.27 shows the principle of measurement set-up.

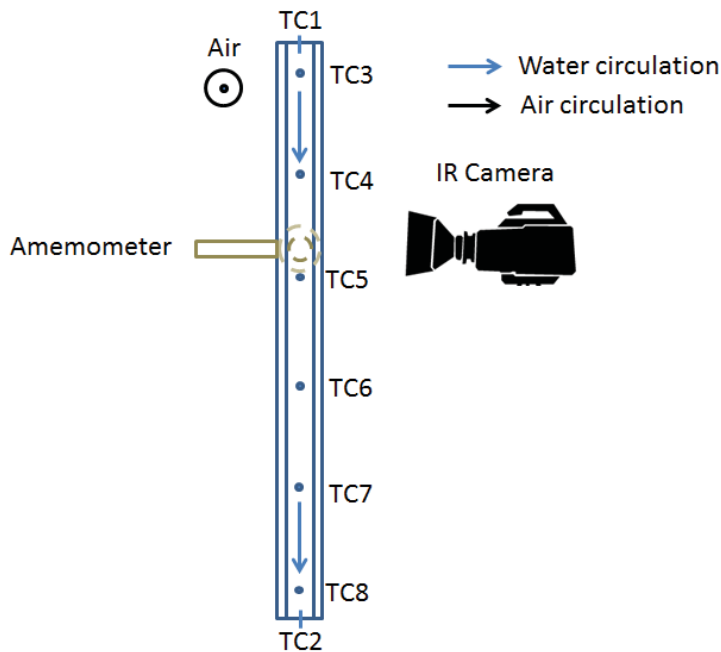


Figure IV.27: External heat transfer coefficient measurement procedure.

The profiles of internal and external wall temperature have been measured. Due to high value of absorption coefficient in the wavelength concerned, water temperature measured by the previous described method is considered equal to the internal wall temperature. External wall temperature profile is deduced from paint infrared radiation. The referent calibration matrix employed in order to determine internal wall temperature is the one created from the 17th November measurements. This is the closest one to the date when the external heat transfer coefficient has been measured. Figure IV.28 shows the internal wall temperature profile according to the column number of the camera sensor.

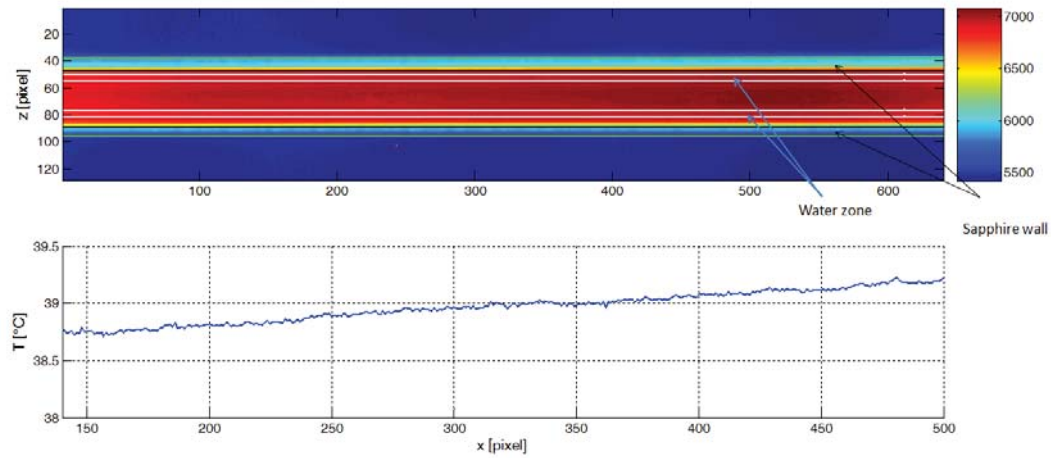


Figure IV.28: Internal wall temperature profile converted from the radiative flux received by thermal camera by using the calibration matrix. a) Original photo obtained by infrared camera with water zone inside white bands b) Converted profile temperature.

A recorded window as presented in this figure corresponds to a 37 mm length. Therefore it is necessary to move the camera many times to cover all the tube. On the other hands, the movement range of the robot is only 290 mm therefore a specific system with a winch has been employed as previously described. A position mark has been done to know the relative position of the robot when it was moved. Finally a profile of internal and external wall temperature has been established. Figure IV.29 presents the internal wall temperature from the inlet to the outlet at the mass flow rate of 30 ml/min with forced air conditioner at both ambient temperature and cold temperature. Moreover, the external wall temperature profiles obtained are constantly close to the internal ones.

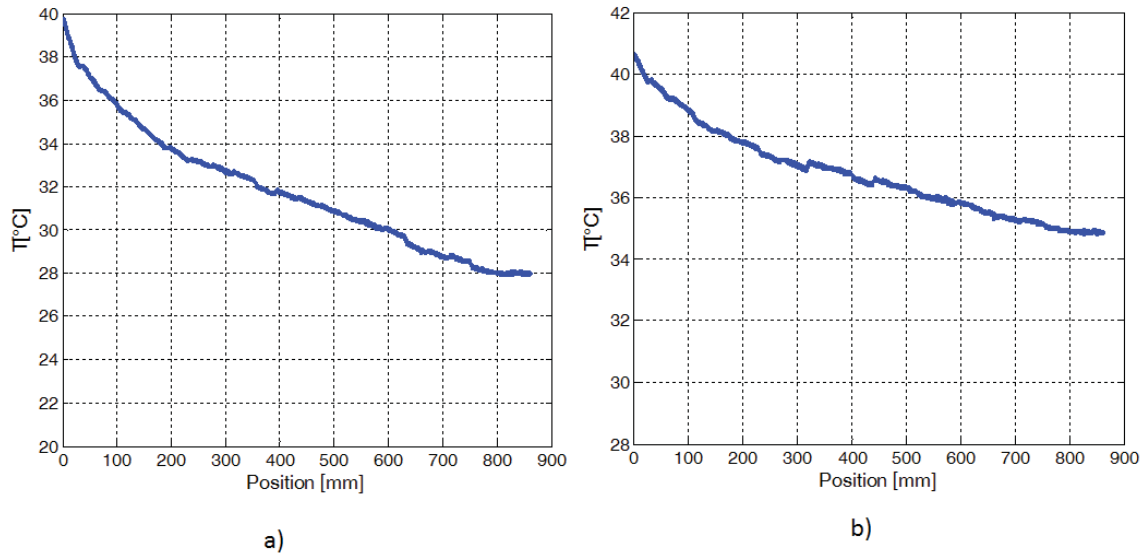


Figure IV.29: Water temperature profiles for a) Water mass flow rate of 33.4 ml/min and forced air conditioner at cooling mode ( $T_{\text{air conditioner}}=15^{\circ}\text{C}$ ) b) Water mass flow rate of 32.3 ml/min at forced air conditioner and ambient temperature ( $T_{\text{air conditioner}}=27.8^{\circ}\text{C}$ ).

While the water temperature profile has been determined, the evaluation of heat transfer coefficient in a small domain from  $z$  to  $z+\delta z$  has been performed as presented in figure IV.30.

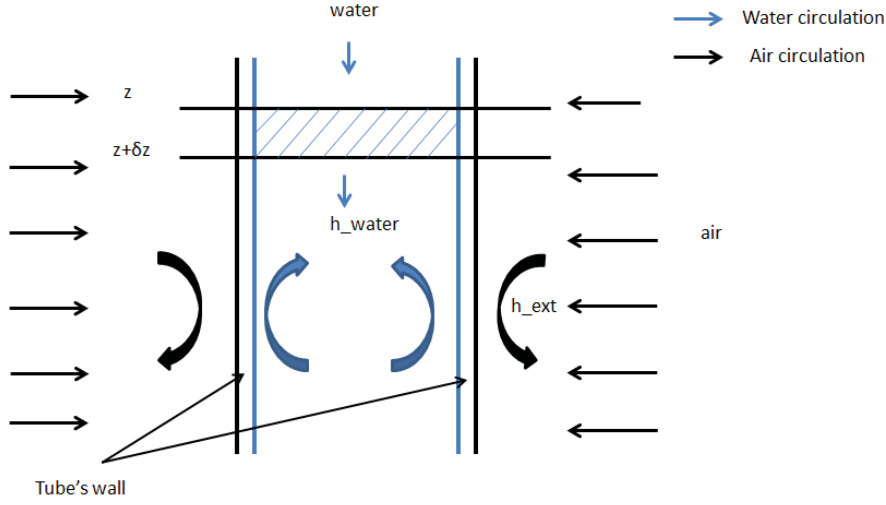


Figure IV.30: Representation of heat exchanges in the domain between  $z$  and  $z + \delta z$ .

The energy balance for the layer between  $z$  and  $z + \delta z$  can be written as:

$$\phi(z)P_{in}\delta z = -\dot{m}_{water}c_{p,water}(T_{water}(z + \delta z) - T_{water}(z)) \quad (IV.2.2.1)$$

Where  $\phi(z)$  is heat flux through the inner wall.

The water temperature in a cross section can be evaluated from the local wall temperature measured by the infrared camera by the following formula:

$$T_{water}(z) = \frac{\phi(z)}{h_{water}(z)} + T_{w,in}(z) \quad (IV.2.2.2)$$

Replacing  $T_{water}$  in equation IV.2.2.2 into equation IV.2.2.1, and assuming that the variations of  $h$  and  $\phi$  over the distance  $\delta z$  are very small, we obtain:

$$\phi'(z) = \phi(z)\left(\frac{h'_{water}(z)}{h_{water}(z)} - \frac{P_{in}h_{water}(z)}{\dot{m}_{water}c_p}\right) - T'_{w,in}h_{water}(z) \quad (IV.2.2.3)$$

Where  $\phi'$ ,  $h'$ ,  $T'_{w,in}$  are spatial derivatives of  $\phi$ ,  $h$  and  $T_{w,in}$ , respectively.

To solve equation IV.2.2.3 and determine the profile of the local heat flux, the internal heat exchange coefficient must be known at each position. To estimate its value, the correlation of Shah and London [78] developed for laminar flow in a cylindrical tube has been employed. This correlation takes into account the development zone of the thermal boundary layer under the assumption of a uniform heat flux. On the other hands, the boundary condition for the internal flow at the inlet must be known.

For this, it is assumed that the internal heat transfer coefficient at the inlet is much more important than the external heat transfer coefficient, inner heat transfer being accentuated by the development of the thermal boundary layer. Therefore the water temperature at the inlet is very close to the wall temperature. Thus, the heat transfer coefficient at the inlet is estimated in a first approximation from equation IV.2.2.1:

$$\phi(z = 0) = -\frac{\dot{m}_{water}c_p}{P_{in}}T'_{w,in}(z = 0) \quad (IV.2.2.4)$$

Equation IV.2.2.3 can be solved and the local external exchange coefficient profile deduced from the local heat flux by the following equation:

$$h_{ext}(z) = \frac{\phi(z)P_{in}}{P_{ext}(T_{w,in}(z) - T_{air})} \quad (IV.2.2.5)$$

Figure IV.31 shows an example of profiles of local heat flux and external heat transfer coefficient obtained for a water flow rate of  $32.5 \text{ ml.min}^{-1}$ . The average speed of air and its temperature are  $3.7 \text{ ms}^{-1}$  and  $15^\circ\text{C}$ , respectively. The air velocity profile measured with a hot wire anemometer for this same experiment is also shown. We see an overestimation of the external heat transfer coefficient at the inlet, induced by the assumption made in equation IV.2.2.4. Indeed, if the temperature of the water is equal to the wall temperature (due to the preponderance of the internal exchange), its axial evolution is quite different from the evolution of the mean temperature in the section. This bias created by this inlet condition, which can be corrected later by taking more detailed account of the axial profile of the water temperature in the inlet zone, induces an error which is limited to the first centimeter of the tube.

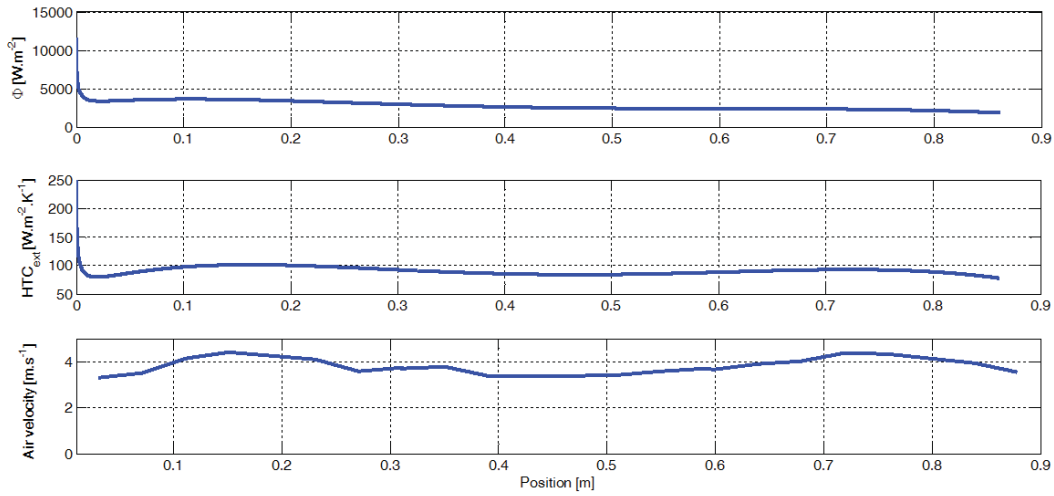


Figure IV.31: Profile of a) The local heat flux b) Heat transfer coefficient obtained with a water mass flow rate of 33.4 ml/min and forced air conditioner at cooling mode ( $T_{air\ conditioner}=15^{\circ}C$ ) b)The forced air conditioner's velocity measured by hot wire anemometer.

From figure IV.31, we found that the profiles of external heat transfer coefficient and air velocity are coherent. In the first part and the last part, at the beginning and the end of condenser, heat transfer is reduced because these positions are furthest to the center of two air conducts. At the middle the same phenomenon can be observed. The external heat transfer coefficient profile has the same shape as the air one.

A vector of external heat transfer coefficient versus position can be saved. From the results obtained the error can reach 6% with two different tests at different mass flow rate due to air temperature variation during experiment. Both two working modes of air conditioner have been employed to measure the external heat transfer coefficient. Figure IV.32 presents the external heat transfer coefficient obtained with these two different modes.

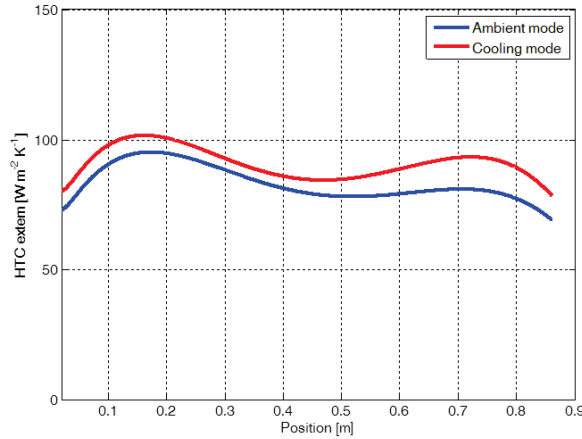


Figure IV.32: Profiles of the external heat transfer coefficient obtained for a water mass flow rate of 33.4 ml/min and with forced air at cooling mode of 15°C air temperature and 20 ml/min and with forced air conditioner at ambient temperature mode.

In the first 10 mm length where the effect of boundary condition is higher, the heat transfer coefficient is difficult to evaluate, so by continuity it is supposed to be equal to the one at the following position (10 mm). The heat transfer coefficient is finally fairly homogeneous, its variation is less than 12% from the inlet to outlet. We note that in cooling mode where the air temperature is smaller, the external heat transfer coefficient is slightly higher.

In the next section, the internal heat transfer coefficient and film thickness will be determined with HFE-7000 as working fluid.

We remind that, before putting HFE-7000 working fluid inside the loop and starting these calibrations, leakage test was done by using a vacuum pump. After filling, the pressure in the apparatus was maintained permanently higher than the atmospheric one, in order to avoid non-condensable air can go inside the rig. This overpressure was obtained by regulating the thermostat bath of the outlet reservoir at 45°C corresponding to an internal pressure of 1.4 bar.

## IV.2.3 Experimental tests

### IV.2.3.1 A test procedure

While all steps described have been done, the thermostated bath which regulates the inlet reservoir is set to 60°C. Therefore the refrigerant pressure inside was also set at the corresponding  $p_{sat}$ . The regulating valve is opened to obtain the desired mass

flow rate. The electrical heating is also regulated both upstream and downstream the regulating valve in order to avoid any condensation of refrigerant due to the vapor expansion or cooling before the fluid enters in the condenser. The refrigerant passes to the inlet of test section at super-heated state where its physical properties are well known by inlet temperature and pressure measurements. The mobile air conditioner is powered-on to condense the fluid inside the tube. At the outlet of the test section, the temperature is measured by a thermocouple. A differential pressure transducer allows measuring the pressure drop from the inlet to the outlet. The refrigerant passes then through the post-condenser to condense all eventual vapor of refrigerant. The transparent pipe after the serpentine post-condenser allows ensuring that the fluid is completely condensed. The refrigerant in liquid state goes then through the flow-meter to measure the refrigerant mass flow rate. It then arrived to the outlet reservoir before being pumped to inlet reservoir. During these experiments, the liquid film thickness and the wall temperature were measured thanks to the interferometer and the infrared camera. An acquisition of all temperatures and liquid film thickness profile takes place for about 45 minutes.

#### **IV.2.3.2 Test series**

Experimental tests have been done systematically to obtain the results corresponding to:

- Different mass flow rate ranging from 10 to 50  $kg.m^{-2}.s^{-1}$ .
- With HFE-7000 working fluid in order to measure film thickness and condensation heat transfer coefficient simultaneously.

### **IV.2.4 Condensation heat transfer coefficient and film thickness measurement of HFE-7000**

When all necessary calibration tests have been done, the condensation test of HFE-7000, can be performed. The heat transfer coefficient measurement is performed simultaneously with film thickness measurement.

#### **IV.2.4.1 Condensation heat transfer coefficient measurement**

The heat transfer coefficient determination needs the knowledge of the external wall temperature as well as other parameters that were directly measured. To measure the external wall temperature profile, the same procedure than the one applied with water has been used. Before each test, a reference point is taken when the condenser is full of liquid at ambient temperature before the test run. The calibration matrix

can then be corrected to determine the calibration curve to use for the day concerned (as previously explained). Then the radiative flux of black paint received by infrared camera is captured and converted to temperature as presented in the next figure (fig. IV.33). First a validation with HFE-7000 inside the sapphire tube has been done with no forced air flow at the outside of the sapphire tube.

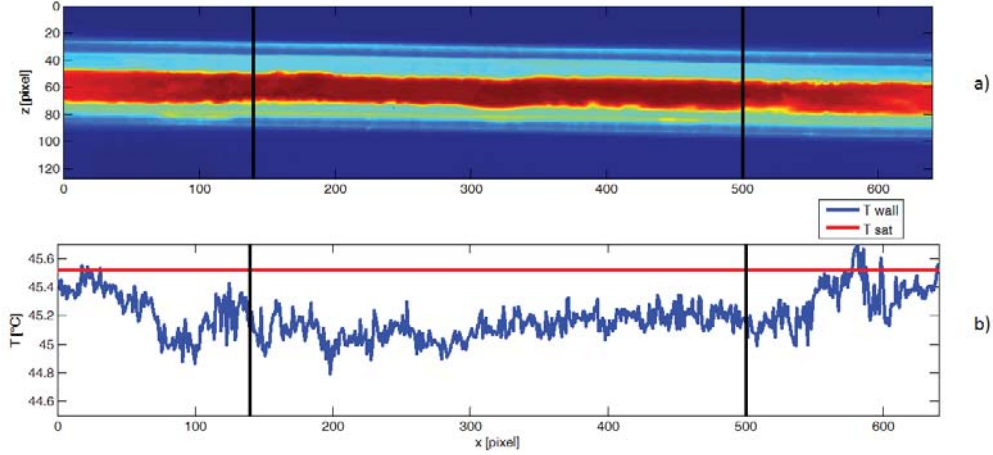


Figure IV.33: Results obtained at 240 mm from the inlet of the sapphire tube in the case of HFE-7000 as the working fluid without forced air flow a) the original image obtained by infrared camera b) the temperature profile versus position converted from radiative flux received from paint. The two black lines represented the borders of the zone taken into consideration (the left and right border zones of the sensor matrix are rejected due to the sensitivity to the focus setting).

In this case the external heat exchange is only due to natural convection so the external heat transfer coefficient is less than  $10 \text{ W.m}^{-2}.\text{K}^{-1}$ ; the temperature drop between the saturation temperature and external wall temperature can be evaluated by:

$$T_{sat} - T_{wall} = h_{nat-conv} \pi D_{ext} (T_{sat} - T_{air}) \frac{\ln\left(\frac{R_{in}}{R_{in}-\delta}\right)}{2\pi \lambda_{HFE-7000}} \quad (IV.2.4.1)$$

With the assumption of pure conduction in liquid film. With a film thickness of less than  $40 \mu\text{ m}$  (which is roughly the value measured with the interferometer), the temperature drop  $T_{sat} - T_{wall}$  is less than  $0.2^\circ\text{C}$ . Moreover, it has been checked that the thermal resistance of sapphire is very small compared to the one of the liquid film.

Figure IV.34 shows an example of profile of temperature difference between saturation and wall along the tube. From this figure we note that the black paint is not perfectly homogeneous. Indeed the measured difference between the saturation and

wall temperature in this case have an average value of  $0.6^{\circ}\text{C}$ , therefore a minimum deviation of  $0.4^{\circ}\text{C}$  compared to the expected maximum value ( $0.2^{\circ}\text{C}$ ) is observed. This effect can be explained by a partial transparency of the paint that was not detected during the calibration of paint with water. It can also be partially induced by the ambient radiative environment created by water. Indeed if the small black paint line does not perfectly cover the tube, radiation coming from the background are collected. In the case of water flowing inside the tube, the background radiation level is very high due to the high value of the absorption coefficient of water. So, as the paint and water radiative heat fluxes are close, defaults in the paint are not detected. In the case of thin liquid film of HFE-7000 inside the tube, the low value of the absorption coefficient (see figure IV.12, wavenumber between  $2000$  and  $3333\text{ cm}^{-1}$  for liquid film thickness about  $60\text{ }\mu\text{m}$  ) creates a background radiative environment close to room radiative level. In that case default on the paint will reduced sharply the radiative level collected by the camera and then the calculated temperature. This effect can be clearly observed for position higher than  $0.5\text{m}$  in figure IV.34. Temperature difference between saturation and tube wall changes sharply with position. Visual observation confirmed that paint not well covered the surface at these axial positions. Nevertheless it seems that even when the surface is well covered by paint the external wall temperature is underestimated by at least  $0.4^{\circ}\text{C}$  (first half-part of the tube). This effect shows that a small part of the radiative environment inside the tube can be detected by the pixel sensor matrix which was normally expected to collect only radiative flux coming from the black paint line. This effect could be created by a bad focus, paint transparency or unexpected reflection /refraction inside the tube wall. This underestimation will not be corrected because it depends of the contrast between paint radiation and background environment. So as the background radiation (emitted by liquid-vapor flow of HFE-7000) is sensitive to the liquid film thickness this dependance is not easy to catch. Nevertheless as the liquid film is very small when no air flow is used to cool the tube we can assume that the value of  $0.4^{\circ}\text{C}$  represents the deviation between estimated temperature and exact temperature when paint well covered the tube and the liquid film thickness is  $40\text{ }\mu\text{m}$ .

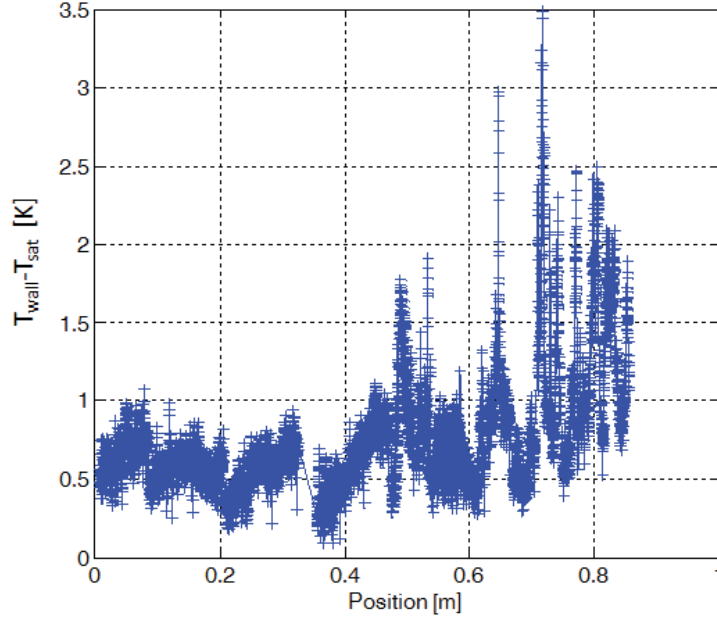


Figure IV.34: Temperature difference between the saturation and the wall temperature versus position with HFE-7000 as the working fluid without forced air flow.

This specific experiment (with no air flow) is used to determine the axial position of these bad points where paint badly covered the tube. To select them, a threshold value has been employed. Its value is presented hereafter.

For the condensation tests (with air flow), the local flux can be calculated as below by using heat balance in air side and in refrigerant side:

$$q(z) = h_{ext}(z)(T_{wall-ext}(z) - T_{air}(z))S_{ext} \quad (\text{IV.2.4.2})$$

The condensation heat transfer coefficient of HFE-7000 can be evaluated as below:

$$h_{int}(z) = \frac{q(z)}{(T_{sat}(z) - T_{wall-int}(z))S_{int}} \quad (\text{IV.2.4.3})$$

Where the external wall temperature is measured by thermal camera via black paint infrared radiation and the internal wall temperature can be deduced as following:

$$T_{wall-int}(z) = T_{wall-ext}(z) + q(z)R \quad (\text{IV.2.4.4})$$

Where R is the sapphire thermal resistance that can be calculated with the following formula :

$$R = \frac{\ln\left(\frac{D_{ext}}{D_{int}}\right)}{2\pi\lambda_{sapphire}L} \tag{IV.2.4.5}$$

Where  $S_{ext} = P_{ext}L$  and  $S_{int} = P_{int}L$   
 And  $P_{ext} = \pi D_{ext}$ ;  $P_{int} = \pi D_{int}$

The procedure for the external wall temperature measurement has been applied as described above. The figure IV.35 shows the profiles of the external wall temperature and of the saturation temperature during condensation test for a mass velocity of  $30 \text{ kg.m}^{-2}.s^{-1}$  and in the case of forced air flow and in the case of natural convection.

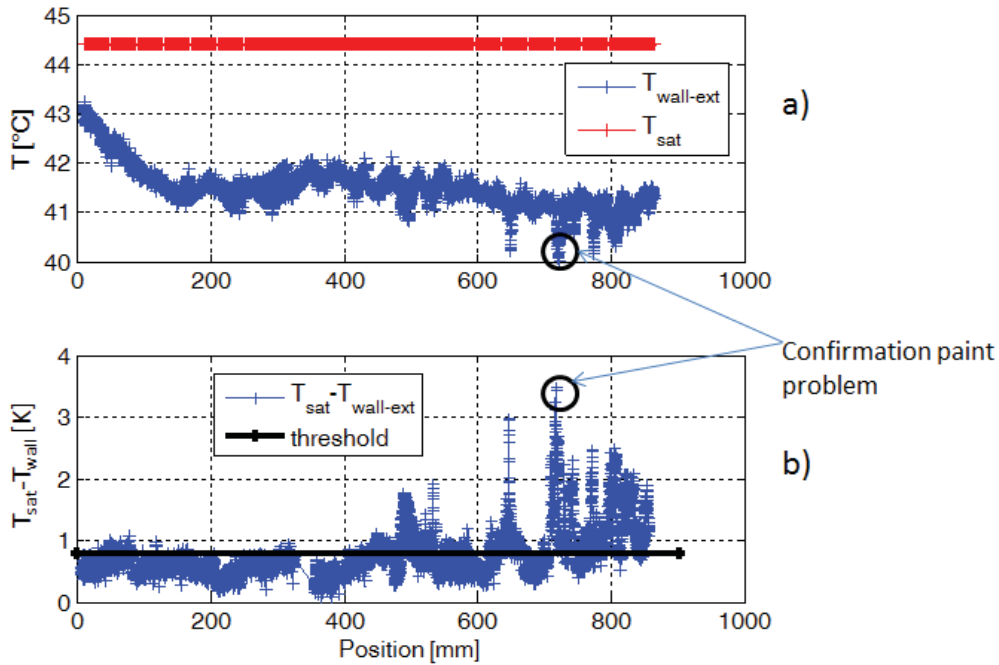


Figure IV.35: The profile of a) external wall temperature and saturation temperature during condensation test at mass velocity of  $30 \text{ kg.m}^{-2}.s^{-1}$  b) temperature difference between saturation temperature and external wall temperature without forced air flow.

From figure IV.35 we check the coherence of position where paint badly covers the tube between experiment with and without air flow. The measurement deviation happens at the same position in the two experiments especially at the end zone of the test section. This confirms the effect induced by a bad layer of black paint. It is why these points need to be removed from the whole profile. A threshold value of the temperature difference between saturation and external wall temperature represented by the black line in figure IV.35 b) has been chosen to remove these points. Only reliable po-

sitions have been stored and used to evaluate the condensation heat transfer coefficient.

On the other hand, the measured temperature is correlated to the real one by:

$$T_{real} - 0.6 < T_{measured} < T_{real} \tag{IV.2.4.6}$$

Therefore the chosen threshold is  $0.8^{\circ}\text{C}$  that is slightly higher than the average value of the temperature difference in the case without forced air flow but small enough to eliminate unreliable points. The final condensation heat transfer coefficient measured at mass velocity of  $30 \text{ kgm}^{-2}\text{s}^{-1}$  has been obtained and presented in figure IV.36.

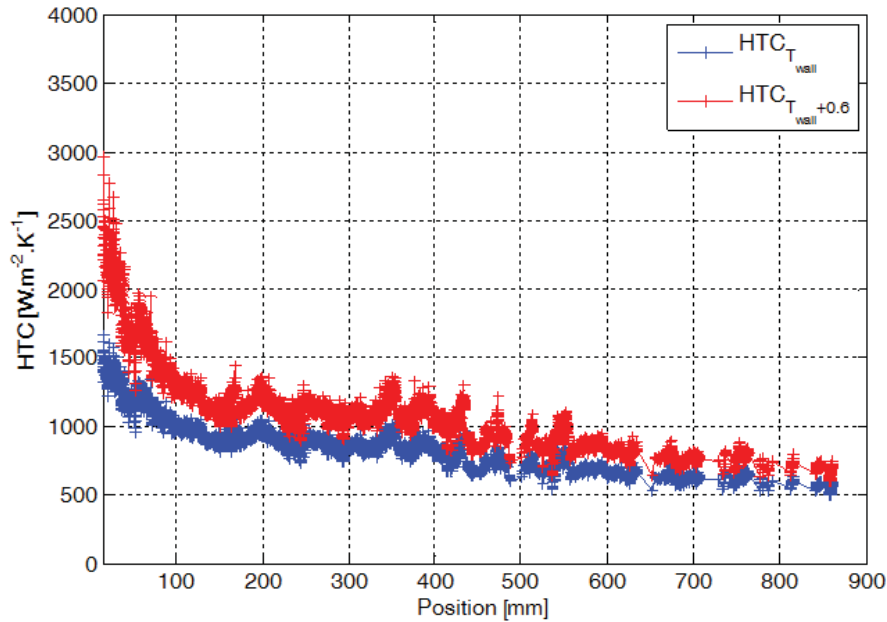


Figure IV.36: Inner heat transfer coefficient of HFE-7000 versus position considering measured wall temperature and measured wall temperature plus  $0.6^{\circ}\text{C}$ .

From the figure we found that the heat transfer coefficient decreases versus the position. The difference between these two estimations is about 12% except the first 20 first cm.

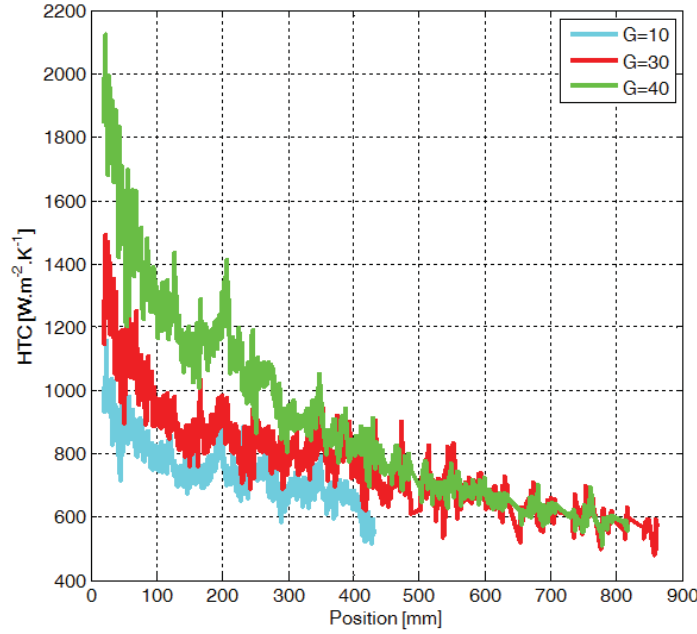


Figure IV.37: Inner heat transfer coefficient of HFE-7000 versus axial position for 3 different mass velocities.

The figure IV.37 presents the heat transfer coefficient as a function of the axial position for 3 different mass velocities. The tests were performed with air at ambient temperature for mass velocity of 10 and 30  $kg.m^{-2}.s^{-1}$  and air conditioner in the cooling mode for mass velocity of 40  $kg.m^{-2}.s^{-1}$ . We find that the heat transfer coefficients in this case are smaller to the ones obtained in microgravity where it was ranging from 4847 to 750  $W.m^{-2}.K^{-1}$  for vapor quality from 1 to 0.2 and for mass velocity of 70  $kg.m^{-2}.s^{-1}$ .

The uncertainty on the heat transfer coefficient measurement reaches about 20 to 25% due to uncertainties on external wall temperature, external heat transfer coefficient and mass flow rate. This error corresponds to the difference between the heat balance on the external side and the heat balance on the internal side.

The heat exchange in refrigerant is:

$$Q_{ref} = l_v \dot{m}_{HFE7000} \quad (IV.2.4.7)$$

And the heat exchange in air side is:

$$Q_{ext} = \int_{z=0}^{z=L_{2phase}} h_{ext}(T_{wall} - T_{air})P_{ext}dz \quad (IV.2.4.8)$$

Where  $h_{ext}$  is measured external heat transfer coefficient,  $l_v$  is refrigerant latent heat,  $\dot{m}_{HFE7000}$  is mass flow rate of HFE-7000. Due to the problem of discrepancy between the internal and external heat balances, it is difficult to evaluate the local vapor quality accurately. Therefore it is important to improve the apparatus before going further.

#### IV.2.4.2 Film thickness measurement

Film thickness is an important parameter for heat transfer coefficient measurement. As it was explained in the paragraph IV.1.2.8, interferometer is used to measure film thickness. As it was previously mentioned the focus of light in a tube is degraded due to the two different radius of curvature of a cylindrical shape. Moreover the external surface of the sapphire tube is not regular. Indeed, due to the manufacturing process the circular external shape of the tube wall has not a regular curvature. So the main difficulty is to obtain a good signal of the reflected light when the probe volume of the interferometer reaches the internal wall and the liquid-vapor interface. The alignment of the interferometer with the tube remains a delicate point.

When the reflected light is captured, the signal is recorded and the post processing of the signal is applied. If interferences can be detected, path difference ( $2.n.\delta$ ) is deduced and allows determining film thickness  $\delta$ . Figure IV.38 presents an example of the path difference measured.

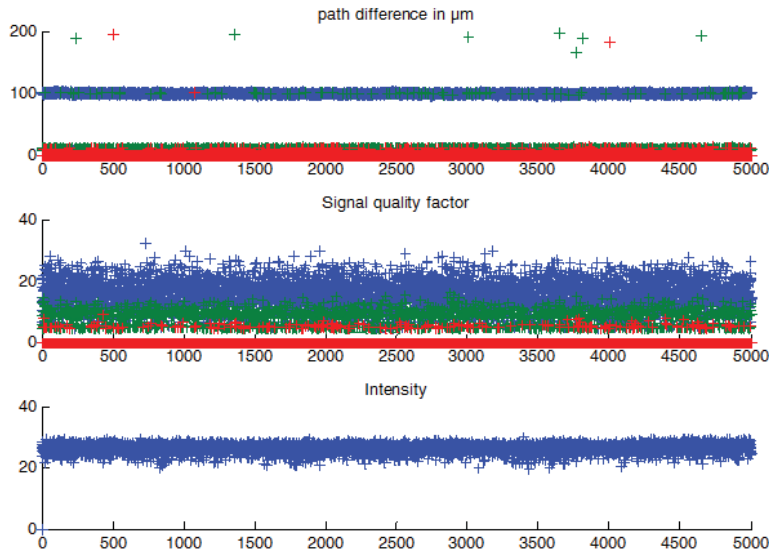


Figure IV.38: The figure presents three temporal evolution in hundred of seconds at 40 mm far from the inlet at mass velocity of  $30 \text{ kg.m}^{-2}.\text{s}^{-1}$ . The first is related to the path difference measured. The second graph presents signal quality factor and the last one the reflected intensity of light.

The first graph of the figure IV.38 is the path difference temporal evolution. Note that the time is graduated in hundredths of a second, due to the fact that a frequency acquisition of 100 Hz has been chosen. The signal processing is able to detect multiple path differences corresponding to the case where the light would pass through different layers. The highest intensity peak in the Fourier transform (i.e. the interference that presents the largest amplitude) is first analysed and the path difference associated with this signal is presented in blue, the second one in green and the third one in red. Depending on the detection threshold selected for detecting frequency peaks in the Fourier transform, noise can be caught. In order to see the level of the detected peak compared to the noise level a signal quality factor is determined for each peak detection in the Fourier transform. The result obtained are presented in the second temporal evolution on figure IV.38. The last temporal evolution gives the mean reflected intensity in order to check the quality of the adjustment of the probe volume of the interferometer. According to these temporal evolutions, the dominant interferences detected (high quality factor) are induced by path difference of about  $100 \mu\text{m}$  (blue points), which are therefore associated to thicknesses of liquid film of the order of  $40 \mu\text{m}$ . A second kind of interference overlaps the first one with a lower intensity (red points) and is associated to path difference equal to  $11 \mu\text{m}$ . However this value is also detected even when the probe of the interferometer is focused on a homogeneous media (air for example), therefore this value is due to the noise of the optical, maybe

produced by connections between two optical fibers. The red points stay most of the time at a value equal to zero, that means no other interferences can be detected. So, the path difference induced by liquid-vapor interface is well determined and can be used to measure film thickness. Then the average film thickness can be evaluated. Nevertheless as mentioned in the section IV.1.2.8, only points corresponding to configurations where the angle between the tube wall and the interface is less than  $17^\circ$  can be detected. Moreover if the path difference is too high, typically  $150\mu\text{m}$  in such a tube, the interference will not be detected. Finally only some reliable points have been recorded because of the interface instability especially far from the entrance. Indeed, beyond a critical distance from the tube entrance, the waves amplitude are too high and it becomes difficult to catch interferences.

To conclude when a liquid wave appears (as it can be seen on the infrared camera) the interferometer will detect only the top and the bottom of the wave (due to the detection limit induced by slope of the interface) and if the top value of the wave is too high, typically greater than  $60\mu\text{m}$  (in the present configuration), this thickness will not be detected.

Thanks to these results, the film thermal resistance per unit length can be determined:

$$R_{film} = \frac{\ln\left(\frac{D_{in}}{D_{in}-2\delta}\right)}{2\pi\lambda_{HFE7000}} \tag{IV.2.4.9}$$

While the the internal thermal resistance per unit length can be evaluated as:

$$R_{HTC,intern} = \frac{1}{h_{int}P_{int}} \tag{IV.2.4.10}$$

Where  $P_{int} = \pi D_{int}$

A comparison of these two terms has been done as presented in figure [?] below.

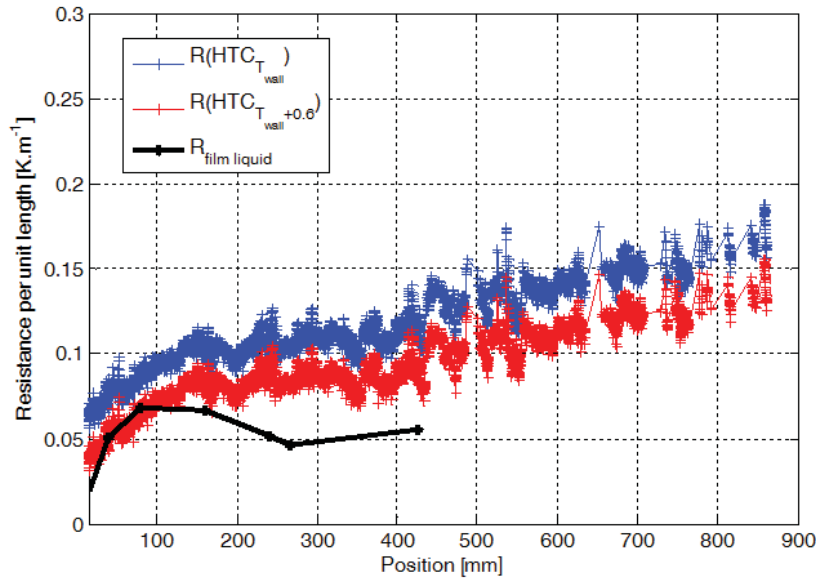


Figure IV.39: Variation of the conduction thermal resistance in the liquid film and of the convective internal resistance as a function of the position for mass velocity of  $30 \text{ kg.m}^{-2}.\text{s}^{-2}$ .

From this figure, we can see that at the beginning of the tube the film thickness measurement is well coherent with the heat transfer coefficient measurement. In the first measurement point of the liquid film thickness (black points) the comparison with the heat transfer coefficient is difficult even if the two results are not so different. Indeed some uncertainties due to the inlet thermal conditions make it difficult to determine precisely the heat transfer coefficient from the wall temperature profile obtained with infrared camera. From the fourth point of the liquid film thickness measurement, the thermal resistance of the liquid film and the thermal resistance deduced from the internal heat transfer coefficient become much more different. Indeed wavy regime appears and the interferometer captures only the bottom of the wave; therefore the film resistance is underestimated. The last three points give a very similar values of the thickness showing that the bottom of the wave has similar thickness even if the quality decrease.

### IV.3 Conclusion and perspective

Experimental tests of convective condensation of HFE-7000 in the range of mass velocity from  $10$  to  $50 \text{ kg.m}^{-2}.\text{s}^{-1}$  have been performed. An experimental apparatus has been built and allows measuring the condensation heat transfer coefficient and liquid

film thickness simultaneously by using infrared camera and white light interferometer at the same position in a sapphire condenser test section of 3.4 mm internal diameter. These tests are challenged. For the first time both condensation heat transfer and liquid film thickness have been measured simultaneously.

Firstly, external heat transfer coefficient has been measured with conditioned air as secondary fluid to prepare the measurement of condensation heat transfer coefficient. The condensation heat transfer coefficient has then been measured, for the different mass flow rates studied. Heat transfer coefficient are greatly affected by qualities variation. While the mass flux influence (range 10 to 40  $kg.m^{-2}.s^{-1}$ ) is small. At the same time, the liquid film thickness has been measured. The comparison between heat transfer coefficient and liquid film thickness demonstrates that the hypothesis of purely conductive heat transfer inside liquid film is valid at the beginning of the condensation process (for high qualities values). Unfortunately due to the limitation of the optical configuration, when liquid waves appear, liquid film thickness can only be determined in the bottom of wave. So for lower quality we can only conclude that the mean thermal resistance of liquid film is higher than the conductive resistance calculated with the thickness measured at the bottom of the waves. For the next step, an improvement of interferometer and apparatus will be studied in order to fulfill the initial objective.



# CONCLUSION AND PERSPECTIVES

This thesis has focused on the investigation of condensation inside low diameter tube for spatial and terrestrial application at intermediate and low mass fluxes. Our investigation aimed to determine simultaneously the heat transfer law and two phase flow pattern inside small diameter round channel in order to study the effect of gravity on convective condensation.

In this context, a first step in the modeling of two-phase flow instabilities was developed using separate phase flow modelisation. Linear instability analysis was performed and a comparison with some usual instabilities was made. Thanks to image processing development, a prediction of two-phase flow transition inside round micro channel, where the gravity is negligible, was done. A comparison with the results obtained inside square cross section micro tube was presented.

On the other hand, two experimental test sections were built dedicated for parabolic flights and on-ground to study the convective condensation inside round mini channel of 3.4 mm. The first test section was in copper and included an adiabatic glass window. Water was used as secondary fluid. Wall temperatures along test section were measured by thermocouples installed inside copper tube wall. The second test section was made with transparent sapphire. It was cooled by conditioned air. A specific procedure using IR camera was developed to determine the boundary condition and to measure wall temperature profile along the tube. Therefore, local condensation heat transfer coefficient can be evaluated. On the other hand, thanks to the transparency of the glass window installed between two copper exchangers in the first set-up and of the sapphire in the second, the flow regime was observed and condensate film thickness was measured using an optic interferometer and high speed camera. A specific tool for image processing was developed to analyze raw images recorded by high speed camera that allows determining hydraulic and thermal parameters for each studied case.

For the condensation test section in copper, the investigation has been performed with HFE-7000 as the working fluid for mass fluxes from  $70 \text{ kg.m}^{-2}.\text{s}^{-1}$  to  $175 \text{ kg.m}^{-2}.\text{s}^{-1}$ . The flow regime and condensate film thickness were determined from video acquired with the high speed camera. On the other hand, the heat transfer coefficient was also evaluated. Some important conclusions in this part can be resumed as following:

- The data reduction for heat transfer coefficient measurement was developed. The evolution of heat transfer coefficient in normal gravity and microgravity has been determined. The same conclusion as Mudawar et al. [12] has been obtained, i.e. the heat transfer coefficient reduces when gravity decreases. On the other hand, at high mass fluxes and high vapor quality, the effect of gravity on heat transfer coefficient is not significant in comparison to the case of low mass fluxes and low vapor quality.

- From images recorded by high speed camera it was highlighted that at low mass velocity and low vapor quality the flow regime changes a lot during the transition from normal to microgravity. The two phase flow which is stratified wavy or annular wavy with invisible film thickness on the top and high film thickness at the bottom in normal gravity becomes annular and axisymmetric in microgravity. At higher mass velocity and higher vapor quality, the two-phase flow is annular whatever is the gravity level. This explains why the heat transfer coefficient changes a lot at low mass velocity and low vapor quality.

- A specific procedure to determine film thickness from images recorded was developed based on ray tracing. By comparing the image recorded by high speed camera and the one calculated in the same condition, the ray-tracing method simulation was validated. The real film thickness is difficult to evaluate in these experimental tests due to the existence of a threshold value below which it can't be measured. Nevertheless, the minorant and majorant of the condensate film thickness have been determined.

For the condenser in sapphire, the goal was to determine the internal heat transfer coefficient and film thickness measurement simultaneously along the test section. The working fluid was HFE-7000 and the secondary fluid was conditioned air. A black paint of 1mm width was deposited on the external surface of the tube in order to make outer wall of the test section visible with thermal camera. Some primary tests have been done to determine the external boundary condition. An interferometer was used with an external light source in order to better capture the interface of condensate film. Annular flow regime was obtained for all experimental tests. First results of heat transfer coefficient and film thickness measurement have been obtained.

The perspectives for this study are numerous. The test section in copper with an adiabatic glass window was built in order to work at low mass fluxes. However, the minimum mass flux for experimental test was only  $70 \text{ kg.m}^{-2}.\text{s}^{-1}$  in microgravity con-

---

dition due to the appearance of instabilities within the loop. Therefore, it should be interesting to perform some other test at lower mass fluxes from 20 to 70  $kg.m^{-2}.s^{-1}$ . On the other hand, difficulties to measure the film thickness were encountered both in the test section dedicated to parabolic flights and the test section in sapphire due to interferometer limitation. Therefore it is necessary to develop and improve the measurement device in order to obtain more informations about heat transfer coefficient as a function of film thickness value. While the test section in sapphire was calibrated and its boundary conditions were determined, it should be interesting to perform experimental tests about the correlation between heat transfer coefficient and film thickness measurement for a large range of mass velocities. Finally, an improvement of the two-phase flow model is necessary in order to be able to predict flow regime transition.



# Annex 1

## Evaporator interface simulation

The liquid-vapor interface of centrifugal evaporator can be described as figure

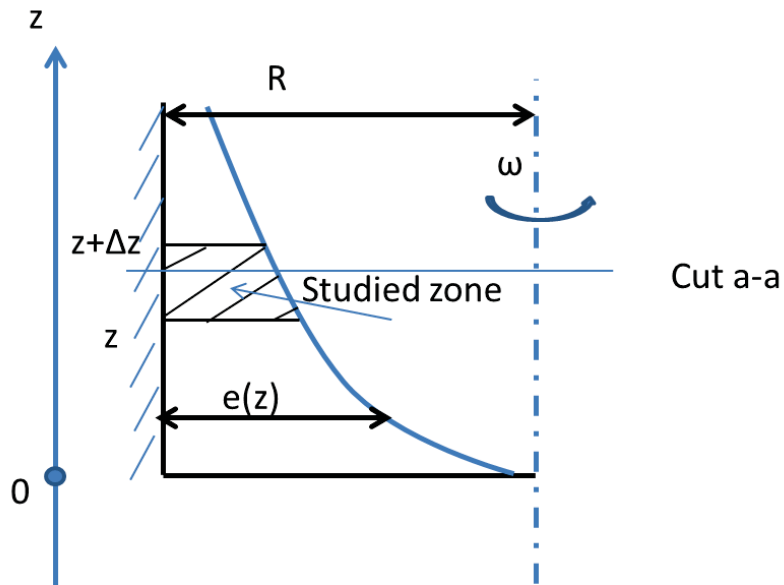


Figure IV.40: Liquid-vapor interface in an centrifugal evaporator.

The studied domain is  $\Omega$  between axial position  $z$  and  $z + \Delta z$  (with  $\Delta z$  is infinite element). By using the mass conservation and momentum equations for stationary regime we have:

$$\frac{\partial}{\partial t} \int_{\Omega, \vec{v}} (\rho_L d\Omega) + \int_{\partial\Omega, \vec{v}} (\rho_L (\vec{U}_L - \vec{V}_\Sigma) n_{ext}^{\vec{v}} dS) = 0 \quad (\text{IV.3.0.1})$$

At stationary regime:

$$\int_{\partial\Omega, \vec{v}} (\rho_L (\vec{U}_L - \vec{V}_\Sigma) n_{ext}^{\vec{v}} dS) = 0 \quad (\text{IV.3.0.2})$$

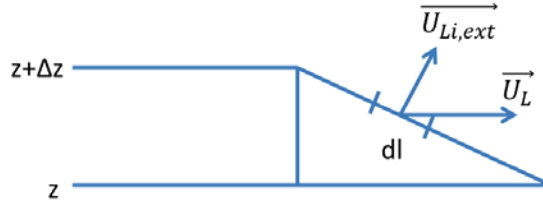
We call  $\bar{U}$  is mean velocity in a cross section and calculated by:

$$\int_S (\vec{U}_L) n_{ext} dS = \bar{U}_L \cdot S \quad (\text{IV.3.0.3})$$

And the mass equation becomes:

$$\rho_L \bar{U}_L(z+\Delta z) \pi (R^2 - (R - e(z+\Delta z))^2) - \rho_L \bar{U}_L(z) \pi (R^2 - (R - e(z))^2) + \int_{Ai} \rho_L (\vec{U}_{Li} - \vec{V}_\Sigma) n_{ext} dS = 0 \quad (\text{IV.3.0.4})$$

For the interface momentum, we have:



Finally, we have the momentum in the interface is:

$$\int_{Ai} \rho_L (\vec{U}_{Li} - \vec{V}_\Sigma) n_{ext} dS = \int_z^{z+\Delta z} \int_{\theta=0}^{\theta} \rho_L \vec{U}_{Li} n_{ext} dl d\theta = 2\pi \rho_L \vec{U}_{Li} n_{ext} dl d\theta \quad (\text{IV.3.0.5})$$

Finally, we have:

$$\int_{Ai} \rho_L (\vec{U}_{Li} - \vec{V}_\Sigma) n_{ext} dS = \int_z^{z+\Delta z} \rho_L \vec{U}_{Li} n_{ext} \frac{dl}{dz} (R - e(z)) 2\pi dz \quad (\text{IV.3.0.6})$$

With:

$$\rho_L \vec{U}_{Li} n_{ext} \frac{dl}{dz} (R - e(z)) 2\pi = \Gamma A_{tube}(z) \quad (\text{IV.3.0.7})$$

Finally the mass conservation becomes:

$$\frac{\partial}{\partial z} [\rho_L \bar{U}_L(z) \pi (R^2 - (R - e(z))^2)] + (\Gamma A_{tube})(z) = 0 \quad (\text{IV.3.0.8})$$

For the momentum equation, we have:

$$\frac{\partial}{\partial t} \int_{\Omega, \vec{V}} \rho_L \vec{U}_L d\Omega + \int_{\partial\Omega, \vec{V}} \rho_L \vec{U}_L (\vec{U}_L - \vec{V}_\Sigma) n_{ext} dS = \Sigma F_{ext}^{\vec{}} + \Sigma F_{volum}^{\vec{}} \quad (\text{IV.3.0.9})$$

Au stationary regime, the momentum becomes:

$$\int_{\partial\Omega, \vec{V}} \rho_L \vec{U}_L (\vec{U}_L - \vec{V}_\Sigma) n_{ext} dS = \Sigma F_{ext}^{\vec{}} + \Sigma F_{volum}^{\vec{}} \quad (\text{IV.3.0.10})$$

We note  $\bar{U}^2$  as mean square of velocity cross a section or calculated by formulate:

$$\bar{U}_L^2(z) = \frac{1}{A_L(z)} \int_{A_L(z)} U_L^2(z) dS \quad (\text{IV.3.0.11})$$

With:  $A_L = \pi[R^2 - (R - e(z))^2]$

Finally the same decomposition of integral, we have:

$$\rho_L U_L^2(z+\Delta z) A_L(z+\Delta z) - \rho_L U_L^2(z) A_L(z) + \int_{A_i} \rho_L \vec{U}_{Li} (\vec{U}_{Li} - \vec{V}_\Sigma) n_{ext} dS = F_G(z) + F_{pc}(z) + F_{shear}(z) \quad (\text{IV.3.0.12})$$

With the interface term can be noted by:

$$\int_{A_i} \rho_L \vec{U}_{Li} (\vec{U}_{Li} - \vec{V}_\Sigma) n_{ext} dS = \int_{A_i} (\Gamma A_{tube}(z) U_{Liz} dz \quad (\text{IV.3.0.13})$$

With  $A_{tube} = \pi \frac{D_h^2}{4}$  and  $U_{Liz}$  is the liquid velocity at the interface projecting to  $\vec{e}_z$ .

Finally the left is:

$$left = \int_z^{z+\Delta z} \left( \frac{\partial}{\partial z} (\rho_L \bar{U}_L^2(z) A_L(z) + (\Gamma A_{tube})(z) U_{Liz}) \right) dz \quad (\text{IV.3.0.14})$$

The composition of force is:

- The gravitational force as presented in figure IV.41

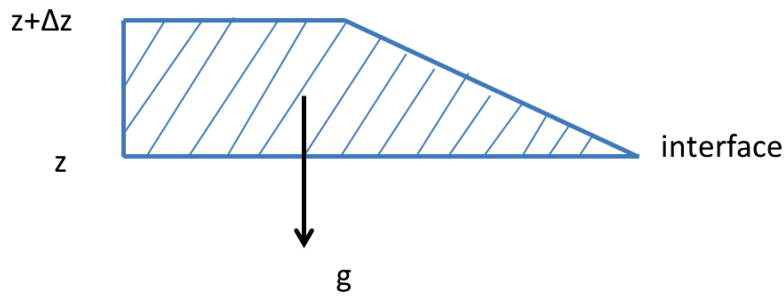


Figure IV.41: Gravitational force in the studied domain.

$$F_G = -g\rho_L V = \int_z^{z+\Delta z} \int_{\theta=0}^{\theta=2\pi} \int_{R-e(z)}^R g\rho_L r dr d\theta dz \quad (\text{IV.3.0.15})$$

or :

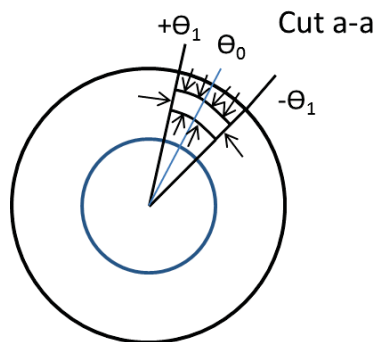
$$F_G = - \int_z^{z+\Delta z} \pi g\rho_L (R^2 - (R - e(z))^2) dz \quad (\text{IV.3.0.16})$$

- The centrifugal force is:

$$F_C = \omega^2 r \rho_L V \quad (\text{IV.3.0.17})$$

With V is volume of liquid.

Firstly, the pressure can be calculated in a layer between (r,r+dr) as figure below:



The equilibrium of all pressure in projecting in  $\theta_0$

$$\int_{-\theta}^{+\theta} p(r) r dz d\theta \vec{e}_\theta \vec{e}_{\theta_0} - \int_{-\theta}^{+\theta} p(r+dr) (r+dr) dz d\theta \vec{e}_\theta \vec{e}_{\theta_0} + 2p(r) dr dz \sin(\theta_1) + \int_{-\theta}^{+\theta} \rho_L \omega^2 r \cos(\theta) dz r d\theta dr = 0$$

Therefore the sum of pressure force is finally:

$$[p(r)rdz\sin(\theta) - p(r + dr)(r + dr)dz\sin(\theta) + \rho_L\omega^2r^2drdz\sin(\theta)]_{\theta_1}^{\theta_1} + 2p(r)drdz\sin(\theta_1) \quad (\text{IV.3.0.18})$$

Or:

$$p(r)r - p(r + dr)(r + dr) - p(r)dr + \rho\omega^2r^2dr = 0 \quad (\text{IV.3.0.19})$$

With infinite element, we have:

$$-\frac{\partial(p(r).r)}{\partial r} + \rho_L\omega^2r^2 + p(r) = 0 \quad (\text{IV.3.0.20})$$

or finally, the equilibrium of centrifugal force becomes:

$$-r\frac{\partial p(r)}{\partial r} + \rho_L\omega^2r = 0 \quad (\text{IV.3.0.21})$$

Therefore the centrifugal pressure is:

$$p(r) = p(R-e(z)) + \rho_L\omega^2\frac{r^2 - (R - e(z))^2}{2} = p_i(z) + \rho_L\omega^2\frac{r^2 - (R - e(z))^2}{2} \quad (\text{IV.3.0.22})$$

- The pressure around the studied domain in projecting in  $\vec{e}_z$  as presenting in figure IV.42:

- The pressure: The sum of pressure in the studied domain can be presented as figure IV.42.

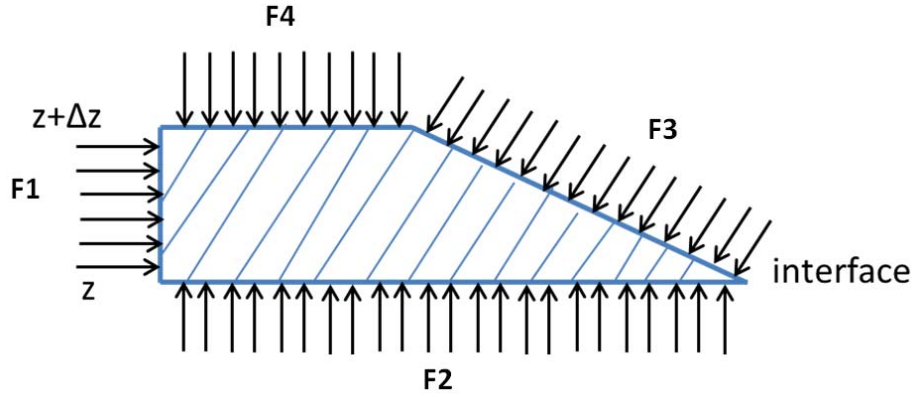


Figure IV.42: Sum of pressure in the studied domain.

In projecting following  $z$ , we have:

- $F_1 = - \int p \vec{n} dS \vec{e}_z = 0$
- $F_2 = - \int p \vec{n} dS \vec{e}_z = \int p dS$
- $F_3 = F_i = - \int p \vec{n} dS \vec{e}_z = \int_z^{z+\Delta z} p_i(z) 2\pi(R - e(z)) \frac{dl}{dz} dz$
- $F_4 = - \int p \vec{n} dS \vec{e}_z = - \int p dS$

We propose:

$$\int p dS = \bar{p} A_L(z) \quad (\text{IV.3.0.23})$$

Therefore:

$$F_2 + F_4 = [\bar{p} A_L](z) - \bar{p} A_L(z + \Delta z) \quad (\text{IV.3.0.24})$$

Or with  $\Delta$  very small:

$$F_2 + F_4 = - \int_z^{z+\Delta z} \frac{\partial \bar{p} A}{\partial z} dz \quad (\text{IV.3.0.25})$$

For shear stress on the wall, we have:

$$\begin{aligned}
& - \int_z^{z+\Delta z} \int_{\theta=0}^{2\pi} \tau_p R d\theta dz - \int_z^{z+\Delta z} \tau_p 2eN dz \\
& = - \int_z^{z+\Delta z} \tau_p (2\pi R + 2eN) dz
\end{aligned}$$

or:

$$- \int_z^{z+\Delta z} \int_{\theta=0}^{2\pi} \tau_p R d\theta dz - \int_z^{z+\Delta z} \tau_p 2eN dz \quad (\text{IV.3.0.26})$$

The final equation for Momentum:

$$\begin{aligned}
& \int_z^{z+\Delta z} \left[ \frac{\partial \rho_L U_L^2 \pi (R^2 - (R - e(z))^2)}{\partial z} + (\Gamma A_{tube})(z) U_{Liz} \right] dz \\
& = - \int_z^{z+\Delta z} [\pi g \rho_L (R^2 - (R - e(z))^2) dz + \frac{\bar{p}A(z)}{\partial z} + p_i(z) 2\pi (R - e(z)) \frac{dl}{dz} \\
& \quad - \tau_i (R - e(z)) 2\pi - \tau_p (2\pi R + 2eN)] dz
\end{aligned}$$

With:

$$\bar{p}A = p(z) \pi (R^2 - (R - e(z))^2) - \rho \omega^2 \pi / 2 (R - e(z))^2 (R^2 - (R - e(z))^2) \quad (\text{IV.3.0.27})$$

$$+ \rho \omega^2 \pi / 4 (R^4 - (R - e(z))^4) \quad (\text{IV.3.0.28})$$

With shear stress can be evaluated as standard correlations:

$$\tau_p = C_f \frac{1}{2} \rho U_L^2 \quad (\text{IV.3.0.29})$$

In the laminar case, we have:

$$C_f = \frac{16}{Re_L} \quad (\text{IV.3.0.30})$$

Where:  $Re_L = \frac{\rho D_h U_L}{\mu}$

With:  $D_h = \frac{4S}{P}$

Where:  $S = \pi (R^2 - (R - e)^2)$  and  $P = 2\pi R + 2eN$

Therefore:

$$C_f = \frac{8\mu(\pi R + eN)}{\rho U \pi (R^2 - (R - e)^2)} \quad (\text{IV.3.0.31})$$

Therefore the shear stress becomes:

$$\tau_p = \frac{4\mu U(\pi R + eN)}{\pi(R^2 - (R - e)^2)} \quad (\text{IV.3.0.32})$$

Finally the momentum becomes:

$$\begin{aligned} & \int_z^{z+\Delta z} \left[ \frac{\partial(\rho_L U_L^2 \pi(R^2 - (R - e(z))^2))}{\partial z} + (\Gamma A)_{tot}(z) U_{Liz} \right] dz \\ = & \int_z^{z+\Delta z} \left[ -\pi g \rho_L (R^2 - (R - e(z))^2) - \frac{\partial(\bar{p} A_L)(z)}{\partial z} + p_i(z) 2\pi(R - e(z)) \frac{dl(z)}{dz} \right. \\ & \left. - \tau_i(R - e(z)) 2\pi - \tau_p(2\pi R + 2Ne(z)) \right] dz \end{aligned}$$

By replacing  $\bar{p} A_L$  by IV.3.0.28 and dividing by  $\rho_L \pi$ , the final equation for momentum is:

$$\frac{\partial(U_L^2(R^2 - (R - e(z))^2))}{\partial z} + \frac{(\Gamma A)_{tot}(z) U_{Liz}}{\rho_L \pi} \quad (\text{IV.3.0.33})$$

$$= -g(R^2 - (R - e(z))^2) - \frac{1}{\rho_L} \frac{\partial(p_i(z)(R^2 - (R - e(z))^2))}{\partial z} \quad (\text{IV.3.0.34})$$

$$+ \omega^2 \frac{1}{2} \frac{(R - e(z))^2 (R^2 - (R - e(z))^2)}{\partial z} - \omega^2 \frac{1}{4} \frac{\partial(R^4 - (R - e(z))^4)}{\partial z} \quad (\text{IV.3.0.35})$$

$$+ p_i(z) \frac{2}{\rho_L} (R - e(z)) \frac{dl(z)}{dz} \quad (\text{IV.3.0.36})$$

$$- \tau_i(R - e(z)) \frac{2}{\rho_L} - \tau_p(\pi R + Ne(z)) \frac{2}{\pi \rho_L} \quad (\text{IV.3.0.37})$$

And the equation of mass conservation:

$$\frac{\partial}{\partial z} (\rho_L U_L(z) \pi (R^2 - (R - e(z))^2)) + \Gamma A_{tot}(z) = 0 \quad (\text{IV.3.0.38})$$

These two equations have been used to evaluate the film thickness  $e$  of liquid along the evaporator.

# Bibliography

- [1] J. W. Palen, G. Breber, and J. Taborek. Prediction of flow regimes in horizontal tube-side condensation. *Int. Heat Transfer Engineering* 102(3), pages 47–57, 1979.
- [2] J.W. Coleman and S. Garimella . Two-phase flow regime in round, square and rectangular tubes during condensation of refrigerant r134a. *International Journal of Refrigeration* 26 (1), pages 117–128, 2003.
- [3] Y. Taitel and A.E. Dukler. A model for predicting flow regime transitions in horizontal and near horizontal gas-liquid flow. *AIChE Journal* 22, pages 43–55, 1976.
- [4] Y.Taitel, D.Barnea, and A.E.Dukler. Modelling flow pattern transitions for steady upward gas-liquid flow in vertical tubes. *AIChE J.*, 26:345–354, 1980.
- [5] J.El Hajal, J.R. Thome, and A. Cavallini. Condensation in horizontal tubes, part 1: two-phase flow pattern map. *International Journal of Heat and Mass Transfer* 46(18), 52:3349–3363, 2003.
- [6] R.Suliman, L.Liebenberg, and J.P. Meyer. Improved flow pattern map for accurate predictions of heat transfer coefficients during condensation of r-134a in smooth horizontal tubes and within the low-mass flux range. *International Journal of Heat and Mass Transfer*, 52:5701–5711, 2009.
- [7] J.W. Coleman and S.Garimella. Characterization of two-phase flow patterns in small diameter round and rectangular tube. *Inter. Journal of Heat and Mass Transfer*, 42:2869–2881, 1999.
- [8] C.Damianides and J.W. Westwater. Two-phase flow patterns in a compact heat exchanger and in small tube. *2nd UK National Conference on Heat Transfer*, 2:1257–1268, 1988.
- [9] Swanand M. Bhagwat and Afshin J. Ghajar. Experimental investigation of non-boiling gas-liquid two phase flow in upward inclined pipes. *Experimental thermal and Fluid Science*, 79:301–319, 2016.
- [10] J. El Hajal, J.R. Thome, and A. Cavallini. Condensation in horizontal tubes, part 1 : two-phase flow pattern map. *International Journal of Heat and Mass Transfer*, 46:3349–3363, 2003.

- [11] Alberto Cavallini, Davide Del Col, Marko Matkovic Luca Doretto, Claudio Zilio Luisa Rossetto, and Giuseppe Censi. Condensation in horizontal smooth tubes: A new heat transfer model for heat exchanger design. *Heat Transfer Engineering*, 27:31–38, 2006.
- [12] Hyoungsoon Lee, Issam Mudawar, and Mohammad M. Hasan. Experimental and theoretical investigation of annular flow condensation in microgravity. *International Journal of Heat and Mass Transfer*, 61:293–309, 2013.
- [13] C.W.Choi, D.I.Yu, and M.H.Kim. Adiabatic two-phase flow in rectangular micro channels with different aspect ratios: Part i - flow pattern, pressure drop and void fraction. *International Journal of Heat and Mass Transfer*, pages 616–624, 2011.
- [14] Georges EL ACHKAR. *Etude experimentale de la condensation convective à faible debit en micro-canaux*. PhD thesis, University Paul Sabatier, Toulouse, France, 2013.
- [15] Virginie Duclaux, Christophe Clanet, and David Quéré. The effects of gravity on the capillary instability in tubes. *Journal Fluid Mech.*, 556:217–226, 2006.
- [16] A. Agarwal, T.M. Bandhauer, and S. Garimella. Heat transfer model for condensation in non-circular microchannels. Seattle, USA, 2007. Proceedings of ASME International Mechanical Engineering Congress and Exposition (IMECE).
- [17] A. Agarwal, T.M. Bandhauer, and S. Garimella. Measurements and modelling of condensation heat transfer coefficients in noncircular microchannels. *International Journal of Refrigeration*, 33:1169–1179, 2010.
- [18] D. Barnea, Y. Luninski, and Y.Taitel. Flow pattern in horizontal and vertical in two phase flow in small diameter pipes. *Canadian Journal of Chemical Engineering*, 61:617–620, 1983.
- [19] O. Baker. Simultaneous flow of oil and gas, oil and gas journal. *International Journal of Refrigeration*, 53:185–195, 1954.
- [20] J.R.Fair. What do you need to know to design thermosyphon reboilers. *Petroleum Refiner*, 39:105, 1960.
- [21] J.M. Mandhane, G.A. Gregory, and K.Aziz. A flow pattern map for gas-liquid flow in horizontal pipes. *International Journal of Multiphase Flow*, 1:537–553, 1974.
- [22] G.F Hewitt and D.N Roberts. Studies of two-phase flow patterns simultaneous x-ray and flash photography. *AERE-M 2159, HMSO*, 1969.
- [23] G. Breber, J.W Palen, and J. Taborek. Prediction of horizontal tube-inside condensation of pure components using flow regime criteria. *Journal of Heat Transfer*, 104:471–476, 1980.

- [24] T. Fukano, A. Kariyasaki, and M. Kagawa. Flow patterns and pressure drop in isothermal gas-liquid concurrent flow in horizontal capillary tube. *ANS National Heat Transfer Conference*, 4:153–161, 1989.
- [25] J. Weisman, D. Duncan, J. Gibson, and T. Crawford. Effects of fluid properties and pipe diameter on two-phase flow patterns in horizontal lines. *International Journal of Multiphase Flow*, 5:437–462, 1979.
- [26] M.K. Dobson and J.C. Chato. Condensation in smooth horizontal tubes. *Journal of Heat Transfer*, 120:193–213, 1998.
- [27] A. Cavallini, D. Del Col, G.A. Longo, and L. Rossetto. Experimental investigation on condensation heat transfer and pressure drop of new hfc refrigerants (r134a, r125, r32, r410a, r236ea) in a horizontal smooth tube. *International Journal of Refrigeration*, 24:73–87, 2001.
- [28] Stéphane Lips and Josua P. Meyer. Experimental study of convective condensation in an inclined smooth tube. part i: Inclination effect on flow pattern and heat transfer coefficient. *International Journal of Heat and Mass Transfer*, pages 395–404, 2012.
- [29] C.T. Crowe. *Handbook of Multiphase Flow*. Washington State University, 2006.
- [30] R.W. Lockhart and R.C. Martinelli. Proposed correlation of data for isothermal two-phase component flow in pipe. *Chemical Engineering Progress*, 45:38–48, 1949.
- [31] L. Friedel. Improved friction pressure drop correlations for horizontal and vertical two-phase pipe flow. *European Two Phase Flow Group Meeting, Ispra*, page E2, 1979.
- [32] Dariusz Mikielewicz, Jan Wajs, Rafal Andrzejczyk, and Michal Klugmann. Pressure drop of hfe7000 and hfe7100 during flow condensation in minichannels. *International Journal of Refrigeration*, 68:226–241, August 2016.
- [33] H. Muller-Steinhagen and K. Heck. A simple friction pressure drop correlation for two phase flow in pipes. *Chem. Eng. Process*, 20:297–308, 1986.
- [34] B. M. Fronk and S. Garimella. Measurement of heat transfer and pressure drop during condensation of carbon dioxide in microscale geometries. Washington, August 8-13, 2010. Proc. of Int. Heat Transfer Conference.
- [35] Stéphane Lips and Josua P. Meyer. Experimental study of convective condensation in an inclined smooth tube. part ii: Inclination effect on pressure drop and void fraction. *International Journal of Heat and Mass Transfer*, pages 405–412, 2012.
- [36] D. Del Col, S. Bortolin, D. Torresin, and A. Cavallini. Flow boiling of r1234yf in a 1mm diameter channel. *Proceedings of 23rd IIR International Congress of Refrigeration, Prague, Czech Republic*, 2011.

- [37] K. Mishima and T. Hibiki. Some characteristics of air-water two phase flow in small diameter vertical tube. *Int. J. Multiphase Flow* 22, 22:703–712, 1996.
- [38] M. Zang and R.L. Webb. Correlation of two-phase friction for refrigerant in small diameter tubes. *Exp. Therm. Fluid Sci.*, 25:131–13, 2001.
- [39] M.M. Shah. A general correlation for heat transfer during film condensation inside pipes. *International Journal of Heat and Mass Transfer*, 22:547–556, 1979.
- [40] L.Tang. *Empirical study of new refrigerant flow condensation inside horizontal smooth hand micro-fin tubes*. PhD thesis, University of Maryland, 1999.
- [41] A. Cavallini, G. Sensi, D. Del Col, L. Doretti, G.A. Longo, L. Rossetto, and C. Zilio. Condensation inside and outside smooth and enhanced tubes - a review of recent research. *International Journal of Refrigeration*, 26:373–392, 2003.
- [42] Y.Yan and T.Lin. Condensation heat transfer and pressure drop of refrigerant r-134a in a small pipe. *International Journal of Heat and Mass Transfer*, 42:697–708, 1999.
- [43] Davide Del Col, Stefano Bortolin, Alberto Cavallini, and Marko Matkovic. Effect of cross sectional shape during condensation in a single square minichannel. *International Journal of Heat and Mass Transfer*, 54:3909–3920, 2011.
- [44] W.W. Akers, H.A. Deans, and O.K. Crosser. Condensation heat transfer within horizontal tubes. *Chemical Engineering Progress Symposium Series*, 55:171–176, 1959.
- [45] M.K. Dobson and J.C. Chato. Condensation in smooth horizontal tubes. *Journal of Heat Transfer*, 120:193–213, 1998.
- [46] W.W.Moser, R.L.Webb, and B.Na. A new equivalent reynolds number model for condensation in smooth tubes. *Journal of Heat Transfer*, 120:410–417, 1998.
- [47] D. Del Col, M. Bortolato, S. Bortolin, and M. Azzolin. Minichannel condensation in downward, upward and horizontal configuration. *Journal of Physics: Conference Series (1)*, 395, 2012.
- [48] S.M. Kim and I. Mudawar. Theoretical model for annular flow condensation in rectangular micro-channels. *International Journal of Heat and Mass Transfer*, 55:958–970, 2011.
- [49] I. Park, S.M. Kim, and I. Mudawar. Experimental measurement and modeling of downflow condensation in a circular tube. *International Journal of Heat and Mass Transfer*, 57:567–581, 2013.
- [50] Aritra Sur and Dong Liu. Adiabatic air-water two-phase flow in circular micro channels. *International Journal of Thermal Science* 53, pages 18–34, 2012.

- [51] P.M.Y. Chung and M. Kawaji. The effect of channel diameter on adiabatic two-phase flow characteristics in micro-channels. *International Journal of Multiphase Flow* 30, pages 735–761, 2004.
- [52] T. Cubaud and C.M. Ho. Transport of bubbles in square micro-channels. *Physics of Fluids* 16, pages 4575–4585, 2004.
- [53] J.L. Xu, P. Cheng, and T.S. Zhao. Gas-liquid two-phase flow regimes in rectangular channels with mini/micro gaps. *International Journal of Multiphase Flow* 25, pages 411–432, 1999.
- [54] K.A. Triplett, S.M. Ghiaasiaan, S.I. Abdel Khalik, and D.L. Sadowski. Gas-liquid two-phase flow in micro-channels, part i: two-phase flow patterns. *Int. J. Multiphase* 25, pages 377–394, 1999.
- [55] Ahmad Odaymet and Hasna Louahlia-Gualous. Experimental study of slug flow for condensation in a single square microchannel. *Experimental Thermal and Fluid Science* 38, pages 1–13, 2012.
- [56] Béatrice Méderic, Pascal Lavieille, and Marc Miscevic. Void fraction invariance properties of condensation flow inside a capillary glass tube. *International Journal of Multiphase Flow*, 31:1049–1058, 2005.
- [57] S. Garimella, J.D. Killon, and J.W. Coleman. An experimental validated model for two phase pressure drop in the intermittent flow regime for noncircular microchannels. *Journal of Fluids Engineering*, 125:887–894, 2003.
- [58] T.J. Rabas and P.G. Minard. Two types of flow instabilities occurring inside horizontal tubes with complete condensation. *Heat Transfer Engineering*, 8:40–49, 1987.
- [59] P.A. Gauglitz and C.J. Radke. An extended evolution equation for liquid film breakup in cylindrical capillaries. *Chemical Engineering Science* 43, pages 1457–1465, 1988.
- [60] H. Teng, P. Cheng, and T.S. Zhao. Instability of condensate film and capillary blocking in small-diameter-thermosyphon condensers. *International Journal of Heat and Mass Transfer*, 42:3071–3083, 1999.
- [61] A. Tabatabai and A. Faghri. A new two-phase flow map and transition boundary accounting for surface tension effects in horizontal miniature and micro tubes. *ASME Journal of Heat Transfer*, 123:958–968, 2001.
- [62] M. Miscevic, P. Lavieille, , and B. Piaud. Numerical study of convective flow with condensation of a pure fluid in capillary regime. *Int. J. Heat Mass Transfer* 52, pages 5130–5140, 2009.

- [63] Benjamin Piaud, Pascal Lavieille, and Marc Miscevic. About stability of a vapour jet condensing in a micro channel. *Proceedings of the International Heat Transfer Conference IHTC14-22862*, 2010.
- [64] S. Koyama, K. Kuwahara, K. Nakashita, and K. Yamamoto. An experimental study on condensation of refrigerent r134a in a multi-port extruded tube. *International Journal of Refrigeration*, 24:425–432, 2003.
- [65] H.Haraguchi, S.Koyama, and T.Fujii. Condensation of refrigerants hfc22, hfc134a and hfc123 in a horizontal smooth tube. *Transactions of JSME*, 60:245–252, 1994.
- [66] T.M. Bandhauer, A. Agarwal, and S. Garimella. Measurements and modeling of condensation heat transfer coefficients in circular microchannels. *Transactions of ASME*, 128-14672:1050–1059, 2006.
- [67] A. Agarwal and S. Garimella. Modeling of pressure drop during condensation in circular and non-circular microchannels. *Proceedings of the IMECE 2006*, IMECE2006-14672:245–252, 2006.
- [68] J.S. Shin and M.H. Kim. An experimental study of condensation heat transfer inside a minichannel with a new measurement technique. *International Journal of Multiphase Flow*, 30:311–325, 2004.
- [69] J.S.Shin and M.H.Kim. An experimental study of condensation heat transfer inside circular and rectangular mini-channels. *Heat Transfer Engineering*, 26:36–44, 2005.
- [70] W.W. Akers, H.A. Deans, and O.K. Crosser. Condensation heat transfer within horizontal tubes. *Chemical Engineering Progress Symposium Series*, 55:171–176, 1959.
- [71] *Experiments on R-22 condensation heat transfer in small diameter tubes*, volume 55, Korea, 1997. Proceedings of the KSME Autumn Conference.
- [72] C. Yang and R.L. Webb. Condensation of r12 in small hydraulic diameter extruded aluminum tubes with and without micro-fins. *International Journal of Heat and Mass Transfer*, 39:791–800, 1996.
- [73] J.R. Thome. *Engineering Data Book III*. <http://www.wlv.com/products/databook/db3/DataBookIII.pdf>, 2008.
- [74] Marco Azzolin, Stefano Bortolin, Lan Phuong Le Nguyen, and Davide Del Col. A new test section for investigation of convective condensation: Calibration and preliminary results. Kyoto, Japan, September 14-18, 2015. 10th International Conference on two phase systems for ground and space applications.

- 
- [75] A. Donniacuo, R. Charnay, R. Mastrullo, A.W. Mauro, and R. Revellin. Film thickness measurements for annular flow in minichannels: Description of the optical technique and experimental results. *Experimental Thermal and Fluid Science*, 69:73–85, 2015.
- [76] Ting Xue, Liuxiangzi Yang, Penghui Ge, and Liqun Qu. Error analysis and liquid film thickness measurement in gas-liquid annular flow. *Optik*, 126:2674–2678, 2015.
- [77] Damien Serret. *Etude expérimentale de l'ébullition nucléée sur un site isolé: dynamique de croissance et transferts de chaleur*. PhD thesis, University Aix Marseille, Marseille, France, 2010.
- [78] R. K. Shah, A. L. London, Thomas F. Irvine, and James P. Hartnett. *Laminar Flow Forced convection in Ducts*. Academic Press, New York, 1978.



Titre : Effet de la gravité sur la condensation convective à faible vitesse massique

Les écoulements diphasiques sont couramment utilisés dans de nombreux domaines dont, en particulier, le domaine spatial. La performance de ces systèmes est entièrement régie par les couplages se produisant entre les écoulements et les transferts de chaleur. Cette particularité a conduit, depuis les dernières décennies, au développement de nombreuses études sur les écoulements diphasiques en microgravité. Afin d'accroître la connaissance sur le comportement thermo-hydraulique de ces systèmes thermiques, la présente étude se focalise sur l'étude de la condensation dans un mini-tube en présence ou non de la force gravitationnelle. Pour étudier l'effet de la gravité sur cette configuration, un premier modèle instationnaire d'écoulement diphasique a été développé. Parallèlement, une analyse des effets de la gravité sur l'hydrodynamique et les transferts thermiques a été menée dans deux sections d'essai possédant un diamètre interne commun de 3,4 mm et des vitesses massiques faibles à modérées. La première étude a été réalisée au cours de la 62e campagne de vols paraboliques de l'ESA. Elle a été dédiée à la détermination des coefficients de transfert de chaleur quasi-locaux se produisant à l'intérieur d'un tube de cuivre. Afin de visualiser également les régimes d'écoulement présents, un tube en verre a été inséré au sein de cet échangeur. L'effet de la gravité sur les écoulements et les transferts a ainsi été déterminé. La seconde expérience, menée au sol, a porté sur l'étude d'un écoulement de vapeur descendant au sein d'un tube en saphir placé verticalement. Un protocole de mesure permettant d'obtenir simultanément l'épaisseur du film de liquide ruisselant et le coefficient d'échange local associé a été développé.

Mots-clés : micro-gravité, condensation convective, HFE-7000, mini-tube, transfert thermique, visualisation, faible vitesse massique

Title: Effect of gravity on convective condensation at low mass velocity

Liquid-vapor two-phase flows have common applications in many fields including space thermal management systems. The performances of such systems are entirely associated to the coupling between thermal and hydrodynamic phenomena. Therefore, two-phase flows in microgravity condition have emerged as an active research area in the last decades. In order to complete the state of the art and to contribute to the increase in the knowledge of hydrothermal behavior of two-phase thermal management systems, the present study was conducted on convective condensation inside a mini tube, both in normal and micro gravity conditions. To analyze the effect of gravity on such flows, a preliminary transient modeling of the two-phase flow has been established. Simultaneously, an experimental investigation was carried out on the hydrodynamic and thermal behaviors of condensation flows in two test sections of 3.4 mm inner diameter at low and intermediate mass velocities. The first experiment was conducted during the 62nd ESA parabolic flights campaign. The test section was made with copper and allowed measurements of the quasi-local heat transfer coefficient. A glass tube was also inserted in the middle of the test section for the visualization of the two-phase flow regime. From this study, the changes in heat transfer coefficient and flow regime according to gravity variations were determined. The second experiment was carried out on ground in a sapphire tube installed vertically considering downward flow. The set-up was designed in order to measure simultaneously the local heat transfer coefficient and the thickness of the liquid film falling down along the tube wall

Keywords : micro-gravity, convective condensation, HFE-7000, mini-tube, heat transfer, visualisation, low mass velocity